Kinematics and physical properties of young proto-clusters

A thesis submitted to The University of Manchester for the degree of
Doctor of Philosophy
in the Faculty of Engineering and Physical Sciences

2010

Ana Duarte Cabral
Jodrell Bank Centre for Astrophysics
School of Physics and Astronomy

Contents

List of Figures

List of Tables

The University of Manchester

ABSTRACT OF THESIS submitted by Ana Duarte Cabral
for the Degree of Doctor of Philosophy and entitled
Kinematics and physical properties of young proto-clusters. November 2010

The formation of stars begins with the fragmentation of molecular clouds and the formation of dense cores. This fragmentation process can either be the result of classical gravitational instabilities or triggered by some external event. The gas and dust of young protoclusters often hold the imprints of the initial conditions and triggers of that specific star forming episode.

In this context, my thesis work is a study of the gas properties of young protoclusters within the Gould Belt. The first part of my work consists of a detailed study of the young Serpens star forming region with CO isotopologues. This study has revealed a complex temperature, column density and velocity structure. I proposed a scenario where a collision between two filamentary clouds or flows is responsible for the observed complex structure and the most recent burst of star formation in Serpens. This hypothesis was tested with SPH simulations and provides a plausible scenario.

I am currently extending this work to other regions with a variety of star formation efficiencies, in search of the particular physical properties and dynamics of a molecular cloud that allow or prevent clouds to be in the verge of forming stars. As such, I have included in this manuscript my study of the gas in the B59 star forming region, the only active clump in the Pipe Nebula. The results from this study have shown it to be very different from Serpens, even though further studies are needed to provide a complete picture of the region. B59 was taken as the starting point for a larger study of the entire Pipe Nebula, driven by the peculiarly low star formation efficiency in the cloud and a test to the physical properties of cores prior to star formation.

Declaration

I declare that no portion of the work referred to in the thesis has been submitted in support of an application for another degree or qualification of this or any other university or other institute of learning.

Ana Duarte Cabral
Jodrell Bank Centre for Astrophysics
School of Physics and Astronomy
Alan Turing Building
University of Manchester
Manchester
M13 9PL

Copyright Statement

Dedication

Por estares sempre lá, independentemente da distância ou do porquê. Por seres para mim muito mais do que o que o teu papel te incumbe, dedico esta tese à minha melhor amiga, a minha mãe.

Acknowledgements

First of all, I would like to acknowledge the financial support from the Fundação para a Ciência e a Tecnologia of Portugal, who have funded my PhD under the grant reference SFRH/BD/36692/2007.

Secondly, I would like to thank my thesis examiners, Eamonn Kerins and João Alves, who not only accepted the role of reading and judging these two hundred pages under a tight schedule, but also made my *viva* a very pleasurable experience. I would like to thank them for being enthusiastic and encouraging, for turning the three hours of my *viva* into a discussion instead of an interrogation, and for making me come out of the room with a big smile.

Throughout the three years of my time in Manchester, a number of people have made my days just that little bit brighter, and made up for a sun who was always too shy to shine.

The very first person is my supervisor, Gary Fuller, who gave me the opportunity to come and work with him. Gary was always enthusiastic about my results (no matter how good they were) and always made me feel that I was on the good direction, even when the answer for my question was in the radiative transfer equation that, for the fifth time around, I still could not remember. “It’s OK”, he’d say. I would like to thank Gary for giving me the freedom to follow and study the bits of science that I loved the most, and for giving me the space to grow and think on my own. It was always a pleasure to discuss science with him and I will undoubtedly miss it.

The second person that I want to thank is Nicolas, for believing in me and making me believe in myself. I have first met him as a postdoc working with Gary, whose assignment was to teach me how to use GILDAS. But he taught me much more than that. He was always there to answer my work questions, no matter how basic they

were saying that “there are no stupid questions, only stupid answers”. But more than making me a better professional, he has made me a better person. More calm, more cheerful, more tolerant and more aware of the people around me. He has shown me a new way to look and appreciate the world. Thanks to him, I have developed a decoder of “frenglish” (English spoken by a French) and I have learned how to appreciate (or at least understand) a whole new set of jokes. I want to thank Nico for his patience and presence throughout this time, and for picking me up whenever I would fall.

Then, the people I have met throughout these three years who contributed to many smiles and laughters and that ultimately became real friends. Firstly Marta who only in Manchester I got the chance to really know, even though we had done our degree in astronomy together. She has been a great company, a great person to talk to and a good friend who was there for me in the hardest times, with her contagious laughter that is always a joy to hear. Then Claire, the first open door in Manchester, my very first Manchester tour guide. She is someone always ready to help, with a very soft heart behind that hard armor. It is pleasure to have her as a friend, despite her very own (and sometimes very bad!) jokes. There is also miss Kerry, who has taught me some funny English (or better yet, “Yorkish”) words. She is a great opposite of me in so many ways that it makes her the best person to show me how it is to see it from the other side. Kerry has a great sense of humour and has a very kind side to those she cares for (I think I’m there!). For the boys, there’s Bruno, zee marseillais, who is always consistent, always ready to offer a hand, always a great listener and always a great fun. I will have trouble finding such a great salsa partner who makes my Tuesday nights so enjoyable. Then Giampaolo who is a gentleman with a big heart and that shares some of my perfectionist (or nitpicking) instincts. With his serious look, he has such a peculiar sense of humour that my jaws end up hurting from laughing so hard. I also want to thank Clive, who is always full of ideas and always busy, and yet always finds time to help me make my IDL work. He has become a good friend and its a joy when he comes now and then to my office, attempting to scare me but usually failing. Finally, there are a lot more colleagues and friends from inside and outside the department, that I have made along this time, which in one way or another, have made a difference to my life experience in Manchester. Among those are Mike, Czarek, Lizette, Adam, Danny, Roisin and other office mates that came and went throughout the years (they know who they are). I also need to thank Jenny Hatchell, Jaime Pineda and Antonio Chrysostomou who have helped me, at different stages of my work, to find a good direction to move towards.

Before coming to Manchester, though, I have left behind some very important people that were part of my life back in Portugal. My very best friends have kept in touch and have always been that solid base behind my path. I would like to thank them for being there all this time, and not let the distance dictate the friendships. Among those are Cátia, Alexandra, Maria João, Margarida and Eurico.

With a link stronger than those friendships, I finish my acknowledgments by thanking my family. My dad, always so proud of me, that even though he never cries, I can see in his eyes that he suffers every single time he sees me go again. My mum, who is indescribably the one that misses me the most, the one that always supports me and trusts me in each and every decision I make, no matter what, the one that would never tell me “I told you so” if it all went wrong. My brother, my lovely brother, for whom I owe so much of the person I am today. He made me a curious person, thrilled by challenges, a lover of gadgets and games. He also taught me how to lose, even if just because he was always winning. He has a great heart and is a great confident, who has never let me down. My sister in law, Sofia, a everlasting friend, that saw me playing with barbies when I was a kid, and that would allow me to paint in her drawing school assignments, even if I was too bad to keep the colour inside the lines. Behind her strong personality and views, she has never judged me. On the contrary, she has become a real sister in my heart, that has been there no matter what.

Supporting Publications

The physical and dynamical structure of Serpens: two very different sub-(proto)clusters

A. Duarte-Cabral, G. A. Fuller, N. Peretto, J. Hatchell, E. F. Ladd, J. Buckle, J. Richer, and S. F. Graves.

A&A, 519:A27+, September 2010. doi: 10.1051/0004-6361/200913919

The JCMT Legacy Survey of the Gould Belt: a first look at Serpens with HARP

S. F. Graves, J. S. Richer, J. V. Buckle, A. Duarte-Cabral, G. A. Fuller, M. R. Hogerheijde, et al.

MNRAS, 409, 1412, December 2010.

Was a cloud-cloud collision the trigger of the recent star formation in Serpens?

A. Duarte-Cabral, C. L. Dobbs, N. Peretto and G. A. Fuller.

Accepted for publication in A&A, January 2011.

Part I

Introduction

Chapter 1

Overview

1.1 Molecular clouds

Molecular clouds (MCs) are the stellar nurseries as they provide the conditions for the fragmentation and collapse of smaller and denser sub-structures which will later give birth to stars. The early stages of star formation in MCs are highly obscured, not due to the molecular component of the cloud, but due to the optical star light absorption by the dust component, the dust grains. Not allowing the external radiation to pass through, these clouds maintain low temperatures, reaching $\sim$ 10K in the most obscured inner regions. Even though it is obscured in the optical, we can access the physical properties of MCs by observing them from infra-red to radio wavelengths, where the dust becomes optically thin. Different environments within a cloud can be probed when observing the continuum emission that traces the dust component or different molecules and transitions that trace the gas emission. Such observations have been the drivers of our current understanding of star formation in the Galaxy.

In this section I will present the major observational characteristics and theories behind the formation and evolution of MCs, before moving into the process of star formation itself. I will summarise the current ideas about the formation of these large structures, their morphology, properties, chemistry, their equilibrium state and what

Figure 1.1: Image of the Carina Nebula, a high mass star forming region, showing dark filaments of cool dust against the glowing gas of the nebula. This glow is mainly from hot hydrogen heated by the strong radiation from massive young stars. This picture was created from images taken through red, green and blue filters in the visible with the Wide Field Imager on the MPG/ESO 2.2-metre telescope at ESO's La Silla Observatory in Chile. Credit: ESO.

can bring them to collapse into the progenitors of stars and stellar clusters.

1.1.1 Formation of molecular clouds

Molecular clouds are the densest and coolest regions in the galactic interstellar medium (ISM). How these clouds form is, however, not clear. One possibility is that a MC results from converging large scale flows of the diffuse warm neutral medium, where mass is gradually gathered to form a cloud with denser regions where the material quickly cools down to 50 K at densities around 30 cm^{-3} and 10 K when densities reach 10^4 cm^{-3}(Ballesteros-Paredes et al. 1999b; Hennebelle et al. 2008; Vazquez-Semadeni 2010, and references therein). Thermal instabilities or large scale gravitational instabilities are thought to play an important role for this transition between the warm medium into a cold-dense molecular phase (Hennebelle et al. 2008). In fact, at the densities needed for molecular hydrogen (H_2) and carbon monoxide (CO) molecules to start being formed, the conditions are such that the cloud also becomes magnetically su-

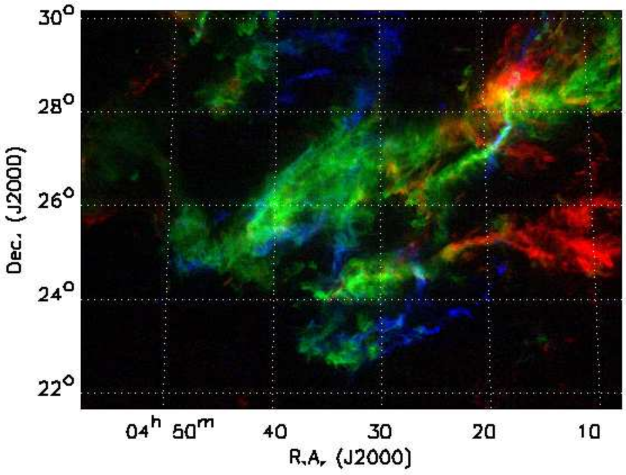

Figure 1.2: Colour-coded image of the integrated intensities in three velocity intervals of FCRAO ^{13}CO J=1→0 in Taurus, with emission at velocities of 3-5 km^{-1} coded blue, 5-7 km^{-1} coded green, and 7-9 km^{-1} coded red (Goldsmith et al. 2008).

percritical (definition in section 1.1.6) and self-gravitating (Vazquez-Semadeni 2010). In this scenario of convergent flows, MCs are continuously gathering mass and are not necessarily in equilibrium with the gravitational energy balanced against overall collapse with turbulence and/or magnetic fields, as is often thought.

1.1.2 Filamentary structure of molecular clouds

MCs are highly structured, with irregular edges, an overall filamentary and often wind-blown appearance (e.g. Fig. 1.1 and 1.2). They comprise several clumps which are velocity coherent parsec-scale structures with a mean density of 10^3 cm^{-3}. Within a clump, there are several dense cores, i.e. sub-parsec scale structures, with mean densities higher than 10^4 cm^{-3} which are typically gravitationally bound single peaked regions from which simple stellar systems will form (e.g. Blitz 1991; Williams et al. 2000; Bergin and Tafalla 2007).

The origin of the filamentary structure (some of which can reach 10pc of length) has been subject of debate over the past years. Not only do the MCs have their mass distributed over a main filamentary structure, as they also appear to “radiate” smaller filaments perpendicular to the main structure. Several hypotheses have been suggested as possibly responsible for such a morphology. For instance, the cavities produced by outflows could contribute to the formation of perpendicular filaments that radiate from the main structure (e.g. Li and Nakamura 2006), but this is unlikely to be the case in all star forming regions, given that we see these perpendicular filaments in quiescent clouds such as the Pipe Nebula. Then, turbulent hydrodynamic simulations (e.g. Klessen et al. 2004; Vázquez-Semadeni et al. 2007) suggest that the collision between flows or clouds is also capable of producing such filamentary structures. In addition, the magnetic field observed in highly filamentary clouds is also thought to have an important role in shaping the MCs. In such observations, e.g. Goldsmith et al. (2008) for Taurus, Alves et al. (2008) for the Pipe Nebula, we see that the magnetic field lines run perpendicular to the main filamentary structure (Fig. 1.3). This idea is supported by Magneto-hydrodynamics (MHD) simulations (e.g. Nakamura and Li 2008) which show that such a magnetic field allows the material to settle along the field lines and then converge onto the perpendicularly aligned main condensation. Finally, when in the vicinity of an OB association, the winds and shocks that arise from the association could compress the material of the cloud and contribute for shaping a more dispersed material into an elongated structure, often with sharp edges (e.g. Lupus I Molecular Cloud, Tothill et al. 2009). Myers (2009) proposed a model, where such compressions turn a given clump into a self-gravitating modulated layer, producing a hub-filamentary structure.

Independently of how molecular clouds form and become filamentary, it is well known that star formation takes place in the denser clumps formed within those thin and long filaments. Most of the material of a MC resides in the larger structures as low density gas at densities between 100 and 1000 cm^{-3}. Only a small fraction of the total mass ($\sim 10\%$) is associated with these dense star forming cores seen in submillimetre emission, at densities higher than 10^4 cm^{-3} (e.g. Enoch et al. 2007).

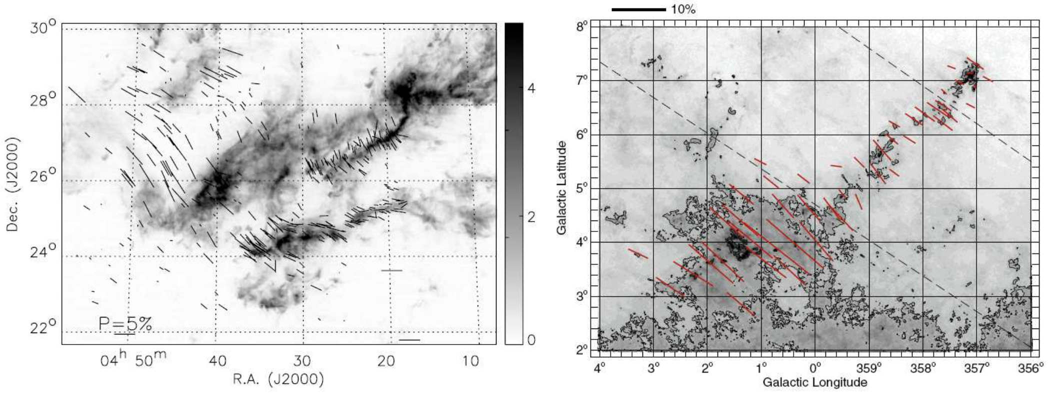

Figure 1.3: Left: Magnetic field direction superimposed on the distribution of ^{13}CO integrated intensity from 5 - 8 kms^{-1} with units of K kms^{-1} indicated on the bar of the right (image from Goldsmith et al. 2008). Right: Mean polarization vectors overplotted on the dust extinction map of the Pipe nebula obtained by Lombardi et al. (2006) (image from Alves et al. 2008).

1.1.3 Mass distribution in molecular clouds

During the last two decades a lot of effort has been made to understand the link between the mass distribution of stars, i.e. the IMF (Salpeter 1955; Chabrier 2003) and the gas/dust mass repartition in molecular clouds. One approach which has been extensively used consists in segmenting molecular cloud images into individual entities for which we measure masses. Then the mass distribution of these entities can be constructed and compared to the IMF. This has been performed for CO clumps for which the mass distribution follows a power-law and turns to be much flatter than the high-mass end of the IMF, the so-called Salpeter slope (e.g. Kramer et al. 1998). A similar approach can be used for prestellar cores, preferentially observed in dust continuum. These core mass functions (CMF) appear to follow a similar shape as the IMF, down to very low masses and with a power law steeper than that for CO clumps, similar to the Salpeter slope, at the high-mass end (e.g. Motte et al. 1998; Alves et al. 2007; Nutter and Ward-Thompson 2007; Rathborne et al. 2009; Könyves et al. 2010, Fig. 1.4). Such a similarity between the IMF and CMF suggests that stellar masses are determined by the processes that fragment molecular clouds at the smallest scales, and that prestellar cores are indeed the direct progenitors of stars. However, the completeness limit and small statistics of the current studies does not allow to probe accurately neither low- nor high-mass ends of the CMF. Other studies also suggested there may not be a one-to-one relation from CMF and IMF if cores of different masses have different lifetimes (e.g. Hatchell and Fuller 2008; Smith et al. 2009), or if cores could merge together to form more massive objects. On the other end, a massive core will not necessarily form a high mass star, as it can fragment into several smaller cores as it evolves. Therefore, the origin of such a shape of the IMF and CMF, and the link between them, if any, is not clear.

Other aspects of the the mass repartition in molecular clouds can be observed by studying their column density distributions. Such studies have been performed in a number of regions, using a number of different techniques. Log-normal column density distributions are observed for column density measurements using near-IR extinction maps, at low extinction ($A_v < 0.2$ mag, Lombardi et al. 2010). A significant deviation is observed at larger extinction values in regions of active star formation, where gravity dominates, with an excess of high column density regions (Kainulainen et al. 2009; Lombardi et al. 2010). These behaviours in the column density distributions were predicted in a number of numerical models (e.g. Vázquez-Semadeni and García 2001), as well as a log-normal probability density function (PDF) of volume density (e.g. Vazquez-Semadeni 1994; Scalo et al. 1998; Klessen 2000). Observationally, by assuming a certain depth, Peretto and Fuller (2010) measured the volume density of fragments within infrared dark clouds (IRDCs) with the objective to constrain the existence of such a log-normal PDF. They found a difference in the volume distribution between bound and unbound fragments. Unbound fragments show a very steep distribution (possibly log-normal) and nearly independent of the mass range considered, whereas the bound fragments have a less steep distribution that evolves with mass range. Their interpretation suggests that the unbound fragments have a common origin (perhaps turbulence generated), and that the physics of bound ones is dominated by an interplay of several processes (likely both gravity and turbulence). Such a result can be used as a test of models or simulation, which have not yet done a similar study for

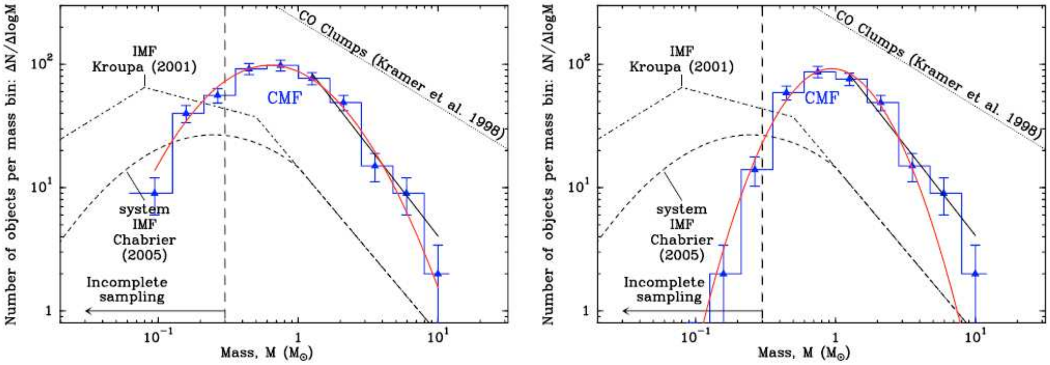

Figure 1.4: Figure from Könyves et al. (2010) showing the differential mass function (dN/dlogM) of 452 starless cores (left) and of 314 candidate prestellar cores (right) in the Aquila main subfield, approximated with a log-normal fit (red curve). The dash-dotted line shows the single-star IMF (e.g. Kroupa 2001) and the dashed curve corresponds to the unresolved system IMF by Chabrier (2005). The high mass end is described by the Salpeter IMF (dN/dlogM$\propto$M$^{-1.35}$) and the dotted line on the top-right corner shows typical mass distribution of low-density CO clumps (as dN/dlogM$\propto$M$^{-0.6}$, e.g. Kramer et al. 1998). For both samples, the high-mass end of the CMF are well fitted by a power law (dN/dlogM$\propto$M$^{-1.5\pm0.2}$), consistent with the Salpeter. The starless cores sample, however, is equally well fitted by a log-normal distribution.

comparison.

1.1.4 Stability of molecular clouds

A molecular cloud in an overall state of free fall collapse would be very efficient turning gas into stars by constantly forming high density regions. This would lead to a high star formation rate (SFR), around 0.1 $M_\odot$ yr^{-1} for an individual giant molecular cloud of 10^5 $M_\odot$, equivalent to 10^3 $M_\odot$ yr^{-1} for the entire Galaxy. However the observed SFR of only ~2 $M_\odot$ yr^{-1} in the Galaxy, suggests that star formation efficiency is very low, around a few %. Hence, molecular clouds are supported against global collapse by some mechanism, but they are too cold (~10K) to be supported by thermal pressure. The cloud's magnetic field or macroscopic motions may be responsible for this support mechanism. In this section, I will present the virial theorem and the physical processes likely to take part in the energy balance of molecular clouds.

Virial theorem

The virial theorem (Clausius 1870) is often used as a measure of a cloud's stability and binding energies. It is derived from the momentum equation (Eq. 1.1):

$$\rho\frac{D\mathbf{v}}{Dt} = -\nabla P - \rho\nabla\phi - \nabla P_{mag} + \frac{1}{4\pi}\mathbf{B}.\nabla\mathbf{B} \tag{1.1}$$

where the first term represents the kinetic term, including the macroscopic (or turbulent) velocities, ρ is the density, $\mathbf{v}$ is the gas velocity field; the term, ∇P, represents the pressure gradient, with P being the sum of external pressure (P_{ext}) and mean internal thermal pressure ($P_{thermal}$); ϕ is the gravitational potential; and finally P_{mag} introduces the effect of the magnetic pressure ($P_{mag} = B^2/8\pi$ where B is the magnetic field) and the last term represents the magnetic tension.

For simplicity and motivated by observational limitations on constraining the magnetic field, I will present the virial analysis in the absence of magnetic fields in the cloud. By taking the scalar product with the position vector and integrate in volume, the first term becomes $\int_V \rho\mathbf{r}\frac{D\mathbf{v}}{Dt}dV = \frac{1}{2}\frac{d^2I}{dt^2} - 2E_{kin}$, where I is the inertia and E_{kin} is the kinetic energy per unit volume correspondent to macroscopic motions (including the turbulence). The pressure term becomes $\int_V \mathbf{r}\nabla P dV = 3V(P_{thermal} - P_{ext})$ and the potential energy term simply becomes $\int_V \rho\mathbf{r}\nabla\phi dV = -E_{pot}$, where E_{pot} is the gravitational potential energy.

Internal Energy

Defining the internal energy of the system, E_{int}, as the sum of the kinetic energy (from macroscopic motions) and the thermal energy (from microscopic motions), we have

$$E_{int} = E_{kin} + \frac{3}{2}VP_{thermal} = \frac{3}{2}\frac{MkT_{turb}}{\mu m_{\mathrm{H}}} + \frac{3}{2}NkT_{kin}. \tag{1.2}$$

where M is the total mass, μ is the mean molecular weight, m_H is the mass of Hydrogen, N is the number of particles, T_{turb} is the temperature equivalent to the non-thermal (or turbulent) motions and T_{kin} is the thermal kinetic temperature. These two temperatures can be grouped into one single effective temperature $T_{\rm eff}$ and equation 1.2 becomes

$$E_{int} = \frac{3}{2}\frac{MkT_{eff}}{\mu m_{\rm H}}. \tag{1.3}$$

We can also express this by the equivalent velocity dispersion. Being $E = (1/2)M\sigma^2$, then E_{int} can be written as a function of the velocity dispersion as $E_{int} = 3M\sigma^2_{obs}$. Note that σ_{obs} is the observed velocity dispersion in a cloud and it comprises both the thermal and non-thermal contributions, i.e., $\sigma^2_{obs} = \sigma^2_{ther} + \sigma^2_{non-ther}$.

Gravitational Potential Energy

On the other hand, the gravitational potential energy of the system is described by

$$E_{pot} = -\int_m \frac{GM(r)}{r}dm \tag{1.4}$$

Assuming a spherical symmetry and a density profile as r^{-a}:

$$dm = \rho(r)dV \tag{1.5}$$

$$\rho(r) = \rho_o r^{-a} \tag{1.6}$$

$$M(r) = \int 4\pi\rho_o r^{2-a}dr = 4\pi\rho_o\frac{r^{3-a}}{(3-a)},\ a \neq 3 \tag{1.7}$$

Equation 1.4 becomes

$$E_{pot} = -\alpha\frac{GM^2}{R} = -\frac{(3-a)}{(5-2a)}\frac{GM^2}{R},\ a \neq 3\,\&\,a \neq 2.5 \tag{1.8}$$

where G is the universal constant of gravitation, M is the mass of the structure, R is the radius and α is a constant dependent on the density profile assumed (r^{-a}): α is 3/5 for a uniform density profile, 2/3 when $\rho \propto r^{-1}$, 3/4 when $\rho \propto r^{-1.5}$ and 1 when $\rho \propto r^{-2}$.

Virial Equilibrium

Equation 1.1 in the absence of magnetic field can be written as

$$\frac{d^2I}{dt^2} = 2E_{int} + E_{pot} - 3VP_{ext}. \tag{1.9}$$

When in equilibrium, the second derivate of inertia is zero. Therefore, the virial equation (1.9) becomes:

$$2E_{int} = -E_{pot} + 3VP_{ext} \tag{1.10}$$

which, in the particular case of absence of external pressure, is simply $2E_{int} = -E_{pot}$ or, in terms of observables,

$$3\sigma_{obs}^2 = \alpha \frac{GM_{virial}}{R}. \tag{1.11}$$

This can be used observationally to calculate a virial mass, M_{virial}, for a given structure for which we know the radius and velocity dispersion, under the conditions of no magnetic field or external pressure. It can give an estimate of the mass that the cloud would need to be gravitationally stable. However, as pointed by Ballesteros-Paredes (2006), the use of this equation to judge the stability of a given cloud can not be used without criticism, given the number of assumptions used and uncertainties associated with this calculation. It is best used as a tool for comparison of stability conditions within a given cloud, rather than an absolute measure of how bound a structure is.

1.1.5 Instabilities: the ingredient for gravitational collapse

To form stars within a molecular cloud in equilibrium, the energy balance has to be perturbed by instabilities that can trigger a gravitational collapse. Depending on the instabilities, perturbations may grow or decay. If decaying, the cloud will remain (or return) to a state of equilibrium. If growing, then they will succeed in providing the necessary ingredients for the gravitational collapse. These are the instabilities we need for star formation to occur in any given cloud. In this section I will describe some of the most common gravitational stability parameters, and will briefly introduce some of the instabilities that can play a role in the fragmentation of a molecular cloud.

Jeans length

Implemented by Jeans (1961), the Jeans length is a parameter to study the scale at which an instability grows to provoke gravitational collapse of a given cloud.

Starting from a static hydrodynamical equilibrium state, and without inclusion of magnetic fields or external pressure, the momentum equation (eq. 1.1) can be re-written as:

$$-\nabla P - \rho\nabla\phi = 0 \tag{1.12}$$

which yields that a molecular cloud is supported against gravity by the internal pressure gradient. The Poisson equation gives

$$\nabla^2\phi = 4\pi\rho G \tag{1.13}$$

and the equation of state for an isothermal gas is defined as

$$P = c_s^2\rho \tag{1.14}$$

where c_s is the sound speed of the medium

$$c_s^2 = \frac{\partial p}{\partial\rho} = \frac{kT}{\mu m_{\rm H}}. \tag{1.15}$$

The analysis of Jeans included other simplifications such as an infinite, isothermal and homogeneous medium (where ρ is constant). As soon as any perturbation is inflicted in such a system, the gravity will attempt to collapse the medium at a free-fall timescale t_{ff}, whereas the thermal pressure will attempt to restore balance at a timescale t_s necessary for the gas traveling at the sound speed to cross the cloud. The free fall time is defined, for a uniform spherical cloud with density ρ_0, and in the absence of any pressure or magnetic fields, as (Spitzer 1978):

$$t_{ff} = \left(\frac{3\pi}{32G\rho_0}\right)^{1/2}. \tag{1.16}$$

If t_{ff} is shorter than t_s then the gravity will win against the thermal pressure. Jeans calculations lead to a typical length scale, the Jeans length (l_{jeans}, eq. 1.17). Any perturbations with a longer wavelength would grow exponentially and cause the gravitational energy to win over the pressure support. Perturbations with a shorter wavelength would decay and the cloud would remain in equilibrium.

$$l_{jeans} = \left(\frac{\pi k T_k}{G \mu m_H \rho} \right)^{1/2} \tag{1.17}$$

The Jeans mass, M_{jeans}, is the amount of mass contained in a sphere with a Jeans length diameter,

$$M_{jeans} = \frac{4\pi}{3} \rho \left(\frac{l_{jeans}}{2} \right)^3 \propto \rho^{-1/2} T^{3/2}. \tag{1.18}$$

Any structure with a dimension of l_{jeans} and with a mass above M_{jeans} is unstable to gravitational collapse under the conditions assumed for this analysis. Evidently the interstellar medium is not as ideal as drawn here, and if a region of a l_{jeans} and $M > M_{jeans}$ is not collapsing, then it suggests that some other physical mechanism is providing the support against gravity.

Instabilities

In a complex medium such as the ISM, a number of instabilities may be responsible for unbalancing the equilibrium state and provoke the gravitational collapse of a molecular cloud. Among the most known instabilities are the Rayleigh-Taylor and Kelvin-Helmholtz instabilities. When the magnetic field is not negligible, other instabilities such as hydromagnetic instabilities may also occur.

The Rayleigh-Taylor instability occurs when two fluids with different densities are interacting and the lighter fluid is pushing/accelerating into the heavier one. In this scenario, the lighter material will not be able to push the heavier material smoothly. In fact, the heavier material will offer resistance to the motion and will create “Rayleigh-Taylor fingers” of material left behind, whereas the lighter material will attempt to penetrate and will inflict a “mushroom-like” shape on the pushed heavier material.

The Kelvin-Helmholtz instability is related to shear motions between two fluids with different densities and traveling at sufficiently different velocities. These instabilities generate waves at the interface between the two fluids.

1.1.6 Magnetic fields of molecular clouds

A cloud's magnetic field is another property that is becoming more and more important to understand, since its impact on the cloud's star forming efficiency and evolution seems to be quite significant. However, this is a hard property to measure. The line of sight strength of the field can be determined by measuring the Zeeman splitting of line transitions (e.g. Heiles and Robishaw 2009) and the plane of the sky component of the field is usually estimated by polarization measurements of background stars, dust emission or spectral lines (e.g. Tang et al. 2010). The presence of the magnetic field in a cloud is felt not only by charged particles, but also by neutral material, through ion-neutral coupling. The strength measurements of the magnetic field are important to help understand its role in the dynamics and balance of the cloud (McKee et al. 1993; McKee and Ostriker 2007, reviews).

A cloud is said to be magnetically subcritical when the magnetic term dominates over the gravitational term. As suggested by Shu et al. (1987), a cloud that is magnetically subcritical can form stars through ambipolar-diffusion that can slowly remove magnetic flux and allow the gravitational forces to "win" over the magnetic field that was supporting the cloud, in long timescales of 10^8 - 10^9 yr. When a cloud is magnetically supercritical, then it will much more quickly and efficiently form stars and clusters. However, a great number of MCs seem to have a field strength value just around the critical one, leaving a persistent doubt as to whether the magnetic field is relevant in their large scale dynamics and stability (Hartmann 2001; Heiles and Crutcher 2005).

1.1.7 Dynamical properties of molecular clouds

Molecular line studies toward molecular clouds show the presence of supersonic motions, where the molecular lines have a typical full width half maximum (FWHM) around 1 - 2 $\mathrm{kms^{-1}}$ (sound speed in Eq. 1.19 assuming a mean molecular weight $\mu = 2.33$). These are the predicted line widths in the virial equilibrium for such clouds (eq. 1.11, assuming a density distribution as r^{-2}, a typical mass of 100 $\mathrm{M_{\odot}}$ and radii of

0.2 pc). However, they are greater than expected for thermal emission at 10 K. Therefore, the observed line widths are usually explained by the presence of supersonic, compressible, non-thermal bulk motions (Lada 1999). These motions may be considered turbulent, due to the lack of any systematic pattern of motion and the existence of a systematic power-law between the velocity dispersion inside a cloud and its physical size (e.g. Larson 1981, estimated $\sigma_v \propto L^{0.38}$, σ_v being the velocity dispersion and L the maximum linear dimension of the cloud).

$$c_s^2 = \frac{kT}{\mu m_{\mathrm{H}}} \overset{T=10\mathrm{K}}{\approx} 0.2\ \mathrm{kms}^{-1}. \tag{1.19}$$

However, on small scales, in dense regions about to form stars the thermal motions dominate over the turbulent ones, and the line width is given by the thermal line width (e.g. Myers 1983; Padoan et al. 2001). It is inside a certain radius (the coherence radius) on the densest cores, that the line width reaches a constant level corresponding to the thermal value. This sharp transition from turbulent to thermally dominated line width is often referred to as the transition to coherence (Myers and Fuller 1992; Barranco and Goodman 1998; Pineda et al. 2010).

1.1.8 Chemistry within Molecular Clouds

The chemistry in molecular clouds is not static. It evolves alongside the evolution of the structures within the clouds and changes with the physical conditions. Observing molecular tracers of different environments and/or evolutionary stages can give us an insight into the overall picture of a given molecular cloud, providing measures of masses, temperatures and dynamics at both large and small scales.

Before star formation occurs, low-temperature gas-phase ion-molecule chemistry dominates. This allows the formation of small radicals and unsaturated molecules (van Dishoeck and Hogerheijde 1999). If the gas is carbon rich, it is possible that long carbon-chains are formed at this point. At this stage, we can observe several molecules, isotopes and/or ions, such as C_2S, HC_3N, HC_5N, N_2H^+, NH_3 and CO isotopes, for example.

In the cold prestellar and collapse phases, many molecules freeze out onto the grains and form an icy mantle. The chemistry is then dominated by surface chemistry and processing by ultraviolet photons, X-rays and cosmic rays. There are some molecules and ions, however, that probably do not freeze out at this point, such as H_2, He, $H_3{}^+$ and N_2 (see van Dishoeck and Hogerheijde 1999, for different models of the chemistry of YSOs envelopes). The ions HCO^+ and N_2H^+ are thought to be good tracers of these cold envelopes, because their abundances increase as molecules such as CO or O, which destroy them, start to deplete by freezing-out onto the grains (e.g. Hogerheijde et al. 1997, 1998).

When a new born star begins to heat the dust and gas to temperatures greater than 90K, the ices of the envelope (such as H_2O, CH_3OH and CO isotopes) begin to evaporate back to the gas phase, integrating the gas-phase chemistry. These inner regions are best studied by observing lines that trace high temperatures (more than 100K), such as $^{13}CO(6-5)$. Outflows from the young sources also penetrate the envelope, creating high temperature shocks and lower temperature turbulent regions, detectable with SiO or SO molecular line observations. The study of H_2 near-infrared emission, HCN and CO isotopes line wing profiles also provide further information about the outflows (van Dishoeck and Hogerheijde 1999, and references therein).

When the envelope is dispersed by winds and/or ultraviolet photons, there is still a circumstellar disc where species like HCO, CN and HCN have been found. Photon dominated regions (PDRs) appear, in which the stellar UV heats the cloud.

1.2 Star Formation

In this section I will introduce the current theories for the formation of stars in isolated and clustered (dynamical) form, and describe the proposed evolutionary sequence for the formation of a single star: from a prestellar core to a pre-main sequence star.

1.2.1 Star formation theories

The formation of prestellar cores by the fragmentation of the parental clumps can be explained by two main different scenarios: the quasi-static individual and independent core formation, based on the Jeans or Kernel model, and the fast star formation mode, where both the dynamical competitive accretion and gravoturbulent theories fall in. These theories vary in the way a clump fragments to form cores, on the time it takes to do so, and on what defines the final mass of a star.

Quasi-static star formation

This first set of theories assumes that a protocluster condensation comes from the fragmentation of one local Jeans mass (a clump) in the parent cloud (e.g. Larson 1985; Myers 1998). The collapse of this clump will provide an increase in the density allowing the formation of more local Jean masses within the clump (cores), since the $M_{jeans} \propto \rho^{-1/2}$.

These models can explain the low star formation efficiency in molecular clouds and the large stellar ages spreads found within a molecular cloud (10-15 Myr). They follow the idea that the forces in the ISM should be balanced, and as such, the magnetic support of the overall cloud should have to decrease so that free-fall collapse can occur (Spitzer 1978; Mestel and Spitzer 1956). Therefore, this would be a slow, quasi-static contraction of a cloud to form protostars, that could take up to $\sim 10^8$ yrs, corresponding to the ambipolar-diffusion timescale, necessary to remove enough magnetic flux to allow free-fall collapse (Shu et al. 1987; Mouschovias 1991). During the dynamic contraction of the cores (although not free-fall collapse), the envelope of the cloud would continue being magnetically supported against collapse.

In these models the IMF is determined prior to the individual collapse of the cores, at the time of the fragmentation of the cloud, and it would reflect the core mass distribution (e.g. Elmegreen 1999; André 2002).

Fast star formation

In the other set of models, the turbulence of the cloud is the main mechanism that induces fragmentation. This mode of star formation would be a rapid and dynamic process with a timescale of $\sim 10^6$ yrs (e.g. Redfield and Linsky 2004; Gazol et al. 2005; Galván-Madrid et al. 2007), invoking that magnetic fields are negligible. Furthermore, the fact that we do not observe many molecular clouds prior to star formation, brings the idea that the difference between the cloud formation and star formation timescales is small. This can be explained by the ISM not being in a state of force balance as suggested by the models of converging flows as the origin of molecular clouds and supported by the strong pressure fluctuations of the ISM (e.g. Hartmann et al. 2001; Vazquez-Semadeni 2010).

The big spread in stellar ages detected within molecular clouds can be explained by different triggering times for collapse, rather than a slow star formation process (Ballesteros-Paredes and Hartmann 2007). This is consistent with the fact the molecular clouds gas is confined to a smaller area, in which the observed age spread of the actually forming stars is lower.

Within this fast star formation mode, there are two main sets of models, those based on competitive accretion and the gravoturbulent models. In the first, the formed young protostars travel in the gas-dominated gravitational potential of the protocluster, gathering mass as they do so. In such a scenario, it is the competitive accretion and dynamical interactions among protostars that fundamentally define the final spectrum of stellar masses. Furthermore, it predicts a mass segregation within protoclusters, as in the cluster potential centre, cores will rapidly accrete mass and become more massive than the low-density outer regions cores (e.g. Bonnell et al. 1997, 2001). On the other hand, in gravoturbulent models turbulence not only sets the initial fragmentation of the cloud as it will dictate the ability of a core to accrete its final mass (e.g. Padoan et al. 1997; Hennebelle and Chabrier 2008). In this set of models, star formation is a fast process but the final mass of a star is predefined by the turbulent fragmentation of the cloud and not by a dynamical accretion of mass, favouring the idea that the CMF is the precursor of the IMF.

1.2.2 The evolution of a core - towards a newborn solar type star

When a pre-stellar core becomes gravitationally unstable it collapses to form a protostellar object and the main protostellar accretion or embedded phase begins. The central protostar will accrete most of its final mass, M_*, from the infalling surrounding envelope (with M_{env}) which, in the presence of angular momentum, will form an accretion disc around the protostar. In this stage, the young stellar object (YSO) is heavily obscured at optical wavelengths by the surrounding dust. The youngest sources are classified as Class 0 sources and are usually associated with highly collimated bipolar outflows. Class 0 sources are characterized by low temperatures around 20-30K, a spectral energy distribution (SED) peak at submillimetre wavelengths (Shu and Adams 1987; André et al. 1993) and a M_{env} greater than the M_* (Figure 1.5, top left panel). Class I sources, more evolved than Class 0, have a SED which peaks at far-infrared or submillimetre wavelengths (Lada 1987) with an “excess” of infrared emission compared to a black body curve, due to the dust which is still surrounding the central protostar (Figure 1.5 top right panel). Here, the YSO’s M_{env} is lower than the M_*, and the sources exhibit less collimated bipolar outflows. At the end of this protostellar phase, the removal of the circumstellar material of the infalling envelope has occurred.

There are also flat-spectrum sources which correspond to the transition between Class I and Class II sources, as their SED has an intermediate form between the two. They are often visible stars (as Class II sources), but are also veiled at infrared wavelengths, like Class I, though not as strongly.

After this, the star enters the pre-main sequence (PMS) phase or revealed phase. At this stage, the star has already $\sim 90\%$ of its final mass and it continues to contract until thermonuclear reactions start to take place in the centre of the star. The infall rate into the stellar core is lower in this phase, as the surroundings of the central object have

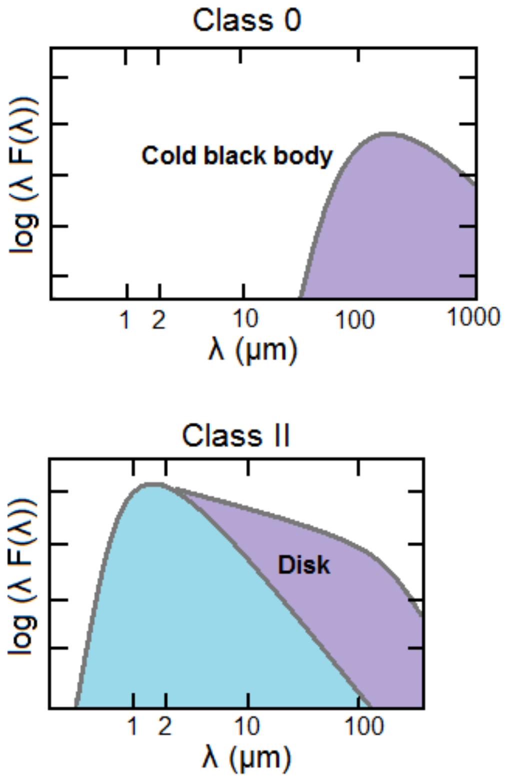

Figure 1.5: Evolution of the SED of a young stellar object, from a protostar with a dusty envelope (Class 0 and I, top panels) to a PMS star with a circumstellar disc (Class II and III, lower panels). Sketch adapted from Lada (1987) and Andre et al. (2000).

been disrupted (Lada 1999; André 2002). The YSOs are now visible at optical and near-infrared wavelengths, becoming Class II and Class III sources (Lada 1987). The Class II SED is broader than a single blackbody and it peaks at visible or near-infrared wavelengths. It shows an infrared excess, but significantly smaller than for Class I sources, indicating that there is less dust surrounding the star (Figure 1.5, lower left panel). This dust is probably in a circumstellar disc. Class III sources also have SEDs which peak between optical and infrared wavelengths, but little to no infrared excess is found in this case as the circumstellar disc is being cleared of gas and dust (Figure 1.5, lower right panel). The dominant mechanism involved in this removal process and leading onto a dust-free environment is still not fully known.

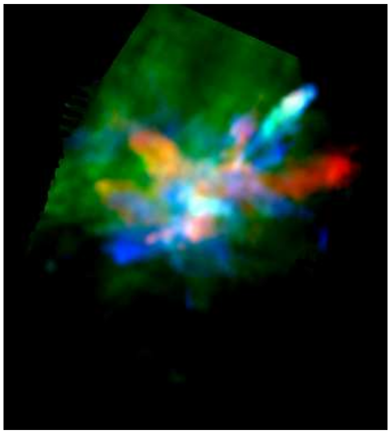

Figure 1.6: Velocity-coded three colour image of the ^{12}CO J=3→2 emission (Graves et al. 2010) observed towards the Serpens star forming region, showing the many outflows from the young population of protostars. Confusion is an issue in such a crowded region, and the identification of the driving source for each flow is nearly impossible. Blue is the integrated intensity from -42.2 to 3.8 kms^{-1}, green is from 4.8 to 10.8 kms^{-1} and red is from 11.8 to 57.8 kms^{-1}.

1.2.3 Gas and dust removal - Outflows

Throughout the evolution of a core to form a star, the material that primarily surrounds the star is removed. Since not all the material that surrounds a prestellar core is accreted by the star, there must be a disruption mechanism that removes some material from the protostellar envelope. Among other possibilities, this disruption may be caused by the interaction of the material with other forming stars in highly populated regions of star formation, by stellar winds or by the bipolar outflow generated by the forming star itself.

All stars have stellar winds throughout their lives. These winds are hot ionized gas ejected from the stellar photosphere, due to radiation pressure. An outflow, however, is associated with the early stages of star formation, with different origins and properties than the common stellar winds. Throughout the infall of the gas and dust of the envelope onto the central YSO, angular momentum is accumulated on the central core and is released by an ejection of matter and injection of energy onto the gas around through a bipolar jet along the rotation axis of the star. This injection affects the gas from short distances up to a few pc from the source (Arce et al. 2007). The gas in the jet can reach high velocities (up to 100 kms^{-1}) and swept up/accelerate the impacted material of the cloud, clearly distinguishing the outflow from the surrounding gas at lower velocities (Fig. 1.6).

By its energetic release, an outflow can induce chemical changes on the cloud. It decreases the gas infall rate onto the protostar and can ultimately be one of the main responsible mechanisms for the envelope's disruption. If the collimation factor (i.e. length/width) of the outflow is high enough that the opening angle of the outflow is less than a few degrees, they can be described as "molecular jets" (e.g. Gueth and Guilloteau 1999). Most YSOs outflows are not jet-like and CO observations have revealed complex outflow structures, when observing at high resolutions, suggesting both spatial and temporal variations of the outflow. Observations of protostellar outflows (e.g. Fuller and Ladd 2002; Arce and Sargent 2006) seem to suggest that outflows evolve with time and age of the driving source (Fig. 1.7). The youngest sources (Class 0) present a high collimation factor, which will decline with time and evolution of the source. At the Class I stage the outflow becomes a wide-angle one (Arce et al. 2007). Furthermore, several shocked regions may appear associated with a single outflow, indicating that episodic ejection events may take place. The ejection phenomenon occurs in most of the YSOs (see e.g. Lee et al. 2000, 2002), but whether they are intrinsically episodic, or continuous but with frequent bursts, is not yet clear (see Arce et al. 2007).

Several models have attempted to address the origin and evolution of outflows (Arce et al. 2007, and references therein). The *jet bow shock models* mimic the highly collimated outflows, thought to be magneto-centrifugally driven close to the protostar. These jets would impact the material forming thin shells surrounding the outflow cone and bow shocks at the head of the outflow (e.g. Ostriker et al. 2001). These models are good at reproducing the observed young and highly collimated outflows with bow shocks and Herbig-Haro (HH) objects (e.g. HH212 and H46/47, Lee et al. 2007; Velusamy et al. 2007, respectively). On the other hand, the *wind-driven shell models* suggest that the observed outflow shells are formed by a wide-angle radial wind that

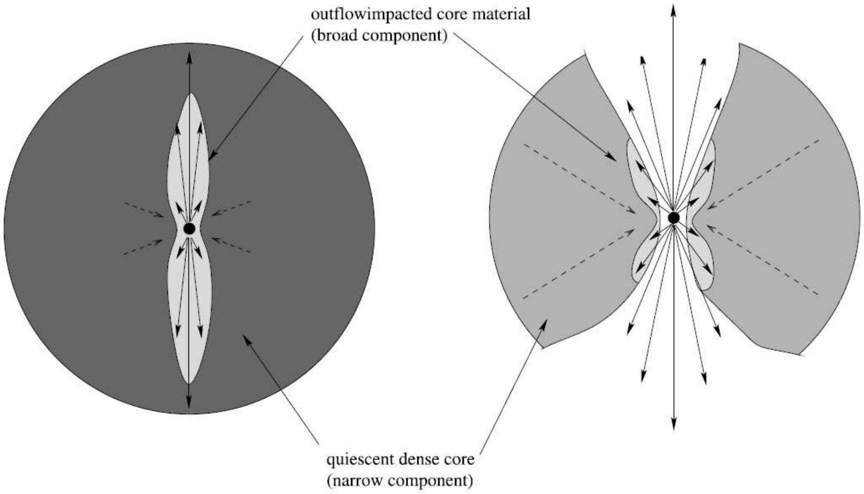

Figure 1.7: Schematic picture, by Fuller and Ladd (2002), of the hypothetical outflow-envelope interaction evolution: darker grey regions represent the dense envelope gas traced by $C^{18}O$, and the light grey regions are the molecular outflow shocked regions traced by the broader ^{12}CO and ^{13}CO emission.

blows into the material infalling onto the protostar and protostellar disc. These models are good at explaining the older outflows with a wide opening angle (e.g. Velusamy and Langer 1998; Cunningham et al. 2005). In fact, a unified model which includes both a primary jet-like flow and a more tenuous wide-angled wind is best capable of describing the overall morphology and evolution of a protostellar outflow (e.g. Shang et al. 2006).

In addition, there are also the *turbulent jet models* where Kelvin-Helmholtz instabilities along the boundary between the jet and the environment form a turbulent layer, which can propagate into the flow and surroundings (e.g. Micono et al. 2000). Finally, the *circulation models* suggest that the outflow is formed by deflected infalling material, thought to occur in a high MHD pressured central torus, where some material may be accelerated to speeds greater than the escape speed (e.g. Combet et al. 2006).

Chapter 2

Observing molecular clouds

Molecular line and dust continuum observations are fundamental to understand the physical conditions of the early stages of star formation in molecular clouds. At (sub)millimetre wavelengths, the continuum emission holds information on the dust particles that surround the young protostars or prestellar cores, tracing the column density and temperature of the clouds. The molecular lines, depending on their optical depth and chemical history, are useful tracers of the dynamics and properties of different parts of the cloud. Moreover, to understand the emission from a molecular line transition toward a MC we need an understanding of the radiative transfer in such environments. This chapter will introduce the radiative transfer theory (based on Rybicki and Lightman 1986; Lequeux 2005, adopting the formalism of the first) and some approximations often used to extract information from molecular transitions and continuum emission in the environments we observe.

2.1 Notions of Radiative Transfer

Considering an isotropic radiation from a source, the radiation energy dE within a solid angle $d\Omega$ that crosses an area dA over a time dt at a frequency interval $d\nu$ can be described in terms of

$$dE = I_\nu \, dA \, dt \, d\Omega \, d\nu \tag{2.1}$$

where I_ν is the specific intensity of the radiation at a frequency ν along a line of sight, in units of $\mathrm{erg\,s^{-1}cm^{-2}\,Hz^{-1}\,ster^{-1}}$.

As the radiation passes through matter, photons can be absorbed, scattered or emitted by the material along the path length. Therefore, the radiative transfer is ruled by the variations of the specific intensity, dI_ν, over the path length.

2.1.1 Emission

The spontaneous emission coefficient at a frequency ν, j_ν, is defined as the amount of energy that is emitted per unit time, volume and solid angle:

$$dE = j_\nu dV dt d\Omega d\nu, \tag{2.2}$$

with j_ν in units of $\mathrm{erg\,s^{-1}cm^{-3}\,Hz^{-1}\,ster^{-1}}$.

The total amount of intensity added to the radiation, dI_ν^+, as it crosses matter over a path-length dS and a beam cross section dA becomes:

$$dI_\nu^+ = j_\nu dS \tag{2.3}$$

2.1.2 Absorption

The amount of radiation we will see depends also on how much of the emission is able to pass through the cloud. Therefore, a change of I_ν along a distance dS is also related to how much of the original emission has been absorbed along that path. The ability of the material to absorb radiation is related to its absorption coefficient α_ν in units of $\mathrm{cm^{-1}}$. The amount of intensity being absorbed, dI_ν^-, is then defined as:

$$dI_\nu^- = -\alpha_\nu I_\nu dS. \tag{2.4}$$

The absorption coefficient α_ν, can also be written as a function of the mass absorption coefficient, k_ν (in units of $\mathrm{cm^{-2}g^{-1}}$), as $\alpha_\nu = \rho k_\nu$.

2.1.3 Radiative transfer

The observed radiation, coming from the balance of the emitted and absorbed emission along the line of sight, is summarised in the radiative transfer equation:

$$\frac{dI_\nu}{dS} = -\alpha_\nu I_\nu + j_\nu \tag{2.5}$$

The source function, S_ν, is defined as $j_\nu = \alpha_\nu S_\nu$ and it is generally assumed to hold for the path length. Furthermore, the absorption coefficient can be seen as a function of the optical depth at a frequency ν (τ_ν) with $d\tau_\nu = \alpha_\nu dS$. For clarity purposes only, for the remainder of this chapter I will simplify the notation of τ_ν to τ.

If the source function is constant over the path length, the general solution of the radiative transfer equation (2.5) can be derived by dividing the equation by the absorption coefficient

$$\frac{dI_\nu}{dS}\frac{1}{\alpha_\nu} = \frac{dI_\nu}{d\tau} = -I_\nu + S_\nu \tag{2.6}$$

multiplying by e^τ

$$\frac{dI_\nu}{d\tau}e^\tau + I_\nu e^\tau = \frac{d(I_\nu e^\tau)}{d\tau} = S_\nu e^\tau \tag{2.7}$$

integrating between 0 and τ

$$I_\nu(\tau)e^\tau - I_\nu(0) = S_\nu(e^\tau - 1) \tag{2.8}$$

and finally dividing by e^τ

$$I_\nu(\tau) = I_\nu(0)e^{-\tau} + S_\nu(1 - e^{-\tau}). \tag{2.9}$$

Equation 2.9 is the general solution for the radiative transfer equation.

2.1.4 Approximations

Either because the background radiation is too weak in comparison with the cloud's radiation, or because we are observing one of the two extreme cases of optical depth, it is usual to use some approximations that simplify the use of the radiative transfer equation. Specific physical conditions such as local thermal equilibrium, allow further simplifications, useful in the context of studying molecular clouds. Some of these cases, in particular the ones I have considered as most relevant for the calculations in this thesis, are here briefly explained.

No background radiation

The approximation to no background radiation is made when the background emission is negligible when compared to the emission from the cloud. As such, the term $I_\nu(0)$ is discarded as all the emission detected is coming from the cloud only and eq. 2.9 becomes

$$I_\nu(\tau) = S_\nu(1 - e^{-\tau}). \tag{2.10}$$

In the case of molecular clouds, this approximation is reasonable, as it assumes that the radiation we detect is originated within the cloud, and that the only background radiation is the cosmic microwave background (CMB) at a temperature of 2.73 K. This approximation would not be valid for a region which is being externally heated, as is the case of e.g. photon dominated regions (PDRs) where the UV radiation from young and nearby OB stars is capable of heating up the gas up to temperatures of more than 100 K. This is not the case for the embedded stages of star formation observed in submillimetre, as the dust grains shield the inner denser regions from these UV fields.

Low optical depth

When a molecular transition is optically thin, i.e., $\tau \ll 1$ it means that its emission is capable of probing the entire cloud, even its deep and dense regions. This limit allows the expansion of the $e^{-\tau}$ to be simplified to:

$$e^{-\tau} \approx 1 - \tau \tag{2.11}$$

which, in the case of no background radiation, turns eq. 2.9 into

$$I_\nu(\tau) = S_\nu(T)\tau \tag{2.12}$$

High optical depth

On the other extreme of optical thickening, when $\tau \gg 1$, it means that we can only observe the emission originated from the cloud at its surface. The numerical approximation becomes:

$$e^{-\tau} \approx 0 \tag{2.13}$$

which means that

$$I_\nu = S_\nu(T) \tag{2.14}$$

2.2 The LTE regime and molecular emission lines

When in local thermodynamic equilibrium (LTE), the source function S_ν, is described by the black body function B_ν (i.e. the Planck function)

$$B_\nu(T) = \frac{2h\nu^3}{c^2}\frac{1}{e^{\frac{h\nu}{kT}} - 1} \tag{2.15}$$

where h is the Planck constant, c is the speed of light, k is the Boltzmann constant and T is the temperature of the source.

When the collisions completely control the excitations (and de-excitations) of a molecular transition, that transition is said to be thermalised (or in LTE conditions). The emission from thermalised transitions have an excitation temperature, T_{exc}, which corresponds to the kinetic temperature of the gas. That excitation temperature is related to the population of the energy levels, as described by the Boltzmann distribution:

$$\frac{n_u}{n_l} = \frac{g_u}{g_l} e^{\left(\frac{-h\nu}{kT_{\mathrm{exc}}}\right)} \tag{2.16}$$

where n_u and n_l represent the number densities of molecules which are in the u (upper) and l (lower) energy levels and g_u and g_l are the degeneracy/statistical weight of those levels (estimated as $g = 2J + 1$ where J is the rotational quantum number), and ν is the frequency of the transition between the level u and l.

2.2.1 Column Densities with optically thin emission in LTE

In LTE, the Einstein probabilities (or coefficients) of emission and absorption are related through the Einstein relation (Eq. 2.17), where A_{ul} is the Einstein probability for spontaneous emission between the levels u and l, and B_{ul} is the Einstein coefficient for stimulated emission.

$$A_{ul} = \frac{8\pi h\nu^3}{c^3} B_{ul} \tag{2.17}$$

The coefficient of absorption α_ν, can be written as a function of the Einstein coefficient A_{ul} as

$$\alpha_\nu = \frac{c^2 n_l(\nu) g_u}{8\pi\nu^2 g_l} A_{ul} \left[1 - \frac{g_l n_u}{g_u n_l}\right] \phi_{ul}(\nu) \tag{2.18}$$

where $\phi_{ul}(\nu)$ is the normalised spectral distribution of the radiation and $\phi_{ul}(\nu) \approx 1/\Delta\nu = c/(\nu\Delta v)$. Using equation 2.16, and assuming that the distribution of $n_u(\nu)$ and $n_l(\nu)$ are identical to the total distributions n_u and n_l, we get

$$\alpha_\nu = \frac{c^2 n_l g_u}{8\pi\nu^2 g_l} A_{ul} \left[1 - e^{\left(\frac{-h\nu}{kT_{\rm exc}}\right)}\right] \phi_{ul}(\nu) \tag{2.19}$$

To estimate τ, we use the relation $\tau = \int \alpha_\nu dS$. The integration in length of n_l becomes a column density, N_l (in particles per unit surface):

$$\tau \approx \frac{c^3 N_l g_u}{8\pi\nu^3 g_l \Delta v} A_{ul} \left[1 - e^{\left(\frac{-h\nu}{kT_{\rm exc}}\right)}\right] \tag{2.20}$$

In the optically thin plus LTE regime we can use these relations to calculate column densities and/or temperatures. From eq. 2.12, 2.15 and 2.20 we have

$$I_\nu = B(T_{\rm exc})\tau = \frac{h\nu N_l g_u}{4\pi g_l} A_{ul} \frac{e^{-\left(\frac{h\nu}{kT_{\rm exc}}\right)}}{\Delta v} \tag{2.21}$$

Using the equivalent of the Boltzmann equation (2.16) applied to the total number of particles N_{total} (of the specific molecule in study) we have

$$\frac{N_u}{N_{total}} = \frac{g_u e^{-\left(\frac{E_{ul}}{kT_{\rm exc}}\right)}}{Q} \tag{2.22}$$

where E_{ul} is the energy difference between the levels u and l, and Q is the partition function defined as the sum over all the energy levels i:

$$Q = \sum_i g_i e^{-\left(\frac{E_i}{kT_{\mathrm{exc}}}\right)} \tag{2.23}$$

What we measure, however, is a radiation flux dF_ν, defined as a measure of the amount of energy dE at a frequency ν that passes through a given area dA over a time dt, in units of $\mathrm{erg\,s^{-1}cm^{-2}\,Hz^{-1}}$. From Eq. 2.5, we can relate the flux with the specific intensity through

$$dF_\nu = I_\nu d\Omega \tag{2.24}$$

which, for a source of angular size Ω_{source}, becomes

$$F_\nu = I_\nu \Omega_{source}, \tag{2.25}$$

In observations, the antenna temperature T_A (in K) is typically measured and is proportional to the amount of flux that we detect within a beam size, Ω_{beam}. This antenna temperature, however, is affected by the atmospheric opacity, and once this effect is corrected we have a T_A^*. To calculate the column densities of a given source, it is useful to convert this T_A^* into a T_{mb} which is the main beam antenna temperature corrected for the telescope coupling to the source. For a source that fills the main beam of the telescope, $T_{\mathrm{mb}} = T_A^*/\eta_{\mathrm{mb}}$, where η_{mb} is the telescope efficiency. For example, at 112 GHz for the IRAM-30m telescope $\eta_{\mathrm{mb}} \sim 0.7$. Converting flux to temperature introduces a constant, $\lambda^2/2k$, where λ is the wavelength and k is the Boltzmann constant. Therefore, we have the following relation:

$$T_{\mathrm{mb}} = \frac{\lambda^2}{2k} I_\nu, \tag{2.26}$$

for a source that fills the main beam of the telescope.

Therefore, from equations 2.21, 2.22 and 2.26 we have:

$$T_{\mathrm{mb}}\Delta\nu = \frac{hc^3 g_u}{4\pi k \nu^2 Q} N_{total} A_{ul}\, e^{-\left(\frac{E_{ul}}{kT}\right)}. \tag{2.27}$$

The term $T_{\mathrm{mb}}\Delta v$ is the observed average integrated intensity over the source covered by the main beam of the telescope, and therefore, N_{total} is the average column density of the molecule in the source.

Equation 2.27 is useful to estimate column densities and temperatures when observing a molecular transition. To convert from the total column density of a given molecule to the total gas column density, we need to assume a fractional abundance of the molecule we are observing with relation to H_2. When there is more than one thermalised transition of the same molecule, this equation allows a fit of both the excitation temperature and the column density, independently of the dust properties. If only one molecular transition of a given molecule is available, then the excitation temperature has to be assumed a priori to be able to calculate the respective gas column densities. When there is a dust temperature estimate it can be used as the excitation temperature of the gas. However, this assumes that the gas and dust are well coupled and that the dust temperatures correspond to the gas excitation temperatures. Even if the molecular transitions are in LTE, this may not be the case as the gas and the dust may not be tracing the same structures - as is the case, for example, in the denser cores where CO is depleted and frozen onto dust grains.

In this thesis, I have used the relations presented in this section and some of the approximations of the previous section (§ 2.1 and 2.2) in the study of the Serpens star forming region (Chapter 3) and the B59 star forming region in the Pipe Nebula (Chapter 5).

2.3 The LTE regime and continuum emission

Most of the mass in a molecular cloud is in the form of H_2 molecules. The second biggest contribution is from He and there is only a very little abundance of other molecular gas species. There is, however, a small percentage of the mass (~ 1%) stored in heavier and bigger particles, small (nanometre to micrometre, Mathis et al. 1977) agglomerations of different materials, referred to as interstellar dust. The continuum emission seen toward molecular clouds at far-infrared (far-IR), submillimetre and millimetre wavelengths originates from these dust grain particles that are seen in the optical as the obscuring element in MCs. In fact, these particles absorb all the radiation in the UV, visible and near-IR wavelengths and re-emit it in far-IR to millimetre wavelengths at an equilibrium temperature, T_{dust}. The dust opacity is described by

$$\tau_{dust}(\nu) = N_{H_2}\,\mu\, m_H\, k_{dust}(\nu) \tag{2.28}$$

where N_{H_2} is the column density of H_2 molecules, μ is the mean molecular weight of species in the molecular cloud, m_H is the atomic hydrogen mass and k_{dust} is the mass absorption coefficient (opacity) of the dust in units of $\mathrm{cm}^2\ \mathrm{g}^{-1}$, representing how efficiently a dust grain emits or absorbs radiation at a particular wavelength. At submillimetre wavelengths, the relation of k_{dust} with the frequency/wavelength is a power law such that $k_{dust} \propto \lambda^{-\beta}$ or, in terms of frequency, $k_{dust} \propto \nu^{\beta}$. The spectral index β varies with the properties of the grains. For molecular clouds at submillimetre and millimetre wavelengths, it has been measured to be between 1 and 2 (e.g., Li 2005, and references therein).

The (sub)millimetre dust continuum emission, generally optically thin, comes as eq. 2.12 with the source function as the black-body function $B_\nu(T)$.

$$I_{dust}(\nu) = B_\nu(T_{dust})\,\tau_{dust}(\nu) \tag{2.29}$$

I_{dust} being a flux per steradian (Eq. 2.25), it is useful to re-write the previous equation in terms of the observed flux within a beam, F_{dust}

$$F_{dust}(\nu) = B_\nu(T_{dust})\,\tau_{dust}(\nu)\,\Omega_{beam}. \tag{2.30}$$

Using the definition of $\tau_{dust}(\nu)$ (eq. 2.28), we can write

$$F_{dust}(\nu) = B_\nu(T_{dust})\,N_{H_2}\,\mu\,m_H\,k_{dust}(\nu)\,\Omega_{beam}. \tag{2.31}$$

where $N_{H_2}\,\mu\,m_H$ is the average column density of $\mathrm{H_2}$ in $\mathrm{g\ cm^{-2}}$ and, therefore, multiplying by the size of the source gives the total mass associated with it. The size of the source is $\Omega_{source} \times d^2$, where Ω_{source} is the solid angle covered by the source and d is the distance to the source. Therefore, we have

$$M = N_{H_2} \mu m_H \Omega_{source}\, d^2 \tag{2.32}$$

which can be used to directly investigate the mass from a dust continuum emission image as

$$M = \frac{F_{dust} d^2 \Omega_{source}}{k_{dust} B(T_{dust}) \Omega_{beam}}, \tag{2.33}$$

or even, if measuring the total flux integrated over the entire source $F_{int} = F_{dust} \Omega_{source} / \Omega_{beam}$, we can use

$$M = \frac{F_{int} d^2}{k_{dust} B(T_{dust})}. \tag{2.34}$$

Through this relation (Eq. 2.33), it is straight forward to estimate the mass of a source from the dust continuum emission. Equation 2.31, on the other hand, is used to derive the $\mathrm{N_{H_2}}$ column densities along a line of sight, at each given position in a dust continuum map.

The dust temperature T_{dust} used throughout these calculations may be well constrained where there are observations at several wavelengths and where the SED can be well reconstructed, but this is not always the case. Finally, the values of k_{dust} become the most critical for these estimates as they are dependent on frequency and on the grain properties, which are still poorly constrained in dense star forming clouds.

Part II

The Serpens Star Forming Region

Chapter 3

Serpens Molecular Cloud

Based on the article Duarte-Cabral et al. (2010): *The physical and dynamical structure of Serpens. Two very different sub-(proto)clusters*

3.1 Overview

Despite the importance of understanding the processes driving the formation of stars in the Galaxy, little is known about the role played by molecular cloud kinematics in triggering or suppressing star formation. Since most stars form in clusters (Lada and Lada 2003), studying the kinematics of young stellar clusters can provide important insights into the dominant mode of star formation, particularly if the initial conditions of clustered star formation are still imprinted in the gas and dust emission properties (e.g. Peretto et al. 2006).

One such young and nearby cluster is in the Serpens Molecular Cloud (MC). Located at ~260 pc (Straižys et al. 1996), the optical extinction map of the cloud covers more than 10 deg^2 (Cambrésy 1999). However, the majority of the star formation is occuring in three clusters covering approximately 1.5 deg^2 (Enoch et al. 2007). The most active region is the Serpens Main Cluster (hereafter Serpens) which has a surface density of YSOs of 222 pc^{-2}, compared to 10.1 pc^{-2} in the rest of the Serpens cloud (Harvey et al. 2007a). In this main cluster, the average gas density is around

10^4 cm^{-3} (Enoch et al. 2007) with H_2 column densities greater than 10^{22} cm^{-2} in the cores. The high density of protostars in this main cluster seems to indicate an early stage of evolution where the cluster gas may still be infalling into the cores (Williams and Myers 1999;2000;Hurt et al. 1996). The star formation rate in this main cluster is 56 $M_\odot$Myr^{-1}pc^{-2}, ∼ 20 times higher than in the rest of the cloud (Harvey et al. 2007a).

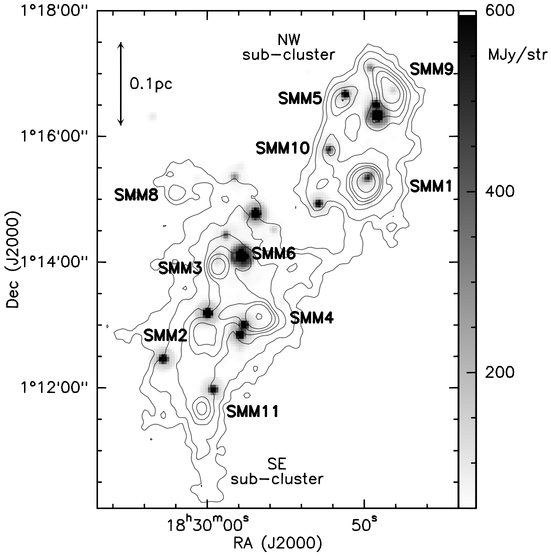

Figure 3.1: Map of the SCUBA 850 μm continuum emission in contours showing the position of the submillimetre sources (labeled). Contours at 400, 600, 1000, 1400, 1800, 2400 and 5000 mJy beam^{-1}. In grey scale are the Spitzer MIPS 24 μm sources (Harvey et al. 2007b). All the sources seen on this figure are classified as being young protostars, mostly between Class 0 and Class I sources, with a minority of flat spectrum sources.

Figure 3.1 shows the Spitzer MIPS 24 μm emission in grey scale and the SCUBA 850 μm emission in contours, tracing the young protostars classified as Class 0 or I, with the oldest objects in the image being a few flat spectrum sources (Harvey et al. 2007a; Kaas et al. 2004). Amongst the youngest YSOs found in Serpens there are the ten sources detected in the 850 μm dust continuum emission (e.g. Hurt and Barsony 1996; Davis et al. 1999), Class 0 and I protostars, hereafter referred to as submillimetre sources (labeled on Fig. 3.1, positions shown on Table 3.1). These protostars are distributed within ∼ 0.2 pc^2 and divided between two sub-clusters, one to the northwest (NW) and one to the southeast (SE). They power a number of outflows, which have been studied using several different approaches (e.g. Eiroa et al. 1992; Davis et al.

1999; Hodapp 1999; Davis et al. 2000; Graves et al. 2010). The presence of Class II and Class III objects (not shown in Figure 3.1) dispersed over a larger area suggests that the region has undergone two episodes of star formation. The first responsible for these dispersed pre-main sequence stars occurring about 2 Myr before the more recent burst which formed the current submillimetre and 24μm protostars (Harvey et al. 2007a; Kaas et al. 2004), 10^5 yr ago.

3.2 Observations

3.2.1 IRAM 30m data

The Serpens region was observed in C^{18}O J=1$\rightarrow$0 and J=2$\rightarrow$1 transitions and C^{17}O J=1$\rightarrow$0 transition with the IRAM 30m telescope, using the facility receivers, in May 2001. The observations consisted of on-the-fly maps of the region, centered at RA = $18^h29^m57.91^s$ and Dec = $1^\circ12'25.2''$ over an area of approximately 10.5 arcmin^2, $\sim 3'$ in Right Ascension and $3.5'$ in Declination.

The C^{17}O J=1$\rightarrow$0 data, at 112.359 GHz, have a spatial resolution of $22''$, a velocity resolution of $\sim$ 0.052 kms^{-1} and a noise level of $\sim$ 0.45 K (in T_A^*) in the raw map – low enough to allow the detection and identification of its hyperfine components. The C^{18}O was observed with a spectral resolution of $\sim$ 0.053 kms^{-1} at 109.782 GHz and 219.816 GHz and with spatial resolution of $22''$ and $11''$ for the J=1$\rightarrow$0 and J=2$\rightarrow$1 transitions, respectively. Both emission lines are detected with a good signal to noise, both with a one sigma noise level of $\sim$ 0.45 K, in T_A^*.

The beam and forward efficiencies of the IRAM 30m telescope ($B_{\rm eff}$ and $F_{\rm eff}$ respectively) are given on the telescope website[1]. From these I estimate for the C^{17}O and C^{18}O J=1$\rightarrow$0 transitions $F_{\rm eff}$=0.95 and $B_{\rm eff}$=0.72, and for the J=2$\rightarrow$1 transition $F_{\rm eff}$=0.91 and $B_{\rm eff}$=0.54.

The main data reduction was performed using the GILDAS software (CLASS90

---

[1] http://www.iram.es/IRAMES/telescope/telescopeSummary/telescope_summary.html

Table 3.1: Submillimetre sources in Serpens Main Cluster

Source name	RA (J2000)	Dec (J2000)	offset RA (″)	offset Dec (″)
SMM 1	18:29:49.87	1:15:16.0	0.3	2.6
SMM 2	18:30:00.25	1:12:51.7	0.8	5.7
SMM 3	18:29:59.26	1:13:56.3	0.3	2.0
SMM 4	18:29:56.77	1:13:08.0	2.7	2.1
SMM 5	18:29:51.35	1:16:34.9	3.3	0.9
SMM 6	18:29:57.99	1:13:59.2	4.7	3.0
SMM 8	18:30:01.88	1:15:08.4	0.5	0.9
SMM 9	18:29:48.34	1:16:42.0	3.3	0.5
SMM 10	18:29:52.04	1:15:44.4	1.5	3.4
SMM 11	18:30:00.41	1:11:41.6	1.4	0.8

and GREG). This included the baseline corrections, hyperfine/gaussian fitting of the data, and construction of the datacubes. Given the good quality of the data, the baselines were well fitted by a simple first degree polynomial function.

3.2.2 JCMT data

The dynamical study and excitation temperature analysis (Sections 3.4 and 3.5) make use of HARP data from the Gould Belt Survey (GBS) at JCMT (Ward-Thompson et al. 2007; Graves et al. 2010). The data I used were the $C^{18}O$ J=3→2 observations, at 329.330 GHz, with 0.055 kms^{-1} spectral resolution, and 14″ spatial resolution. The telescope main beam efficiency at this frequency is $\eta_{\rm mb} = 0.66$ (Curtis et al. 2010a), and the rms level achieved is of the order of 0.2 K (T_A). A full description of these data is given in the GBS Serpens First Look paper (Graves et al. 2010).

The submillimetre continuum data at 850 μm was observed with SCUBA at the JCMT, with a beam size of 14″. The initial reduction, analysis and discussion of these data was presented by Davis et al. (1999), where they estimate the overall dust properties and characteristics of the cloud. I have used the pipeline reduced SCUBA data from the Canadian Astronomy Data Centre (CADC) archives[2] to investigate the structure of the dust continuum emission and for comparison with the IRAM 30m $C^{17}O$ and $C^{18}O$ data.

An initial inspection of the SCUBA data indicated good agreement in the position of SMM3 and those of the sources determined by Davis et al. (1999, SMM8 and SMM11). However, as shown with interferometric continuum observations (Hogerheijde et al. 1999), the positions of the remaining SMM sources needed to be revised compared to those listed in Davis et al. (1999). In Table 3.1 I present redetermined positions for all sources, extracted from the 850 μm map of Serpens, which now agree within $1''$ of the positions in the SCUBA cores catalogue published by Di Francesco et al. (2008). These positions are accurate within the $2''$ SCUBA pointing errors (Davis et al. 1999). The offsets in RA and Dec between the revised positions and those previously published (listed in Davis et al. 1999) are also shown on Table 3.1.

3.3 The gas structure of Serpens

The structure of Serpens was studied using the $C^{17}O$ J=1→0 emission, after fitting its hyperfine structure, by decomposing the space-velocity structure of the datacube to find the $C^{17}O$ clumps, and to try to correlate the gas structures with the submillimetre dust continuum emission in Serpens. Such a clump decomposition was also performed on the $C^{18}O$ J=1→0 datacube for comparison.

3.3.1 Hyperfine structure fitting of $C^{17}O$ J=1→0

The $C^{17}O$ J=1→0 line comprises three, partially blended, hyperfine features. Under the assumptions that all the components have the same excitation temperature, the opacity as a function of frequency has a Gaussian profile, and the components all have the same width and they do not overlap, we can fit the hyperfine structure (HFS) of

---

[2] http://www.cadc.hia.nrc.gc.ca/jcmt/

a spectrum to extract the line width, central velocity and optical depth (τ). The line shape in the presence of hyperfine structure can be described by

$$T(v) = T_S(1 - e^{-\tau(v)}), \tag{3.1}$$

where

$$\tau(v) = \tau_0 \sum_{i=1}^{3} r_i \exp\left(-\frac{(v - v_{0,i})^2}{2\sigma^2}\right), \tag{3.2}$$

$T(v)$ is the line brightness temperature as a function of velocity v, T_S is the source temperature and τ is the optical depth. The optical depth is the sum over the three hyperfine components of the transition where r_i and $v_{o,i}$ are the relative weight and the central velocity for each hyperfine component respectively, v the velocity, σ the velocity dispersion and τ_0 the total optical depth of the three components (Fuller and Myers 1993). The spacing and weight of the hyperfine components were adopted from Ladd et al. (1998). Further details about the hyperfine structure fitting procedure within the GILDAS software can be found on the IRAM website[3].

I extracted the spectrum from each pixel of the $C^{17}O$ J=1→0 datacube after convolving spatially the raw datacube with a 20” Gaussian, reducing the r.m.s. noise levels to ~0.2 K. I then fitted the hyperfine structure of the spectra, under the assumption of a single velocity component contributing to the emission. A model Gaussian spectrum for each pixel was then reconstructed using the derived peak intensity, line width and central velocity. Only pixels where both the line width and line peak intensity were determined with a signal to noise ratio of 5 or greater were considered.

The initial fitting showed that within the uncertainties, all the emission was consistent with being optically thin (Fig. 3.2). Therefore, to reduce the uncertainties on the fitted quantities, the HFS fitting was redone fixing the τ at 0.1 for the whole map, consistent with optically thin emission.

Figure 3.3 shows the final $C^{17}O$ J=1→0 datacube, modelled with a single velocity component equivalent Gaussian, as integrated intensity maps over 1 kms^{-1} intervals,

---

[3] *http://www.iram.fr/IRAMFR/GILDAS/doc/html/class-html/node8.html*

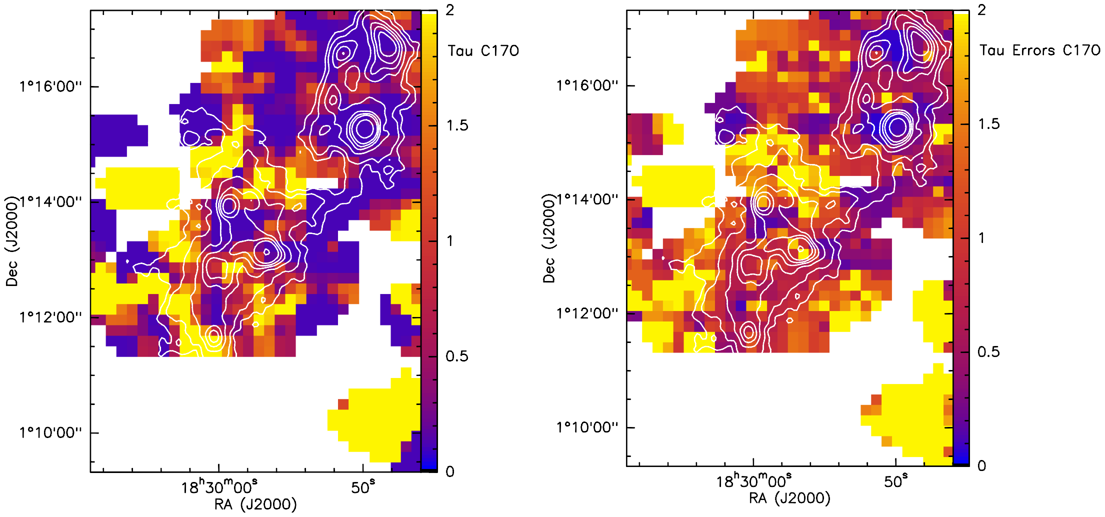

Figure 3.2: Left: map of the $C^{17}O$ J=1→0 optical depth, τ, from the initial hyperfine fit in colour scale. Right: map of uncertainties in the $C^{17}O$ J=1→0 τ from the initial hyperfine fit, in colour scale. Both images are overplotted on SCUBA 850μm emission in white contour (same as in Fig. 3.1).

from 6 to 10 kms^{-1}. Here we are able to identify clear peaks at different velocities and positions in the region. Note that in the North, the stronger gas emission is coincident with the two stronger submillimetre sources (SMM1 and SMM9), whereas in the South the peaks of the gas emission do not coincide with any of the submillimetre protostars. A detailed study of these peaks is presented in Section 3.3.2, where I performed a 2D and 3D CLUMPFIND analysis of the region.

3.3.2 Clump extraction methods

To determine the structure of the molecular gas I have carried out a clumping analysis in 2D and 3D. Using the velocity information from the gas emission it is possible to identify the individual clumps within the cloud, whereas the larger structures (the NW and SE sub-clusters) are recovered when using the total integrated intensity of the gas emission. The aim for the extraction of the smaller scale molecular structures is the comparison with the structure visible in the dust continuum. I use this analysis to quantify the sizes and masses of molecular gas associated with protostars, and carry out a virial analysis to determine the clump stability.

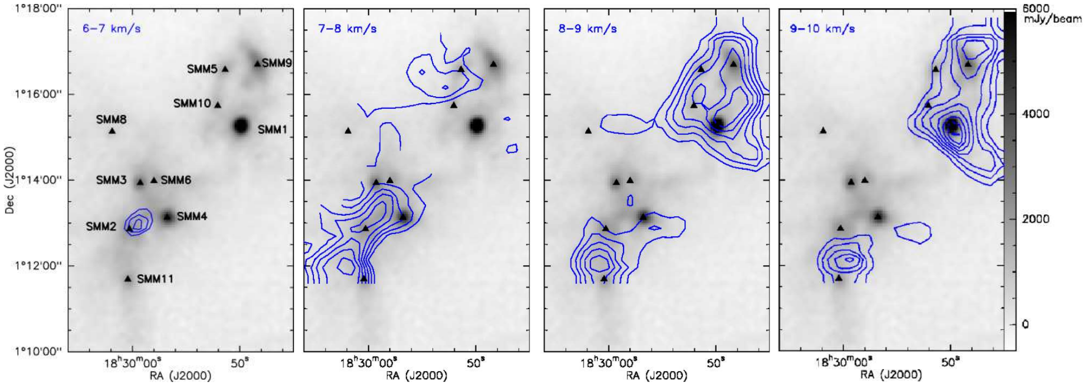

Figure 3.3: Contour maps of $C^{17}O$ J=1→0 modelled emission from the hyperfine fit, overplotted on SCUBA 850μm emission in gray scale. The submillimetre sources are identified on the left figure with labels and triangles. These symbols will be used from this point forward. Each figure represents a mean intensity map over 1 kms^{-1} intervals, from 6 to 10 kms^{-1}. Contours range from 0.4 K kms^{-1} increasing by steps of 0.1 K kms^{-1} (in T_A^* scale).

The $C^{17}O$ J=1→0 channel maps show a significant number of emission features which are not directly associated with the SCUBA cores (Fig. 3.3). For this reason I call these molecular structures “clumps” from here after, although this term is often used to describe parsec-scale structures (Blitz 1993).

The 2D analysis was based on Figure 3.3. From here, I identified three main peaks in the SE sub-cluster: one north of SMM11, one between SMM2 and SMM6, and one west of SMM4 (Fig. 3.3). In the NW sub-cluster, I have also identified at least four other peaks: one on SMM1, one close to SMM9, one south-west of SMM1 and finally another weaker peak east of the sub-cluster. The properties of each of the identified clumps (Fig. 3.4), was subsequently extracted using the IDL 2D version of the source extraction CLUMPFIND algorithm code by Williams et al. (1994) on the maps integrated over the velocity range in which each clump appeared.

With the size of each clump and their respective integrated intensity corrected for telescope efficiency, I estimated the clumps’ LTE column density and mass (M_{cf}) assuming a temperature of 10 K, a mean molecular weight of 2.33 and a $C^{17}O$ fractional abundance with respect to H_2 of 4.7×10^{-8} (Frerking et al. 1982; Jørgensen et al.

2002). I also calculated the clumps virial masses using Eq. 3.3, where $M_{\rm vir}$ is the virial mass, $\sigma_{\rm obs}$ is the observed velocity dispersion, G is the gravitational constant and α is a coefficient dependent on the adopted density profile: α is 3/5 for a uniform density, 2/3 for a profile $\rho \propto r^{-1}$, 3/4 when $\rho \propto r^{-1.5}$, and 1 when $\rho \propto r^{-2}$ (Spitzer 1978, and Section 1.1.4),

$$M_{\rm vir} = \frac{3R\sigma_{\rm obs}^2}{\alpha G}. \tag{3.3}$$

The listed virial mass of each clump adopts a density profile of $\rho \propto r^{-2}$. The velocity FWHM of each clump was estimated by averaging all the spectra assigned to that clump and has an estimated uncertainty of ~0.1 $\rm km s^{-1}$. The clumps identified by this method will be referred to as 2D-clumps hereafter.

The virial mass ($\rm M_{virial}$) and the gas mass ($\rm M_{cf}$) were also calculated for the two sub-clusters, NW and SE. The method used was the same as for the clumps except the density profile for the sub-cluster gas was assumed to be $\rho \propto r^{-1.5}$, which is expected to be more appropriate for these larger size regions. If the same $\rho \propto r^{-2}$ as for the clumps had been adopted, the derived sub-cluster mass would be a factor of 25% smaller.

Observational sources of uncertainty in these masses include the distance to Serpens and the line width. Uncertainties on the line width in particular might be a special issue in the SE region where two velocity components are observed in $\rm C^{18}O$ (Section 3.4.2) and may become important in broadening the $\rm C^{17}O$ line. Systematic uncertainties in $\rm M_{cf}$ include the uncertainty in the adopted gas temperature and fractional abundance of $\rm C^{17}O$. Finally, the systematic uncertainties on the $\rm M_{virial}$ include source geometry effects and neglecting additional terms (due to external pressure, magnetic pressure, etc.) in the virial equation. Amongst all the possible sources of uncertainty, the greatest is likely to be the factional abundance of $\rm C^{17}O$, given that our non-LTE study of $\rm C^{18}O$ at 8 positions (Sec. 3.5.2) shows a mean depletion factor of 2.5. Given the observational and possible systematic uncertainties on the calculations, the virial ratio is perhaps best seen as a useful tool to compare the different structures within a cloud rather than absolute measure of the gravitational equilibrium of any given clump.

Although the 2D clump-finding is valuable for comparison with the dust continuum, it is limited in its ability to represent the true structure of the cloud. The 3D CLUMPFIND analyzes the datacube in all three dimensions of space-space-velocity. In particular, 3D CLUMPFIND should provide a better understanding of the cloud's structure where clumps may overlap along a line of sight but have different velocities, or where the emission is narrow in velocity making it weak in integrated intensity maps and undetected in a 2D search for structures. Therefore I have complemented the 2D study of the $C^{17}O$ structure using the 3D version of the CLUMPFIND within the Starlink package.

In agreement with Pineda et al. (2009), I also found the results on the 3D CLUMPFIND analysis to be very sensitive to the parameters used, especially in characterising the weaker emitting regions. Stronger clumps were unequivocally detected with a wide range of parameters, but changing the step size and/or the number of pixels per clump allowed to be adjacent to a bad pixel would result in the merging of several clumps into one, or unrealistic extensive splitting of clumps into several small structures, or even non-detection of some structures expected to be detected. For this reason, the initial 2D study is essential as a reference point to understand the main structure of the cloud, which could be significantly misrepresented by relying, uncritically and exclusively on the 3D CLUMPFIND analysis. The best configuration parameters I found for this analysis were: the first contour level, $T_{\rm low}$, of 0.6 K; the global noise level of the data, r.m.s., of 0.2 K (equivalent to the r.m.s. of the fitted data); and the spacing between the contour levels, ΔT, of 0.05 K.

Due to the difficulty in interpreting partial spectra split by CLUMPFIND between multiple spatially coincident clumps, the mean line width of the 3D-clumps was recovered using a different approach to the one used for the 2D-clumps. The velocity dispersion, σ, of each clump was estimated by determining the velocity range where the emission of that clump was above $e^{-1/2}$ of its peak intensity. This was done by visually inspecting these thresholded channel maps of each clump. The quoted FWHM is 2.35 σ and has an estimated uncertainty of 0.1 kms^{-1}, twice the uncertainty of the peak velocity, 0.05 kms^{-1}.

3.3.3 Results from the clump extraction

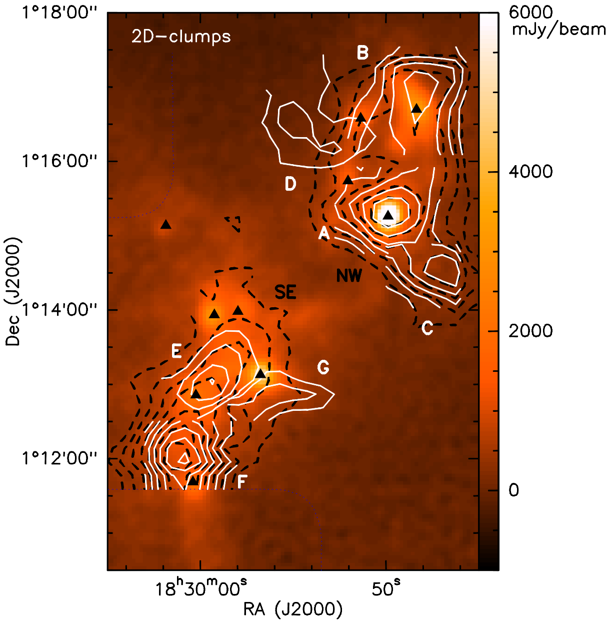

Figure 3.4: SCUBA map of the 850 μm continuum emission (colour scale) overplotted with the positions of the submillimetre sources (triangles), the $C^{17}O$ J=1-0 2D-clumps (solid white contours and letters) and the NW and SE sub-clusters (black dashed contours). The solid white contours are the intensity integrated over the corresponding velocity range for each clump. These are stepped by 0.2 K kms^{-1}, except for weaker 2D-clumps G and D, stepped by 0.1 K kms^{-1} (in T_A^*). The lower level of each clump is the same as the specified on Table 3.2. The NW and SE sub-cluster contours are integrated intensity over the entire velocity range. Contours are stepped by 0.25 K kms^{-1}, with the lower contour set at 1.25 K kms^{-1} (in T_A^*). The blue dotted line represents the edges of the $C^{17}O$ map.

Table 3.2: Properties of the 2D-clumps

2D-clump ID	RA_{peak} (J2000)	Dec_{peak} (J2000)	V_{peak} (kms^{-1})	Area (arcmin^2)	FWHM (kms^{-1})	M_{cf} ($M_\odot$)	M_{virial} ($M_\odot$)	Ratio (M_{virial}/M_{cf})	I_{low} (K kms^{-1})	I_{peak}
A	18:29:49.89	01:15:15	8.61	2.30	1.1	9.0	9.3	1.0	1.15	2.42
B	18:29:48.43	01:17:04	8.55	1.83	1.1	5.4	8.3	1.5	0.90	1.90
C	18:29:46.97	01:14:31	8.65	1.33	1.4	4.7	12.9	2.7	1.10	2.17
D	18:29:55.43	01:16:25	7.73	0.98	1.3	1.9	11.8	6.2	0.50	0.74
E	18:29:59.40	01:13:04	7.43	1.00	2.2	2.0	25.2	12.6	0.60	1.99
F	18:30:00.87	01:11:58	8.29	1.63	1.8	7.1	23.4	3.3	1.35	2.89
G	18:29:55.75	01:12:53	8.36	0.70	1.4	1.6	8.5	5.3	0.90	1.33
NW	18:29:49.89	01:15:15	8.61	9.06	1.2	31.3	33.2	1.1	1.00	2.42
SE	18:30:00.87	01:11:58	8.29	7.49	1.9	26.0	70.3	2.7	1.00	2.89

The identified 2D-clumps are shown on Fig.3.4, and the physical parameters summarized on Table 3.2, where: $\mathrm{RA_{peak}}$ and $\mathrm{Dec_{peak}}$ are the position where the emission peaks within each clump; $\mathrm{V_{peak}}$ is the velocity at the peak position, with an uncertainty of 0.05 $\mathrm{kms^{-1}}$; area is the surface in the map occupied by each clump; $\mathrm{M_{cf}}$ is the mass of the clump calculated from CLUMPFIND outputs; $\mathrm{M_{virial}}$ is the virial mass; Ratio $\mathrm{M_{virial}/M_{cf}}$ is a measurement of how bound each clump is - a gravitationally bound structure should have a ratio around unity, but given the uncertainties of these calculations, I consider a structure to be unbound if the ratio is above 2; $\mathrm{I_{low}}$ is the lower contouring level assumed when running the 2D-CLUMPFIND for each different clump (increasing with steps of 0.10 $\mathrm{K\,kms^{-1}}$), also shown on Fig. 3.4; and, finally, $\mathrm{I_{peak}}$ shows the integrated intensity in $\mathrm{K\,kms^{-1}}$ in $\mathrm{T_A^*}$ units as measured at the peak position.

The NW and SE sub-clusters are extended regions, and therefore, the peak positions and velocities correspond to one of the smaller identified clumps lying within the sub-cluster. The NW sub-cluster peaks at the position of clump A (& SMM1) and the SE sub-cluster peaks at the position of clump F (north of SMM11). Similarly, the presented velocities of the peak for the sub-clusters are not the mean velocity of the sub-clusters, but the velocity at the peak of the stronger clumps.

The 3D CLUMPFIND analysis identified a total of 16 clumps which will be called the 3D-clumps hereafter. These clumps are shown on Figure 3.5 as integrated intensity maps in $\mathrm{K\,kms^{-1}}$ (in $\mathrm{T_A^*}$) plotted over the continuum 850 μm data from SCUBA. Table 3.3 shows the properties of the 3D clumps as numbered and plotted on Figure 3.5. The nine first columns are as in Table 3.2 the last column being the intensity at the peak position in $\mathrm{T_A^*}$. Once again, masses were calculated after correcting for the IRAM 30m telescope efficiency for the $\mathrm{C^{17}O}$ J=1→0.

Since the velocity structure in the region, in particular the existence of two velocity components in some parts of the cloud, can affect the deduced clump structure, I also experimented with 3D CLUMPFIND on the $\mathrm{C^{18}O}$ J=1→0 data. The results from this differed from those of $\mathrm{C^{17}O}$ only in that two clumps (3D-clumps 3 and 10) were

Table 3.3: Properties of the 3D-clumps

3D-clump ID	RA_{peak} (J2000)	Dec_{peak} (J2000)	V_{peak} (kms^{-1})	Area ($arcmin^2$)	FWHM (kms^{-1})	M_{cf} ($M_\odot$)	M_{virial} ($M_\odot$)	Ratio (M_{virial}/M_{cf})	T_{peak} (K)
1	18:29:51.0	1:15:04	8.64	3.93	1.0	9.0	10.5	1.2	2.0
2	18:29:49.2	1:16:09	8.56	3.46	1.4	7.3	20.0	2.7	1.6
3	18:30:01.6	1:11:47	8.67	2.30	2.0	6.3	31.2	4.9	1.3
4	18:29:49.2	1:09:57	8.20	1.43	0.3	0.6	0.4	0.7	1.1
5	18:29:47.0	1:13:58	8.80	1.53	1.2	2.5	9.1	3.6	1.0
6	18:29:55.0	1:12:41	8.51	1.13	1.1	1.3	6.4	4.9	0.9
7	18:30:10.3	1:13:25	8.09	1.00	0.4	0.6	1.0	1.7	1.1
8	18:29:44.8	1:17:04	8.80	1.77	0.9	1.2	5.3	4.4	1.1
9	18:29:47.0	1:09:24	8.41	0.73	0.4	0.3	0.6	2.0	1.0
10	18:30:00.1	1:12:52	7.68	1.13	1.5	1.6	13.7	8.6	0.8
11	18:29:58.7	1:15:04	8.23	0.73	0.9	0.8	4.0	5.0	0.8
12	18:30:06.0	1:11:58	7.36	1.07	1.2	0.8	8.4	10.5	0.7
13	18:29:57.9	1:15:48	7.88	1.67	0.6	0.7	2.6	3.7	0.7
14	18:29:57.2	1:11:47	8.67	0.90	0.8	0.4	3.0	7.5	0.7
15	18:29:55.7	1:16:20	7.73	1.37	0.8	0.6	3.9	6.5	0.8
16	18:29:47.0	1:11:48	8.80	0.93	0.3	0.2	0.3	1.5	0.7

subdivided into 2 and 3 sub-clumps respectively. Collectively, these sub-clumps had properties very similar to their respective $C^{17}O$ clumps. The presence of these possible sub-clumps does not significantly alter the interpretation of the region for the purpose of this analysis, indicating that the $C^{17}O$ clumps adequately describe Serpens.

3.3.4 Discussion

The north region has two clear clumps unequivocally identified in both 2D and 3D methods: 2D-clumps A and B, which correspond to 3D-clumps 1 and 2 respectively. Both peak close to the position of the strongest submillimetre sources in this region (SMM1 and SMM9), and trace the gas around them in good agreement to the cold dense dust traced by the 850 μm emission.

A region with higher velocity gas was detected with the 2D analysis as 2D-clump C which corresponds to 3D-clump 5. This region has quite strong integrated emission making it detectable in the 2D search. However, due to its proximity, similar velocities

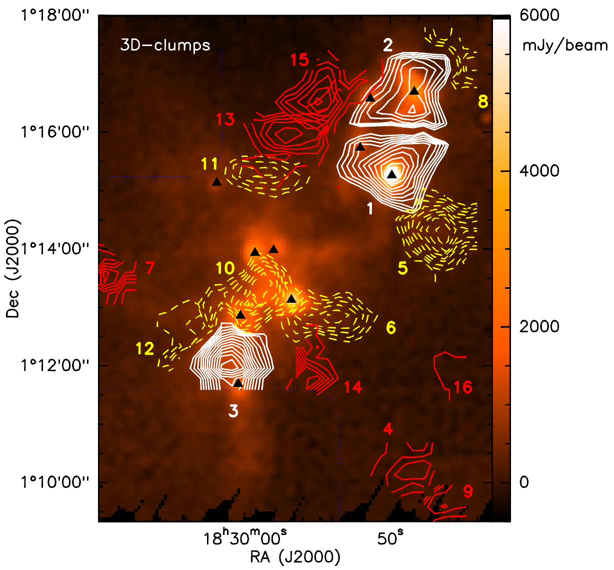

Figure 3.5: SCUBA map of the 850 μm continuum emission (colour scale) overplotted with all the $C^{17}O$ J=1-0 3D-clumps integrated intensity maps (contours and numbers) in K kms^{-1} (in T_A^*). The numbering of the cores is based on their peak intensity. The different contour style and colours identify clumps starting at different contour levels. The white solid contours are the clumps with the stronger integrated emission, with contours starting at 1 K kms^{-1}, the dashed yellow contours start at 0.3 K kms^{-1}, and the solid red contours start at 0.1 K kms^{-1}. For all clumps, the contour step is 0.1 K kms^{-1}. The blue dotted line represents the edges of the $C^{17}O$ map.

and weaker relative peak with respect to clump 1/A, the 3D search failed to separate these two in some of our trial runs of the 3D analysis, sensitive to the input parameters, in particular the step size. This clump is associated with very little submillimetre continuum emission but quite strong $C^{17}O$ (and $C^{18}O$) emission. The fact that it is also seen in N_2H^+ (Olmi and Testi 2002) and not in ^{12}CO tracing outflows (Graves et al. 2010), is consistent with the possibility of this being a denser region directly associated with the NW sub-cluster and close to being bound. It could, for example, be a very young prestellar core about to become gravitationally unstable and collapse (e.g. Walsh et al. 2007).

A region detected with the 3D analysis which was not seen in the 2D search was 3D-clump 8. This clump is detected at high velocities (8.80 kms^{-1}) and seems to surround the clump 2/B associated with SMM9, perhaps as a shell. Although apparently a somewhat super-virial clump, if affected by a depletion of $C^{18}O$ by a factor of 2-3 (Section 3.5.2), this clump could represent gas undergoing gravitational collapse.

Finally, there is also a low velocity region situated east of the main clumps of the NW sub-cluster, detected as a single clump with the 2D method (clump D, on Fig. 3.4) and as three separate clumps with the 3D CLUMPFIND (11, 13 and 15 on Figure 3.5). This region has a very small total mass (~ 1 - 2 $M_\odot$) and is a factor of ~ 6 super-virial. It seems to represent a quiescent region at lower velocities than the main cloud and connecting to the main cloud very close to the edge of the NW sub-cluster as seen on dust emission.

The bulk of emission on this NW sub-cluster presents a very coherent structure in space and velocity throughout. It does not appear to be as filamentary as the SE sub-cluster and the emission appears confined to relatively dense, cool compact regions.

The SE sub-cluster is quite different from the NW cluster, both in spatial structure and velocity, even though this is not obvious from the dust emission. A comparison of the 2D and 3D results shows the $C^{17}O$ emission to be more complex with none of the gas emission peaks coincident with the compact submillimetre sources. The main peaks of the $C^{17}O$ emission in this region lie in the filament seen in dust continuum emission, between the compact sources. The 2D-clumps E and F were detected as 3D-clumps 10 and 3 respectively. The edges of these two clumps overlap spatially with each other, with another more diffuse clump found by the 3D search peaking east of the filament, 3D-clump 12, and also another clump west of the filament, 3D-clump 6 (equivalent to 2D-clump G). 3D-clump 12 is the one further east and has the lowest velocity of the four, 7.36 kms^{-1}. Despite being adjacent, 3D-clump 10 and 3 have 7.68 kms^{-1} and 8.67 kms^{-1} respectively, representing a difference of 1 kms^{-1} between their peak velocities. There is another similar velocity difference between clump 10 and clump 6, west of the filament: 3D-clump 6 has a peak velocity of 8.51 kms^{-1}, ~0.8 kms^{-1} higher than its neighbour. These four 3D-clumps (3, 6, 10 and 12), with two sets of different peak velocities (around ~7.5 kms^{-1} and ~8.5 kms^{-1}), overlap with each other at low intensities mainly throughout this filamentary structure of the SE sub-cluster, even though their emission peaks are spatially offset. This shows that the double velocity structure in the SE sub-cluster (as detailed in Section 3.4) is, to some extent, recoverable from a single line fit using a 3D CLUMPFIND analysis.

The remaining clumps detected in the SE sub-clusters trace the less dense gas around this main filament. These were not detected in the 2D search mainly due to their very narrow line widths, between 0.3 and 0.5 kms^{-1}, making them faint in integrated intensity maps. Note that the dominant emission from regions detected east of the filament has lower velocities (3D-clump 7 has a peak velocity of 8.09 kms^{-1}), whereas the regions detected west (3D-clumps 4, 9 and 16) have higher velocities, from 8.20 kms^{-1} to 8.80 kms^{-1}.

Globally, there appears to be a velocity gradient from east to west of nearly 1 kms^{-1} over slightly more than 0.1 pc. However, this is not a smooth gradient throughout, as in the filamentary structure we have spatially-overlapping clumps with very different velocities. This velocity structure is further investigated using the C^{18}O lines, which are not split by hyperfine structure, in Section 3.4.

With both methods (the 2D and 3D clump extraction), about 67% of the mass in the NW region and 40% of the mass in the SE region is found to be comprised in the clumps. Even though both sub-clusters, SE and NW, have similar total masses (M_{cf}), they have a different equilibrium status, with a factor of 3 difference between their respective virial ratio. This translates into a higher kinetic support in the SE sub-cluster when compared to the NW. Interestingly, even when considering the possibility of depletion (Section 3.5.2), the SE region is still likely super-virial whereas the NW, due to its smaller line width, is marginally sub-virial. Note also the higher virial ratios for the individual smaller (both 2D or 3D) clumps within the SE sub-cluster when compared to the ones in the NW. This supports the idea of more kinetic support in the south, independently of a 2D or 3D approach to reveal the clumpy structure of the region.

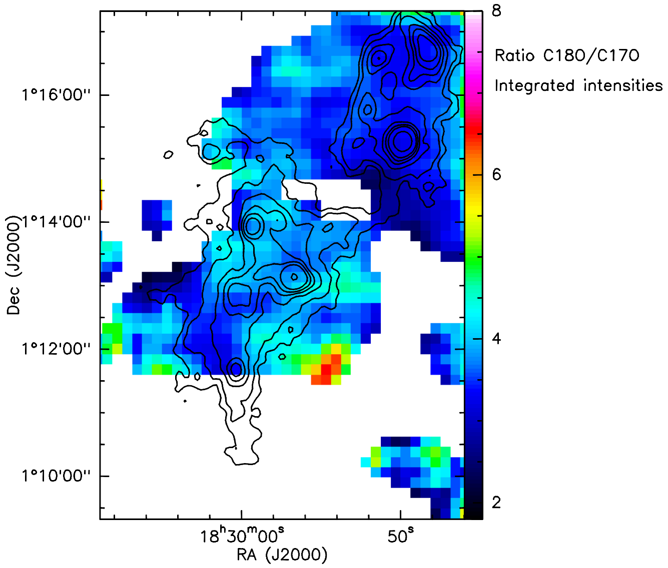

Figure 3.6: Ratio of the total integrated intensities of $C^{18}O$ and $C^{17}O$ J=1→0 transitions in Serpens. The blank regions within map are either originally non-observed areas (top and bottom-left corners) or regions where the hyperfine fitting of $C^{17}O$ was not well constrained and therefore not considered.

3.4 The kinematics of Serpens

The Serpens velocity structure was then comprehensively studied by imaging position-velocity (PV) diagrams of $C^{18}O$ J=1→0 and J=3→2 and by fitting the $C^{18}O$ J=1→0 emission at each position with a choice of a single or double Gaussian fitting to further study each component of the spectra separately. A detailed description of all the methods used as well as the results from the dynamical study of the region are presented in the subsequent subsections.

3.4.1 Optical depth and outflow influence

When studying a region with a given molecular transition it is important to understand the effect of optical depth on the emission that we are observing. The low optical depth of $C^{17}O$ suggests that the $C^{18}O$ is also reasonably optically thin. One way to constrain the optical depth of the $C^{18}O$ is through the ratio of the integrated intensities of the $C^{18}O$ and $C^{17}O$ J=1→0 transitions. If these species are both reasonably optically thin

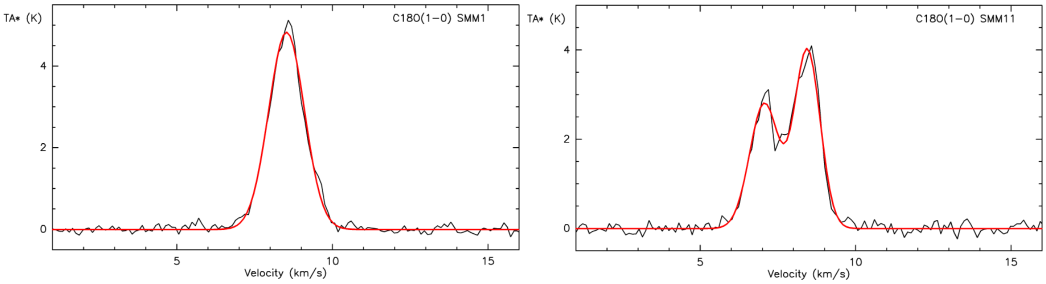

Figure 3.7: Observed $C^{18}O$ J=1→0 spectra (black solid line), smoothed in velocity to 0.1 kms^{-1} width channels, at two different positions: on SMM1 (left) and on SMM11 (right); with the respective Gaussian fit (red line). These are examples of a single peaked spectrum as seen in the NW sub-cluster and a double peaked profile, as seen in the SE sub-cluster.

and tracing the same gas, the ratio of their integrated intensities is expected to approach the ratio of their abundances, ~3.5 (e.g. Penzias 1980; Frerking et al. 1982). Over the mapped region the observed ratio (Fig. 3.6) is constant at ~ 3.5, consistent with having optically thin emission from both species, with very little spatial structure even in the denser regions. The greatest variations seen in the ratio are found toward the less dense parts around the sub-clusters, where the ratio ranges from 2.5 to 4.5. No peaks or dips in the ratio were found toward any submillimetre source, which would be where we might expect higher optical depth.

Another important issue when studying gas dynamics in regions of active star formation is the extent to which the line widths of molecular species are influenced by outflows. Using the available data, I looked for the influence of outflows on the size scale of the cores by investigating the spectra associated with all the submillimetre sources, looking for possible wing emission.

Although wings on $C^{18}O$ lines have proven to be able to trace outflow interaction (Fuller and Ladd 2002), in Serpens and with the 0.45 K r.m.s. noise of our original dataset (Section 3.2.1) no wings were found, and the lines in sources with known outflows are well fitted by a single Gaussian. For example, Fig 3.7 (left panel) shows that the $C^{18}O$ J=1→0 spectra towards SMM1 is well represented by a single Gaussian component, when this source is known to have an outflow (e.g. Hurt and Barsony

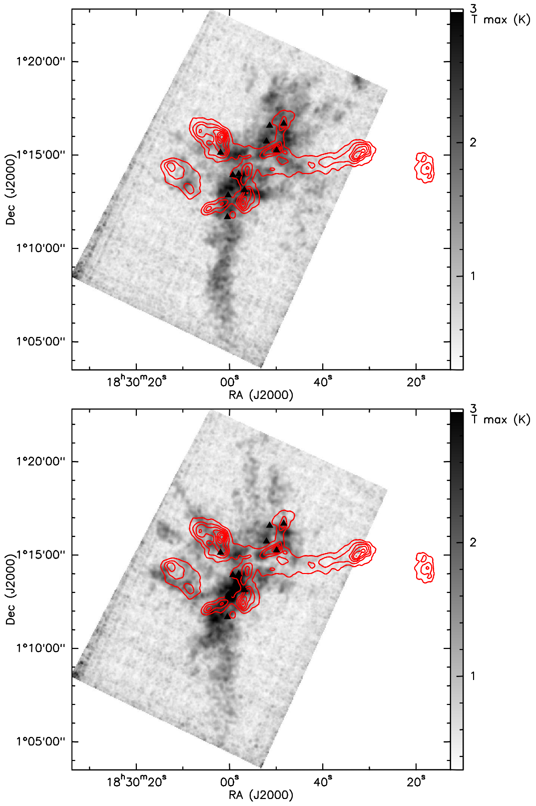

Figure 3.8: In grey scale is the blue and red maximum emission of $C^{18}O$ J=3→2: the top two panels correspond to the red $C^{18}O$ emission (above 8 kms^{-1}) and the two lower panels correspond to the blue $C^{18}O$ emission (below 8 kms^{-1}). The blue and red contours represent the ^{12}CO blue and red integrated emission respectively, with the blue being from -4 to 4 kms^{-1} and the red from 14 to 22 kms^{-1}. The contour levels are from 0.25 $K\,kms^{-1}$ with steps of 0.4 $K\,kms^{-1}$

1996). I have also searched for evidence of the influence of outflows in the $C^{18}O$ emission by comparing the $C^{18}O$ J=3→2 maximum emission to the ^{12}CO J=3→2 from the HARP Gould Belt Survey at JCMT (Fig. 3.8). I chose to show the maximum emission for $C^{18}O$ instead of integrated, to be able to see the narrow line width filamentary structures transversal to the main filament, otherwise missed in the integrated intensity maps. No obvious correlation nor anti-correlation between the $C^{18}O$ emission and the outflows is found in the region (also investigated in Graves et al. 2010).

As such, the Serpens $C^{18}O$ emission is not influenced by outflows nor it is optically thick and therefore the velocity structure we detect in $C^{18}O$ is associated with the global

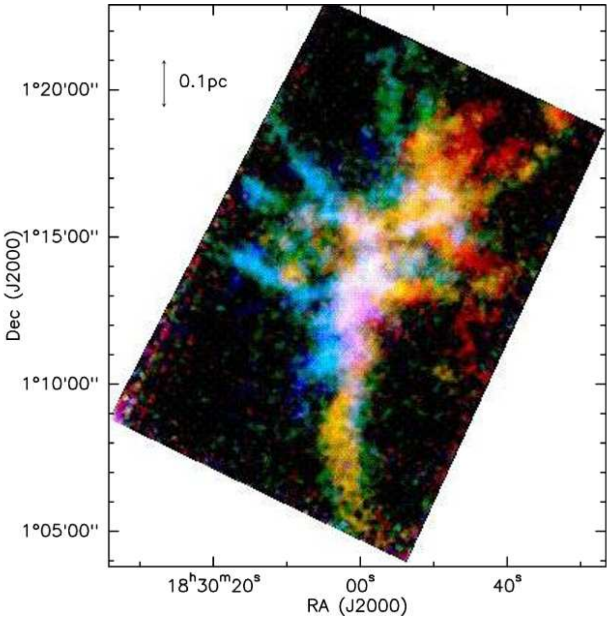

Figure 3.9: Velocity coded 3 colour plot of the GBS $C^{18}O$ J=3→2. Each colour represents the maximum value in the following velocity intervals: blue: 5 – 7.7 kms^{-1}; green: 7.7 – 8.3 kms^{-1}; and red: 8.3 – 11 kms^{-1}

cloud dynamics.

3.4.2 Position-velocity diagrams

As revealed by the $C^{17}O$ (Section 3.3.3), the NW region is mostly traced by higher velocity emission, the exception being the region offset to the east of the sub-cluster. On the other hand, the SE is not so homogeneous, containing both higher and lower velocity components, which overlap approximately where the filamentary structure is seen in the continuum observations.

In Fig. 3.7 I present two examples of the typical spectra in Serpens, showing an evident double peaked emission towards SMM11. In this section, I will show that this double peaked emission is present throughout the SE sub-cluster (e.g. Fig. 3.12) and I will further investigate the nature of this emission. In particular, the existence of a double-peaked spectrum in other optically thin tracers such as N_2H^+ (Olmi and Testi 2002) rules out self absorption as an explanation of the line profile of the $C^{18}O$

emission.

On the basis of a study of the line centroid velocity, despite the presence of double peaked lines, Olmi and Testi (2002) argued that the region is undergoing global rotation. Figure 3.9 illustrates the overall velocity trends and indeed, a velocity gradient that could mimic rotation is present.

However, position-velocity diagrams of the data show the evolution of the velocities along the map to be inconsistent with simple rotation and reveal a more complex dynamics. Moving from north to south, and slicing horizontally at the declination of each SMM source (Fig. 3.10), we can see the evolution of the emitting gas (Fig. 3.11 and 3.12). We can see that in the north the emission is confined to one single velocity (Fig. 3.11) and that moving to the south we gradually start to distinguish two velocities from two separate clouds, which are very well separated close to SMM11 (Fig. 3.12). For simple rotation, one would expect to see a smooth gradient along the velocity axis as the RA changes. Instead we observe two velocity components, clearly separated in the southern part of Serpens (see e.g. PV10) and merging together when moving to the north of the SE sub-cluster (see e.g. PV7). At this point, the two components are barely distinct lines, producing broad, non-gaussian profiles.

I also looked at the velocity structure using both horizontal and vertical PV diagrams on the GBS $C^{18}O$ J=3→2 dataset (Graves et al. 2010, vertical PV diagrams also shown here in Fig. 3.13). The information we get from here adds to the horizontal diagrams, in the sense that we can confirm the complex velocity structure, including the double velocity component towards the south sub-cluster (best seen on Fig. 3.13 top right panel). We can also see velocities below 8 kms^{-1} towards the northern region, in the first two panels. Because this corresponds to higher RA positions, these lower velocities in the north are only seen in regions offset to east from the sub-cluster seen in 850 μm emission. The two last panels of this Fig. 3.13 (bottom row, centre and right panels) show the bulk of emission towards the NW sub-cluster, which traces well the 850 μm continuum emission, showing us the velocities all concentrated between 8 and 8.5 kms^{-1}.

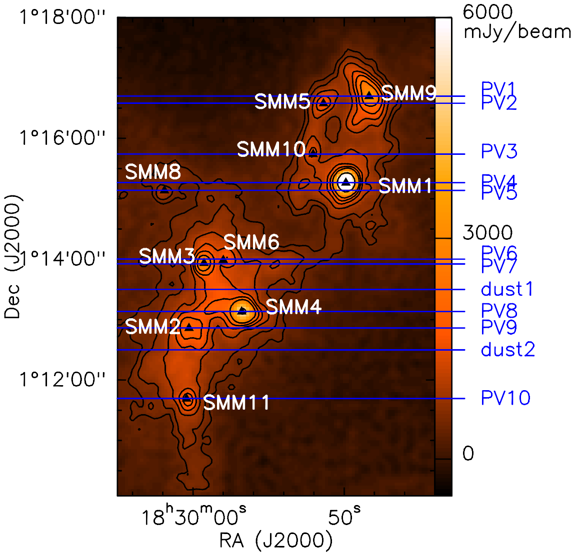

Figure 3.10: SCUBA 850 μm map of Serpens in colour scale and contours (contours as in Fig.3.1), showing the cuts made along the map for the position-velocity diagrams of $C^{18}O$ J=1→0 emission (Fig. 3.11 and 3.12). The cuts made crossing the SMM sources are denoted as PV#, where the # is the number of the cut, starting from the north. There are two cuts which are denoted as "dust" which do not intercept any source, but were made to understand the velocity structure around the dust filament.

3.4.3 Decomposition of the $C^{18}O$ spectral components

To investigate the complex velocity structure of the $C^{18}O$ J=1→0 emission seen on the PV diagrams I have decomposed the datacube, by fitting two velocity components to the $C^{18}O$ spectra and creating one model datacube for each component, from the Gaussian fits. This procedure allowed to study each of the two clouds independently.

The data were first rebinned to 0.1 kms^{-1} velocity channels. From the binned data, I created a script in CLASS to fit each spectrum with a single Gaussian and a double Gaussian, and select the best of the two fits to proceed with the modelling according to a selection criteria. The two Gaussian fit was selected as the model for the line only if *i)* the difference between the central velocities of the two Gaussian fit (ΔV) was greater than 0.35 kms^{-1} or *ii)* both lines were relatively strong with the peak intensity ratio of the stronger to the weaker line less than 2.4. The value of 2.4 was determined by a careful analysis of various line fits which showed that if the ratio was more than 2.4, the weaker line was poorly fit. The remaining spectra were fitted with a single

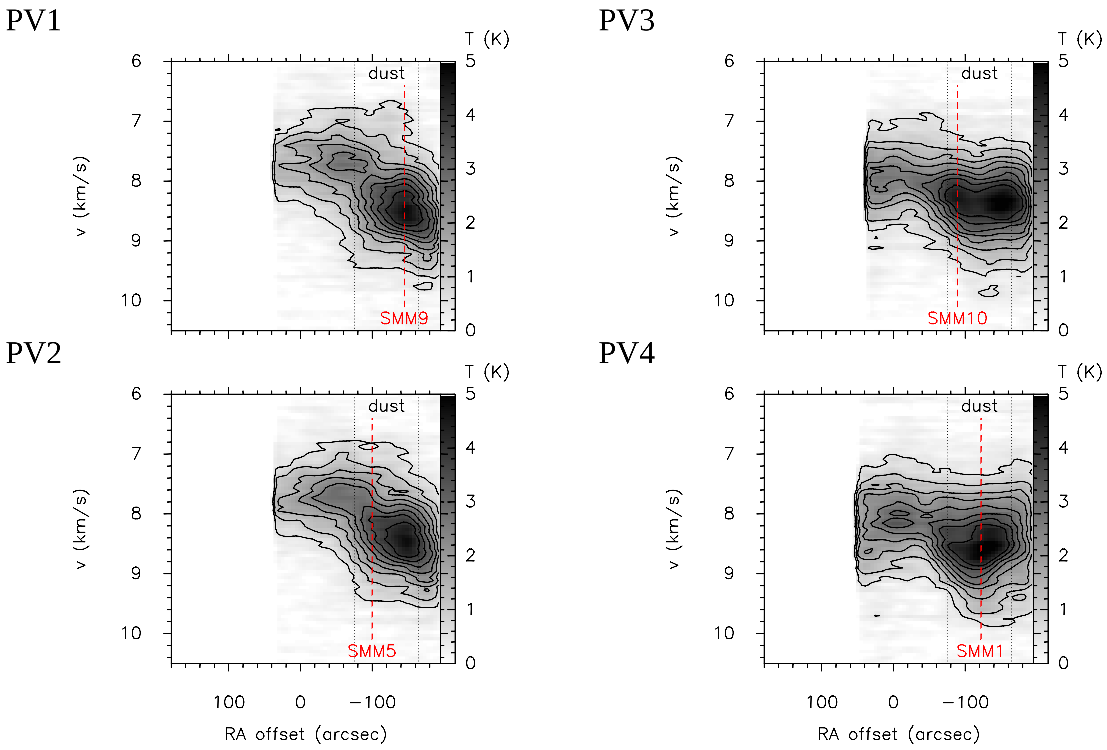

Figure 3.11: Position-velocity diagrams of the $C^{18}O$ J=1→0 emission in the NW sub-cluster. The cuts are horizontal slices of the map, as plotted and labeled in Fig. 3.10. The sources name and RA position are indicated in each figure (dashed red line). The dotted black lines delineate the region of strong dust emission in 850 μm. The declinations of each PV diagram are presented in Table 3.1 and the RA varies from $18^h30^m10^s$ to $18^h29^m45^s$ (from 180 to -195 $''$ offset respectively). The colour scale and contours represents the line intensity in units of T_A^*.

Gaussian.

The higher velocity component (hereafter, HVC) of the double peaked lines, as well as the single lines with central velocity greater than 7.8 kms^{-1}, were included in the HVC datacube; lower-velocity lines and single lines peaking below 7.8 kms^{-1} were incorporated in the lower velocity component (hereafter LVC) model datacube. The two separate datacubes from the modelled emission are shown in Fig. 3.14 and 3.15.

3.4.4 Results of the $C^{18}O$ velocity structure

Figure 3.14 shows the spatial distribution of the LVC and HVC using the integrated intensity from the model datacubes. It shows the HVC tracing the spacial distribution

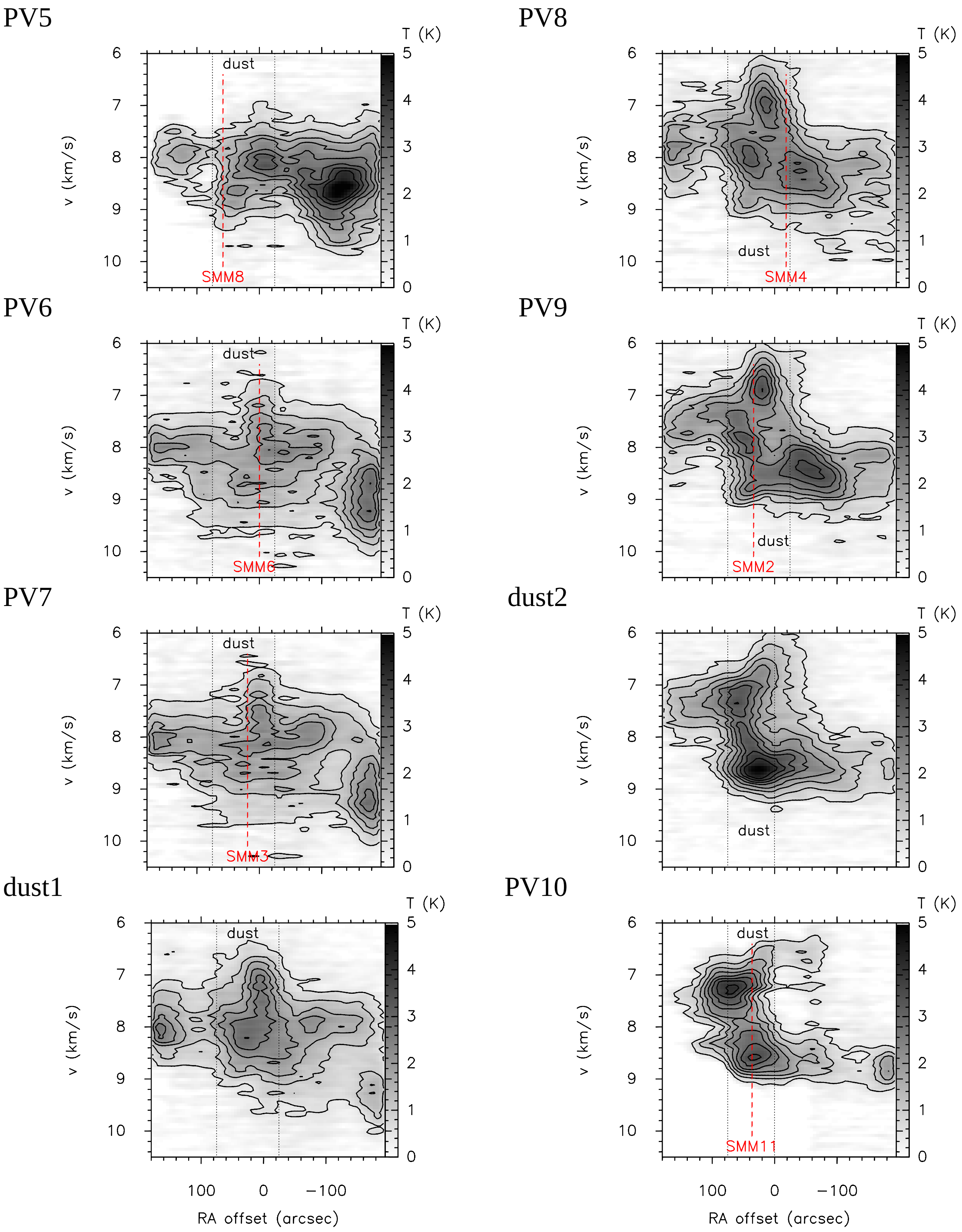

Figure 3.12: Same type of position-velocity diagrams as Fig.3.11 for the SE sub-cluster. The RA also varies from $18^h30^m10^s$ to $18^h29^m45^s$ (from 180 to -195 ″ offset respectively). PV diagrams displayed in descending declination, as they appear on Fig. 3.10.

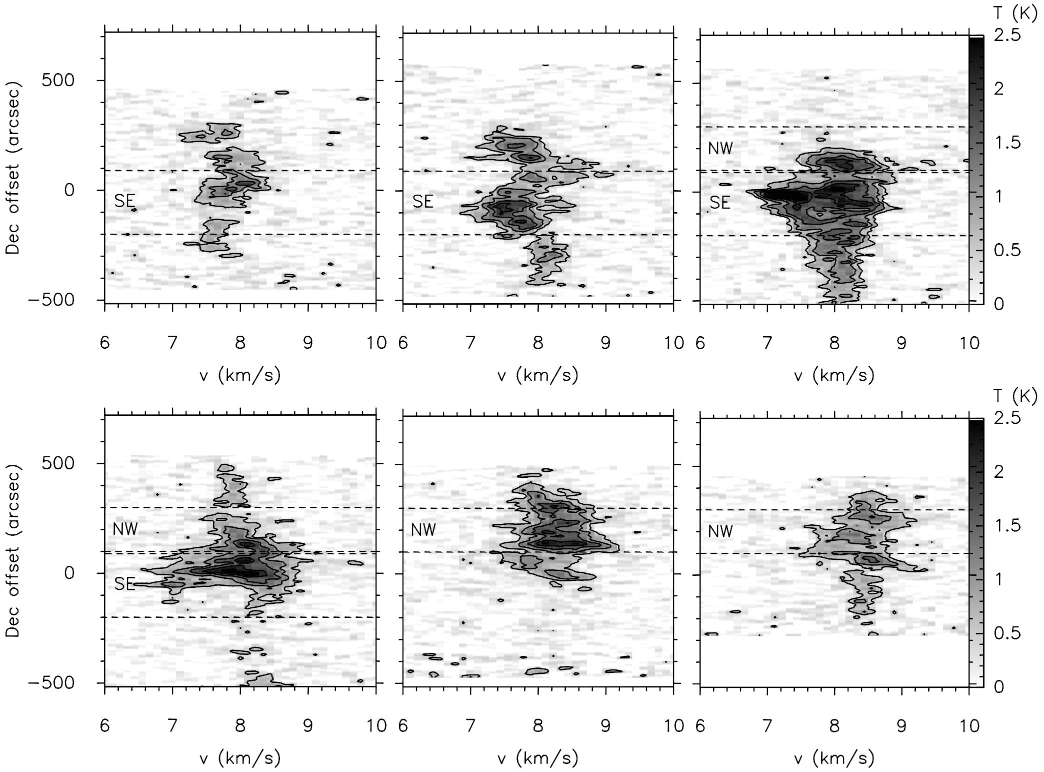

Figure 3.13: Vertical position-velocity diagrams in grey scale and contours representing the $C^{18}O$ J=3→2. Declination ranging for 1°4'24.1" to 1°25'0.8" (offset from -515" to 720" respectively) on all diagrams. The NW sub-cluster lies in Dec offsets of +90" to +270" and the SE sub-cluster between -180" and +90". Panels are displayed with decreasing Right Ascension (i.e. from East to West), with upper row being mostly representative of the SE sub-cluster whereas the lower row represents the NW sub-cluster. From top-left to lower-right diagrams, the cuts are at constant RA of $18^h30^m8.4^s$, $18^h30^m4.4^s$, $18^h30^m0.4^s$, $18^h29^m56.4^s$, $18^h29^m50.4^s$ and $18^h29^m44.4^s$.

of the 850 μm submillimetre continuum emission much better than the LVC. The HVC emission is stronger in the north, but it lies along the filament containing both sub-clusters, extending in a SE-NW direction. The LVC is roughly aligned along the S-N direction and is stronger in the south, where it meets the HVC. This region where the two clouds meet, i.e. where we detect two velocity components along a line of sight, will be hereafter referred to as the interface of the two clouds.

Figure 3.15 shows the integrated intensity of the modelled datacubes for each component as in Fig.3.14, along with the velocity structure of each cloud. In the NW

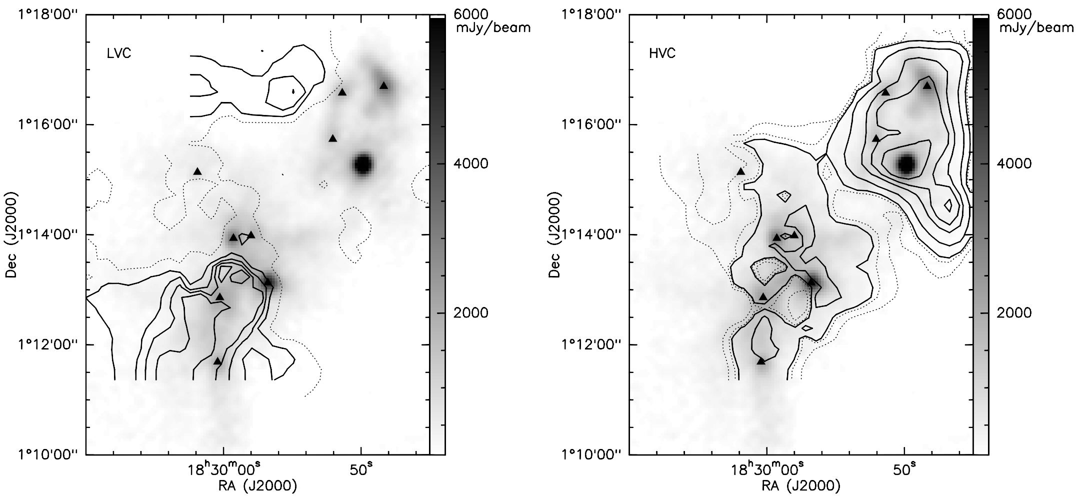

Figure 3.14: Integrated intensity maps as a result of the separation of the two line components of the $C^{18}O$ J=1→0 transition, under the assumption of two different clouds seen along the line of sight. The LVC is shown on the left and HVC on the right. The background grey scale shows the 850 μm emission tracing the cold dust, with its respective submillimetre sources plotted as triangles. The contours represent the integrated intensity of the modelled Gaussians (fitting the data in T_A^*). Contour key: left (LVC) at 0.2 K kms^{-1} (dashed) and 1.5, 2.5, 3.2 and 4.0 K kms^{-1} (solid); right (HVC) at 2.5 and 3.0 K kms^{-1} (dashed) and 3.2, 4.0, 5.0, 5.5 and 6.0 K kms^{-1} (solid).

sub-cluster, the HVC appears at velocities around 8.4 kms^{-1}, with the exception of a few regions at the edges of the cloud reaching velocities as high as 8.8 kms^{-1}. The region which stands out from the bulk of this sub-cluster in the HVC is the region SW of SMM1, by reaching the highest velocities of the entire cloud towards its edges (9 kms^{-1}). This region was also detected as an individual clump in the $C^{17}O$ analysis and it does not have a strong 850 μm dust emission, in contrast to its gas emission. The LVC in the NW sub-cluster is spatially offset to east, with velocities of 7.5 - 7.8 kms^{-1}, similar to most of the emission in the south. For both the HVC and LVC, the typical line widths in the NW are around 1 kms^{-1}.

The region between the two sub-clusters, mainly represented by the emission from the HVC, has the systemic velocity of Serpens (around 8.0 kms^{-1}) possibly due to the merging of the two components. Note that the emission here is rather weak, and the presence of SVS2, a more evolved (flat spectrum) near-IR source (Kaas et al. 2004), suggests this region to be already relatively deprived of gas and dust content.

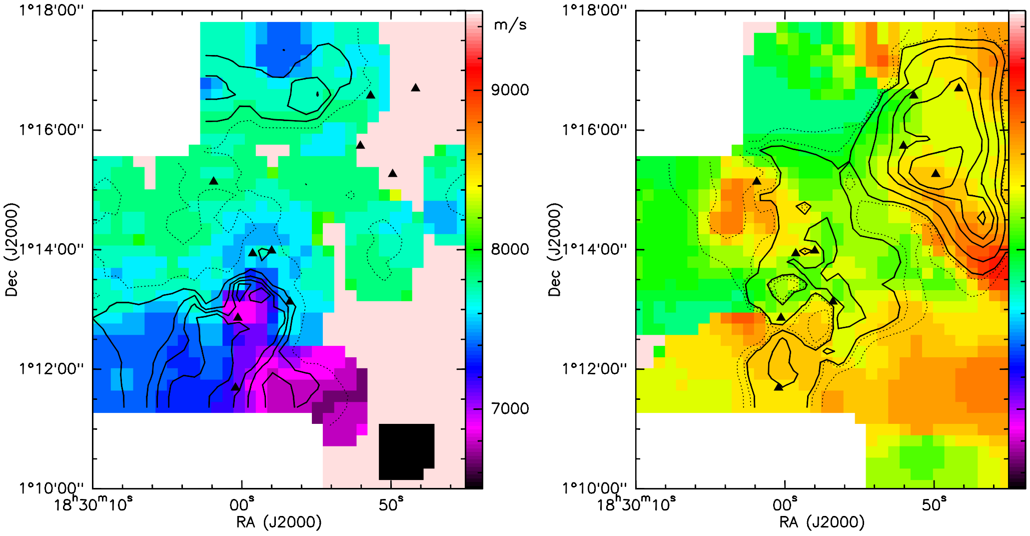

Figure 3.15: Maps of the velocity structure of Serpens from the separation of the two line components of the $C^{18}O$ J=1-0 transition. As in Fig. 3.14, the LVC is represented on the left and HVC on the right. The submillimetre sources are plotted as triangles, and the contours represent the integrated intensity as in Fig. 3.14. The colour scale is now the centroid velocity of the same modelled Gaussians, where the light pink colour represents the lack of a fit to that velocity component.

In the SE sub-cluster, the HVC velocities range between 8 and 8.5 kms^{-1}, being higher towards the southern end of the filament. On the other hand, the LVC shows a velocity gradient contrary to the HVC, increasing from west to east. The material west of the filament has velocities of about 6.8 - 7 kms^{-1} whilst at the filament axis velocities are around 7.5 kms^{-1}. This translates into a gradient of $\sim$ 5 $kms^{-1}pc^{-1}$. To the east of the filament the velocities are approximately constant at around 7.5 kms^{-1}. Therefore, the clouds seem to have a greater offset in velocities in the far-south end of the filament, converging into one velocity as one moves north. When two lines can no longer be separated, the emission becomes a single broader line, centered at the intermediate velocities of $\sim$ 8 kms^{-1}. The line width in the SE sub-cluster, specially where the two components merge, is around 2 kms^{-1}.

3.4.5 Discussion

The study of the dynamical properties of Serpens has shown some clear differences between the two sub-protoclusters of Serpens.

From the clump decomposition of the $C^{17}O$ emission (Sec. 3.3), after modelling the hyperfine structure assuming a single velocity component, we see that in the NW sub-cluster there is a good correlation between the gas clumps and dust structures. The stronger clumps detected in the gas correspond to the main submillimeter sources and are likely to be tracing their respective envelopes and surroundings. In contrast, the SE sub-cluster presents a more complex structure, with the gas distribution tracing clumps in-between the submillimeter sources. The virial analysis of all the Serpens clumps showed that the NW sub-cluster is more bound than the SE, as consequence of the broader line emission in the SE sub-cluster.

The analysis of the line profiles of $C^{18}O$ and PV diagrams in the entire region showed the existence of two velocity components, coming from two different clouds in the line of sight towards the SE sub-cluster. I have separated the emission coming from these two clouds in the line of sight to understand their spatial distribution and dynamical properties separately. With this study we can see that the overlap of the two clouds corresponds to the dust lane seen in the 850 μm continuum emission in the SE sub-cluster. The velocities of the clumps detected in $C^{17}O$ show that they correspond either to one cloud or another, explaining the existing spatial overlap of some of the clumps in the SE. The line width increases between the north and the south, reflecting four times greater kinetic support in the SE region, in comparison to the NW region, consistent with the $C^{17}O$ $J=1\rightarrow0$ analysis. The SE is therefore much more complex and much more dynamic than the NW.

As a final remark, note from Fig. 3.12 that the SMM sources in the SE sub-cluster appear at the edges of the interface between the two clouds, whilst the filamentary structure seen in dust follows the interface region itself (see the PV diagrams labeled as “dust”). It is, therefore, not surprising that at this interface there is an interaction between the LVC and the HVC, provoking the enhanced dust emission between SMM2, SMM3, SMM4 and SMM6, as well as the elongated filament that extends south towards SMM11 and beyond. A dynamical interaction between two clouds, as indicated by this space-velocity structure and the turbulent motions found towards the south, could be at the origin of this episode of star formation along the filament. However, the dynamics are not sufficient to understand if this is the case and the physical properties of the cloud need to be understood. The study I performed to unravel the physical properties of Serpens is presented in the following section.

3.5 Study of the physical properties

Given the low optical optical depth of $C^{18}O$, estimated from the ratio of the integrated intensities of the $C^{18}O$ and $C^{17}O$ J=1→0 transitions (Sec. 3.4), one can reliably study the physical properties of the gas around the protostars. Though surely suffering from some depletion at the inner parts of the envelopes, the three lower transitions of $C^{18}O$ are a valuable tool to investigate the dense regions, providing a measure of the gas column densities and excitation temperatures.

I have studied the physical properties of Serpens using two different methods. One assuming local thermodynamical equilibrium conditions (rotational diagram) and another using a non-LTE radiative transfer code (RADEX) for predicting the conditions for which $C^{18}O$ would have the observed intensities. Each method is described briefly in the following section (§3.5.1), with the results presented and compared later.

3.5.1 Considerations on the methods used

LTE: rotational diagram

When in the local thermodynamic equilibrium (LTE) regime, a molecule's population distribution in the energy levels is entirely determined by collisional excitations and de-excitations and described by the Boltzmann distribution. For each transition, there is a critical density where the collisional and radiative excitations have equal rates. Therefore, for collisions to be dominant in populating a given energy level, the densities need to be higher than the critical density for that transition. In Table 3.4, I present the critical densities for the three lower transitions of $C^{18}O$ that I used for this study.

Table 3.4: Critical densities ($n_{critical}$) at 10K and 20K for $C^{18}O$

$C^{18}O$ transition	A_u (s^{-1})	K_u (10^{-11} cm^3s^{-1}) 10K / 20K	$n_{critical}$ (10^3 cm^{-3}) 10K / 20K
J=1→0	6.266×10^{-8}	3.3 / 3.3	1.9 / 1.9
J=2→1	6.011×10^{-7}	7.2 / 6.5	8.3 / 9.3
J=3→2	2.172×10^{-6}	7.9 / 7.1	27 / 30

These values were derived using the information provided by the Leiden Atomic and Molecular Database (Schoeier et al. 2005) : A_u being the Einstein Coefficient for the upper level, and K_u the respective collision rate at both 10 K and 20 K.

In LTE the particles are well mixed and their kinetic temperature corresponds to a single excitation temperature (T_{exc}). When several transitions of a same molecule are thermalised, we can use them to calculate the gas properties, using a rotation diagram analysis. From chapter 2.1 (Eq. 2.27) we know that

$$T_{mb}\Delta v = \frac{c^3 h g_u A_{ul}}{4\pi k \nu^2 Q} N_{tot} e^{-E_{ul}/kT_{exc}}. \tag{3.4}$$

For each transition i between the levels u and l of energy $E_i \equiv E_{ul}$, we can introduce a variable W_i as being the observed average integrated intensity of the transition i ($W_i = T_{mb}\Delta v$) and the variable γ_i as being $\gamma_i = \frac{c^3 h g_u A_{ul}}{4\pi k \nu^2 Q}$ and is constant for each transition. By doing so, we can re-write the previous relation as:

$$W_i = \gamma_i N_{tot} e^{-E_i/kT_{exc}} \tag{3.5}$$

which is equivalent to:

$$\ln\frac{W_i}{\gamma_i} = \ln(N_{tot}) - \frac{E_i}{kT_{exc}}. \tag{3.6}$$

Using equation (3.6) I performed a linear fit of the observed quantities (W_i for all the three transitions) and extracted the total column density (N_{tot}) and excitation temperature (T_{exc}) from the constant and the slope of the fit, respectively. I show an example of this fit at eight positions in Serpens in Fig. 3.16. This method is called the population or rotation diagram method and has been extensively used in the literature (e.g. Goldsmith and Langer 1999) and has shown to be reliable when the transitions are in LTE. The temperature fit from this method is robust as it does not depend on the absolute values of the intensities of the lines, but rather on their relative strength. On the other hand, the absolute value of column densities retrieved from this method is very sensitive to fluctuations of the absolute values of the observed intensities. Despite its uncertainties, the rotation diagram method is robust in retrieving the structure and trends of the column density throughout the region, as well as the approximate absolute column densities.

Non-LTE: RADEX

The radiative transfer equations are difficult to solve due to the non-linear behaviour of the interdependence of the level populations and the radiation field, i.e., the local level populations depend on the radiation field and the radiation field depends on the overall level populations. Therefore, the statistical equilibrium and radiative transfer equations are coupled and have to be solved simultaneously for the entire cloud. The escape probability formulation allows a simplification of these calculations when only the global properties of a medium are of interest. It uses the averaged probability for a photon created at a given optical depth in a cloud to escape, and it assumes that a photon created locally can only be absorbed locally, allowing the decoupling of the statistical and radiative transfer equations.

RADEX is a statistical equilibrium radiative transfer code, part of the Leiden Atomic and Molecular Database[4] (LAMDA), that uses the escape probability formula-

---

[4] http://www.strw.leidenuniv.nl/moldata/

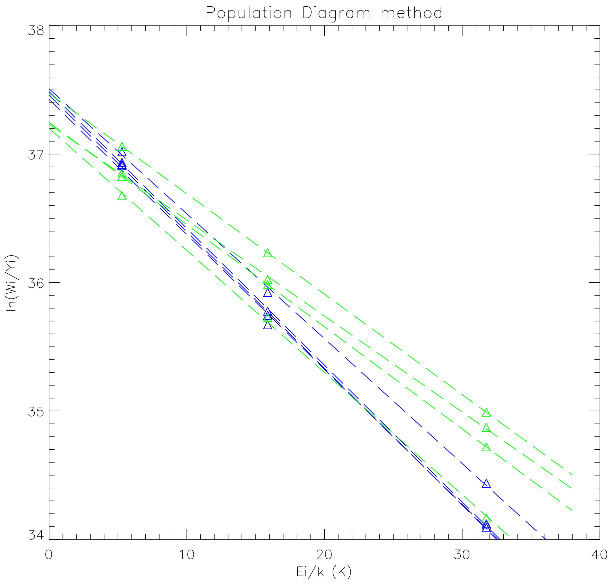

Figure 3.16: Example of fits using the LTE approach, i.e., the rotational diagram method, for eight positions. These positions are the same as the ones where I have studied using the non-LTE approach (Section 3.5.2; Fig. 3.17 and 3.18). There are three triangles per position, corresponding to the three transitions considered, which are connected by their respective line fit (dashed lines). The blue and the green distinguish the positions in the north and the south respectively.

tion to calculate expected line intensities for a given molecule (van der Tak et al. 2007). It is a one-dimensional radiative transfer code that does not assume LTE nor optically thin lines and considers an isothermal and homogeneous medium without large-scale velocity fields. For the escape probability formulation, it requires the choice between three given geometries: an expanding spherical shell, a static spherically symmetric homogeneous medium or a plane-parallel slab. It also requires a choice of the collision partners and the input of a molecular data file with the collisional rate coefficients for the molecule under study. The other inputs, mainly retrieved from observations, include the volume density, background temperature, kinetic temperature, gas line width and gas column density. With this, RADEX quickly estimates the intensities for the requested molecular line transitions. It does not make any assumption as to beam filling factors, so if justified, this needs to be corrected for before comparing these intensities with the observed ones. The way it estimates the intensities is by starting to solve the statistical equilibrium in the optically thin case and iteratively find a consistent solution for the level populations and the radiation field.

For this non-LTE study I have used the RADEX source code as well as the example python scripts made available from LAMDA for more robust calculations. I adapted the python code to provide a fit of the column densities of $C^{18}O$, as well as the kinetic temperature. I have assumed a static spherically symmetric homogeneous medium and the collision partners to be only H_2. The molecular data file with the collisional rate coefficients for $C^{18}O$ was retrieved from LAMDA. Finally, I chose eight positions in Serpens as a sample of different conditions to proceed with this study, four in the NW and four in the SE sub-cluster.

For each position modelled, the input volume density was determined from the submillimetre dust continuum emission, assuming a cloud depth of 0.2 pc (based on the projected size of the dust emission), a dust absorption coefficient of 0.02 cm^2g^{-1} at 850 μm (van der Tak et al. 1999; Johnstone and Bally 2006) and a dust temperature of 10 K for all but three positions. The three exceptions are: position NA (≡SMM1) where 38 K was adopted from the SED fit by Davis et al. (1999), and positions NB(≡SMM9) and SA(≡SMM4), where we adopted a temperature of 25 K, consistent with the $>$ 20 K determined by Davis et al. (1999). Where two velocity components existed (in the SE positions) I assumed the H_2 volume density to be the same for both $C^{18}O$ velocity components. Changing the dust temperature or the assumed cloud depth changes the estimated H_2 volume densities, but this change only becomes important if the volume densities becomes lower than the critical densities for the considered transitions. I tested these effects using RADEX, and the resulting gas column densities and kinetic temperatures remain unaffected by changes in the assumed dust temperature between 10 K and 40 K, or in the assumed depth between 0.1pc and 0.3pc. If the transitions are thermalised, only the fractional abundance of $C^{18}O$ will be affected by changing the assumed H_2 column density.

The central velocity, line widths and integrated intensity of each transition were retrieved from the data by fitting the average spectrum within a 5″ radius of each position. The central velocity and line widths shown in Table 3.5 are the average over the three transitions, and have an uncertainty of the order of 0.1 kms^{-1}. For the 4 positions in the NW sub-cluster, this procedure is straight-forward as the lines of all three transitions are well represented by single Gaussians. However, the spectra of the SE sub-cluster positions, having two velocity components, was separately fitted with 2 Gaussians in order to investigate any possible differences between the two components.

For each of the eight positions, I created a 500 × 500 grid of gas column densities (ranging from 10^{12} to 10^{19} cm^{-2}) and temperatures (ranging from 5 K to 40 K). For each grid point, I used RADEX to calculate the C^{18}O integrated intensities for all three transitions (denoted as $I^{\rm radex}_{(J_{up}-J_{low})}$). I used a χ^2 comparison to find the best fit of the RADEX models to the observed ratios $I_{(1-0)}/I_{(2-1)}$ and $I_{(1-0)}/I_{(3-2)}$ as well as the absolute value of $I_{(1-0)}$. The χ^2 has been calculated using Eq. (3.7), where $I^{\rm obs}_{(J_{up}-J_{low})}$ is the observed integrated intensity of the transition between J_{up} and J_{low}, and $\Delta(x)$ is the uncertainty on the quantity x.

$$\chi^2 = \left(\frac{I^{\rm obs}_{(1-0)}/I^{\rm obs}_{(2-1)} - I^{\rm radex}_{(1-0)}/I^{\rm radex}_{(2-1)}}{\Delta(I^{\rm obs}_{(1-0)}/I^{\rm obs}_{(2-1)})}\right)^2 + \left(\frac{I^{\rm obs}_{(1-0)}/I^{\rm obs}_{(3-2)} - I^{\rm radex}_{(1-0)}/I^{\rm radex}_{(3-2)}}{\Delta(I^{\rm obs}_{(1-0)}/I^{\rm obs}_{(3-2)})}\right)^2 + \left(\frac{I^{\rm obs}_{(1-0)} - I^{\rm radex}_{(1-0)}}{\Delta(I^{\rm obs}_{(1-0)})}\right)^2 \tag{3.7}$$

In calculating the χ^2, I assumed that the relative errors of the input integrated intensities are independent, and therefore the uncertainty in their ratio is described by

$$\left(\frac{\Delta(I^{\rm obs}_{(1-0)}/I^{\rm obs}_{(2-1)})}{(I^{\rm obs}_{(1-0)}/I^{\rm obs}_{(2-1)})}\right)^2 = \left(\frac{\Delta(I^{\rm obs}_{(1-0)})}{I^{\rm obs}_{(1-0)}}\right)^2 + \left(\frac{\Delta(I^{\rm obs}_{(2-1)})}{I^{\rm obs}_{(2-1)}}\right)^2 \tag{3.8}$$

I have estimated the relative errors of the input integrated intensities as approximately the relative errors in the intensity, $T_{\rm mb}$ (Eq. 3.9), i.e, not including the error in velocity. This assumption will overestimate the values of χ^2 for each position, but changes on the best-fit result are only of the order of 1% (tested when assuming an overestimated uncertainty in the line widths of 20%). The error in $T_{\rm mb}$ is given by the r.m.s. of the line fit given by CLASS.

$$\Delta(I^{\mathrm{obs}}_{(1-0)})/I^{\mathrm{obs}}_{(1-0)} = \Delta(T_{mb(1-0)})/T_{mb(1-0)} \tag{3.9}$$

The results from the RADEX models are presented in Table 3.5. For each position it shows the input parameters, the best fit integrated intensities for the three lines, the best fit temperature and column densities as well as the implied abundances from the non-LTE analysis. For comparison, the table also includes the temperatures retrieved using the rotation diagram method. The χ^2 surfaces in the temperature versus column density domain for each position studied with the non-LTE approach are shown in Sec. 3.5.2.

3.5.2 Results on the physical properties

To understand the correlation between the dust and gas in this region, I show, in Fig. 3.17, a pixel-by-pixel comparison of the 850 μm flux density against the integrated intensity of the three transitions of C^{18}O, all convolved to a common resolution of 24″. For the purpose of these scatter plots, I oversampled the data to a pixel size of 2.5″, in order to better distinguish the trends.

Overall, the distribution of points is similar for the three transitions. There is a general correlation between dust and gas, especially for the weaker emission (Fig. 3.17). However, the distributions also show structure which consistently appears across all three transitions. The very prominent peaks of dust emission corresponding to the stronger submillimetre sources are obvious, and although in general there is an increase in the C^{18}O emission at these positions, the dust peaks do not correspond to global peaks in the C^{18}O emission. In fact, the nature of the relationship between the C^{18}O emission and the dust appears different in the NW and SE sub-clusters.

Focusing on the NW region (blue in Fig. 3.17), the plots are dominated by two dust peaks, each of which is associated with a well defined, but separate, increase in C^{18}O emission. Comparing the C^{18}O intensity, the emission becomes weaker moving to higher energy transitions. On the other hand, the SE sub-cluster (green in the figure)

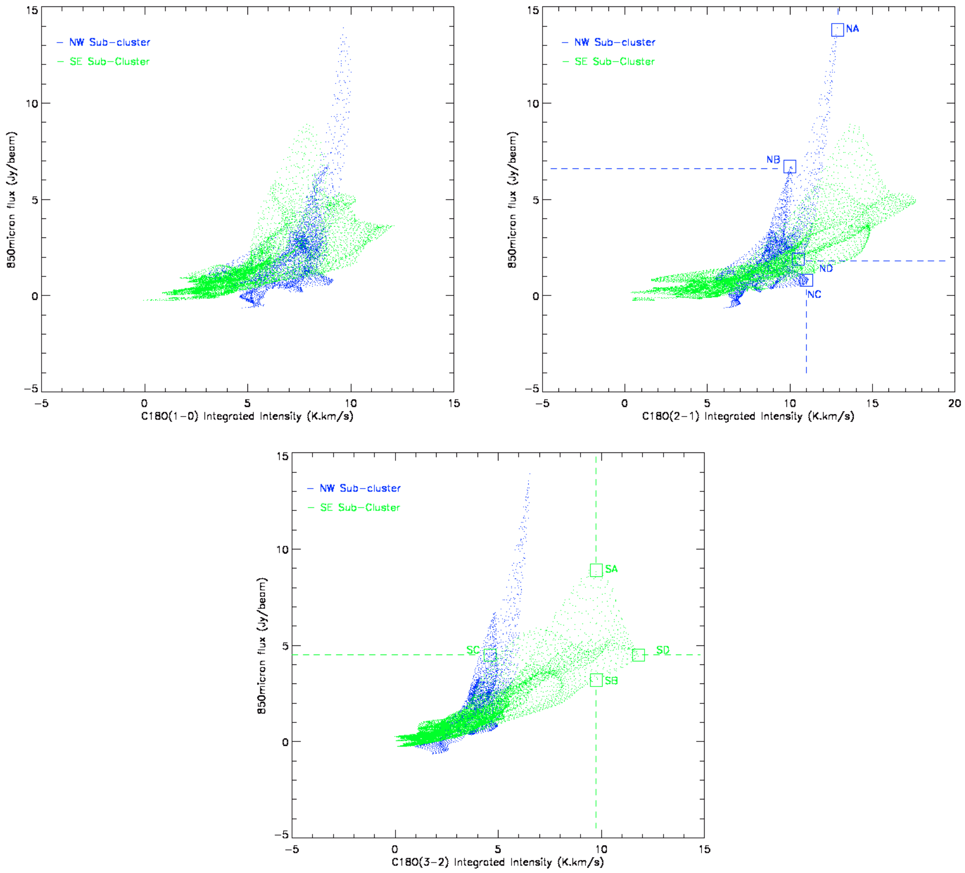

Figure 3.17: Scatter plots of the SCUBA 850 μm dust emission against the C^{18}O integrated intensity over the whole range of velocities (top left: J=1→0, top right: J=2→1, bottom: J=3→2). Blue points show the NW sub-cluster and green points the SE sub-cluster. The four positions chosen in each sub-cluster to investigate with non-LTE modelling shown on the middle panel for the NW region and the lower panel for the SE region. These positions are also indicated on Fig. 3.18.

shows a different trend from transition to transition, becoming stronger at higher transitions. In addition, there appears to be a more pronounced general correlation in this region between the dust and line emission. Nevertheless, there are clearly structures departing from this trend: several 850 μm peaks corresponding to SMM sources; and C^{18}O peaks, which do not have significant submillimetre emission.

The four positions in the NW and another four in the SE marked in the scatter plots (Fig. 3.17) are the positions selected for a detailed study with RADEX. Their position in the map is indicated on Fig. 3.18. These positions were chosen from the scatter

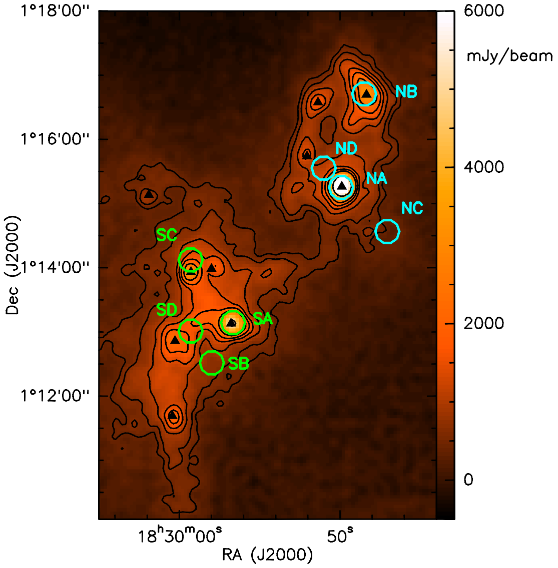

Figure 3.18: Map showing the positions of the selected regions for the non-LTE RADEX study indicated by blue and green circles (for the positions in the NW and SE sub-clusters, respectively) and labeled as in Fig. 3.17. The contours and colour scale show the SCUBA 850 μm emission as in Fig. 3.10.

plots as corresponding to interesting features in the correlations between the dust and gas emission, selected to span the range of the correlation.

LTE results

In the LTE approach, I applied the rotation diagram method in the entire map, as a pixel-by-pixel comparison of the emission from the three transitions, after convolving the integrated intensity maps of the three transitions with the same resolution (24″) and pixel re-sampling for an exact match (5″ pixels, as in the original IRAM data). From these, and using the linear relation as described in Sec. 3.5.1, I constructed the map of the excitation temperature across the region (Fig. 3.19, left). This shows the NW and SE sub-clusters to have different temperature structures. The NW appears very homogeneous with no significant temperature peaks and with temperatures ranging from 9 to 10 K. This can also be seen in Fig. 3.16, where the blue lines, corresponding to the four positions in the NW (shown in Fig. 3.18), are approximately parallel. Since

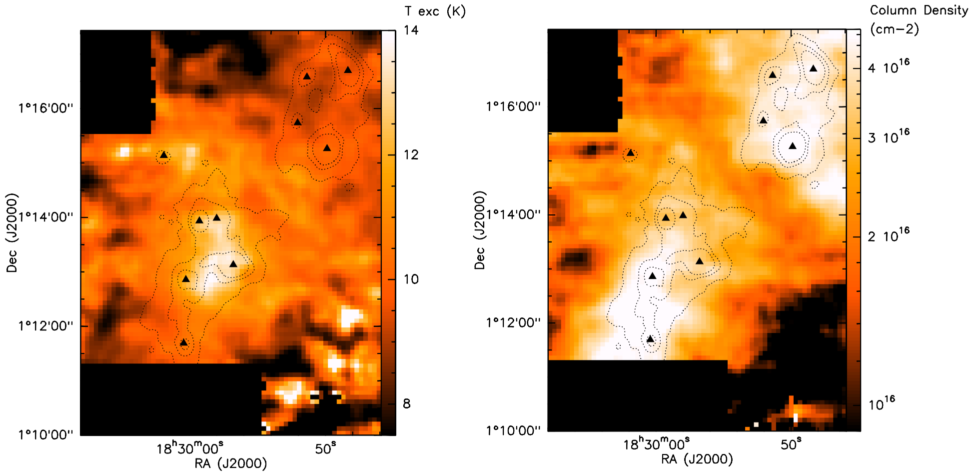

Figure 3.19: Left: LTE excitation temperature map in colour scale. Right: Column density map (colour scale) derived from the rotation diagram method. The dotted black contours show the dust 850 μm emission at 0.6, 1.2 and 1.8 Jy beam^{-1}.

the slope of this curve is related to the temperature, this shows that the temperatures in the North are all very similar. In contrast, the SE region has both higher temperatures, ranging from ~ 10 to 14 K, and a much more peaked distribution. In Fig. 3.16 this is shown by a range of different slopes in green. Interestingly, Fig. 3.19 shows that this enhanced temperature in the south does not peak on the SMM protostars but rather between them, along the dust filament which corresponds to the interface region seen on the PV diagrams (Fig. 3.12).

The C^{18}O column density map (Fig. 3.19, right) calculated from the rotation diagram follows more of the dust structure than the temperature map. Both the south and north sub-clusters are evident as denser regions, even though the dust and gas column densities peaks are not always coincident, especially in the SE. The mean C^{18}O column densities are very similar in the north and the south. The regions with higher gas column density (the entire NW sub-cluster and the filament between SMM11 and SMM2 in the SE sub-cluster) have a lower temperature. Conversely the regions with slightly lower gas column density (between SMM2, SMM4, SMM3 and SMM6 in the SE sub-cluster) have higher temperature. The region south-west of the NW sub-cluster which appears to have a relatively high gas column density seems to have very similar properties to the rest of the NW sub-cluster and yet it is not detected in dust emission.

Non-LTE results

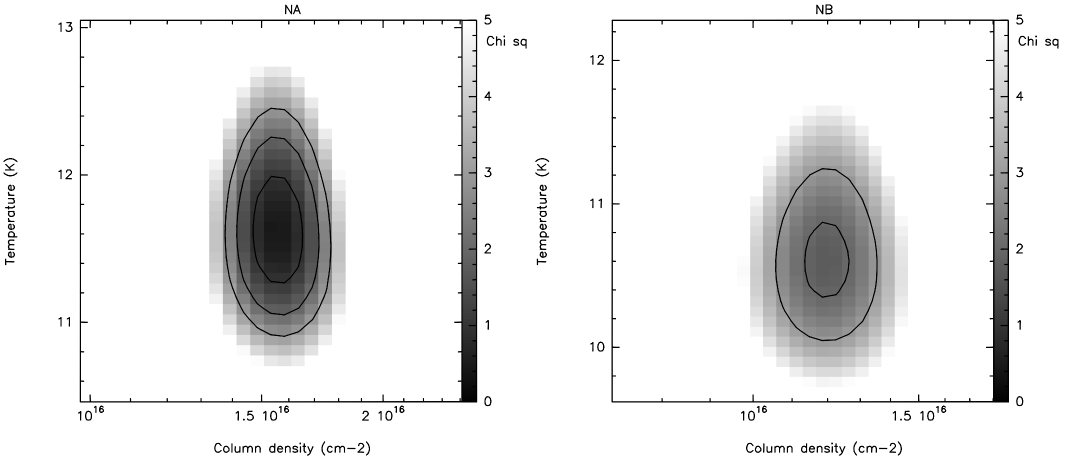

Figure 3.20: Left: χ^2 surface for the integrated intensity ratios at position NA. Right: χ^2 surface for the integrated intensity ratios at position NB.

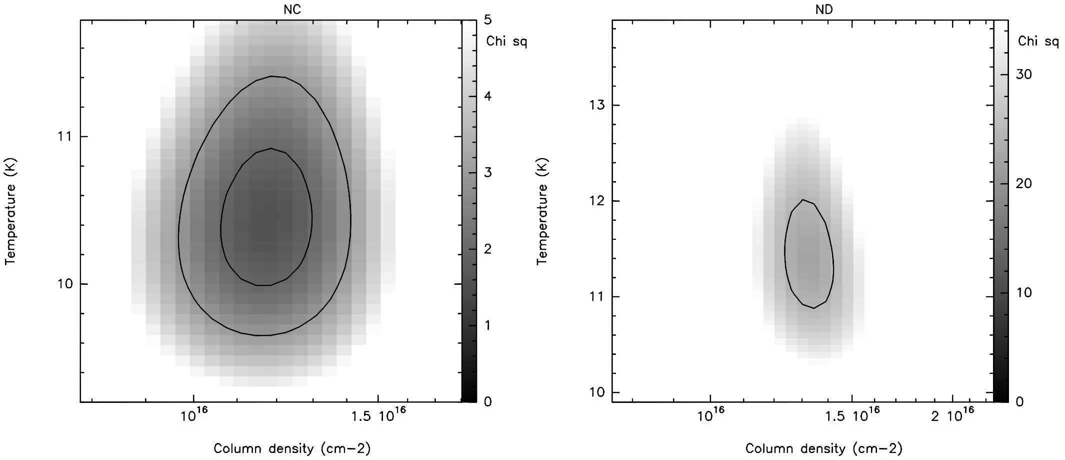

Figure 3.21: Left: χ^2 surface for the integrated intensity ratios at position NC. Right: χ^2 surface for the integrated intensity ratios at position ND. Contour at 25.

In Figures 3.20 to 3.25 I present the χ^2 surfaces from the non-LTE analysis of the line integrated intensity ratios for each of the eight positions studied. For each position, the χ^2 is plotted as a function of the RADEX output temperature and gas column density. Given the use of three quantities in the fit, I consider the reduced$-\chi^2$ (i.e. $\chi^2/3$) to be a good fit when it is smaller than unity. All figures have contours at χ^2 = 1, 2 and 3 with the exception of ND (Fig. 3.21) and SD (Fig. 3.25).

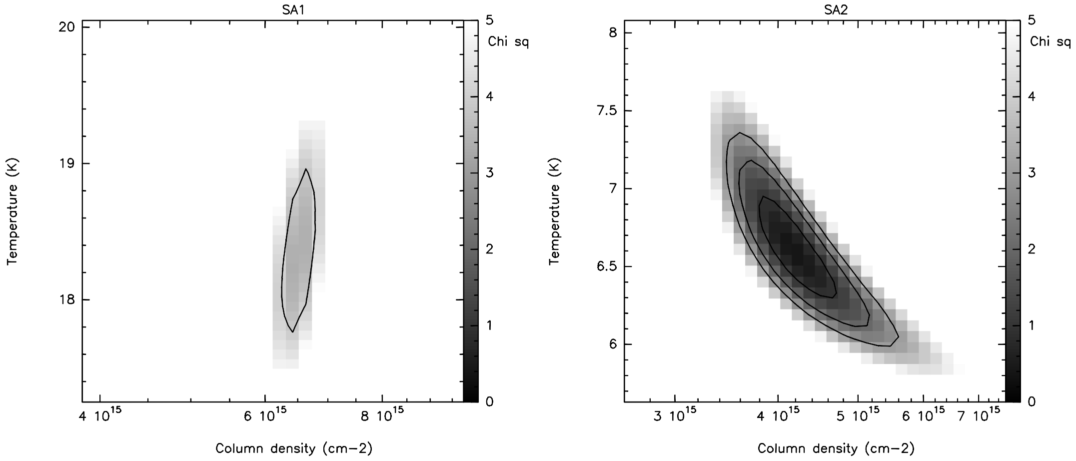

Figure 3.22: χ^2 surfaces for the integrated intensity ratios at position SA: SA1 (LVC) on the left, and SA2 (HVC) on the right.

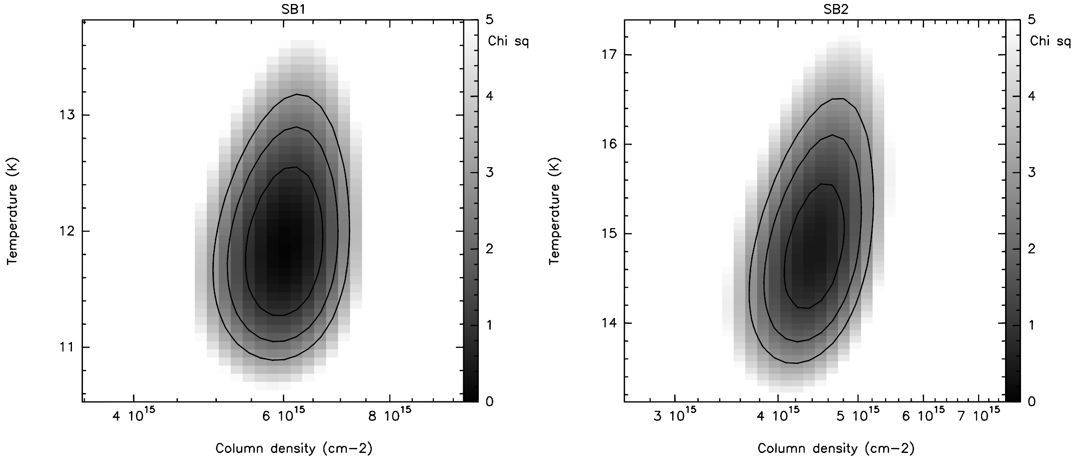

Figure 3.23: χ^2 surface for the integrated intensity ratios at position SB: SB1 (LVC) on the left, and SB2 (HVC) on the right.

In Table 3.5, from the second to the fourth column I present some observed parameters at each position, identified in the first column. With the exception of the central velocity, these parameters were used as an input in RADEX. Columns five to seven are the observed integrated intensities of the three transitions, used to find the best fit through a χ^2 comparison. The following three columns (entitled RADEX best

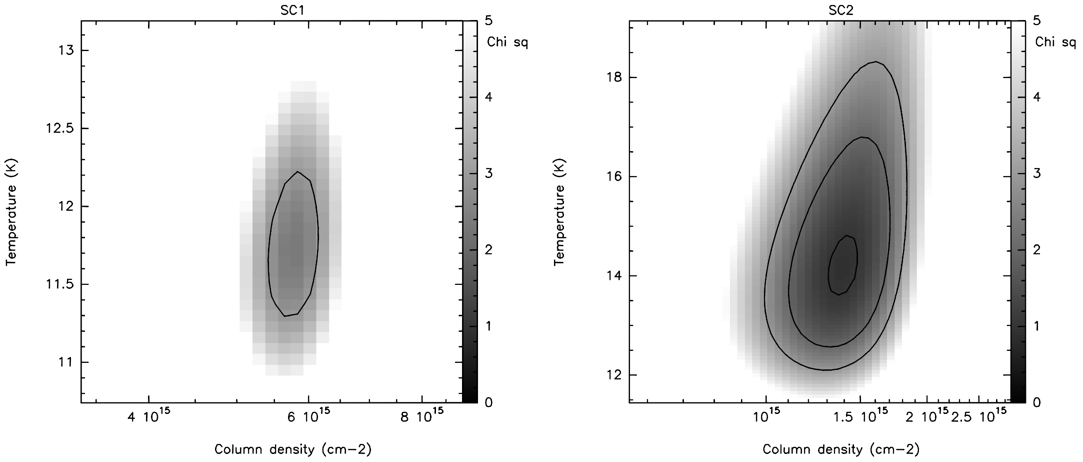

Figure 3.24: χ^2 surface for the integrated intensity ratios at position SC: SC1 (LVC) on the left and SC2 (HVC) on the right.

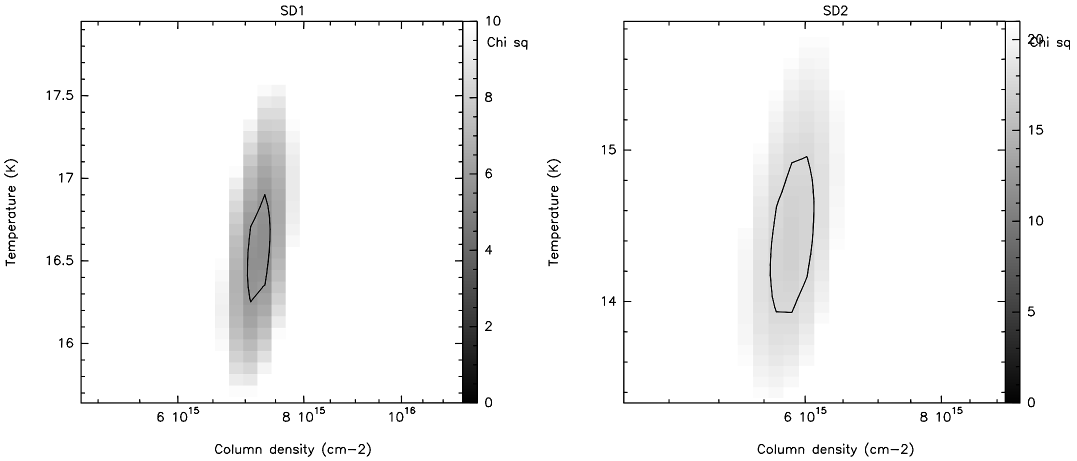

Figure 3.25: χ^2 surface for the integrated intensity ratio at position SD: SD1 (LVC) on the left, and SD2 (HVC) on the right. Note the different colour scale for SC2. Contours are 6 for SD1 and 18 for SD2

fit) present the integrated intensities from the RADEX modelling which achieved the minimum χ^2. I present the values of τ implied by the conditions at the best fit situation, with the associated uncertainties, estimated by retrieving the variations of τ within the contoured regions in Fig. 3.20 through to 3.25. The column densities of H_2 derived from the dust emission for each position are presented next, followed by the column densities of $C^{18}O$ from the best fit (columns twelve and thirteen) and by the implied $C^{18}O$ abundances. Finally, I present the best fit for T_{kin} from the RADEX (non-LTE), side-by-side with the excitation temperatures, T_{exc}, retrieved for those positions, from the LTE method.

For positions ND, SB, SC and SD, the H_2 column densities derived from the dust and used to estimate the abundance of $C^{18}O$ were calculated using a dust temperature of 10K. Assuming a temperature of 15K for all 4 positions (ND, SB, SC and SD) would reduce the H_2 column densities by a factor of 2.1, representing an equivalent rise of the fractal abundance of $C^{18}O$ by the same amount.

The derived $C^{18}O$ fractional abundance (which is averaged along the line of sight) implies a depletion of $C^{18}O$ of between a factor of 1.4 (for NC) and 4.3 (for SC), with an average of 2.5 compared to the abundance of 1.7×10^{-7} in dark clouds (Frerking et al. 1982). Given that the ratio between $C^{17}O$ and $C^{18}O$ has shown these two species to be reasonably optically thin with an integrated intensity ratio of $\sim$3.5, a factor 2.5 depletion of $C^{18}O$ implies the same depletion factor for $C^{17}O$.

3.5.3 Discussion

Table 3.5 shows that in the NW region the LTE (rotation diagram) and non-LTE (RADEX) analysis are in good agreement. Both the rotation diagram and RADEX show variations in T_{ex} of only 1 K. They produce absolute values of temperature which differ by at most 10%, and the trend in temperature between positions is similar. Comparison of the $C^{18}O$ column densities and the H_2 column density calculated from the dust continuum emission at the same positions, imply $C^{18}O$ abundances a factor of $\sim$2.5 smaller than typical values (Sec. 3.5.2). Given the low optical depth of the $C^{18}O$ emission (Sec. 3.4), the low $C^{18}O$ column density, and hence abundance, implies that the $C^{18}O$ is depleted with respect to the molecular hydrogen, even in the warmer envelope of SMM1, consistent with the results of Hogerheijde et al. (1999).

The RADEX results also showed that $C^{18}O$ may only be marginally optically thin in some regions, with opacity values approaching the unity. Somewhat surprisingly given the low optical depth of the $C^{18}O$ (below 1) and despite its depletion, neither the LTE nor the non-LTE analysis finds evidence of increased temperatures towards the apparently warmer inner regions of the embedded protostars. Although the dust emission indicates the presence of warm dust towards the protostars (Davis et al. 1999), the $C^{18}O$ emission implies low and uniform temperatures. Although dilution of the warm inner region within the 24″ beam may contribute to the difficulty in detecting the warmest gas, it is surprising that no evidence of any temperature increase is seen. CO is predicted to freeze-out on to grain surfaces at temperatures below ~ 18K, consistent with the low $C^{18}O$ excitation temperature, but not at dust temperatures of, for instance, ~ 30K seen towards SMM1. Since this is above the sublimation temperature of pure CO ice it is possible the CO could be trapped in a water rich ice, which would only sublime and return CO to the gas phase at temperatures of ~100 K (e.g. Visser et al. 2009).

The southern region is more complex. In terms of column density, for all four positions the non-LTE results show the LVC to have slightly higher column density than the HVC. The LTE and non-LTE approaches agree in the sense that the northern positions and SD have higher values of $C^{18}O$ total column density (summed over both velocity components where necessary). These are followed with decreasing column density by SB, then SA and finally SC.

SA is at the position of SMM4, where there are two components of the $C^{18}O$ emission, a strong low velocity component (SA1) plus a weaker high velocity component (SA2). In the J=3→2 transition, the high velocity component becomes faint and difficult to separate from the lower velocity component (see Table 3.5). This weak J=3→2 emission constrains the temperature to 6.6 K for the higher velocity component (SA2). At SC the two cloud components are also significantly blended. The temperature of the LVC at this position (SC1) is ~11 K, constrained within ~1 K, with the weaker HVC warmer, but somewhat less well constrained.

In general, in the south, the lower velocity component has a higher temperature toward the most central positions studied (SA and SD). Then at SB and SC, at the edges of the dust emission, the temperatures are similar with both components still higher than the temperatures generally found to the north (~12 K and 14 K in the south versus ~11 K in the north). Overall, and with the exception of SA, the HVC has higher temperatures than in the north, around ~14 K. On the other hand, the LVC traces the temperature trend as identified by the LTE study (Fig. 3.19) better than the HVC, but the absolute LTE temperatures are between the non-LTE values for LVC and HVC.

Therefore, I conclude the temperature rise toward the south to be real. Such a rise is consistent with a scenario where this region is tracing the interaction/collision between two clouds, with a shock layer with higher temperatures and complex motions at the interface.

3.6 Summary and discussion

My study of the Serpens Main Cluster has shown that two apparently very similar protoclusters as seen in submillimetre dust continuum emission can reveal very different dynamical and physical properties in molecular lines. Despite all the outflows seen in ^{12}CO in the region, the denser gas around the cores seen in C^{18}O and C^{17}O does not seem to be perturbed and is able to provide details of the quiescent material in the cloud.

In the NW sub-cluster the bulk of emission has a velocity around 8.5 kms^{-1}. However, there is a lower velocity component of the gas east of the sub-cluster (Fig. 3.11) with the transition between these component being rather smooth. The velocity difference between the submillimetre sources in this sub-cluster is small, ranging from 0.1 to 0.3 kms^{-1}.

The physical conditions in this NW sub-cluster are also rather coherent. Temperatures and column densities derived from both LTE and non-LTE analysis are consistent and show little variation within the sub-cluster. The C^{18}O emission peaks are mostly consistent with the dust peaks. Clump-finding studies of this region retrieved two main peaks which are directly related to the two stronger submillimetre sources in the NW sub-cluster: SMM1 and SMM9. However there are no evident temperature peaks associated with the submillimetre sources. The remaining gas emission in the sub-cluster is either associated with these main peaks or weaker structures surrounding the main bulk of the dust emission. The gas column density very closely follows the clumps/integrated intensity distribution of the gas, particularly in the lower J transitions tracing the colder gas.

The SE sub-cluster on the other hand is a much richer region in its dynamics and properties. There are two velocity components/clouds along the line of sight, clearly identified using both clump-finding and position-velocity diagrams. These two clouds appear to be interacting. They are more offset in velocity in the south and start to mix moving to the north within the sub-cluster. Most of the southern submillimetre sources appear to have a stronger association with the HVC, despite having some emission from the LVC along the same line of sight. A counterexample however is SMM2 which, as can be seen in the PV diagrams, has a stronger $C^{18}O$ J=1→0 lower velocity component. The overall dust filament, as seen in 850 μm, coincides with the N-S lane where the two components overlap, suggesting it is tracing the interface region between the components, the region where they are interacting. Ultimately, this interaction might have been responsible for triggering the star formation episode in the SE sub-cluster.

In contrast to the NW sub-cluster, the LTE temperature in the SE sub-cluster is both higher and more structured, peaking close to the ridge of dust continuum emission. Unlike the north, the two velocity components in the south are difficult to fit with a single well defined temperature. The general trend, however, points to higher temperatures in the southern sub-cluster than in the northern sub-cluster.

The modelled column density map (Fig. 3.19) closely traces the emission from the lower transitions (J=1→0). The high $C^{18}O$ column density regions in the SE are not associated with any of the submillimetre sources, but rather the southern filament. The region with enhanced temperature, however, does not coincide with the highest column density regions. The uniform dust emission over this SE region results from the southern filament having lower temperature but higher column density whereas the northern part of the SE sub-cluster is slightly less dense, but warmer, resulting in equivalent 850 μm dust emission.

3.6.1 Proposed Scenario

The velocity, temperature and density structure of Serpens suggest a more complex picture than simple rotation which has previously been invoked to explain the velocity structure (e.g. Olmi and Testi 2002).

It is known that cloud-cloud or flow collisions happen in the Galaxy as molecular clouds move within the spiral arms. Furthermore, simulations of cloud-cloud collisions (e.g. Kitsionas and Whitworth 2007) have shown that density enhancements in the collision layers can be high enough to trigger star formation. Additionally, clouds are commonly seen as filamentary structures, not only during, but also prior, to star formation. We suggest that the two velocity components seen in Serpens are tracing two clouds along the line of sight and that the interaction of these clouds is a key ingredient in the star formation in Serpens.

We propose that we are seeing two somewhat filamentary clouds traveling toward each other and colliding where the southern sub-cluster is being formed. The cloud coming toward us is to the east while the cloud moving away from us is to the west, and represents the main cloud. An inclination angle between the two filaments could explain why the two velocity components are spatially offset in the north but overlapping in the south. This scenario explains both the double peaked profiles of the optically thin lines and their distribution along what has previously been identified as the ‘rotation axis’ of this region.

If the north region was initially close to collapse, the direct collision of the clouds in the south could indirectly trigger or speed up this collapse in the north without significantly enhancing the temperature or perturbing the intrinsic, ‘well behaved’ velocity and column density structure. In the south, however, such a collision makes it easy to understand why the density and temperature enhancements are not necessarily associated with the sources, as they are being generated by an external trigger: the collision.

Note in addition, that in the south, unlike the majority of the sources in the north, there is a poor correlation between the submillimetre sources (Davis et al. 1999) and 24 μm sources (Harvey et al. 2007b), as shown in Fig. 3.1, suggesting a wider spread of ages of the protostars in the south than in the north. Such an age spread would be consistent with a collision in the sense that a collision is not an instantaneous event but rather an ongoing process.

A first test to this collision scenario is the timescale for which such clouds would cross each other, their interaction time. If we assume that each cloud is a filament of radius of 0.1 pc (similar to the size of the dust 850 μm emission), and we adopt a collision velocity of 1 km s^{-1} (approximately the mean observed velocity difference, along the line of sight, between the two components), the timescale from when the clouds start colliding until they are completely separated, assuming a head on collision, is 4×10^5 years, consistent with the estimated $\sim 10^5$ year age of the region (Harvey et al. 2007a; Kaas et al. 2004).

Several simulations of cloud collisions such as proposed here exist in the literature. For example, SPH simulations of clump-clump collisions from Kitsionas and Whitworth (2007), have shown that two approaching clumps with a slow collision velocity of 1 kms^{-1} (Mach number of 5), can indeed trigger star formation in the collision layer. Specific simulations of the proposed collision in Serpens will be presented in the next chapter.

Table 3.5: Modelling results for the 8 positions selected from the scatter plots

Position	H_2 density ($\times10^5$ cm^{-3})	Line width (kms^{-1})	Central velocity (kms^{-1})	Observed			RADEX best fit				Column density		Abundance	Non-LTE	LTE
				$I_{(1-0)}$ (K kms^{-1})	$I_{(2-1)}$ (K kms^{-1})	$I_{(3-2)}$ (K kms^{-1})	$I_{(1-0)}$ (K kms^{-1})	$I_{(2-1)}$ (K kms^{-1})	$I_{(3-2)}$ (K kms^{-1})	$\tau_{(1-0)}$	H_2 (10^{23}cm^{-2})	$C^{18}O_{radex}$ (10^{15}cm^{-2})	$C^{18}O/H_2$ ($\times10^{-8}$)	T_{kin} (K)	T_{exc} (K)
NA	2.60	1.6	8.5	9.15	10.65	6.94	9.23	10.42	7.28	1.0 ± 0.2	1.60	15.4	9.6	11.7	10.3
NB	2.25	1.5	8.4	7.47	8.87	4.76	7.44	8.15	5.20	1.0 ± 0.2	1.39	11.9	8.6	10.6	9.5
NC	1.62	1.9	8.5	8.14	10.35	4.90	8.13	9.29	5.57	0.8 ± 0.2	1.00	11.9	12.0	10.5	9.5
ND	6.50	1.4	8.5	7.90	10.09	4.82	7.99	8.88	6.20	1.0 ± 0.2	4.01	13.5	3.4	11.4	9.5
SA1	2.98	2.2	7.8	4.69	10.57	8.46	4.75	9.84	9.01	0.13 ± 0.01	1.84	6.4	5.8	18.2	13.4
SA2	2.98	1.0	8.3	2.42	1.98	0.50	2.50	2.02	0.64	1.1 ± 0.3		4.2		6.6	
SB1	3.99	1.5	6.9	4.63	6.66	4.20	4.74	6.72	4.37	0.4 ± 0.1	2.46	6.0	4.2	11.9	12.7
SB2	3.99	1.1	8.5	3.32	5.99	4.31	3.35	5.73	4.50	0.3 ± 0.1		4.4		14.8	
SC1	6.28	1.7	7.7	4.61	7.37	3.87	4.72	6.82	4.37	0.37 ± 0.05	3.87	5.8	1.9	11.7	10.2
SC2	6.28	1.2	8.7	1.17	2.58	1.45	1.21	2.23	1.71	0.09 ± 0.05		1.4		14.2	
SD1	7.81	1.1	6.9	4.81	7.44	7.31	5.01	8.53	7.34	0.38 ± 0.02	4.82	7.3	2.7	16.6	12.8
SD2	7.81	1.4	8.2	4.41	8.66	4.66	4.45	7.42	5.74	0.31 ± 0.02		5.8		14.4	

Positions of the NW sub-cluster are identified as starting with N, while the south positions start with S. For the positions in the SE, the labels 1 and 2 identify the lower (LVC) and higher velocity (HVC) components respectively. Where there are two velocity component lines, the H_2 volume density was assumed to be the same for both components. For this case $C^{18}O$ fractional abundance was calculated using the total column density of $C^{18}O$, summing both components, to be compared with the total column density of H_2. Finally, the LTE T_{exc} was calculated assuming the total integrated intensity, and therefore, no distinguishing was made between the two velocity components where these existed.

Chapter 4

Numerical tests of the trigger of star formation in Serpens

Based on the article Duarte-Cabral et al. (2011): *Was a cloud-cloud collision the trigger of the recent star formation in Serpens?*

4.1 Overview on simulating Star Formation

Observations indicate that stars form in dense, clumpy filaments in molecular clouds. However what controls how gas evolves into these structures, and where and when star formation occurs, is widely debated. Some clouds may simply be undergoing global gravitational collapse (Goldreich and Kwan 1974; Larson 1981; Bate 1998; Klessen et al. 2005; Glover and Mac Low 2007; Heitsch et al. 2009; Offner et al. 2009; Gao and Lou 2010). On the other hand, external triggers such as ionisation and shock fronts around OB stars (Elmegreen and Lada 1977; Klein et al. 1983; Dale et al. 2007; Gritschneder et al. 2009) or large scale colliding flows due to turbulence or supernovae (Clark and Bonnell 2005; Heitsch et al. 2008) may induce localised star formation in a molecular cloud. An additional mechanism for triggered star formation is cloud collisions, long thought to be important in inducing star formation in molecular clouds, both from observations of individual regions (e.g. Scoville et al. 1986) and numerical simulations (e.g. Gittins et al. 2003).

In the strive to reproduce the observations and test the theories behind the formation of molecular clouds and stars, numerous simulations have been preformed to date. Many have been able to reproduce the collapse of an isolated cloud with subsequent formation of a filamentary structure and successfully reproduce many of the observed characteristics, just by using self-gravity and hydrodynamics (e.g. Klessen et al. 1998; Bate et al. 2003). However, the star formation efficiency on these simulations was too high. The absence of stellar feedback, turbulence and magnetic fields meant that no mechanism was stopping the material from being accreted onto a star. The most recent simulations (e.g. Price and Bate 2009; Bate 2009b) in this field have been able to start incorporating these mechanisms into the codes and the results are becoming more consistent with what is observed in MCs. Nevertheless, initial conditions, assumptions and simplifications/approximations of the models have proven to play an important role on the final results in terms of star formation efficiency and the dynamics of the overall environment.

Simulations of cloud collisions and flow driven star formation have been performed to test the importance and efficiency of these processes to trigger star formation (e.g. Gittins et al. 2003; Kitsionas and Whitworth 2007; Anathpindika 2009b, 2009a). Simulations of other types of triggered star formation, such as shocks from supernovae, have also been conducted (e.g. Leão et al. 2009). However, few simulations have directly tried to model a specific observed cloud. For instance, Ballesteros-Paredes et al. (1999a) modelled turbulent flows and use their results to argue that Taurus-Auriga formed from colliding flow; Peretto et al. (2007) used hydrodynamic simulations to model NGC 2264 with the collapse and fragmentation of an elongated cloud along its major axis; and Heitsch et al. (2009) compare models of flow-driven formation of an isolated molecular cloud with the Pipe Nebula.

Any model of star formation needs to account for the filamentary nature of the star-forming regions. For turbulent regimes, filamentary structures can arise from shocks (e.g. Klessen et al. 2005). If magnetic fields are dominant, the material starts by being preferentially aligned with the field lines and then infall into a perpendicular main filamentary structure (Nakamura and Li 2008). Myers (2009) proposed a model based on self-gravitating and density-modulated layers forming and preserving filamentary structures.

Generally we can only hypothesise about the relevance of different star formation scenarios for clouds in the Milky Way. However for some local clouds, we are beginning to acquire enough details on the density and velocity structure to generate a more informed picture of how star formation has progressed in those clouds. In this chapter, I present the numerical simulations we have performed to test the validity of the proposed scenario for the triggering event in Serpens.

4.2 Attempting to reproduce a specific region: Serpens

4.2.1 Motivation

Following the study on Serpens presented on Chapter 3, we have attempted to test the scenario proposed as a possible trigger for the star formation in the region using numerical simulations.

As a quick summary, the motivation for this study came from the interesting differences between the two sub-clusters of Serpens. From Kaas et al. (2004) and Harvey et al. (2006) it is suspected that there were two different episodes of star formation separated by 2 Myr, responsible for the YSOs found in the region. The older sources found in the field (Class II and III) appear dispersed, with no obvious connection to the current protostars, and no longer embedded nor surrounded by any cold dust seen at submillimetre wavelengths. The younger sources, with an average age of 10^5 yr, are the Class 0/I protostars found embedded in the cold dust and seen in Spitzer 24 μm and 850 μm (Fig. 3.1 on Chapter 3).

Despite the similarities of the dust emission throughout the region, the velocity structure and molecular emission from each sub-cluster are strikingly different. The

NW is a “well behaved” sub-cluster with a very uniform temperature around 10K and one main velocity throughout with only a smooth velocity shift towards its edges. This is shown in the PV diagrams of C^{18}O in Fig. 3.11 on Chapter 3 and in the top panel of Fig. 4.2. In this NW sub-cluster, not only is the Spitzer 24 μm emission in good agreement with the 850 μm emission, but also the gas emission follows the 850 μm dust distribution closely.

In contrast, in the SE sub-cluster the velocity structure is complex: optically thin tracers show some locations with one component along the line of sight, others with two clearly separated components, plus some locations with components at intermediate velocities (Fig. 3.12, 4.1 and two lower panels of Fig. 4.2). In terms of temperature, this sub-cluster has both higher and more varied temperatures than the NW, ranging between 10 and 20K, with the temperature peaks between the 850 μm dust peaks, in the region where the two velocity components begin to merge. Finally, not only is the gas emission not very well correlated with the 850 μm emission, but also the 24 μm and 850 μm dust continuum emission are poorly correlated (Fig. 3.1). The overall picture of the SE sub-cluster resembles that of a region where star formation is an on-going process, with some younger sources (the purely submillimetre sources) and others older (the purely 24 μm sources), unlike the NW sub-cluster where the sources appear to be all at the same evolutionary stage.

Thus the differences between the two sub-clusters indicate that they had a complicated history. A scenario capable of explaining the trigger of Serpens star formation has to reproduce the inhomogeneities in the sources’ age, velocity structure and temperature distribution. Inspired by the spatial distribution of the two clouds in Serpens as shown in Fig. 4.1, a collision of two filament-like clouds, colliding only over a portion of their length could provide such a trigger.

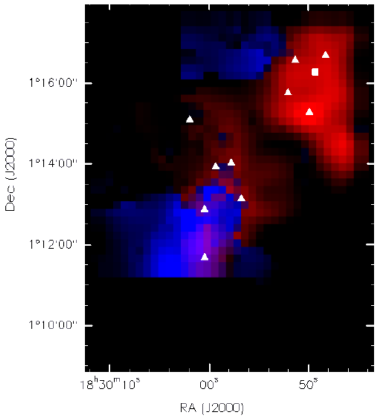

Figure 4.1: C^{18}O J=1→0 emission separated into blue and red components, using the line fitting and splitting described in Chapter 3 and Duarte-Cabral et al. (2010). The blue emission corresponds to the total integrated intensity of the low velocity cloud and the red emission corresponds to the high velocity cloud. The submillimetre sources from the 850 μm emission (Davis et al. 1999) are marked with white triangles to serve as a guide to the location of the dust emission.

4.2.2 Method

To test the proposal that the structure and star formation in Serpens may have been the result of a triggering by a cloud-cloud collision, we have performed a set of smoothed particle hydrodynamics simulations (SPH) which are compared in detail with the observations of the Serpens cluster as presented in Chapter 3. The collision of two filament-like clouds was numerically reproduced by a collision of two cylindrical clouds. We have changed the geometry and initial conditions of the simulations according to the results from the comparison with the observations. The description of the code and the choice of initial conditions are provided in more detail in the following Section (§ 4.3).

4.3 Smoothed Particle Hydrodynamics (SPH)

Smoothed particle hydrodynamics is a computational method used for modelling fluids. This method is a gridless, Lagrangian particle method which divides the fluid into a discrete number of particles, and instead of dividing the space into a grid of points

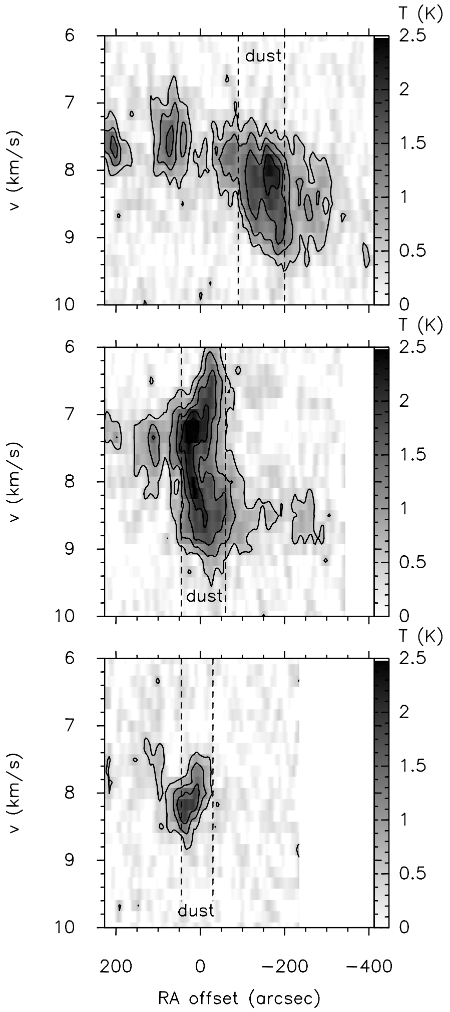

Figure 4.2: Position-velocity diagrams of $C^{18}O$ J=3→2 emission in Serpens (Graves et al. 2010). These are similar to the PV diagrams of Chapter 3 (Fig. 3.11 and 3.12), but given the spatial coverage of this data, these allow a comparison of the evolution of the velocity structure to a greater extent. The diagrams are displayed with decreasing Declination, i.e. from north to south, and at constant Declinations of 1°16’24” (top), 1°12’24” (middle) and 1°08’24” (bottom). Right Ascension varies from $18^h30^m18.5^s$ to $18^h29^m32.5^s$ (offset of +277” to -412” respectively) on all the diagrams.

and calculating the solutions for each grid point (as adaptive mesh refinement codes do), it follows each particle and calculates its properties individually. To be able to do so, each particle is described by a “smoothing length”, i.e. the properties at a given point are calculated using the weighted properties of all the particles within a smoothing length radius, using a kernel function. The resolution of an SPH simulation can be adapted by increasing the number of particles and adapting the smoothing length with space and time. The SPH method allows the inclusion of different mechanisms that can affect a given fluid. Fluid viscosity, gravity, turbulence, radiative transfer and magnetic fields are some of the physical processes that have gradually been incorporated into SPH simulations in the field of star formation. One other addition to this code is a sink particle. The purpose of a sink particle is to simplify the computational effort to calculate the evolution of a system when densities reach very high levels. In the context of star formation, this is the case of, for example, an accreting protostellar core. Bate (1995) introduced a method where all the particles at high densities which are part of a self-gravitating object can be replaced by a single ‘sink’ particle. While this avoids modelling the internal dynamics of the dense objects themselves, interactions with the surrounding gas continue to be calculated, including, for example the accretion of more particles into the sink particle.

4.3.1 The code

The calculations in this chapter were performed using a SPH code. The code is based on a version by Benz et al. (1990), modified to include sink particles (Bate 1995), variable smoothing lengths (Price and Monaghan 2005) and magnetic fields (Price and Bate 2007). The code has been frequently used for simulations of star formation (e.g. Dobbs et al. 2006; Bate 2009a).

We perform calculations including the hydrodynamics and self gravity, but do not include magnetic fields. We use sink particles, which are inserted in regions of high density ($> 10^{-12}$ g cm^{-3}) that are undergoing collapse, to represent protostars. However for all the analysis in this chapter we use the frame of the simulation when the first sink particle appears, i.e. before stellar feedback is likely to have an effect. Therefore our results are not dependent on the details, or dynamics of the sink particles. Finally, for all the calculations we adopt an isothermal equation of state. Again, we are only interested in the evolution of the clouds until star formation takes place, so this simplification is reasonable given that we consider the structure of the gas prior to stellar feedback.

4.3.2 Initial conditions

Given the elongated appearance of both high and low velocity clouds in Serpens, we hypothesised the velocity structure of the Serpens cluster to be due to the collision of two filament-like clouds. A filamentary nature of molecular clouds has been seen towards most of the known star forming regions and dark clouds (well summarised in Myers 2009). It is not surprising that within the Galaxy, two such filamentary clouds or flows could collide as predicted by galactic-scale simulations (e.g. Dobbs 2008; Tasker and Tan 2009). Cloud collisions are thought by many authors to occur and be important for star formation, even though there is only limited observational evidence of collisions (presumably they would happen on relatively short timescales). Numerical simulations of a single giant molecular cloud (GMC), as e.g. the simulation performed by Bate (2009a), show that an initial supersonic turbulence in the cloud can form shock waves and flow collisions that slowly damp the supersonic motions and provoke local density enhancements where gravity prevails over turbulence and protostars begin to form. Most simulations of molecular clouds, however, start with very artificial conditions such as a uniform sphere (e.g. Bate 2009a), by necessity. Obviously there are no uniform, spherical GMCs. For our purpose of individual cloud collisions, the alternative from producing our own initial conditions would be to take clouds from a larger scale simulation but this is far beyond the scope of the present study. Given that we are not starting from a large scale simulation, we required an initial condition that could mimic possible already existing filamentary structures that would later collide. Observations of molecular clouds (Koda et al. 2006) show the distribution of the ratio of major and minor axis to peak at around 2. If we assume that cloud collisions do occur, then it is likely that the clouds could actually have dimensions similar to those we use. We have used an initial cylindrical shape for each cloud, as a mathematical approximation of a filament. This approximation has been investigated in the literature by e.g. Bastien (1983) driven by the observational evidence for elongated and filamentary clouds. Though we do not believe the clouds would be exactly cylinders, departures from cylindrical shapes, and uniform densities would presumably have secondary effects on the dynamics and comparisons we make. In our specific models, the runs with turbulence quickly depart from a cylindrical shape, and resemble much more realistic molecular clouds.

For our calculations, we based the properties of the cylinders on the observations of Serpens, but with the requirement that the cylinders are not too far from virial equilibrium. We required the star formation to be primarily driven by the collision, and preferably the cylinders should retain their elongated shape as much as possible prior to the collision. Based on the observed spatial distribution of Serpens' high and low velocity clouds, all the simulations we run involved two cylindrical clouds with radii of 0.25 pc. We have kept one of the cylinders vertical with a height of 0.75 pc and the second tilted with an angle of 55^o with respect to the horizontal plane (i.e. 35^o between the axis of the two cylinders), with a height of 1 pc.

To ensure the stability of the cylinders prior to the collision, we used the formula for stability of finite cylinders given in Bastien (1983) to estimate the masses of the cylinders,

$$J = \frac{GMf(L/D)}{LR_gT/\mu} \tag{4.1}$$

where R_g is the gas constant, G is the gravitational constant, M is the mass of the cylinder, L the length, T the temperature and μ the mean molecular weight (we assumed $\mu = 2.0$ for these calculations). $f(L/D)$ is a function measuring the shape of the cloud, but is of order unity for the dimensions of our cylinders. The cylinder is stable providing $J \lesssim 0.8$, a condition which reduces to approximately $M(\mathrm{M}_\odot)/\mathrm{T(K)} \lesssim 0.8$ for a 1 pc cylinder. In addition to ensuring that the cylinders do not collapse, we also use constant pressure boundaries to place the cylinders in a low density medium, which minimises diffusion of the outer parts of the cylinders, particularly in the runs including turbulence.

To mimic the supra-thermal line widths observed in Serpens each model was also run for the same initial configuration adopting a turbulent velocity field for the particles. The turbulent field was set up using the method of Bate et al. (2002), and described in depth in Dubinski et al. (1995). The energy of the turbulent field $E(k)$ is chosen to follow a power law of $E(k) \propto k^{-4}$, with k being the wavenumber. This gives, for a given scale (r), a velocity dispersion (σ_v) as $\sigma_v \propto r^{0.5}$. This is similar to the observed Larson relations for clouds, although we do not aim to capture the precise details of the internal motion, but rather to compare results with and without turbulence.

We performed several calculations with different geometries, masses, initial temperatures and turbulence levels. These properties were tuned according to the results from the comparison of each model with the observations, until we reached a final set of simulations that we consider to be relevant for the comparison with Serpens. I will briefly describe these initial runs before moving onto the explanation of the relevant simulations.

Preliminary models and evolution onto the relevant simulations

For the very initial run we performed, we assumed the direction of motion to be coincident with the axes of the two cylinders, and we chose a perspective such that the lower half of the cylinders would collide first. The relative velocity of the cylinders prior to the collision is of 1.4 $\mathrm{kms^{-1}}$. We ran a non-turbulent model where the particles have no initial dispersion, and a turbulent model with an initial turbulent field with an amplitude of $\sim$1 $\mathrm{kms^{-1}}$. We originally envisioned to gather a mass of around 150 $\mathrm{M_\odot}$ and 250 $\mathrm{M_\odot}$ in the cylinders, so that the region which would suffer from gravitational collapse would account for the total mass observed in Serpens (in dust continuum emission). We also required a low temperature of about 15K, typical of a star forming region and similar to the values retrieved in Chapter 3. But using Equation 4.1, to obtain stability with a 1 pc lengh cylinder with 200 $\mathrm{M_\odot}$ would require a temperature of about 200 K. We therefore considered the two cylinders with 150 $\mathrm{M_\odot}$ and 250 $\mathrm{M_\odot}$

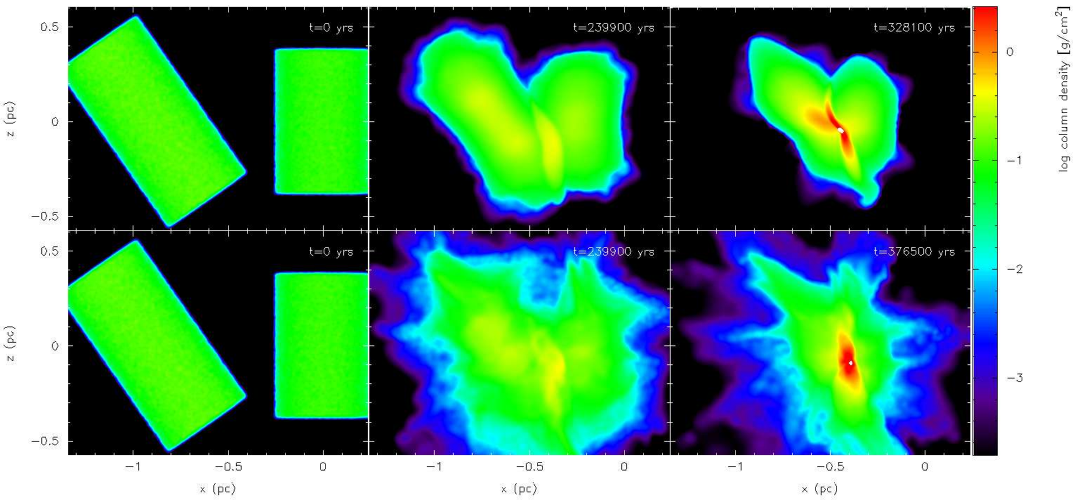

Figure 4.3: This show the column density of three time frames of the first simulation we have run. The two cylinders are moving towards each other uniquely along the x axis. The top three panels show the non-turbulent run, whereas the three lower panels show the turbulent run.

at a temperature of 200 K. Though unrealistic for a star forming region, these were the inital conditions adopted for the first run. A three time-step plot of this simulation is shown on Fig. 4.3.

Encouraged by these initial results we tried to bring the conditions closer to a star forming region. For that, we kept the same geometrical configuration but decreased the temperature and the masses by a factor of 10. This means that we had 15 $M_\odot$ and 25 $M_\odot$ cylinders with a gas temperature of 20K. The main differences of these results from the previous are the column densities and hence the timescales by which the region becomes gravitationally unstable after the clouds collide. On the spatial configuration of these two runs, however, the two cylinders are purely aligned with the direction of the collision. With this configuration, there is no portion of the cylinders that does not eventually collide. Given that in Serpens the two clouds do not seem to overlap in the north, for the following simulations, I proposed a geometry that would allow the two cylinders to have a portion that does not collide. This was achieved by changing the direction of the axis of the tilted cylinder with respect to the direction of motion. Furthermore, from an observer point of view we know that what we observe in reality are only the line of sight velocities and therefore, we have also used different line of sights for some of the runs. These runs started to become more realistic, not only because the initial conditions approached possible observed ones, but also because their analysis has proved fruitful in helping our understanding of Serpens. Their initial conditions and configurations are described in detail in the following section.

Relevant models for Serpens

Bearing in mind the previous simulation where we had adopted a temperature of 20 K, we found that this required unrealistically low masses in order for the cylinders to be relatively stable before the collision. Hence we used 30 K, which is not too inconsistent with the observations and allowed the cylinders not to collapse before the collision. We chose masses of 30 and 45 $M_{\odot}$ for the two cylinders, and verified that the cylinders did not collapse prior to the collision.

We have assumed two sets of different geometries, assuming either an off-centered or direct collision. Each of the calculations were run with and without a turbulent velocity field. The differences between the four runs, sketched in Figures 4.4 to 4.8, are summarised in Table 4.1 where “Collision” specifies if the collision is off-centered or head-on with respect to the centre of the cylinders; “LOS $\sphericalangle$ *v*” represents the angle between the line of sight and the direction of the cylinders’ motion (*v*); “Tilted axis $\sphericalangle$ *v* ” is the angle between the axis of the tilted cylinder with respect to the motion of the cylinders, as projected in the xy plane; “Length” is the height of the longer (i.e. the tilted) cylinder in each run; “Velocities” specify the initial distribution of velocities: “Non-Turb”, indicates a zero velocity dispersion in the initial conditions, Turb stands for a turbulent-generated velocity dispersion amplitude of 0.5 kms^{-1} (in each dimension), and Med-Turb stands for a turbulent-generated intermediate velocity dispersion amplitude of 0.3 kms^{-1}. Note that in simulation D the cylinders were made longer by extending both the top and bottom of the cylinders and the cylinders’ centres are offset from one another by 0.25 pc.

All other properties of the cylinders, e.g. temperatures, densities, are fixed and described below. In the “short-cylinder” runs (A, B and C) we used 500,000 particles

Table 4.1: Configuration of the different simulations

Run	Collision	LOS $\sphericalangle v$	Tilted axis $\sphericalangle v$	Length	Velocities
A_{non-T}	Direct	45^o	135^o	1pc	Non-Turb
A_T	Direct	45^o	135^o	1pc	Turb
B_{non-T}	Offset	45^o	135^o	1pc	Non-Turb
B_T	Offset	45^o	135^o	1pc	Turb
$B_{mediumT}$	Offset	45^o	135^o	1pc	Med-Turb
C_T	Offset	0^o	90^o	1pc	Turb
$B_T^{rotated}$	Offset	0^o	135^o	1pc	Turb
D_{non-T}	Offset	0^o	135^o	1.5pc	Non-Turb
D_T	Offset	0^o	135^o	1.5pc	Turb

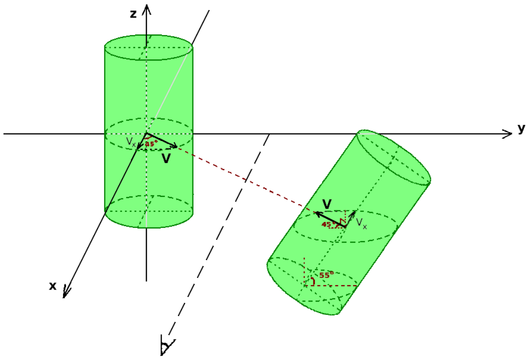

Figure 4.4: Diagram showing the configuration of the two cylinders for the A models: the centres of the cylinders collide directly, and the motion has an angle of 45^o with the line of sight.

in total, with 250,000 particles in each cylinder. The particles are initially randomly distributed, to provide a roughly uniform density distribution within each cylinder. Note that turbulence is set-up initially and not maintained throughout the runs.

We tried various different configurations for the cylinders, and in each case compared the resulting column density and velocity distributions with the observations. Initially, we set the cylinders to collide at an angle of 45^o relative to the line of sight. In addition, we chose to position the cylinders so that either they collide centered/head

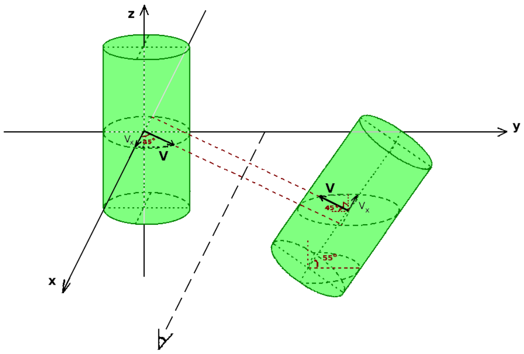

Figure 4.5: Diagram showing the configuration of the two cylinders for B models: the centres of the cylinders are offset when they collide and the motion has an angle of 45^o with the line of sight.

on (run A), or their major axis centres are offset by 0.25 pc (run B). In the direct collision, model A, we centre one cylinder at Cartesian coordinates (0,0,0) pc and the second (longer) cylinder at (0.8,0.8,0) pc (Fig. 4.4). For the offset collision, model B, the second cylinder is instead placed at (0.8,1.05,0) pc, thus half of the cylinders intersect when they collide. We illustrate the offset configuration in Fig. 4.5.

To match the simulations with our line of sight perspective, the higher velocity component corresponds to the longest and tilted cylinder (by 55^o, parallel to the y direction) moving away from us on the right-hand side, whereas the lower velocity component corresponds to the vertical cylinder which is coming toward us from the left-hand side (see Fig. 4.4 and 4.5). In this case, the angle drawn between the axis of the tilted cylinder and the direction of motion projected on the xy plane is of 135^o. We have also experimented a configuration where this angle was 45^o (Fig. 4.6).

The velocities of the cylinders are chosen to agree with the velocity difference of the gas in the Serpens cluster (see two lower panels on Fig. 3.12 or Fig. 4.2, middle), which would correspond to the velocities of the clouds during the collision. The initial velocities of each cylinder are ± 1 kms^{-1}, i.e. ± 0.77 kms^{-1} in the x and y direction in Fig. 4.4 and 4.5. The cylinders have no initial net velocity in the z direction (and without turbulence the particles have zero velocity in the z direction).

The results from the runs A and B are summarised in Section 4.4.1. These runs,

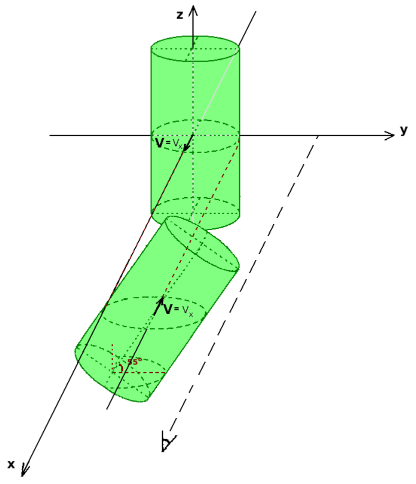

Figure 4.6: Diagram showing the configuration of the two cylinders for model C: Off-centered collision with the motion along the line of sight, but with the axis of the tilted cylinder perpendicular to the motion.

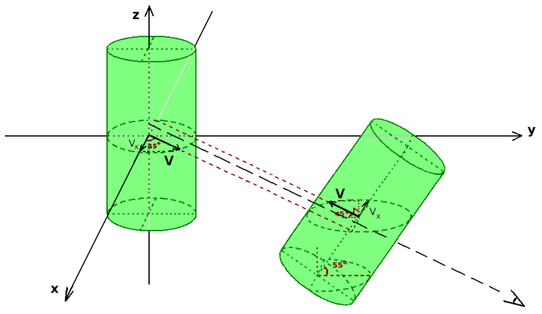

Figure 4.7: Diagram showing the configuration of the two cylinders for model B$^{\text{rotate}}$: same as model B, but now with line of sight is parallel to the direction of motion.

however, show that by the time sink particles are formed the two cylinders fully overlap along the line of sight, even though they did not interact everywhere. This means that we can see two velocity components co-existing in most regions (e.g. Fig. 4.14 top left panel), inconsistent with the observations where the two velocity components overlap only where the collision takes place.

Therefore, we changed the perspective so that the motion of the cylinders is purely along the line of sight, model C and B$^{\text{rotate}}$ (Fig. 4.6), to restrict the region where the two-components overlap to where the cylinders interact directly. Finally model D

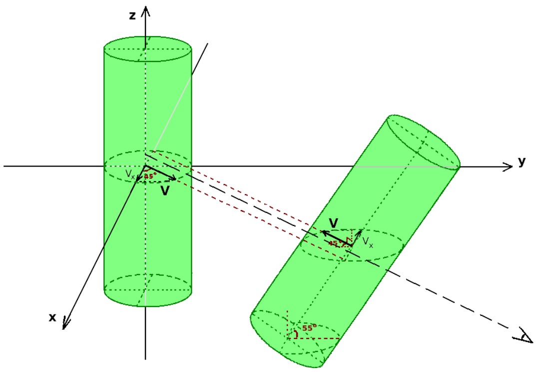

Figure 4.8: Diagram showing the configuration of the two cylinders for D models: Same as B^{rotate} but with longer cylinders.

(Fig. 4.8), is similar to model B^{rotate}, except the cylinders were one and half times as long to aim to reproduce the whole extent of the observed cloud and both clusters. The number of particles was correspondingly increased in this calculation.

4.3.3 Comparison with observations: what and how

In the present study, I am predominantly focused on studying the triggering of the more recent star forming burst in Serpens. Given the nature of simulations, we cannot reproduce the observed line emission of Serpens and, as such, I have based this comparison on the velocity and column density distributions.

The comparison of the simulations with the observations is primarily focused on observational characteristics of the Serpens SE sub-cluster given that this is the region which appears to be directly influenced by the collision. However, even in the short-cylinder runs which do not form the NW sub-cluster, some of the velocity characteristics of the entire cloud are also taken into account. Thus, the following characteristics are the main focus points for comparison:

- Column density structure: an elongated/filamentary shape aligned in a NW-SE direction, sub-clumped (Fig. 3.1).

- The mass and size of the southern clump compared with those of the denser parts of the SE sub-cluster (~30 $M_\odot$ within ~0.025 pc^2, measured using the 850 μm emission above 190 mJy beam^{-1}, which corresponds to column densities above 0.1 g cm^{-2} at a temperature of 10K).

- Overall velocity structure: a single red-shifted component in the north, with a fainter blue component spatially offset to east (top panel of Fig. 4.2 and Fig. 4.1). Double (overlapping) components on the south, where the sources are being formed (Fig. 4.2 lower panel and Fig. 4.1) with a gradient from east to west of increasing velocities, up to 1.5 kms^{-1} (Fig. 3.9). Moving further south, this velocity structure should evolve back into one component along the less dense gas of the filament (Fig. 3.9, and lower PV diagram of Fig. 17 of Graves et al. (2010)).

- Velocity structure of less dense material: thin eastern filaments perpendicular to the main filament of Serpens (seen in blue and green on the left-hand side of the main filament in Fig. 3.9).

In order to compare with the observations, we first constructed a datacube from the simulated 3D cloud collisions. Using the direction shown as dashed black lines in Figures 4.4 to 4.8 as the line of sight and choosing the frame of the simulations where the first sink particle is formed, we created a datacube of column density for a space-space-velocity 3D grid. In the spatial planes I convolved the models with a Gaussian of FWHM of 10 pixels (0.02 pc) which corresponds to the 22” spatial resolution of the IRAM 30m telescope observations of $C^{18}O$ J=1→0 at the distance of Serpens. To reproduce the thermal velocity dispersion of Serpens, I convolved the velocity space with a normalised Gaussian of 0.4 kms^{-1} FWHM (correspondent to the thermal line width of H_2 at 10 K).

Gas temperature, density and abundance all affect the relationship between the true column density of a cloud and the emission seen in a molecular line. However as discussed in Chapter 3 and Graves et al. (2010) in Serpens the $C^{18}O$ appears to be a faithful tracer of the overall velocity structure of the cloud and not significantly affected by outflow or infall motions, while globally the 850 μm emission traces the mass distribution in the region. To assess the success of the simulations in modelling Serpens, I therefore compared the velocity structure of the models with the one from $C^{18}O$ and the overall column density distribution with the dust emission.

4.4 Results of the models

4.4.1 Reproducing the Serpens SE sub-cluster

When attempting to reproduce the characteristics of the SE sub-cluster, where we see the direct impact of the collision, we looked at the short-cylinders simulations: runs A, B and C. Comparing these to the observations then allowed us to chose the best fit, which provided the base for extending the cylinders to try to reproduce the whole cloud. In this section, we investigate the density and velocity structure resulting from these short-cylinder calculations.

Non-Turbulent Runs: $\mathbf{A_{non-T}}$ and $\mathbf{B_{non-T}}$

The time evolution of the non-turbulent runs is shown on Fig. 4.9 with three time snapshots: The top and lower panels are the direct and offset collision respectively.

The mass distribution of the simulations we have performed with no turbulence generally produce a very well defined filamentary structure on which sink particles quickly start to form (Fig. 4.10). For models A_{non-T} and B_{non-T} the portions of the cylinders which do not suffer from the direct collision maintain their initial velocity and density structure.

For run A_{non-T} (direct collision) a filament is formed where the initial cylinders collide. Since the cylinders merge almost totally, there is a large enhancement in density only in this interface, preventing any sub-clump forming elsewhere (Fig. 4.10, left panel). The total mass above a column density of 0.1 gcm^{-2} is 36 $M_{\odot}$, 48% of the total mass of the cylinders, in an area of 0.032 pc^2.

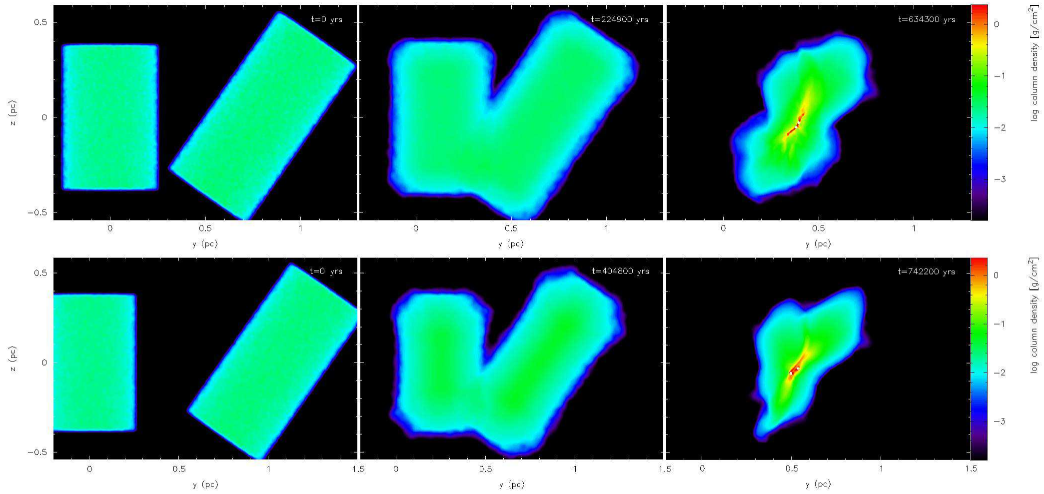

Figure 4.9: Three time snapshots with the total column density along the line of sight, for the non-turbulent runs: the centered collision, $A_{\rm non-T}$, on the top; and off-centered collision, $B_{\rm non-T}$, on the bottom. The three frames correspond to the beginning of the simulation (first frame), as soon as the cylinders start to collide (second frame) and when the first sink particle is formed (third and last frame).

In model $B_{\rm non-T}$ (offset collision), given that only a smaller fraction of the cylinders merge, it takes longer for the collapse to occur and density enhancements occurred in regions not at the interface of the cylinders (Fig. 4.10 right panel). At the end of the simulation, there is a filament connecting the interface region and the major axes of the two cylinders, along which several sink particles are able to form. Even though this is a very long and twisted filament, along the line of sight it appears smaller, straight, and tilted from SE to NW as is Serpens. By the time we have collapse in this run, the total mass above a column density of 0.1 $\rm g cm^{-2}$ is within an area of 0.027 $\rm pc^2$ and is 39 $\rm M_\odot$, 52% of the total mass of the cylinders.

In terms of dynamics, in the non-turbulent runs all particles within a cylinder have the same velocity with no initial velocity dispersion allowing us to identify very sharp velocity changes (Fig 4.11), which although unrealistic, provides an important test of the effect of including turbulent motions in later simulations. In both the direct and offset collisions, the portions of the cylinders which did not collide keep their original line of sight velocities, at ± 0.77 $\rm kms^{-1}$. Closer to the interface, however, the velocity

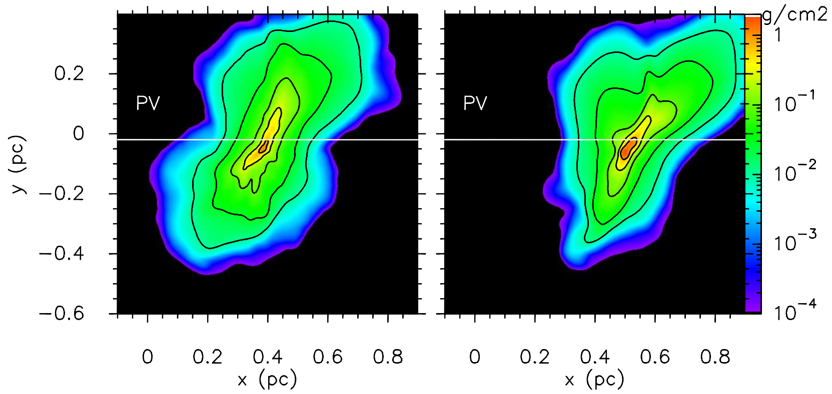

Figure 4.10: Colour scale and contours of the total column density along the line of sight, for the non-turbulent runs: the centered collision, A_{non-T}, on the left; and off-centered collision, B_{non-T}, on the right. These are the datacubes, spatially smoothed to match the observed spatial resolution. The contours levels are 0.01, 0.03, 0.1, 0.3 and 0.5 g cm^{-2} for both figures. The white line shows the position of the PV diagram of Fig. 4.11.

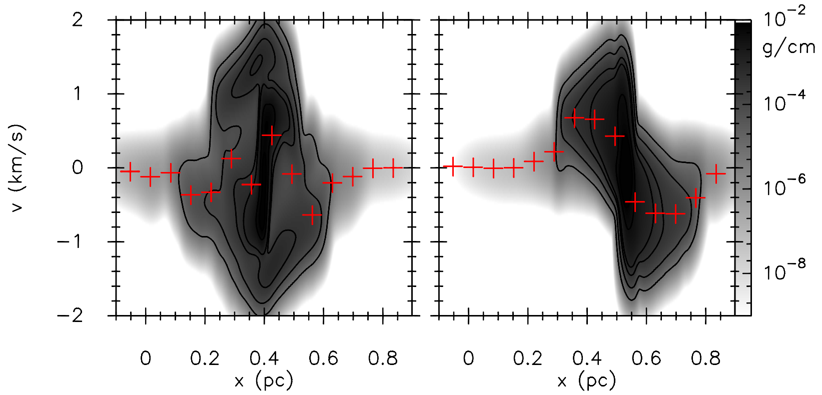

Figure 4.11: Position-velocity diagram at y = -0.02 pc (colour scale and contours) for the non-turbulent direct and offset runs, A_{non-T} and B_{non-T}, left and right respectively. The velocity shown is only the velocity along the line of sight. Contours at 10^{-5}, 10^{-4}, 5×10^{-4}, 10^{-3}, $5{\times}10^{-3}$, 10^{-2} and 3×10^{-2} g cm^{-2}. The red crosses represent the column density weighted velocities, and are plotted as an auxiliary tool to see the velocity changes along the diagram.

dispersion of the lower density material increases (e.g Fig 4.11 right panel), most likely due to the gravitational interaction of the particles between the two cylinders.

The most significant difference between the results of these simulations occurs at the collision interface. In the direct collision (A_{non-T}), due to the larger fraction of the cylinders merging, the interface region becomes larger and more prominent, and the velocities at the interface reach intermediate velocities between the two initial cylinder

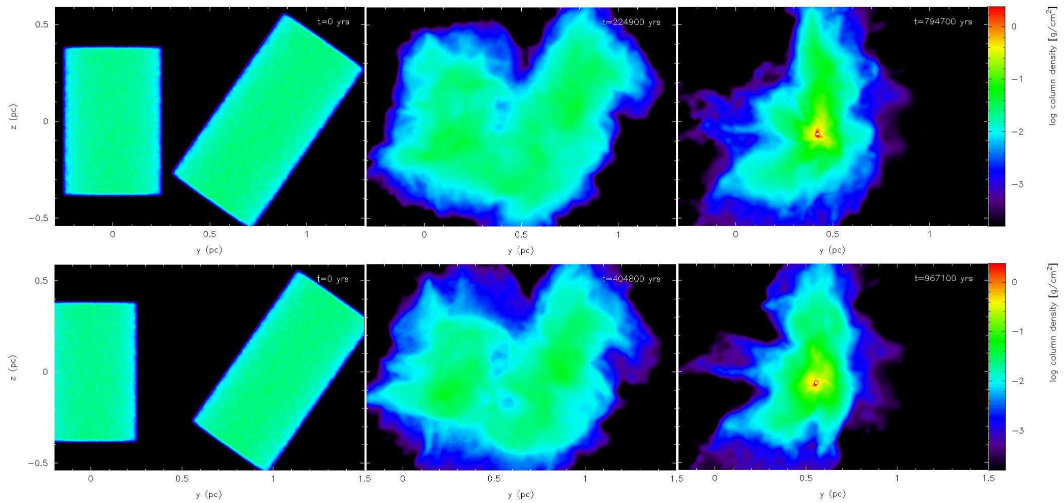

Figure 4.12: Three time snapshots with the total column density along the line of sight, for the turbulent runs: the centered collision, A_T, on the top; and off-centered collision, B_T, on the bottom. The three frames correspond to the beginning of the simulation (first frame), as soon as the cylinders start to collide (second frame) and when the first sink particle is formed (third and last frame).

velocities. Therefore, along the dense filament, three velocity components are present: the two velocities of the individual cylinders, plus the velocity of the particles at the interface (Fig. 4.11 left panel). In the offset case (B_{non-T}), the cylinders merge on a thinner surface, traced by a sharper change in velocity almost continuously connecting the original velocities of the cylinders (Fig. 4.11 right panel).

Turbulent Runs: A_T and B_T

The column density distribution resulting from the turbulent runs, A_T and B_T, are similar (Fig. 4.12 and Fig. 4.13). They show a less filamentary clump which is undergoing collapse, even though the less dense material is distributed along a filamentary structure. These runs also show some “channels” of material perpendicular to the main filament, reminiscent of features sometimes observe in molecular lines or extinction (e.g. Myers 2009). At first sight these look like material from the filaments which has been “left” behind by the cloud as it moved in space, likely to infall onto the filament

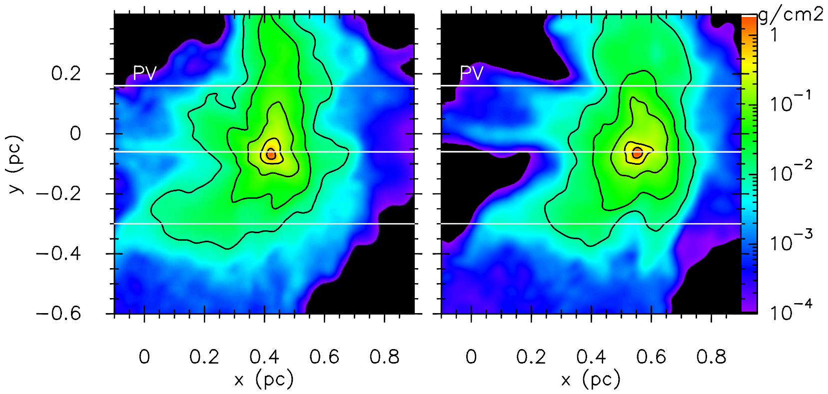

Figure 4.13: Colour scale and contours representing the total column density along the line of sight, for the turbulent runs: the centered collision, A_T, on the left; and off-centered collision, B_T, on the right. The contour levels are as in Fig. 4.10. The white line shows the position of the PV diagrams of Fig. 4.14.

later on. However, as later simulations show, this interpretation is too simplistic.

Before the first sink particles start to form, we see several regions where the density is starting to grow, even though as soon as one of these regions starts to be dense enough, it will attract the remaining less dense sub-clumps to a major single structure.

The material at a column density higher than 0.1 gcm^{-2} is distributed over similar sized regions to the non-turbulent models, 0.025 pc^2 and 0.032 pc^2, for runs A_T and B_T respectively. However the total mass of gas above this column density is less. For A_T 29 $M_\odot$ are in these high column density regions (39% of the total mass of the cylinders), while B_T has 34 $M_\odot$ (45% of the total mass).

The left column on Fig. 4.14 shows that model A_T has similar dynamical properties to the non-turbulent run of the direct collision (model A_{non-T}) with a velocity structure much more complex and "wavy" than observed (Fig. 4.2). There is no smooth trend from north to south, nor east to west and we have lost almost all traces of the original velocities of the cylinders except in the low density regions, which are not interacting (Fig. 4.14 top left panel). The spatial distribution of material with respect to velocity also does not agree greatly with the observations.

In model B_T, the collision volume is smaller than the direct collision case and as

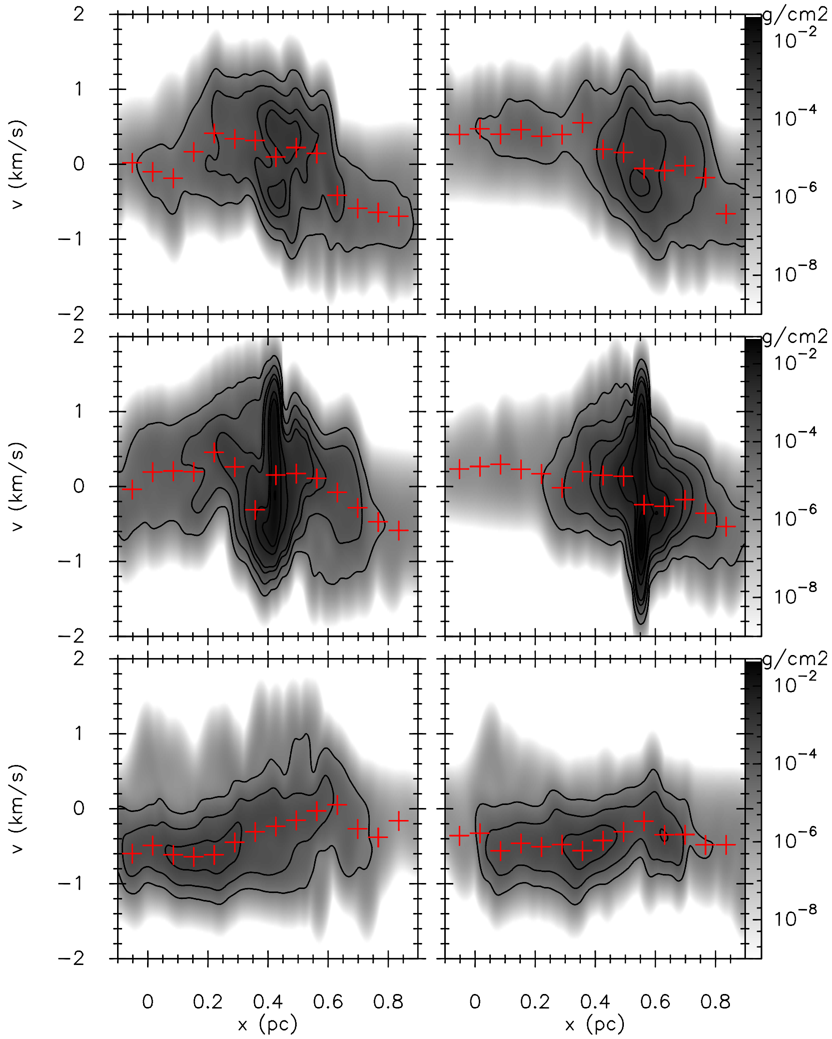

Figure 4.14: Position-velocity diagrams in colour scale and contours, at y = 0.16 pc (top), y = -0.06 pc (middle) and y = -0.30 pc (bottom) for the turbulent direct and offset runs, A_T and B_T, left and right respectively. The red crosses are the column density weighted velocities and the contour levels are as in Fig. 4.11.

such, more of the original velocity structure of the initial cylinders survives (Fig. 4.14 right column). In the north we see mainly the tilted cylinder and we begin to detect the vertical cylinder on the left-hand side. The transition between the two is not sharp nor double peaked, but a rather broad smoother transition (Fig. 4.14 top right panel). A well defined double peak structure is only detected in the central region of the model where sink particles have formed (Fig. 4.14 middle right panel). South of this region, the column density becomes again dominated by one component from the tilted cylinder traveling away from us (Fig. 4.14 bottom right panel), as we had also found towards the south end of the Serpens filament (Fig. 4.2 and Graves et al. 2010). The results from this run (B_T) are now more consistent with the observations of the SE sub-cluster of Serpens (Fig. 4.2 and Chapter 3).

An Intermediate Turbulence Run: $B_{mediumT}$

This model adopted the offset collision configuration (run B), which have given the best match to the observed velocity field so far. The goal was to reproduce the velocity structure of the offset turbulent run B_T, and recover the more filamentary shape of the non-turbulent runs.

The resulting mass distribution for this model ($B_{mediumT}$) is between the turbulent and non-turbulent models (Fig. 4.15 versus Fig. 4.10 and Fig. 4.13) as might be expected. It reproduces a filamentary structure, but not as well delineated as in the non-turbulent model. When dense regions form, they lay on the original filamentary shape. However, as before, whenever one of these enhanced regions has accreted enough mass to become dominant, the different clumps merge into a single clump. Both the area and fractional mass of the high column density region, > 0.1 g cm^{-2}, are the same as for the turbulent run B_T.

This model tests the importance of the level of turbulence in reproducing the observed column density and velocity features of Serpens. This medium turbulence run shows a similar general velocity trend as the higher turbulence run, while the column density is indeed a bit more filamentary. An example of a PV diagram for this run is shown in Fig. 4.16 which should be compared with the middle panels of Fig. 4.14. Given that the B_T was the best run on reproducing the velocity field, $B_{mediumT}$ shows us that the geometric configuration is the dominant factor in determining the main velocity characteristics of the resulting cloud, while the density distribution is sensitive to the level of turbulence. Lower levels of turbulence result into a more filamentary structure, with more sink particles forming along the denser filament. Increased values of initial turbulence tend to disrupt the distribution of cloud's material, inhibiting the

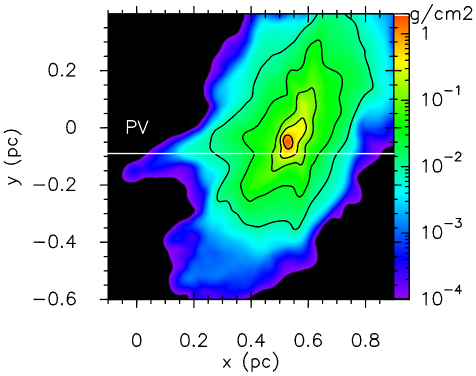

Figure 4.15: Colour scale and contours of the total column density along the line of sight, for the intermediate turbulence, off-centered collision, B_{mediumT}. The contour levels are as in Fig. 4.10. The white line shows the position of the PV diagram of Fig. 4.16.

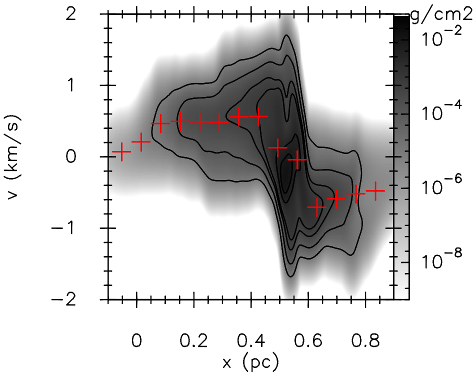

Figure 4.16: Position-velocity diagram at y = -0.09 pc, for the medium turbulence offset run, B_{mediumT}. The red crosses are the column density weighted and the contour levels are as in Fig. 4.11.

formation of further clumps.

Line of sight, short cylinder Run: C_T

The runs where the clouds move purely along the line of sight were motivated by the fact that by the time the collision of the two clouds was able to form an initial protostar, the two cylinders are already crossing each other. Even though they have a portion of their length (the top part) which does not interact, they will still be overlapping as seen through our previously chosen line of sight. Since in Serpens we have the NW subcluster where the two clouds do not overlap, we attempted to change the geometry to bring it closer to the observations.

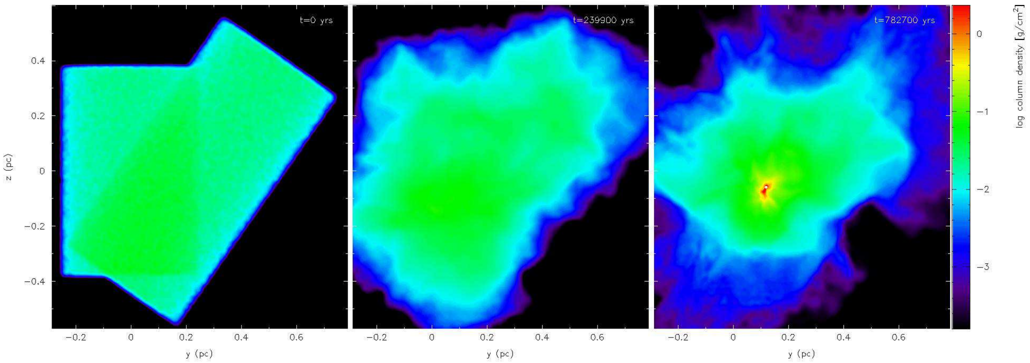

Figure 4.17: Three time snapshots with the total column density along the line of sight for C_T. The three frames are as before.

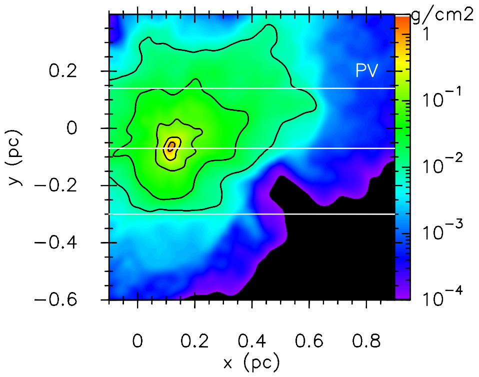

Figure 4.18: The total column density for the purely along the line of sight turbulent run, C_T. Unlike runs A and B, we find a low density region in the north (high y), as with this orientation we see regions which have not collided. The contour levels are as in Fig. 4.10. The white line shows the position of the PV diagrams of Fig. 4.19.

The first line of sight run, C, was performed by merely changing the initial position of the tilted cylinder. The velocities were redirected to coincide with the x axis. We kept everything else the same: the line of sight is along x, the absolute velocities are the same, the cylinders collide off-centered by 0.25 pc and the tilting angle of the cylinder is the same as before. However, such a change in the position of the cylinder (and direction of the collision), without changing the tilting angle, means that now the angle between the axis of the tilted cylinder and the collision direction is reduced to 90^o.

However, the results from this run (Fig. 4.17) showed a less filamentary structure

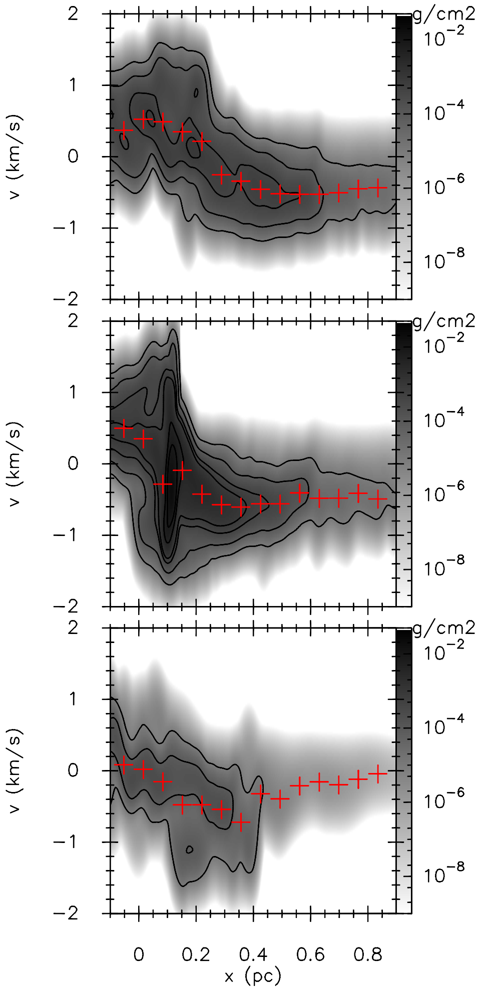

Figure 4.19: Position-velocity diagram in colour scale and contours, at y = 0.14 pc (top), y = -0.07 pc (middle) and y = -0.30 pc (bottom), for the turbulent, line of sight, short cylinders run C_T. The red crosses are the column density weighted and the contour levels are as in Fig. 4.11.

in terms of column density (Fig. 4.18). In fact the upper part of the clouds that do not collide is clearly seen here as the clouds extend to the sides much more than what we observe in Serpens, in particular to the right hand side of the cloud. In terms of velocity structure (Fig. 4.19), the trends depart only slightly from those of run B. However, it seems to show more of the cloud moving away from us (the equivalent of the Serpens HVC) throughout the map.

The less filamentary structure from this model resulted from having a higher portion of cylinders that did not collide. Therefore, we went back to run B where less

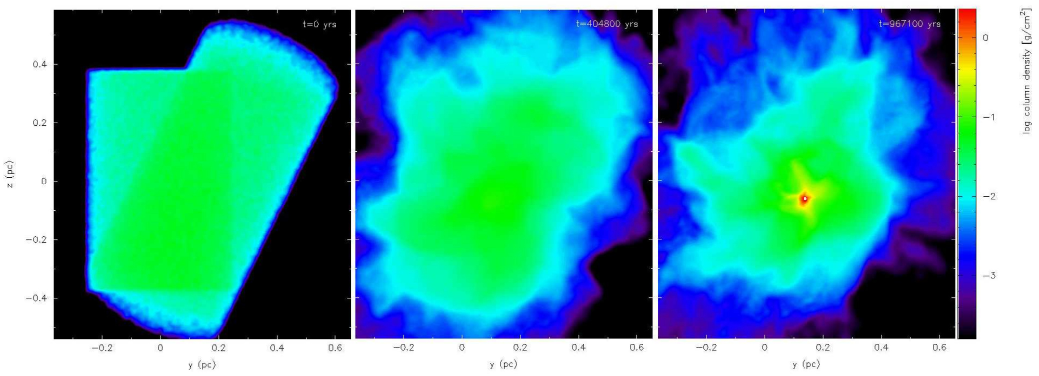

Figure 4.20: Three time snapshots with the total column density along the line of sight for B_T^{rotated}. The three frames are as before. Note that this is the exact same model as B, but viewed from a different perspective

dispersed material exists, thanks to a greater portion of the clouds that does end up by merging. Run B was the best fit of Serpens so far, with the exception of the spatial disposition of the two clouds. Therefore, we studied run B through a perspective parallel to the motion of the cylinders (B_T^{rotated}).

Rotated line of sight, short cylinder Run: B_T^{rotated}

The second line of sight run was achieved by simply changing our line of sight with respect to a previous model. Model B_T^{rotated} is therefore simply a re-projection of model B_T so that it is viewed along the axis of the relative motion of the cylinders. The choice of model B_T for a reprojection were the encouraging results from its analysis of the velocity and spacial structure. That said, we were not expecting to see great changes on the structures seen, even though some velocity structure was bound to appear somewhat different, since we are looking at the component of the velocity which is most affected by the collision.

From this perspective (Fig. 4.20 and 4.21) the low density material is less filamentary and more spatially extended, as the parts of the cylinders which do not interact do not overlap along the line of sight any longer. Therefore, the extent of the lower density material is greater in the north, where the cylinders do not merge, than in the

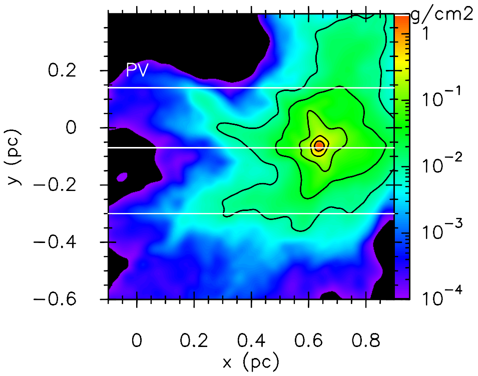

Figure 4.21: The total column density for the purely along the line of sight turbulent run, $B_T^{rotated}$. Unlike runs A and B, we find a low density region in the north (high y), as with this orientation we see regions which have not collided. The contour levels are as in Fig. 4.10. The white line shows the position of the PV diagrams of Fig. 4.22.

south. In this reprojected turbulent run, $B_T^{rotated}$, the material at column densities above 0.1 gcm^{-2} covers a region of 0.02 pc^2 in area with a mass of 22 $M_\odot$.

The general shape and trend of the velocity structure (Fig. 4.22), although slightly more complex, is similar to that seen in B_T, and is still consistent with the velocity trend seen on the observational PV diagrams.

4.4.2 Representation of both SE and NW Serpens sub-clusters

Line of sight, long cylinders, Runs: D_{non-T} and D_T

Overall model $B_T^{rotated}$ satisfactorily reproduces the observations of the SE sub-cluster. However it does not have enough mass to form a second sub-cluster comparable to the NW sub-cluster in Serpens even though the velocity structure of the simulation is very similar to that observed. Therefore, we increased the length and mass of the cylinders to investigate the possible formation of a separate structure in the north where the cylinders do not interact. If the non-interacting northern region is massive enough to be close to being gravitationally unstable, the collision in the south of the cylinders may induce its rapid collapse without greatly affecting its systemic velocity.

A non-turbulent model with ~1.5 pc long cylinders, colliding off-centre and along the light of sight (model D_{non-T}) does indeed form two sub-clusters (timesteps shown

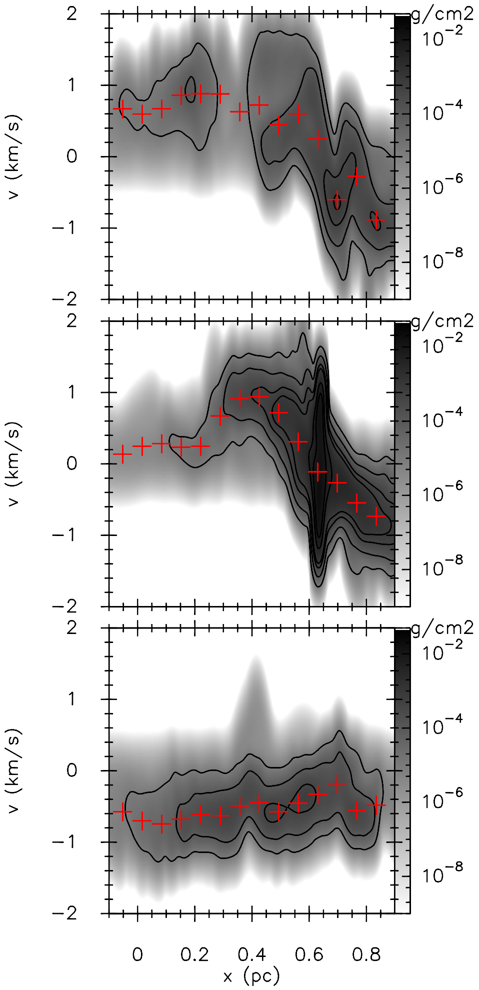

Figure 4.22: Position-velocity diagram in colour scale and contours, at y = 0.14 pc (top), y = -0.07 pc (middle) and y = -0.30 pc (bottom), for the turbulent, line of sight, short cylinders run B_T^{rotated}. The red crosses are the column density weighted velocity and the contour levels are as in Fig. 4.11.

on Fig. 4.23). The collision in the south leads to the formation of a sink particle, equivalent to the SE sub-cluster. Later on, a sink particle is formed in the north of the tilted cylinder, along the cylinder axis. Finally, more sink particles are formed in the south, as the vertical cylinder crosses through the tilted one (Fig. 4.25). At the end of this run, when sink particles are formed throughout the clouds, the column density distribution is much more filamentary than for the short cylinder calculation. There are two visible sub-clusters: one in the NW and one in the SE. The total mass in these sub-clusters amounts to 57 $M_\odot$, 52% of the total mass in this case, distributed over an area

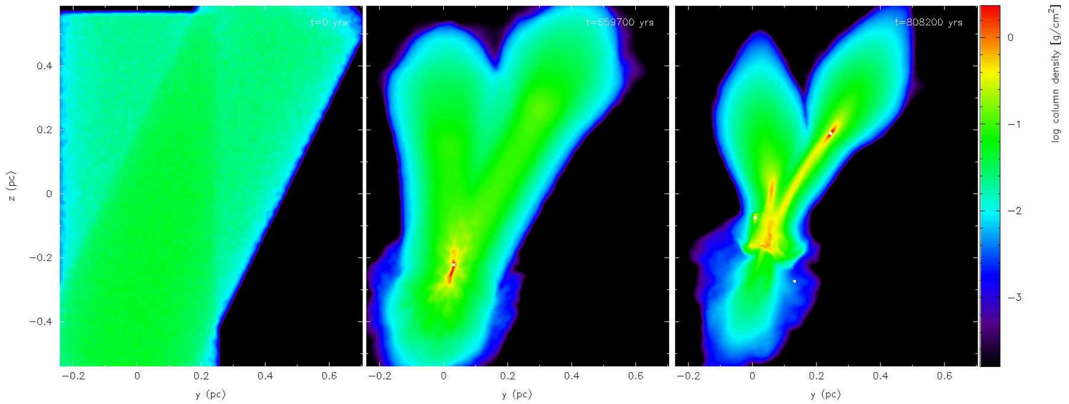

Figure 4.23: Three time snapshots with the total column density along the line of sight for D_{non-T}. The three frames are at the start of the simulation (left), when the first sink particle forms in the south (middle) and when a sink particle is formed in the north (right).

of 0.035 pc^2. However, the relative size and mass of each individual sub-cluster is not quite as similar as seen in Serpens. The simulated SE sub-cluster has a mass of about 30 $M_\odot$ in an area of ~0.015 pc^2, whereas the NW sub-cluster contains only 12 $M_\odot$ in a similar area.

The formation of a sink particle in the north occurs at 8×10^5yr and is mainly due to the initial instability of the cylinder itself. As a test, we ran a simulation with only an isolated non-turbulent cylinder, with the same mass and size as the tilted one. This simulation showed that it would form sink particles along the cylinder axis by 10^6yr (Fig. 4.24). Therefore, the collision in the south does not trigger the formation of this sink particle in the north, but only speeds up its collapse.

Several different turbulent runs with this configuration failed to induce the collapse of any structure in the north. The collapse only occurs with extremely low levels of turbulence (with amplitude of $\sim$ 0.05 kms^{-1}), almost indistinguishable from the non-turbulent run. This is because the turbulent velocities cause the cloud to disperse from its initial configuration and become less gravitationally unstable.

From this, we can conclude that the effect of the collision felt by the north region is quite subtle, and would only have an influence on the collapse there if the region is

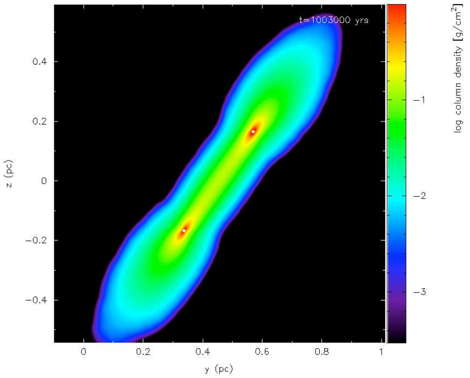

Figure 4.24: Total column density for the non-turbulent, isolated long cylinder run to test the timescale by which the cylinder will undergo self-gravitational collapse without any effect from a collision. This run showed that it takes 1×10^6 yr to form sink particles without any collision, longer than the time that it takes for the sink particles to form when there is a collision.

almost gravitationally unstable prior to the effect any external perturbation.

The discrepancy in the relative masses of the two sub-clusters in the simulation compared to Serpens, and indeed the failure to form two sub-clusters in the turbulent simulations, could both be addressed by relaxing the over-simplistic uniform conditions in our initial conditions. Both the density distribution and turbulent velocity distributions are likely to be more inhomogeneous in real colliding clouds than in our models. However we refrained from adding such additional complexity to the models as the nature of the inhomogeneities is poorly constrained and unlikely to provide any further significant physical insight into the processes in this region.

In terms of its spatial evolution, the velocity structure of the D_{non-T} is similar to the observed one. Note that the two upper panels of Fig. 4.26 show the main velocity structure that we should see in the north sub-cluster. Also note that the column densities are higher at velocities corresponding to the tilted cylinder. Any increase in the density of the tilted cylinder to produce a more massive NW sub-cluster would increase the contrast in column densities between the two velocity components, more closely matching the observations where most of the gas emission comes from the higher velocity cloud (Fig. 4.2).

This simulation, D_{non-T}, shows the formation of a south sub-cluster where particles

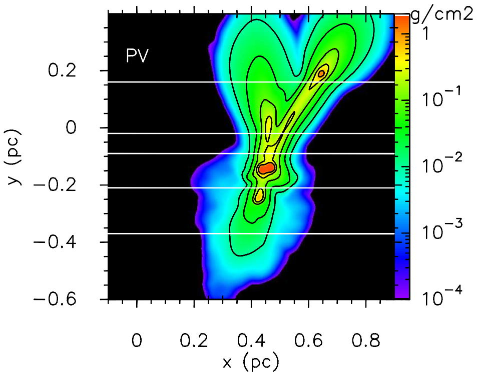

Figure 4.25: Total column density for the non-turbulent, purely along the line of sight run with longer cylinders, $D_{\mathrm{non-T}}$. At this stage, sink particles have been formed where the collision is happening and in the north-west (within the tilted/longer cylinder). Given the geometry of the collision, the two cylinders do not end up colliding in the north. Therefore, the only perspective where we do not see the cylinders overlap is the one we took for this run, where the line of sight is aligned with the motion of the cylinders. The contour levels are as in Fig. 4.10 and the white line shows the position of the PV diagrams of Fig. 4.26.

are being formed at the interface of the two clouds, and along an elongated structure which becomes more filamentary as one moves south. Again, south of this southern sub-cluster, the less dense and remnant gas velocity shifts back into a single component (lower panel on Fig. 4.26), as seen in observations (Graves et al. 2010).

4.4.3 Timescales

One interesting question for the star formation history of Serpens is to confirm whether or not the older population of pre-main sequence star of 2 Myr of age could be formed in the same cloud-cloud collision event. For this we need to estimate a number of characteristic timescales. First, all the simulations correspond to a total elapsed time of $\sim 8-9\times10^5$ years. However, it is only after about $2-3\times10^5$ years, about a third of the total simulation time, that the two cylinders start to interact. This time delay is needed, especially in the turbulent cases, to allow the cylinders to relax their initial density distributions. The time from the start of the interaction between the two clouds until they start forming sink particles is of the order of 6×10^5 years. For the 2 Myr stellar population to be able to form through this collision, the duration of

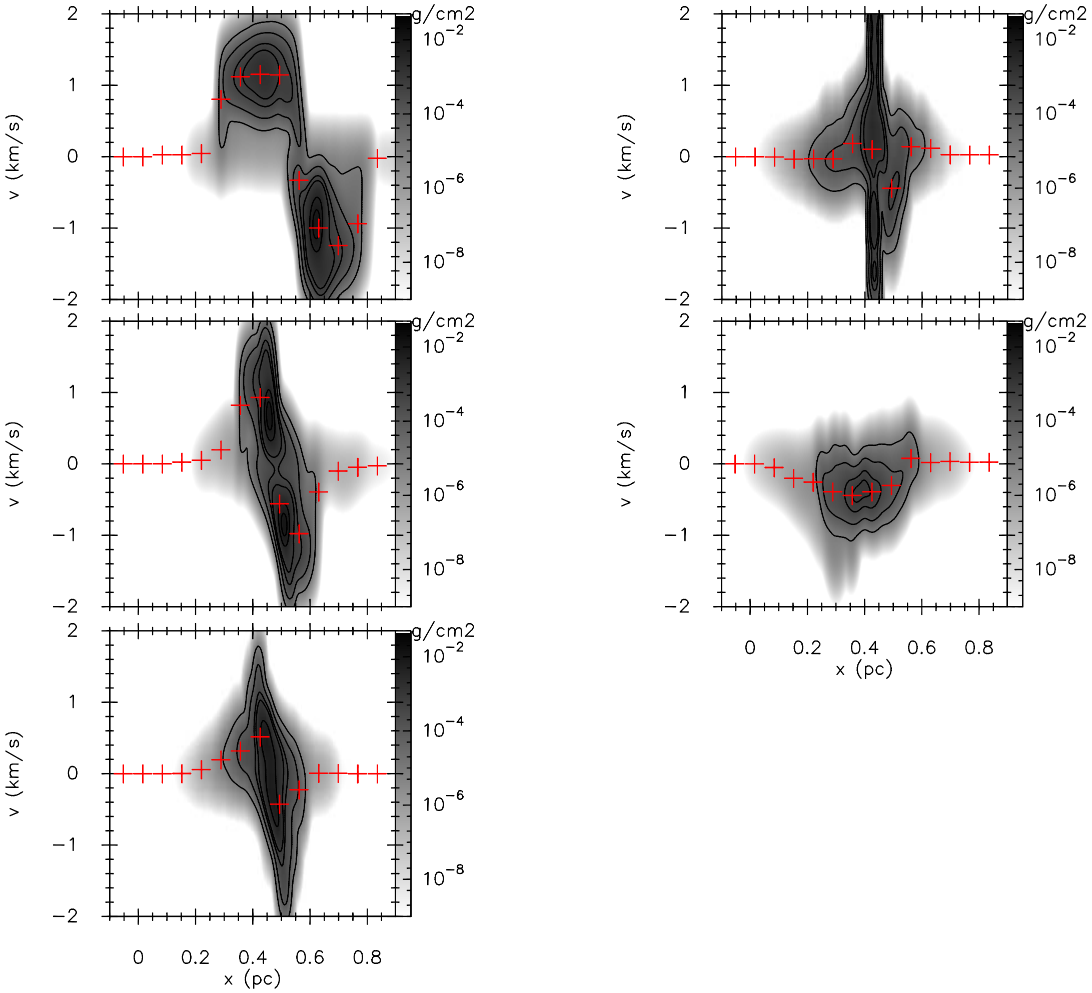

Figure 4.26: Position-velocity diagrams of the non-turbulent, long cylinder run D_{non-T}. Panels of the PV cuts, starting on the left column, from top to bottom at y = 0.16 pc, y = -0.02 pc, y = -0.09 pc; and continuing on the right column from the top at y = -0.21 pc and y = -0.37 pc. The red crosses are the column density weighted and the contour levels are as in Fig. 4.11.

the interaction time has to be at least 2 Myr. In fact, we would need the cloud to be an order of magnitude larger (i.e a few parsec wide) in order to still have an ongoing collision 2 Myr after the formation of the first protostars. This seems unrealistic, rather the cloud collision scenario we present for Serpens is consistent with the idea of two separate bursts of star formation in the region.

4.5 Discussion: Comparison with observations

All the simulations run, including a number not shown here, have shown that the kinematics can be altered substantially with a simple geometry change. For example, comparing the offset with the direct collision runs (models A and B) where even though the resulting column density structures are similar, the velocity distributions of the particles is not.

Overall the simulation which best represents the SE sub-cluster of Serpens star forming region is the model $B_T^{rotated}$, the offset turbulent model with short cylinders, reprojected so that the line of sight is coincident with the direction of motion. It has a velocity structure similar to that observed, both comparing PV diagrams and the general trend on the velocity coded 3-colour plots (Fig. 3.9 and Fig. 4.27). Note that the simulation (Fig. 4.27) is only representing the southern part of Serpens, and therefore, should be compared to the lower-half of the 3-colour plot of the observations in Fig. 3.9. This simulation shows higher column densities where the two velocity components overlap, with less dynamical complexity than model A_T. Model $B_T^{rotated}$ shows an overall velocity gradient of $\sim$2 kms^{-1} over 0.2 pc^{-1}, from blue in eastern regions to red on the west (Fig. 4.27), similar to what is observed.

The 3-colour velocity figures show the resemblance of the simulation $B_T^{rotated}$ with the observations in the way that the filament extending south is mostly represented by the red/green velocities, while the blue part is mainly seen on the denser parts where the stars are being formed. The green-blue component is also seen further east, forming some less dense filaments perpendicular to the main filament. Note that we do not see these type of filaments on the red side.

If these filaments had been caused by the initial turbulence, then we would expect these to exist on both directions. In Section 4.4.1, referring to simulations A and B, it was thought these filaments were due to some particles being left behind, resembling a tail, as the cylinder moves. However, in simulation C, the cylinder's motion is along the line of sight, so if these filaments resulted from a tail of material left behind during the collision they would be behind the main structure. Their appearance therefore indicates that these perpendicular filaments are caused by the geometry of the collision, in particular, its asymmetric nature. These filaments place a strong constraint to the geometry of the collision. The geometry of simulation A (as well as other tests not referred here) do not reproduce them.

In terms of its total column density distribution, 22 $M_{\odot}$ in 0.02 pc^2, model C closely matches the SE sub-cluster. Even the projected distribution of material above a column density of 0.1 gcm^{-2} resembles the shape of the SE sub-cluster.

To start to reproduce the NW sub-cluster in addition to the SE sub-cluster requires the longer non-turbulent clouds used in model D_{non-T}. In this model a region close to being gravitationally unstable can be perturbed and its collapse hastened by the collision, even though it is not directly involved in the collision. This second sub-cluster forms with the velocity of its native cloud and collapses smoothly and independently of the southern region. If this model is allowed to run further, the NW sub-cluster falls onto the SE sub-cluster. Intriguingly, recent observations of the magnetic field in Serpens (Sugitani et al. 2010) appear to suggest the start of such a collapse which could result in the merging of the two sub-clusters.

4.6 Conclusions

Serpens is a very interesting star forming region, not only for its youth, but also for the striking differences between the two sub-clusters that compose the active star-forming portion of the cloud. Even though they are at similar stages of evolution, with most sources between Class 0 and Class I protostars and similar dust continuum properties, the gas emission reveals that these have not only different velocity characteristics but also different temperature distributions (Chapter 3, Duarte-Cabral et al. 2010).

Motivated by the two velocity components seen in the southern sub-cluster of Ser-

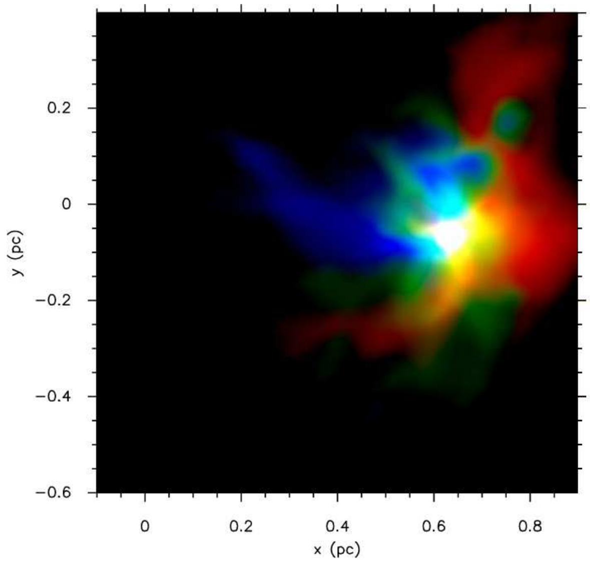

Figure 4.27: Velocity coded 3 colour plot of $B_T^{rotated}$. Each colour represents the total column density summed over the following line of sight velocities: blue: 0.3 → 2 kms^{-1}; green: -0.3 → 0.3 kms^{-1}; and red: -2 → -0.3 kms^{-1}.

pens, and the higher temperatures detected there, we performed several SPH calculations of cloud-cloud collisions. The configurations used for these simulations were based on the observational evidence, and were improved as the comparison with observations would either rule out or support a determined configuration.

The results from this study support the idea that Serpens' current star formation may, indeed, have been triggered by a collision of two filamentary clouds or flows. If this scenario is correct, then the SE sub-cluster of Serpens is the direct result of the collision, being exactly in the collision layer, whereas the NW sub-cluster is most likely just marginally affected by the collision, only feeling the remnant perturbations it generated.

For the SE sub-cluster, a model of two colliding clouds is able to reproduce both the column density structure, a centrally condensated filament aligned in a NW-SE direction, and the two velocity components seen where the collision is occurring. The same simulations did not, however, produce a second sub-cluster, similar to the NW sub-cluster of Serpens. Therefore, this sub-cluster does not seem to be the direct result of the collision. This suggestion was already supported by the NW sub-cluster's "well behaved" temperature profile and velocity structure, as well as the uniform age of sources within the sub-cluster. However, the similar stage of evolution of the sources from the two sub-clusters and their proximity, suggests that the two events are not totally independent.

A simulation with elongated cylinders and increased masses provides a possible explanation. The presence of a marginally stable region in the northern part of one of the colliding filaments can have its collapse induced and quickened by perturbations driven by the cloud-cloud collision.

We consider a cloud-cloud collision scenario to be the best description of the driving of the star formation history in Serpens. Not only can it reproduce the observed velocities and column densities, as it offers a plausible explanation for why the two sub-clusters are so similar in some regards and yet so different in others. Although cloud rotation may produce similar general velocity gradients to those observed, the complexity of the region is better explained with such a collision scenario, which is in essence similar to a shear-motion also suggested by Olmi and Testi (2002).

Despite the successful scenario provided by a cloud-cloud collision model, we failed to reproduce all of the Serpens characteristics in one single run. An additional support against gravity is required in order to sustain the existence of two different sub-clusters as in Serpens. The existing magnetic field of the region (Sugitani et al. 2010) could provide such a missing support.

Part III

The Pipe Nebula

Chapter 5

The Pipe Nebula

5.1 Overview of the region

The Pipe Nebula is a molecular cloud located at ∼ 130pc from the Sun (Lombardi et al. 2006). Although the global features of the cloud appear similar to other nearby molecular clouds, with a total mass comparable to the few $\times\ 10^4$ $M_\odot$ of the Taurus-Auriga complex and a filamentary structure (extending over 8 deg^2) with a magnetic field threading the cloud (Alves et al. 2008), little is known in detail about the molecular gas in the region. The highest resolution molecular line image of the region is the $4'$ resolution map of the $J = 1 \rightarrow 0$ transitions of ^{12}CO, ^{13}CO and C^{18}O by Onishi et al. (1999). Beyond this, molecular line observations of the Pipe Nebula consist of single spectra of dense gas tracers (NH_3, CCS and HC_5N) by Rathborne et al. (2008) and C^{18}O $J = 1 \rightarrow 0$ (Muench et al. 2007) towards the peaks of cores identified in the $1'$ resolution extinction maps (Fig. 5.1; Lombardi et al. 2006; Gerardo Román-Zúñiga et al. 2010). More recently, Frau et al. (2010) have observed continuum emission and molecular lines at 3 and 1 mm of early- and late-time molecules also only toward four selected starless cores inside the Pipe Nebula.

Interest in the Pipe Nebula is enhanced by its extremely low star formation efficiency (less than 0.1%) compared to other Gould Belt clouds (2-20%). In fact, only one

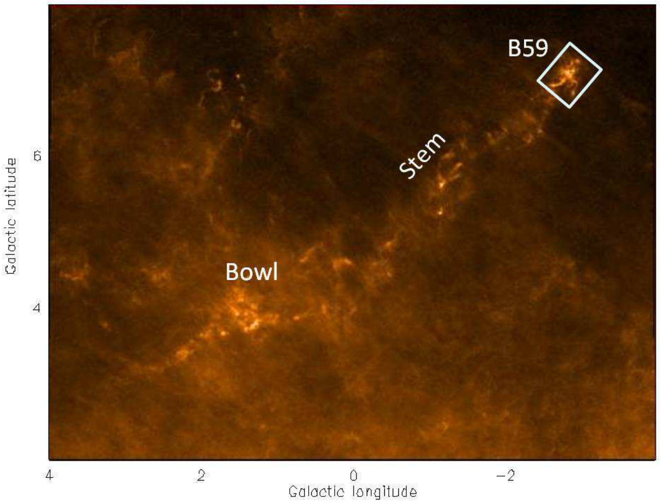

Figure 5.1: Extinction map of the Pipe Nebula, courtesy of Marco Lombardi, João Alves and Charles Lada, showing the location of the star forming region B59 and a number of extinction cores throughout the Stem and Bowl of the Pipe.

active star forming clump (in B59) has been found so far in the whole cloud (Fig. 5.2). It contains a small group of protostars (Brooke et al. 2007; Covey et al. 2010) powering possibly more than one molecular outflow (Onishi et al. 1999; Riaz et al. 2009). Throughout the remainder of the cloud, a number of $C^{18}O$ $J = 1 \rightarrow 0$ “dense” cores found in extinction (Alves et al. 2007) were observed by Muench et al. (2007) using single point spectra. These cores are thought to be pressure confined cores (Lada et al. 2008), and apparently have non-thermal subsonic motions and a mean density of 8×10^3 cm^{-3}, slightly lower than the mean density of cores usually associated with star formation (Alves et al. 2007; Lada et al. 2008; Gerardo Román-Zúñiga et al. 2010). IR and X-ray data studied by Forbrich et al. (2009, 2010) suggest the majority of the remaining extinction cores in the Pipe Nebula to be starless, with only 1 YSO candidate outside B59.

Numerical simulations suggest that large scale flows play an important role in forming molecular clouds and their cores (e.g. Heitsch and Hartmann 2008). The apparent youth of the Pipe makes it an important region where signatures of such flows could be identified. Such signatures could include large scale velocity coherence due

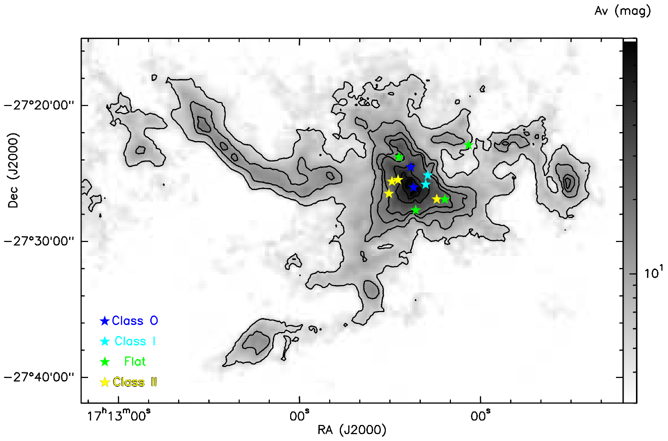

Figure 5.2: Extinction map of B59 in colour scale and contours (Román-Zúñiga et al. 2009), showing the known YSOs in the region (from Brooke et al. 2007; Forbrich et al. 2009). Contours are from an of A_V 5 to 20 by steps of 5, and onwards by steps of 20. Note that there are only four known protostars (between Class 0 and I). The known extinction cavity thought to have been pierced by an outflow lies on the NE of the central region.

to the converging flows and velocity discontinuities at the boundaries of cores (e.g. Ballesteros-Paredes et al. 1999a). Recently, Heitsch et al. (2009) have in fact compared their numerical simulations directly with the Pipe Nebula, and conclude that the Pipe is consistent with a large-scale infalling model, with very young cores capable of accreting at high rates and potential to become an active star forming cloud similar to Taurus in 1 Myr.

5.2 Observations

5.2.1 Motivation and strategy

Even though no evidence for a chemical evolution of individual cores has been found so far (Frau et al. 2010), it has been suggested that the Pipe Nebula holds a variety of very early star forming stages, from the dormant Bowl to the possibly eminent-star-forming Stem, and the active B59 (e.g. Alves et al. 2008). If that is the case, then the Pipe Nebula provides the opportunity to understand the physical conditions that provide the ingredients to star formation or the ones that prevent it.

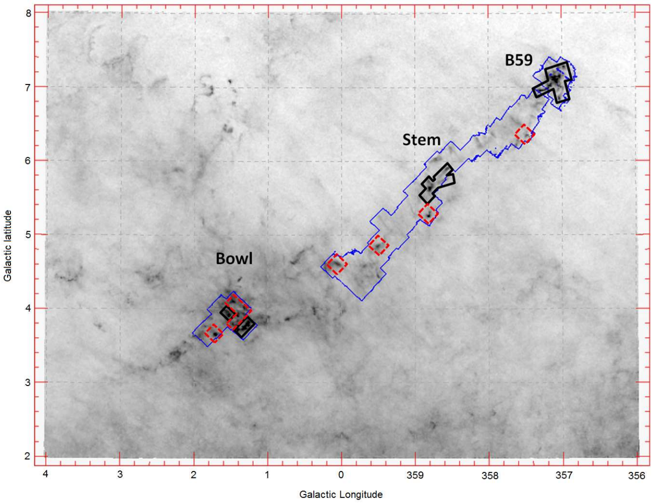

Figure 5.3: Extinction map of the Pipe Nebula in gray scale (same as in Fig. 5.1), showing the regions that we have observed with HARP at JCMT. The blue-delimited areas show the observed ^{12}CO J=3→2 emission. The black boxes are the simultaneously observed ^{13}CO and C^{18}O J=3→2. The red-dashed boxes represent cores in the Stem and Bowl that we also want to observe in ^{13}CO and C^{18}O.

As such, we have undertaken the most complete high resolution molecular line maps of the Pipe Nebula to date, by mapping ^{12}CO in the entire cloud, and ^{13}CO and C^{18}O in the bulk of the dense cores of the cloud. The combined information from ^{12}CO, ^{13}CO and C^{18}O observations aims to probe the cloud kinematics and the physical conditions within the Pipe Nebula, plus for the first time provide a complete, sensitive survey for outflows from hitherto unidentified embedded sources. Being the only clump in the cloud known to contain young stars and outflows, mapping B59 provides a benchmark for comparison with the more populous star forming cores in other nearby clouds and the starless cores in this cloud. We strive to reveal if the apparent absence of star formation along most of the Pipe is genuine and, that being the case, understand whether the bulk of the Pipe Nebula is a transient feature never destined to form stars, or if the local environment is responsible for the cloud's apparent sterility.

5.2.2 Data

Using HARP at JCMT in May and June 2010, we have mapped ^{13}CO and C^{18}O J=3→2 (at 330.6 and 329.3 GHz respectively) in the entire B59 star-forming region ($\sim$ 400 arcmin^2) and areas surrounding the stronger extinction cores in the Stem and the Bowl of the Pipe (another $\sim$ 400 arcmin^2; black boxes in Fig. 5.3). These data have an original spatial resolution of 15” and a spectral resolution of 0.05 kms^{-1}. The r.m.s. noise level on the B59 dataset is of 0.22 K (in T_A^*) with 0.25 kms^{-1} channels (example of spectra in Fig. 5.7). Due to time constrains, the cores in the Stem and the Bowl were not observed as deep, currently reaching an r.m.s. noise level of ~0.3 K and 0.45 K (in T_A^*) in 0.25 kms^{-1} channels, respectively. With the narrow lines and very weak emission found towards these cores, with emission peaks at ~0.8K in the Stem and 0.6K in the Bowl in C^{18}O J=3→2, an analysis of these data at the moment is extremely hard and further observations are needed to complete these observations down to the noise levels required. For this reason, here I will focus only on the B59 region for which the dataset is complete.

For each area mapped, the data reduction was performed using the ORAC-DR pipeline, using the package REDUCE SCIENCE NARROWLINE, without applying the flatfield algorithm, and with a pixel size of 7.4”. This reduction procedure automatically fits and corrects the baselines and removes the bad detectors based on the time-series data and on the r.m.s. noise levels of the final maps. The final reduced maps of each area were gridded together using the Starlink software. Fig. 5.4 and 5.5 show the final reduced maps of C^{18}O and ^{13}CO, convolved to a 20” resolution.

A complementary ^{12}CO J=3→2 (at 345.8 GHz) deep and high resolution (15”) map of the entire cloud has been carried out with HARP using JCMT DDT time (available to A. Chrysostomou), of which we have already mapped nearly 5 degrees along the length of the Pipe (blue areas in Fig. 5.3). These data reached a 0.2 K-0.4 K noise level (in T_A^*) at 0.5 kms^{-1} velocity resolution (example of spectra in Fig. 5.7). The final reduced B59 datacube in ^{12}CO is shown on Fig. 5.6 and it reveals clearly and for the

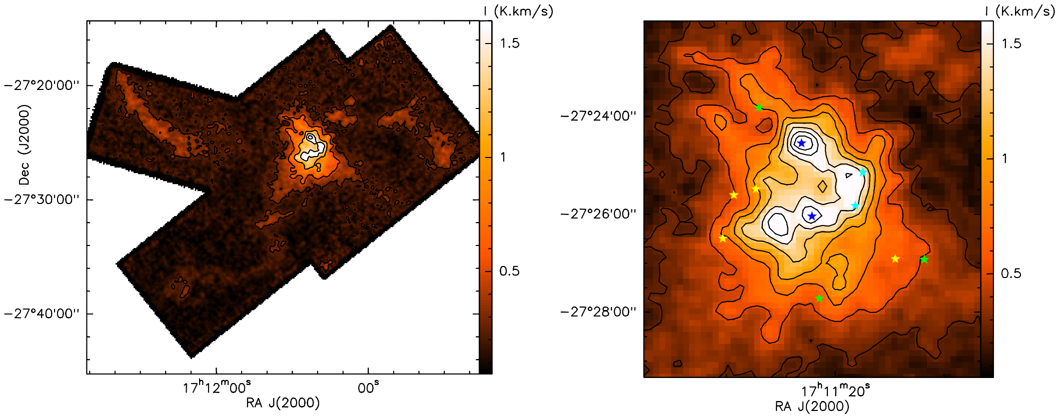

Figure 5.4: Left: integrated intensity map of $C^{18}O$ J=3→2 in the entire B59, with contours at 0.25, 0.5, 1, 1.5 and 2 $K\,kms^{-1}$. Right: zoom of the central region of B59 in $C^{18}O$ integrated intensity, with the young stellar objects as in Fig. 5.2. Contours from 0.25 to 2 $K\,kms^{-1}$ by steps of 0.25 $K\,kms^{-1}$.

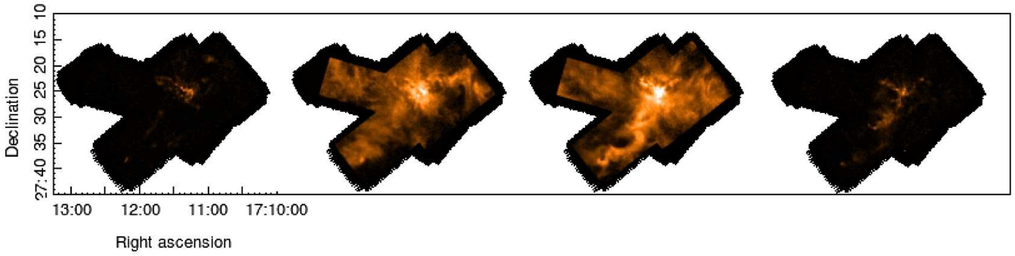

Figure 5.5: Channel maps of the ^{13}CO J=3→2 emission in B59, from 2 kms^{-1} to 5 kms^{-1} (from left to right). The colour scale ranges from 0 to 3 $K\,kms^{-1}$.

first time a number of outflows bursting from the central core of B59. The telescope main beam efficiency is $\eta_{\rm mb} = 0.66$ (Curtis et al. 2010a) for these three observed molecular transitions.

5.3 Physical properties of the gas in B59

5.3.1 Optical depth of $C^{18}O$ and ^{13}CO

The variation of optical depth across a cloud can be examined by looking at the ratio of intensities of the different isotopologues. I used this approach only qualitatively in Serpens with $C^{18}O$ and $C^{17}O$ (Chapter 3), given the ability of calculating the opacities

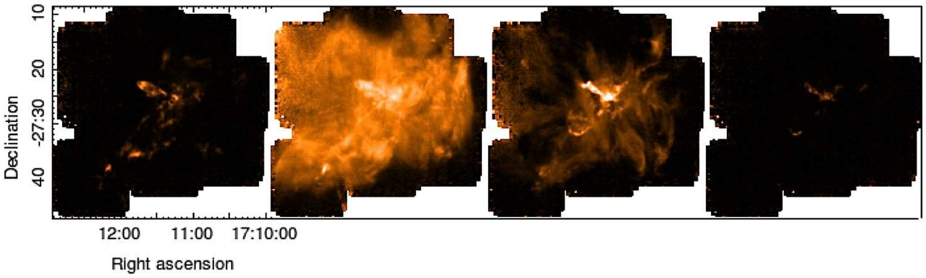

Figure 5.6: Channel maps of the ^{12}CO J=3→2 emission in B59, from 0 kms^{-1} to 8 kms^{-1} (from left to right). The colour scale ranges from 0 to 5 K kms^{-1}.

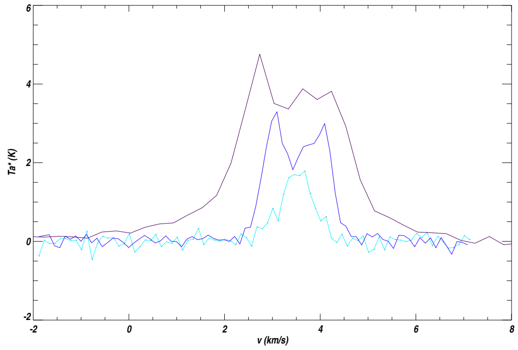

Figure 5.7: Overplot of a spectrum of C^{18}O (light blue line), ^{13}CO (dark blue line) and ^{12}CO (dark purple line) in B59, at the position with RA = 17^{h}11^{m}32.5^s and Dec = -27°28'20", showing the outflow wings and self absorption dip in ^{13}CO and ^{12}CO.

directly through the hyperfine structure fitting of C^{17}O.

For B59 however, this was the method I used to estimate the opacities for the three isotopoloques. Assuming the same excitation temperature for both species, the relation between the line intensity ratio and the optical depth, (e.g. Rohlfs and Wilson 2000) at a specific velocity is given by:

$$\frac{T_{^{13}\mathrm{CO}}(v)}{T_{\mathrm{C}^{18}\mathrm{O}}(v)} = \frac{1 - e^{-\tau_{13}(v)}}{1 - e^{-\tau_{18}(v)}} \tag{5.1}$$

where T is the brightness temperature and τ is the optical depth of each given line. This relation is valid for a channel-by-channel comparison, but the self absorption present in both ^{12}CO and ^{13}CO (Fig. 5.7) limit the validity of this approach, because the T$_{\mathrm{exc}}$ is different where the line is self absorbed. Therefore, I followed the method in Ladd

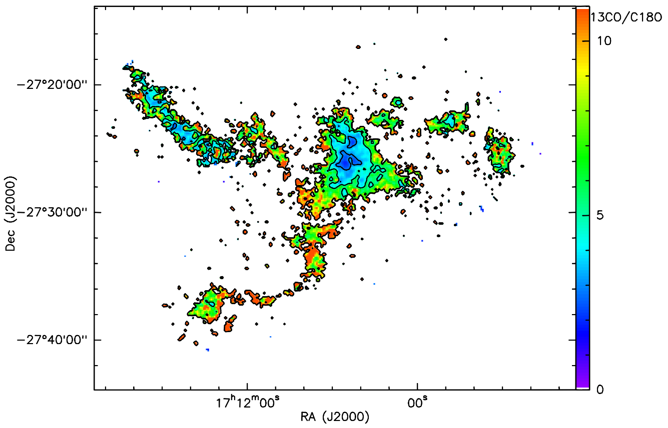

Figure 5.8: Ratio map of the integrated intensities of ^{13}CO and C^{18}O in B59 in colour scale and contours. The contours are at ratio values of 3 and 5.

et al. (1998) to study the ratio of the integrated intensities. With this method, the ratio will still be underestimated but with a lower relative error than if using the intensity ratio at velocities close to the peak. This systematic under-estimation will however boost the C^{18}O optical depth, particularly in the central regions where the ^{13}CO self absorption is strongest.

As such, I estimated the C^{18}O and ^{13}CO peak opacities (τ_{18} and τ_{13} respectively) using the ratio of the integrated intensities and equation 5.2, where $\tau_{13}(v) = \tau_{13} e^{-v^2/2\sigma^2}$, σ is the velocity dispersion, $\tau_{18} = \tau_{13}/f$ and f is the fractional abundance of ^{13}CO with respect to C^{18}O.

$$\frac{\int_{-\infty}^{+\infty} T_{^{13}\mathrm{CO}}(v)dv}{\int_{-\infty}^{+\infty} T_{\mathrm{C^{18}O}}(v)dv} = \frac{\int_{-\infty}^{+\infty} 1 - e^{-\tau_{13}(v)}dv}{\int_{-\infty}^{+\infty} 1 - e^{-\tau_{18}(v)}dv} \tag{5.2}$$

Given that this method is quite insensitive to the line width assumed, I have adopted a velocity dispersion of 1 kms^{-1}. I produced the ratio map between the integrated intensities of the two molecules, after convolving both datacubes to a 20” resolution, in order to suppress some of the high frequency noise, and after masking the datacubes to pixels where the signal to noise (estimated at each pixel) was higher than 4. The resulting map of ^{13}CO to C^{18}O ratio is shown on Fig. 5.8, where values range from 2 to 4 in the denser regions, and approaching 9 towards the edges of the cloud. Adopting a fractional abundance of ^{13}CO with respect to C^{18}O, f, of 8.4 (Frerking et al. 1982),

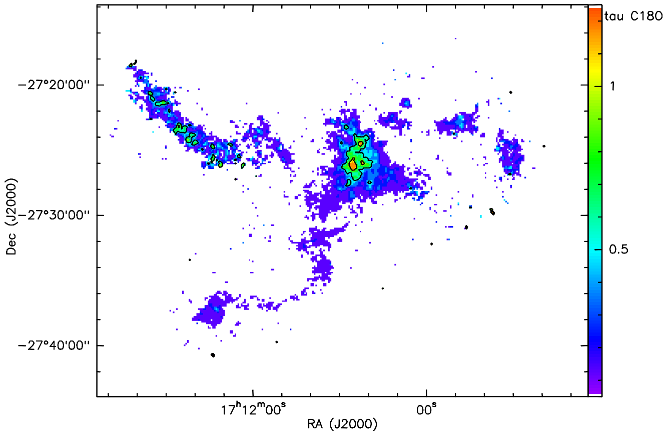

Figure 5.9: Colour scale and contours represent the B59 map of the $C^{18}O$ optical depth calculated from the ratio of ^{13}CO to $C^{18}O$ (Fig. 5.8). The contours are at opacities of 0.5 and 1, showing $C^{18}O$ to be optically thin in most of the cloud and marginally optically thin towards the central region, even though the self absorption of ^{13}CO could have boosted the opacity values in these regions.

this translates into a τ_{18} ranging from 0.1 to 1.25 towards the central core (Fig. 5.9). However, as referred before, the possible stronger self absorption of ^{13}CO towards the central cores is likely to be responsible for boosting this value. Therefore, I will consider $C^{18}O$ to be optically thin throughout the cloud, and marginally optically thick only towards the central cores.

5.3.2 ^{13}CO excitation temperatures

Since ^{13}CO is mainly optically thick ($\tau_{13} > 1$) in the bulk of the cloud, I have estimated the excitation temperature of ^{13}CO assuming LTE conditions and optically thick emission. From Chapter 2, equations 2.14, 2.15 and 2.26, we have the relation:

$$T_{\rm exc}(^{13}CO_{3-2}) = \frac{15.87}{\ln[1 + 15.87/(T_{max}(^{13}CO) + 0.045)]} \tag{5.3}$$

where 15.87 is $h\nu/k$ for the frequency of ^{13}CO (3-2) and T_{max} is the peak main beam temperature of the line. This is not accounting for the self absorption dip, and when this occurs, the peak used will correspond to the absolute maximum of the emission.

This excitation temperature map is shown in Fig. 5.10, where we can see that most of the cloud is at 8 - 9 K, and the star forming core is at 11 - 12 K. Given that the

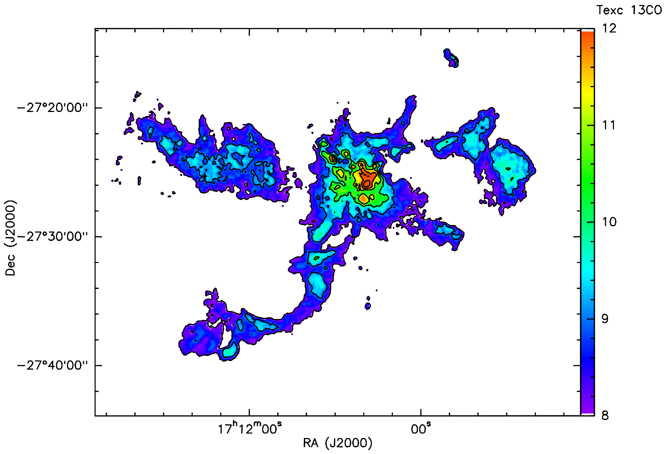

Figure 5.10: Colour scale and contours represent the ^{13}CO excitation temperature map of B59. The contours are at 8 K through to 13 K, by steps of 1 K.

^{13}CO picks up the outflow emission and this excitation temperature was measured at the peak of emission, when there is self absorption we will be measuring the excitation temperature of the denser gas which is already likely to be affected by the outflows. As such, these outflow shocks can be seen in this image as local temperature maxima. Outside the contoured region shown in Fig. 5.10 the temperatures reach as low as 5 K. However, in these ^{13}CO diffuse emission regions where little C^{18}O is detected within our noise levels, is it likely that the ^{13}CO has lower optical depth, limiting the validity of this approach to estimate the excitation temperature since it is only for optically thick emission.

5.3.3 Relation between H_2 and CO column densities

Even though for the previous calculations of the optical depth I have taken the standard value for the relative abundances of ^{13}CO to C^{18}O, I have estimated a "conversion" factor, X_{molecule}, to estimate the gas masses and column densities in the region (e.g. Pineda et al. 2008), as being:

$$X_{\mathrm{molecule}} = N(\mathrm{H_2})/I_{\mathrm{molecule}} \tag{5.4}$$

where $N(\mathrm{H_2})$ is the H_2 column density and I_{molecule} is the integrated intensity of the molecular transition. This conversion factor was estimated for both ^{13}CO and C^{18}O

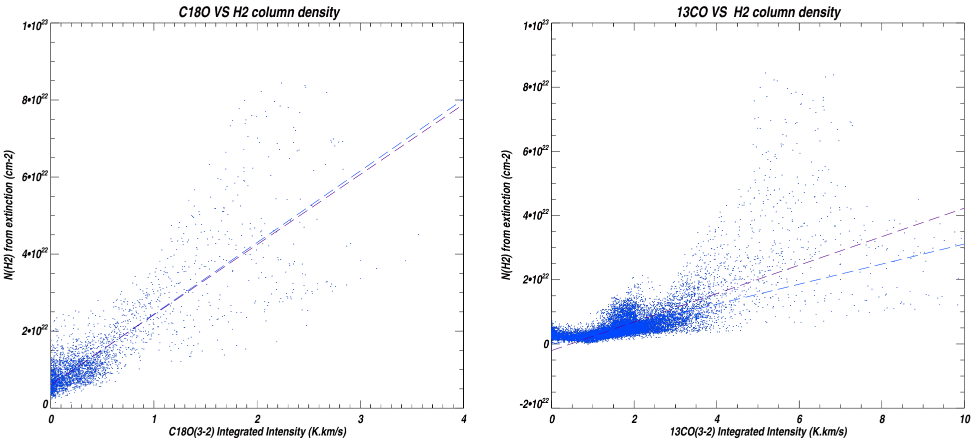

Figure 5.11: Scatter plots of the H_2 column density retrieved from the extinction map against $C^{18}O$ (left) and ^{13}CO (right) integrated intensities, where each point corresponds to a pixel in the map. The blue and purple dashed-lines represent the linear fit of the data points, with and without an upper limit constraint (respectively) on the column densities and integrated intensities.

and is later used for calculating the properties of the structures found within the region using a hierarchical stratification of the emission (Section 5.4). This is a simplistic approach and it does not account for possible depletion or optical thickening. Therefore, a linear relation between H_2 column density and ^{13}CO and $C^{18}O$ integrated intensities is a reasonable assumption for intermediate densities but it only provides a lower estimate of the H_2 mass for higher densities. In fact, this method is equivalent to using Eq. 2.27, but allowing a calculation of $N(H_2)$ without having to assume a temperature or an abundance ratio of the studied molecule with relation to H_2.

The H_2 column density was derived from the extinction map of B59 (Román-Zúñiga et al. 2009) assuming a relation between the visual extinction and the H_2 column density as: $N(H_2)/A_v = 9.4 \times 10^{20}$ cm^{-2} mag^{-1} (e.g. Bohlin et al. 1978; Pineda et al. 2008). This was plotted against the ^{13}CO and $C^{18}O$ integrated intensities corrected for the telescope efficiency and masked for regions with 4σ detections or higher. All maps had 20" resolution and were resampled to a common area and pixel size, for a pixel-by-pixel comparison. The resulting scatter plots are shown in Fig. 5.11.

It is clear that there is a correlation between the H_2 column densities and the integrated intensities of the two lines, even though, both lines show some departure from a linear correlation specially towards higher column densities and integrated intensities. As such, I have estimated the conversion factor for $C^{18}O$ using a linear fit to all the data points (purple fit on left panel of Fig. 5.11) or constraining the upper limit of H_2 column density to 4×10^{22} cm^{-2} and $C^{18}O$ integrated intensity to 1.5 K kms^{-1} (blue fit on left panel of Fig. 5.11). The results are very similar with a $X_{C^{18}O} = 1.82 \times 10^{22}$ cm^{-2}K^{-1}km^{-1}s when including all the data points. This little difference in the fits shows that the $C^{18}O$ is tracing the bulk of the cloud as seen in extinction, from low to high column densities.

However, given the high optical depth of ^{13}CO towards the denser regions, departures from the linear trend seen at lower densities are undoubtedly found. Therefore, to estimate the relation between the H_2 column density and the ^{13}CO integrated intensities I have only used the pixels where the H_2 column density was below 4×10^{22} cm^{-2} and ^{13}CO integrated intensity was below 4 K kms^{-1}. This will more reliably estimate the relation for the bulk of the cloud than if considering all the column density ranges, but it will result in underestimating the total mass when considering higher densities. This is not surprising and it is rather expected when the line becomes optically thick and self absorbed. The two linear fits to fit either all the data points, or restricting the upper limit are shown in the right panel of Fig. 5.11 as a purple or blue dashed-line respectively. The slope I will use is from the restricted upper limit and corresponds to a $X_{^{13}CO} = 3.12 \times 10^{21}$ cm^{-2}K^{-1}km^{-1}s.

5.4 The hierarchical structure of B59

To understand the cloud structure of B59, I have used a dendrogram technique, alternative to the clumpfind approach used in Serpens (Chap. 3), which takes into account the hierarchical structure of the cloud, rather than just attempting to split the cloud into several clumps. It provides a tree-like structure of the cloud, and has been developed and applied to star forming regions by Rosolowsky et al. (2008). To be able to interpret

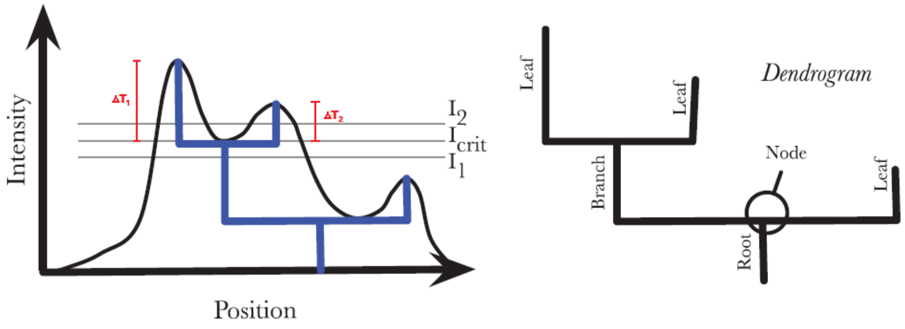

Figure 5.12: Diagram from Rosolowsky et al. (2008) illustrating the dendrogram process of stratification of a one dimensional structure. The left panel shows the one dimensional profile (black curve) with the underlying dendrogram in blue. This same dendrogram is shown again on the right panel, where the nomenclature used (leaves, nodes, branches and roots) are identified. On the left panel we can also see three examples of contour levels, in grey, and the height of a leaf in red.

this hierarchical study of B59 however, I made use of the previously studied opacities of the lines observed as well as the relation between the extinction maps and the gas emission, as it is important to understand the impact of the optical depth on the gas emission that we are detecting.

5.4.1 Dendrograms

The dendrogram technique reveals the structures and sub-structures of a given 1D, 2D or 3D image, by analysing the isosurfaces which recreate the input image. This method identifies the peaks of the emission (leaves) and connects different leaves through nodes as soon as separate structures are comprised by a common contour. These nodes are then followed down to lower levels as branches, until they connect through another node with another branch or leaf. An example of such a stratification is shown on Fig. 5.12. The height of a leaf (shown in red in Fig. 5.12) is defined as the difference from the peak of the emission to the I_{crit}, which is the contour where the dendrogram splits the emission into two sub-structures and therefore represents the “base” of the leaf.

The code I used to implement this dendrogram technique is fully described in

Rosolowsky et al. (2008), and consists of semi-publicly available IDL routines that are capable of finding the hierarchical structure of a cloud using 2D or 3D datacubes. A benefit of this method is that it does not split the cloud into independent clumps, but it keeps the information as to how these clumps are interconnected, and what is the underlying gas structure. The other benefit of such an approach is that it is much less sensitive to input parameters than other clump-finding algorithms. This code finds the local maxima of a datacube that will comprise the top level of the dendrogram, and it then contours the data down using a large number of levels. At each contour level, the code will check for sub-structures that merged. When more than two sub-structures merge at a same node, then the code will refine the contours into further levels, so that only two structures are merged at a time. This is a robust method to find structures, not dependent on input contour levels or spacing, and the only tunable input parameter is the minimum height for which a leaf is considered to be a separate structure.

This dendrogram code is also built such that it can calculate several properties of the cloud at each contour level, such as the integrated intensity, the size of the structure, the velocity dispersion, the mean velocity and mean position. To do so, the user also needs to specify the distance to the cloud and method by which it associates the intensity onto a given structure. The three methods available to assign emission to a given structure are bijection, clipping or extrapolation, as described in Rosolowsky et al. (2008). A diagram of how each paradigm works is shown on Fig. 5.13.

As soon as the characteristics of each structure are calculated, we can retrieve the mass by considering the linear relation previously calculated (Sec. 5.3.3) between the H_2 column density and the integrated intensity of the molecular line considered. The masses are calculated within the code, following the procedure described in Rosolowsky et al. (2008), where:

$$M_{\mathrm{molecule}} = 1.84 \times 10^{-20} X_{\mathrm{molecule}} L_{\mathrm{molecule}} \tag{5.5}$$

where M_{molecule} is the gas mass in $M_{\odot}$ derived from the CO molecule in consideration, X_{molecule} is the CO-to-H_2 conversion factor described in § 5.3.3 in units of $\mathrm{cm}^{-2}\mathrm{K}^{-1}\mathrm{km}^{-1}\mathrm{s}$,

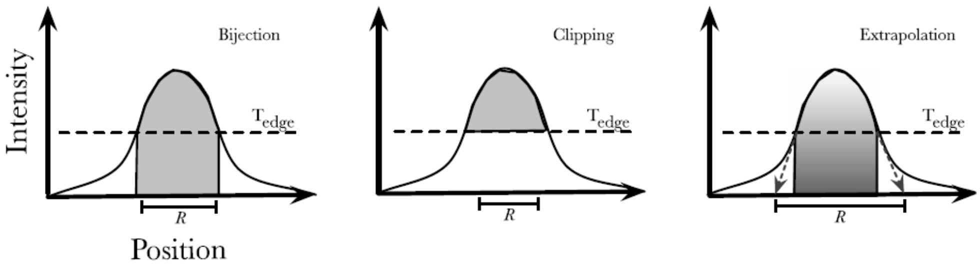

Figure 5.13: Diagram from Rosolowsky et al. (2008) illustrating the three paradigms available for calculating the properties of the structures solved by the dendrogram process at each isosurface. The three panels show the same one-dimensional emission profile with the contour at which the properties are being calculated, and the shaded area shows the emission used to compute cloud properties for each different approach.

and $L_{\rm molecule}$ is the luminosity from the considered CO emission in K km s^{-1}pc^2. This luminosity $L_{\rm molecule}$ is calculated as $L = Fd^2$, where d is the distance to the cloud and F is the flux of the region, i.e. the sum of all the emission in the region, calculated as $F = \sum_i T_i\ \delta\theta_x\delta\theta_y\ \delta v$. The value of 1.84×10^{-20} arises from the units conversion, assuming a molecular weight of 2.33, similarly to that assumed in Serpens (Chapter 3).

Once the masses are calculated, the virial parameter α is estimated from the virial balance between the kinetic and gravitational potential energy, i.e. $\alpha = 2E_{int}/E_{pot}$ (see Sec. 1.1.4). Assuming a uniform density profile, this translates into:

$$\alpha = \frac{5\sigma_v^2 R}{M_{\rm molecule} G} \tag{5.6}$$

where σ_v is the velocity dispersion and R is the size of the structure as estimated by the dendrogram code. Similarly to the mass, the virial parameter is calculated for each structure at each contour level. If in virial equilibrium, $\alpha = 1$ and we retrieve equation 1.11. However, given the uncertainties and similarly to what was assumed for Serpens (Chapter 3), I consider a structure to be gravitationally bound when the virial parameter is less than 2. However, note that for ^{13}CO in particular, the optical depth and self absorption in the denser regions will result on underestimating the mass $M_{^{13}\rm CO}$, and therefore, overestimating the virial parameter.

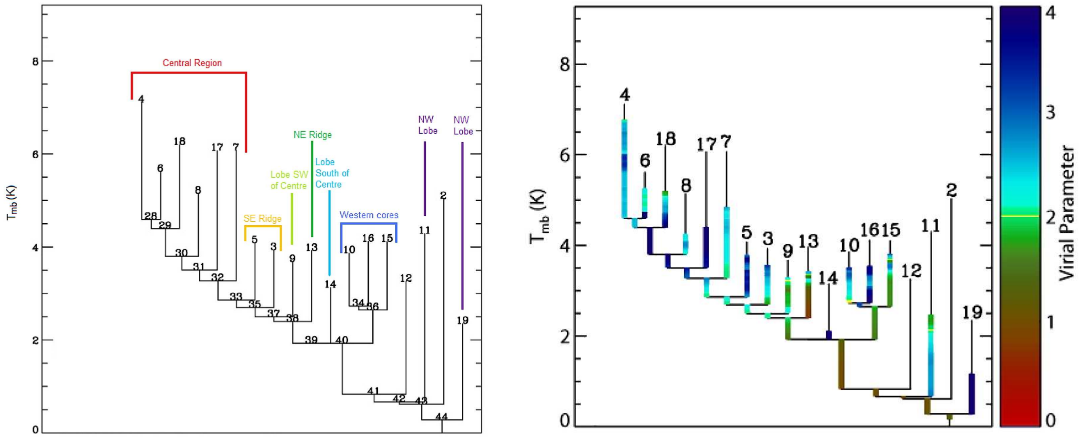

Figure 5.14: Dendrogram of the ^{13}CO emission in B59. Left: leaves labeled and grouped according to the regions in the map where they belong to. Right: the virial parameter calculated for each contour. The regions where no virial parameter is shown (e.g., the tips of the leaves) are due to the lack of sufficient quality data to calculate the properties, such as insufficient number of pixels.

5.4.2 Results from the dendrogram analysis

To study the structure of B59, I have performed a dendrogram analysis of the region using the intermediate density tracers ^{13}CO and C^{18}O. I convolved the maps to a resolution of 20” to help suppress the noise, trimmed the noisier map edges, and run the dendrograms on these two 3D datacubes. For both, I considered the minimum height of a leaf to be one-sigma of the r.m.s. noise level, I chose the bijection method when calculating the cloud properties and, finally, I adopted a distance to the Pipe Nebula of 130 pc (Lombardi et al. 2006). The $X_{\mathrm{C^{18}O}}$ and $X_{\mathrm{^{13}CO}}$ used for the calculations of cloud properties were the ones estimated in § 5.3.3.

^{13}CO dendrogram

The resulting dendrogram for ^{13}CO is shown on Fig. 5.14. The positions of each leaf in the map are identified with labels in the left panel dendrogram, and can be seen in the channel maps of Fig. 5.15. This hierarchical stratification finds the entire structure of B59 to be interconnected and part of a same cloud. The only sub-branch which diverts

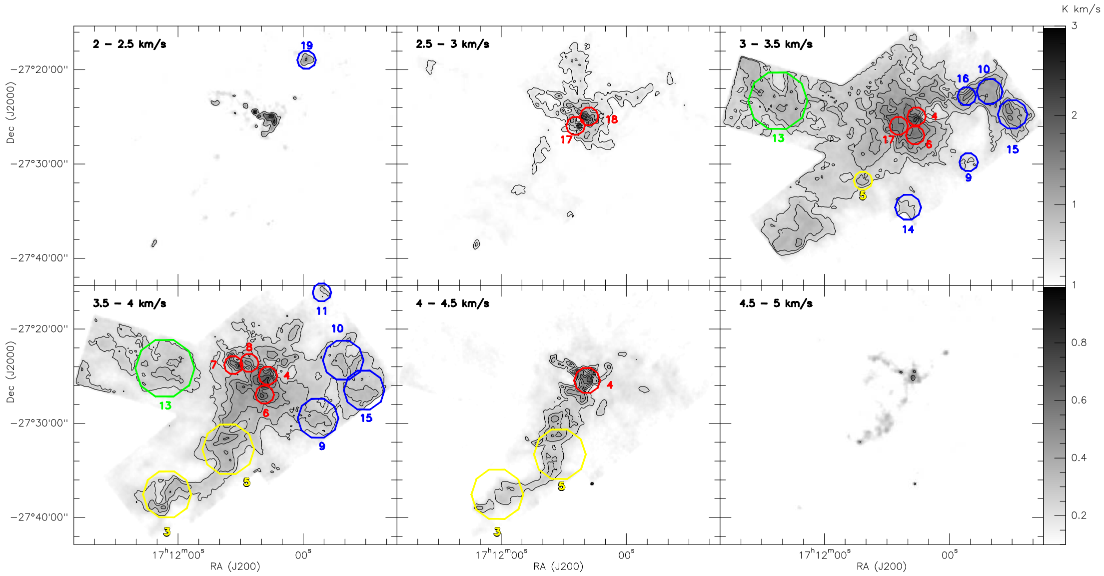

Figure 5.15: ^{13}CO integrated intensity maps in T_A^* over intervals of 0.5 kms^{-1}, from 2 kms^{-1} to 5 kms^{-1}. The contours are from 0.25 to 2 K kms^{-1}, by steps of 0.25 K kms^{-1}, and from 2 K kms^{-1} onwards with steps of 1 K kms^{-1}. The gray scale in the first and last panels (from 2-2.5 kms^{-1} and from 4.5-5 kms^{-1}) is from 0.1 to 1 K kms^{-1} (lower-right colour bar), and in the remaining panels is from 0.1 to 3 K kms^{-1} (upper-left colour bar). The positions of the leaves from Fig. 5.14 are shown as they appear in each of the maps (coloured circles and labels).

from the main branch is that of the western cores (as labeled on Fig. 5.14) which seem to be a sub-structure on its own, connecting to the main cloud at lower levels.

The right panel of Fig. 5.14 shows the virial parameter calculated for each of the structures at each contour level. From these figures, we can see that the central region is divided into 6 leaves. Leaves 4, 6, 7, 8 and 18 have a virial parameter just above 2. Taking into account that there is an optical depth effect which is not being taken into account, these masses are likely underestimated, and the virial parameter is likely overestimated. The three leaves at the top of the dendrogram (leaves 4, 6 and 18) are connected to the rest of the tree by a branch which has a much higher virial parameter. Leaves 7 and 8 have a virial parameter just above two and they correspond to the gas which seems to be compressed by the NE directed outflow. Leaf 17 has an even higher virial parameter, likely to represent the initial part of the outflow as it is making its way out of the cloud. For the rest of the cloud, all the branches that connect all the way

Table 5.1: Properties of the ^{13}CO dendrogram leaves

Leaf #	Radius (pc)	V_0 (kms^{-1})	σ_v (kms^{-1})	Mass ($M_\odot$)	α
4	0.03	3.9	0.19	0.70	2.1
6	0.02	3.7	0.13	0.11	3.2
18	0.02	2.9	0.13	0.11	3.4
8	0.01	3.9	0.07	0.04	1.9
17	0.04	3.2	0.15	0.34	2.9
7	0.03	3.7	0.11	0.21	1.7
5	0.06	3.9	0.14	0.64	2.2
3	0.07	4.0	0.10	0.52	1.5
9	0.04	3.6	0.11	0.31	1.8
13	0.14	3.5	0.13	4.15	0.7
14	0.03	3.4	0.08	0.07	3.2
10	0.05	3.4	0.14	0.70	1.7
16	0.03	3.2	0.15	0.22	3.5
15	0.06	3.4	0.15	1.28	1.4
11	0.04	3.5	0.11	0.23	2.4
19	0.04	2.2	0.20	0.14	12.3
Total	0.44	-	0.41	81.7	1.03

until the root, seem to be reasonably bound. From all the leaves that come out of it, four have a high virial parameter (leaves 5, 14, 16 and 19) and are likely to represent lobes of outflows. The remaining leaves seem to be reasonably virialised, showing virial parameter values around 2. Only leaf 13, which represents the entire NE ridge, seems to be undoubtedly bound, with a virial parameter below 1.

Table 5.1 summarises the characteristics of all the ^{13}CO leaves in B59. The first column shows the identification number attributed by the dendrogram, as shown in Fig. 5.14 and 5.15. These properties were derived for the lowest contour where each leaf was detected. The "Radius" is equivalent to the radius of a projected circular cloud which would comprise the number of pixels of each leaf. V_0 is the mean velocity (weighted by the intensity) of each leaf with an uncertainty of 0.1 kms^{-1}, σ_v is the velocity dispersion of each leaf, "Mass" is the leaf mass (eq. 5.5) and finally, α is the

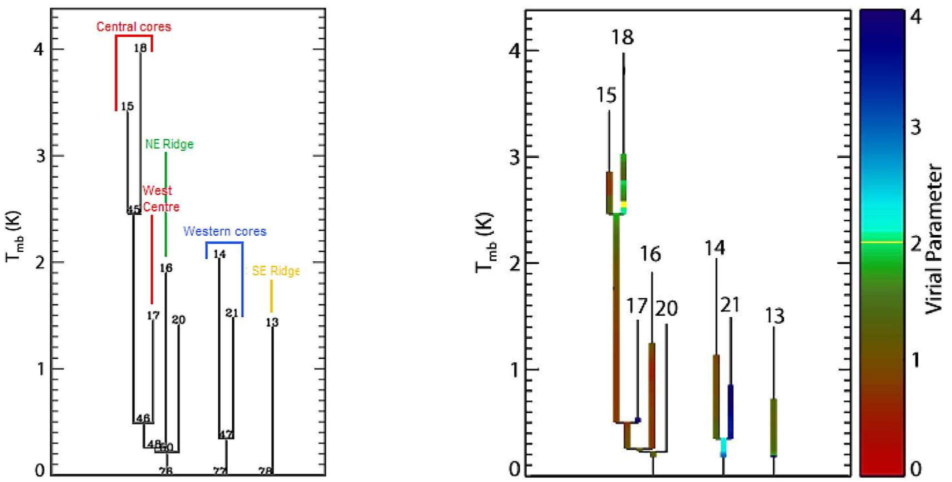

Figure 5.16: Dendrogram of the $C^{18}O$ emission in B59. Left: leaves labeled and grouped according to the regions in the map where they belong to. Right: the virial parameter calculated for each contour. The regions where no virial parameter is shown (e.g., the tips of the leaves) are due to the lack of sufficient quality data to calculate the properties, such as insufficient number of pixels.

virial parameter as by eq. 5.6. The last line of the table shows the total mass, equivalent size and virial parameter of the cloud, measured on the root of the dendrogram of Fig. 5.14.

$C^{18}O$ dendrogram

The $C^{18}O$ dendrogram is shown on Fig. 5.16, with the positions of each leaf in the map identified with labels in the left panel dendrogram. These positions are also shown on the channel maps of Fig. 5.17. In the case of $C^{18}O$, the entire cloud is no longer part of a same sub-structure. However, this is only due to signal to noise limitations, that do not allow the detection of the lower density $C^{18}O$.

The central region of B59 is described by two main cores, both gravitationally bound. The NE ridge is found with the $C^{18}O$ dendrogram as a whole structure (leaf 16) also with very low values of the virial parameter. The dendrogram also shows two cores to the west of the central region (leaves 14 and 21) of which only one seems to be gravitationally bound. Finally, this method recovered an isolated leaf towards the

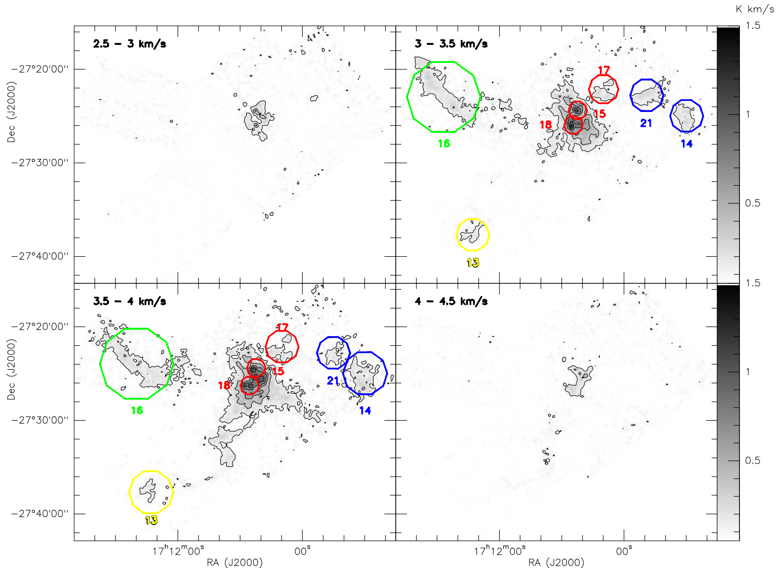

Figure 5.17: $C^{18}O$ integrated intensity maps in T_A^* over intervals of 0.5 kms^{-1}, from 2.5 kms^{-1} to 4.5 kms^{-1}. The contours are from 0.12 to 2 K kms^{-1}, by steps of 0.2 K kms^{-1}, and from 2 K kms^{-1} onwards with steps of 1 K kms^{-1}. The positions of the leaves from Fig. 5.16 are shown as they appear in each of the maps (coloured circles and labels).

end of the SE ridge, again, with a low virial parameter.

Table 5.2: Properties of the $C^{18}O$ dendrogram leaves

Leaf #	Radius (pc)	V_0 (kms^{-1})	σ_v (kms^{-1})	Mass ($M_\odot$)	α
15	0.02	3.4	0.14	0.29	1.2
18	0.03	3.5	0.21	0.91	1.7
17	0.05	3.5	0.17	0.52	3.3
16	0.15	3.5	0.15	5.82	0.7
14	0.07	3.4	0.15	1.51	1.2
21	0.07	3.3	0.21	1.15	2.9
13	0.06	3.4	0.13	0.91	1.50
Total	0.30	-	0.39	32.8	1.4

Table 5.2 is analogous to Table 5.1 and summarises the characteristics of all the $C^{18}O$ leaves in B59. The last line of this table shows the total mass, equivalent size and virial parameter of the cloud, but measured by combining the information of the three disconnected roots (see Fig. 5.14). The "Radius" shown is the radius equivalent

to a circle whose area equals the summed areas, the σ_v is the square root of the sum of the squared velocity dispersions of each three branches, the "Mass" is the sum of all three masses, and the shown virial parameter α is an average of the virial parameter of the three branches. The optical depth of C^{18}O towards the central cores, will affect this estimate of the masses, as they do not account for optical thickening of the line. If we would correct for optical depth, the mass estimate would increase and the virial parameter would become even smaller.

5.4.3 Discussion

Despite the non-interconnected structure found with C^{18}O, its hierarchical stratification has similarities with that found with ^{13}CO though with less branching. Even though the emission in C^{18}O still follows the NE outflow walls (i.e. the ^{13}CO leaves 7 and 8) the dendrogram did not recover these as being individual peaks in the C^{18}O emission. The only leaf that was not separated in ^{13}CO was the C^{18}O leaf 17. This leaf has a very high virial parameter, and could be a part of material swept by a possible outflow to the west side of the central core. In fact, it seems to lay spatially side-by-side with the ^{13}CO leaf 16, also with a high virial parameter.

Both the ^{13}CO and C^{18}O dendrograms find the NE ridge to be a whole structure with little sub-structure (no inner leaves), and with very low values of the virial parameter, supporting that it is a gravitationally bound structure.

The western cores are found with both molecules to be a somewhat separate sub-structure on its own. The C^{18}O leaf 14 ($\equiv$ ^{13}CO leaf 15) is a relatively bound structure whereas C^{18}O leaf 21 ($\equiv$ ^{13}CO leaves 10 and 16) seems to be quite more dynamic.

The SE ridge in C^{18}O is also divided in two, similar to what is seen in ^{13}CO. The lower-left half of the ridge is described by C^{18}O leaf 13 ($\equiv$ ^{13}CO leaf 3). The rest of the ridge, even though it is found as a leaf in ^{13}CO, it is part of the underlying structure of the central region, described by the C^{18}O node 46. In fact, this node also includes the non-detected lobe SW of the centre (the ^{13}CO leaf 9).

Finally, there are lobes which were not detected in C^{18}O, most likely due to the noise. In fact, the dendrograms do find some of these structures as isolated leaves (such as the ^{13}CO leaves 11, 14 and 19), but since it fails to calculate any virial parameter due to the lack of sufficient information from the data, I did not present them here. Note that the C^{18}O line widths are quite narrow outside the central region of B59, making those (also spatially small) structures described by very few data points.

A brief comparison of the masses derived from the ^{13}CO and C^{18}O emission shows that the structures which are commonly found have similar mass estimates. C^{18}O, however, seems to recover more mass from the NE ridge and some of the cores. This difference is likely to arise from the higher optical depth of ^{13}CO which will underestimate the gas mass. Nevertheless, both lines show a total of $\sim$ 10 M$_\odot$ to be comprised in the leaves. However, they differ in the total mass of the cluster by a factor of 2.5, mostly due to the gas mass present in a more diffuse state, traced only by ^{13}CO. This said, the fraction of mass comprised in the leaves is of $\sim$11 % using the ^{13}CO, and $\sim$ 33% for the C^{18}O estimate.

5.5 Dynamics of B59

5.5.1 Ambient cloud

To study the dynamics of B59, I have used the information from the intermediate density tracers ^{13}CO and C^{18}O, through position velocity diagrams along constant Declination and Right Ascension. The position of each cut is shown in Fig. 5.18, and the PV diagrams are shown on Fig. 5.19 and 5.20.

As can be see from these diagrams, the emission from C^{18}O is very narrow throughout the region, with the exception of the star forming central region of B59. Furthermore, the C^{18}O emission seems to be pretty well constrained to where the ^{13}CO is stronger. ^{13}CO, on the other hand, seems not only to be able to trace the dense regions, but it also picks up a lot of the outflows, seen in the PV diagrams as spatially-narrow

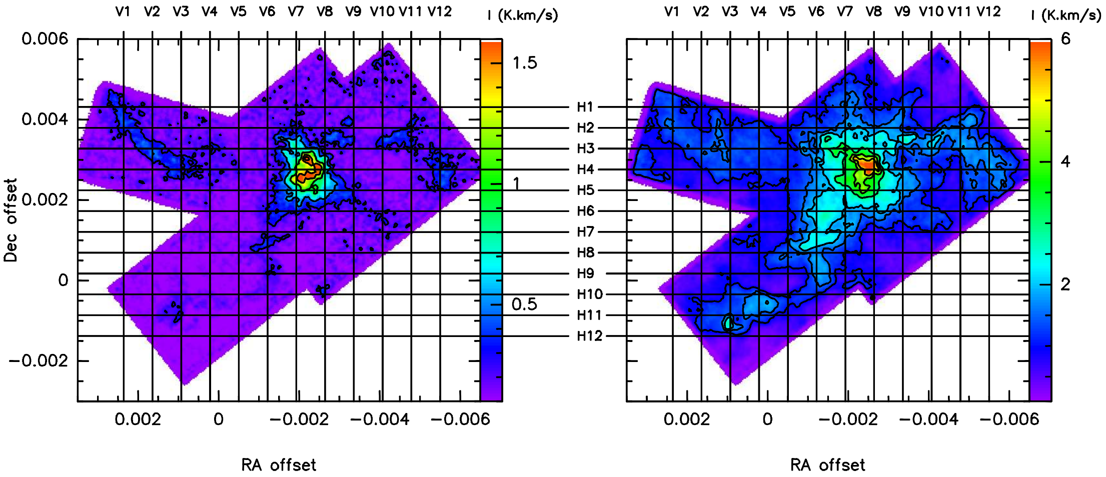

Figure 5.18: Integrated intensity maps of $C^{18}O$ (left) and ^{13}CO (right) showing the position of the PV diagrams of Fig. 5.19 and 5.20. Each cut is labeled as H# (for the horizontal cuts) and V# (for vertical cuts). Contours are at 0.27, 0.5, 1, 1.5 and 2 K kms^{-1} for $C^{18}O$ and at 1, 1.5, 2, 3 and 4 K kms^{-1} for ^{13}CO (in T_A^*).

but velocity-broad emission. Some of these outflows are pointed out in the PV diagrams (Fig. 5.19 and 5.20).

Looking in detail to the diagrams, we can see that the NE ridge is very well traced by one single velocity (around 3.2 kms^{-1}), showing little broadening or internal structure (see PV diagrams V1 to V4 and H1 to H4). The SE ridge, on the other hand, shows a much more complex structure (PV diagrams V1 to V6 and H7 to H12). The eastern end of the ridge itself seems to be better described by velocities around 3.2 kms^{-1}, whereas the western end of the ridge has stronger emission at ~4 kms^{-1}. Even though the ^{13}CO detects these two velocities throughout the cuts, $C^{18}O$ is only detected where the emission is stronger. The ^{13}CO also seems to pick up a possible outflow lobe at the intersection of V3 and H11, which could maybe be responsible for the difference in the velocities at this steep edge, as well as perhaps shaping the edge itself.

The central region of B59 is seen in PV diagrams V7, V8 and H2 to H5. The lobes from two outflow edges are seen both in blue and red emission. In fact, even $C^{18}O$ seems to pick up some of the emission from this outflow gas closer to the cores. There is a significant line broadening of the line emission from both molecules, nearly a factor of 3, indicating that the gas in this central region is being significantly affected

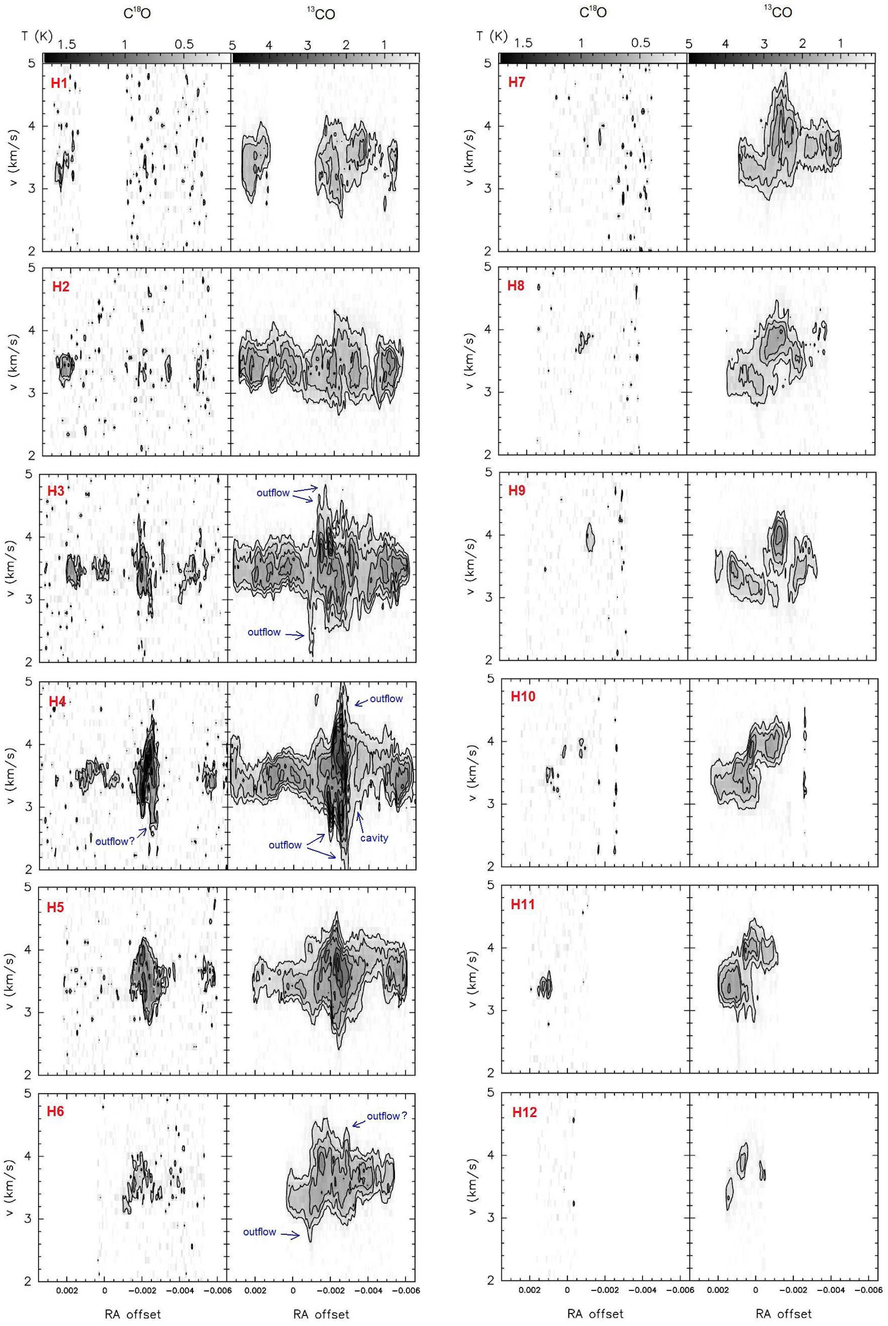

Figure 5.19: PV diagrams of B59 at constant declinations in C^{18}O (left-hand side on each column) and ^{13}CO (right-hand side on each column). Each cut is labeled in the top-left corner as in Fig. 5.18. The position of some of the possible outflows and cavities are pointed and labeled. Contours are from 0.5 K onwards with steps of 0.5 K for both molecules, plus a lower contour of 0.3 K for C^{18}O (in T_A^*).

by these outflows.

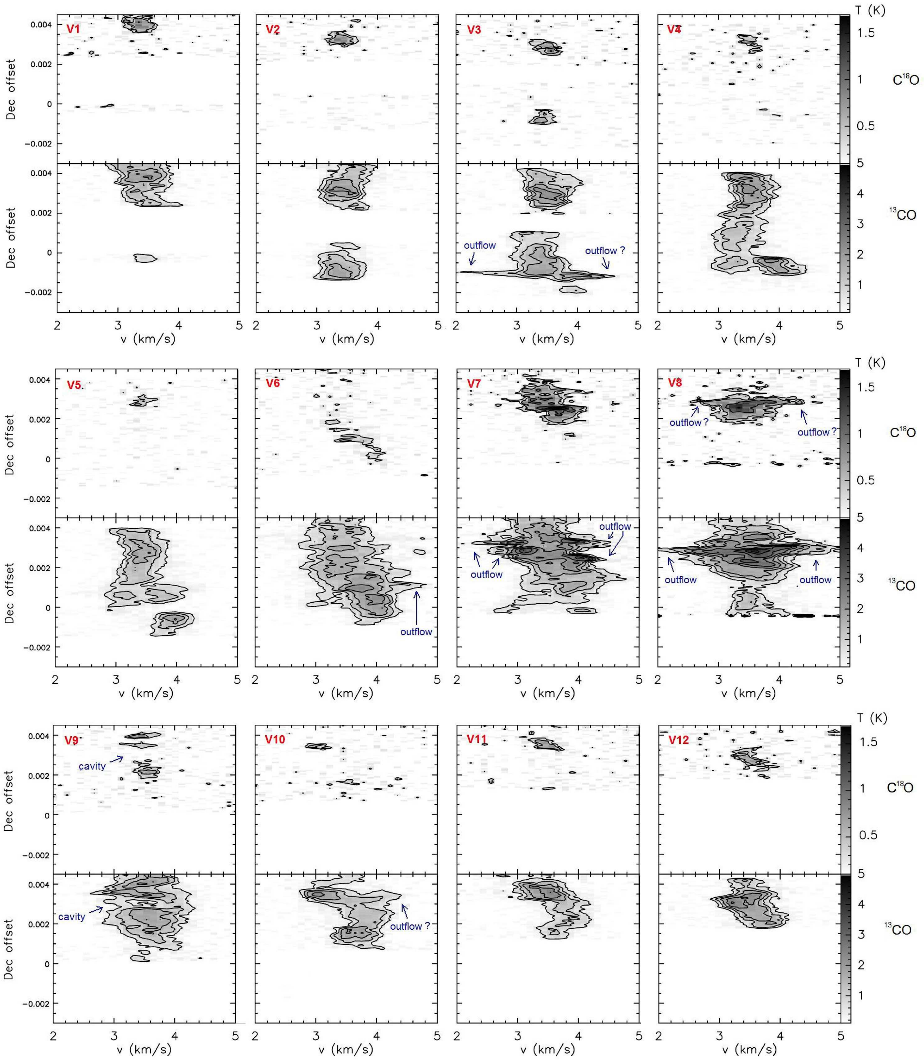

Figure 5.20: PV diagrams of B59 at constant RA in C^{18}O (upper panel of each row) and ^{13}CO (lower panel of each row). Each cut is labeled in the top-left corner as in Fig. 5.18. The position of some of the possible outflows and cavities are also pointed and labeled. Contours are as in Fig. 5.19

Finally, when looking at the western cores (PV diagrams V8 to V12 and H2 to H5), we can see that they are separated from the central region by a cavity in the gas emission, best seen in V9. As moving westwards, this cavity is followed by a slight broadening of the line emission, and then by gas with the typical line widths and velocities (~3.4 kms^{-1}) of the cloud. The gas where the broadening is was found with

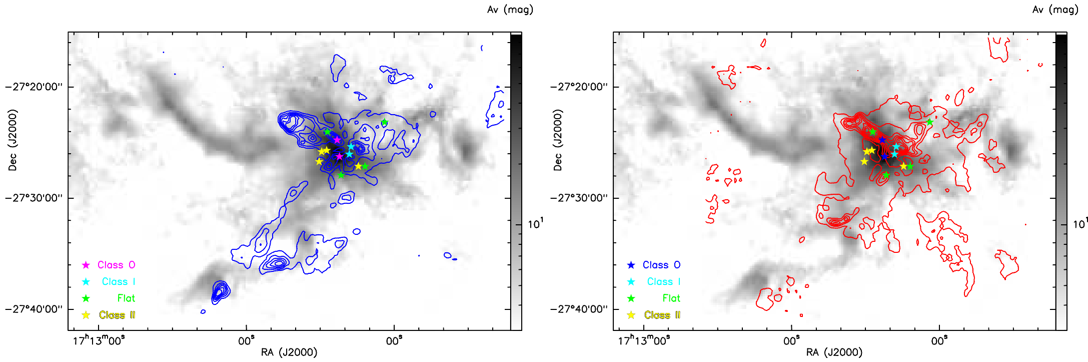

Figure 5.21: Left: ^{12}CO blue emission in blue contours. The emission was integrated from -5 to 2.7 kms^{-1}, and the contours are from 2 to 10 K kms^{-1} by steps of 1.5 K kms^{-1}. Right: ^{12}CO red emission in red contours. The emission was integrated from 4.2 to 15 kms^{-1}, and the contours are from 3 to 20 K kms^{-1} by steps of 2 K kms^{-1}. Both panels are overlayed on the extinction map of B59 as from Fig. 5.2 in gray scale, and with the YSOs positions plotted. The colour change on the Class 0 objects is only for clarity.

the dendrograms as having a high virial parameter, consistent with being an outflow shocked region.

5.5.2 Outflows

These observations of ^{13}CO and ^{12}CO are the first high resolution molecular line mapping of the high velocity gas from the outflows in B59. Even though there were already suspected outflows, this study not only confirms their existence, as it also shows a number of outflows bursting from the central core of B59. ^{13}CO already revealed some of the outflow structure, but it also traces some of the dense material. Therefore, to understand the impact of the outflows on the cloud, and see up to which extent they may or may not be sufficient to disrupt or shape B59, I have studied the complementary data set of ^{12}CO, an excellent tracer of the high velocity gas in molecular clouds (Fig. 5.21).

Figure 5.21 shows the ^{12}CO blue and red emission in B59, where we can see a number of outflows and a couple of shells and knots. For instance, the more compact outflow bursting to the NE of the central region falls in an extinction cavity, and this image shows that is has a blue outflow arc, coincident with another outflow lobe in red, indicating that this flow may be very close to the plane of the sky. The emission from these two lobes seems to trace back to one of the youngest sources in the field. Then, to the SE, we can see a few blue knots, and another red arc, roughly towards the same direction. The blue knots in particular seem to be correlated with spots of outflow impacting the lower velocity/higher density material seen in extinction.

^{12}CO is one of the most abundant species in molecular clouds, but it becomes highly optically thick very quickly. Therefore, only when there are high velocity outflows the wings of ^{12}CO become visible, tracing lower density gas offset from the could's ambient velocity. However, even in these wings, some optical thickening is likely to occur, and to estimate the mass of gas which is contained in the outflows, the optical depth of ^{12}CO has to be corrected for. One way to do so is to compare it with another isotopic emission. Since we are only interested in the wing emission, the isotopologue for comparison has to emit also in such velocities. That is the case of ^{13}CO emission.

Similarly to the ^{13}CO and C^{18}O case, under LTE conditions and assuming similar excitation temperatures for both isotopologues, the optical depth of ^{12}CO can be determined as:

$$\frac{T_{^{12}\mathrm{CO}}}{T_{^{13}\mathrm{CO}}} = \frac{1 - e^{-\tau_{12}}}{1 - e^{-\tau_{13}}} \tag{5.7}$$

for each given velocity. Assuming that ^{13}CO is optically thin in the wings and ^{12}CO is optically thick (Cabrit and Bertout 1990), Eq. 5.7 becomes:

$$\frac{T_{^{12}\mathrm{CO}}}{T_{^{13}\mathrm{CO}}} = \frac{1 - e^{-\tau_{12}}}{\tau_{13}} \tag{5.8}$$

and $\tau_{13} = \tau_{12}/f$, where f is the fractional abundance of ^{12}CO relative to ^{13}CO, taken to be 62 (Langer and Penzias 1993).

Given that I am only interested in the properties of the outflows as a whole and the difficulty of identifying all the outflows separately, I have estimated average properties for the blue and the red emission of ^{12}CO. To attain an estimate of the τ_{12}, I have used the ratio of the integrated intensities over the wings of the two isotopologues, similarly to what I used for τ_{18}. The velocity ranges for each wing were chosen to exclude the cloud's ambient velocity where ^{12}CO is self absorbed. The blue emission includes the emission below 2.7 kms^{-1} and the red emission includes all the emission above 4.2 kms^{-1}.

With the ratio maps of the blue and red emissions between the two isotopologues, in pixels where the ^{13}CO integrated emission was greater than the respective r.m.s. (i.e. 0.1 K kms^{-1}), we see that the ratio ranges between ~2 in the core of B59 and ~46 in some of the outflow lobes. That corresponds to τ_{12} values ranging from ~35 to ~2, respectively. To estimate the column densities for the blue and red emission, I have applied the correction factor of $\tau_{12}/(1 - e^{-\tau_{12}})$ (Curtis et al. 2010b; Cabrit and Bertout 1990) at each pixel. Assuming a kinetic temperature of the outflows of 25 K, a CO abundance with respect to H_2 of 10^{-4} and for a distance of 130 pc, the gas masses can be derived as:

$$M = 1.78 \times 10^{-6} N_{pix} < \int T_{mb} dv > \tag{5.9}$$

where M is the gas mass in $M_{\odot}$ assuming a molecular weight of 2.33, N_{pix} is the number of pixels included in the outflows (i.e. a measure of the area covered), and $< \int T_{mb} dv >$ is the average integrated intensity, after the opacity correction of the T_{mb} at each pixel.

Similarly, I have estimated the average momentum and kinetic energy of the outflows. The momentum, $p_{outflow}$, along the jet axis is defined as,

$$p_{\mathrm{out}} = \int m(v) |v - v_0| dv \tag{5.10}$$

where v_0 is the velocity of the driving source and $m(v)$ the mass corrected for the optical depth as from equation 5.9. The outflow kinetic energy $E_{outflow}$, on the other hand, is defined as:

$$E_{\mathrm{out}} = \frac{1}{2} \int m(v)(v - v_0)^2 dv. \tag{5.11}$$

Observationally, however, it is hard to infer these properties with precision, due to the inclination angle of the outflow jet. A correction of the velocities for the inclination angle (i, defined as 0 if the outflow is along the line of sight) comes as $1/\cos(i)$ for the momentum, and $1/\cos^2(i)$ for the energy. For the outflows in B59, a comparison of the blue and red emission can shed some light on the inclination of the flows. In particular, the main flows (Flow 1, 2 and 3 in Fig 5.22) show both blue and red emission towards the same direction. This points to the possibility of these flows to be very close to the plane of the sky. Therefore, I have estimated the opening angle of the flows and used this value to estimate the angle of each side of the outflow cone relative to the plane of the sky. For the NE lobes (Flow 1) the opening angle is of ~20° and for the SE lobes (Flow 2 and 3) it is closer to ~30°. Therefore, the angle of each of the outflow cone walls with respect to the plane of the sky would range between 10 and 15°, and the inclination angle against the line of sight would range between 75° and 80°.

Table 5.3: Outflow properties

	M	p_{out}	$p_{\text{out}}/\cos(75)$	E_{out}	$E_{\text{out}}/\cos^2(75)$
	($M_\odot$)	($M_\odot$ kms^{-1})	($M_\odot$ kms^{-1})	($M_\odot$ km^{2}s^{-2})	($M_\odot$ km^{2}s^{-2})
Blue	0.59	0.83	3.19	0.81	12.0
Red	0.63	0.55	2.13	0.40	5.98

The results from this study are shown on Table 5.3, where M is the gas mass contained in each of the outflow high velocity lobes, p_{out} is the momentum and E_{out} is the kinetic energy, both shown here without the correction for an inclination angle and also assuming an angle of 75°.

If studying independent flows, it is possible to calculate a momentum flux, which is defined as:

$$F_{\text{out}} = p_{\text{out}}/t_d \tag{5.12}$$

where t_d is the dynamical time of the outflow, defined as $t_d = L/v_{max}$, L being the length of the flow, and v_{max} the maximum velocity of that flow. The momentum flux is often used to distinguish between Class 0 and Class I driving sources (e.g. Bontemps et al. 1996; Curtis et al. 2010b). However, the dynamical time is not very precisely calculated given the variability of the accretion rate, the mass loss of the protostar and the expansion rate of the outflow. Furthermore, inclination plays an important role on the measured L and v_{max}. For instance, for outflows close to the plane of the sky, the L appears at its maximum, whereas the v_{max} is small, overestimating the true t_d of the outflow. However, without accurate inclination angles, such an effect is hard to account

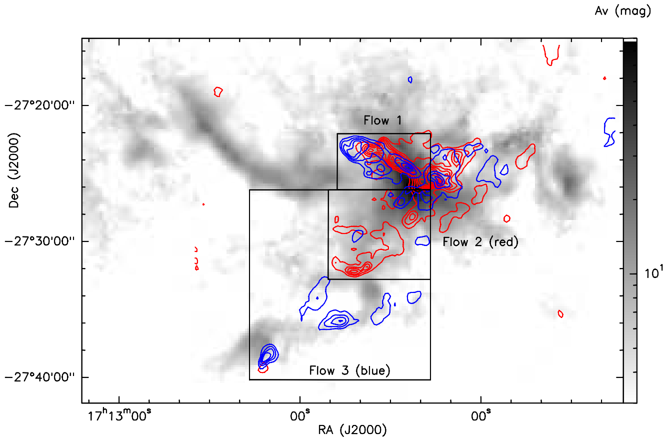

Figure 5.22: ^{12}CO blue and red emission as in Fig 5.21 in blue and red contours respectively, starting at 3 K kms^{-1} with steps of 2 K kms^{-1}, overlayed on the extinction map of B59 as from Fig. 5.2 in gray scale. The boxes show the regions used to calculate the individual outflow properties for the four flows: Flow 1 (blue and red), Flow 2 (red) and Flow 3 (blue).

Table 5.4: Momentum flux of individual outflows

	L (pc)	i degrees	v_{max} (kms^{-1})	$v_{max}/cos(i)$ (kms^{-1})	t_d ($\times 10^3$ yr)	$p_{outflow}/cos(i)$ ($M_\odot$ kms^{-1})	$F_{outflow}$ ($M_\odot$ kms^{-1}yr^{-1})
Flow 1 - Blue	0.19	80	-5.5	-31.7	5.8	1.44	2.5×10^{-4}
Flow 1 - Red	0.11	80	5.0	28.8	3.9	0.97	2.5×10^{-4}
Flow 2 - Red	0.23	75	5.5	21.3	10.4	0.77	7.4×10^{-5}
Flow 3 - Blue	0.45	75	-4.0	15.5	28.7	0.88	3.1×10^{-5}

for.

Nevertheless, I have estimated the momentum flux for the four main flows of B59 (Fig 5.22). The results are shown on Table 5.4, where L is the projected length of the outflow in the plane of the sky, i is the assumed inclination angle of each flow, v_{max} is the maximum velocity with respect to the cloud's ambient velocity of 3.5 kms^{-1}, $v_{max}/\cos(i)$ represents the "true" maximum velocity of the flow, t_d is the dynamical time, $p_{\rm out}/\cos(i)$ is the momentum of the flow corrected by the inclination, and finally, $F_{\rm out}$ is the momentum flux. From here, we can see that the momentum flux of Flow 1 is higher than the momentum flux for Flow 2&3. However, if assuming the same inclination angle for both, though still existent, the difference would be less accentuated. For instance, an inclination angle of 75° for Flow 1 would result in a momentum flux of 1.1×10^{-4} $M_\odot$ kms^{-1}yr^{-1}. The values for momentum flux for the four main outflows in B59 retrieved with this method are consistent with the expected values for Class 0 sources. Flow 2, however, starts to approach those expected for a Class I driving source. When looking at the relation between the outlows and the protostars (Fig. 5.21), we can see that the two main blue outflows are tracing back to the two younger protostars in the region, consistent with the values derived from the momentum flux. However, it is not clear which source is the driving source of the red Flow 2, and it may be that it is not the same as for Flow 3. Interferometry data would be important to disentangle these outflows close to their driving source.

5.5.3 Discussion

The study of the dynamics of B59 has shown that there are no general trends or gradients in the region. In general, the velocities are all around 3.4 kms^{-1} and narrow line widths around 0.5 kms^{-1} (FWHM). All the motions that depart from these values seem to be in close relation to regions where there are outflow bows and shocks. There are a number of cavities close to these shocks and, in particular, the shape of the cloud seems to be affected by these flows.

The impact of the outflows in the cloud can be estimated by comparing the kinetic energy carried out by the outflows and the binding energy of the denser material. The total kinetic energy of the outflows (Sec. 5.5.2) is of $\sim$18 $M_\odot$ km^{2}s^{-2}, when assuming an inclination angle of 75° for the outflows. I have estimated the binding energy (i.e. the potential energy) of the dense material using the $C^{18}O$ masses. For 33 $M_\odot$ and a radius of 0.30 pc (Sec. 5.4.2), and assuming a density profile as $\rho \propto r^{-1.5}$, the gravitational potential energy is 12 $M_\odot$ km^{2}s^{-2}, lower than the kinetic energy from the outflows. The value of the outflow kinetic energy is comparable to the binding energy of the dense material. And even though we have to account for the fact that the kinetic energy of the outflows is being deposited outside the cores, and therefore may not be disrupting the dense cores themselves, the outflows seem to carry enough energy to be responsible for shaping the material around the central region.

5.6 Final Discussion of B59

B59 is a star forming region with a small and young proto-cluster. The known protostars are located only in the central core of B59, and the lower density material that surrounds this central region seems to be suffering from the impact of the outflows from these young sources.

A hierarchical study of the region has shown that the entire cloud is interconnected and mostly gravitationally bound. The only regions which come out as a separate sub-structure are the western cores. The PV diagrams revealed that these cores are separated from the main cloud by a gas cavity. The line broadening after this cavity may indicate that the gas has been pushed through and cleared out by an outflow and that the cores after the cavity are being compressed by this flow.

On the opposite side, in the SE ridge, two flows are seen as blue and red emission in ^{12}CO along the same direction (Flow 2 and 3). Such a coincidence would suggest that the driving source is the same, and that the flow is close to the plane of the sky. However, the spatial extent of these two flows is not the same, and therefore, they might not be part of the same outflow burst. Either they are from two different driving sources or, if driven by the same source, they may represent two different outflow bursts. Furthermore, the coincidence of the outflow knots with the sharp edge seen in the extinction map, in C^{18}O and in ^{13}CO makes it possible that these two outflow bursts are indeed responsible for pushing the gas as they make their way out of the cloud.

The other clear outflow in B59 is the one on a NE direction (Flow 1). The red and blue coincidence in extent and direction show this is most likely a single flow extremely close to the plane of the sky. This outflow in particular seems to be responsible for carving another cavity in the dust and gas. The loops of the flows trace down to the walls of the cone-shaped swept-up material close to the protostars, seen even in the less abundant C^{18}O. The line broadening of C^{18}O in this particular case, seems to indicate that the outflow is interacting closely with the dense material. This is in marked contrast with Serpens, for instance, where no evidence for the outflows is seen on the $C^{18}O$ emission. No clear flow was found on the opposite direction of Flow 1. It may be that there is just not enough material on the opposite direction for it to be detected, or that the flow is embedded in the denser material of the central region, contributing to the line broadening seen there.

The origin of the NE ridge is unclear. This is the structure of B59 which appears to be most gravitationally bound in both ^{13}CO and $C^{18}O$, but with very little substructure. It does appears parallel to Flow 1 and it could represent some material that has also been pushed sideways by the flow, though there is no evidence of shocks throughout this quiescent structure. In fact, Frau et al. (2010) studied a core in this NE ridge, and found it to be chemically young, supporting that this structure may be in the verge of fragmenting, but it is not very evolved.

Finally, there are some knots and blobs found in ^{13}CO to the south and to the northwest of the central region. These could represent the counterparts of the main flows of the region, but since they do not present very large velocities offsets from the systemic velocity, it is not trivial to understand if that is the case.

Overall, B59 has shown to be very different from Serpens. Both velocity, outflow and structure-wise, little is common between these two regions. Perhaps thanks to a very different initial trigger or conditions, B59 seems to be much less dynamic than Serpens, except for the regions where there are major outflows. The fact that the effect of these outflows is seen in the higher density tracer ($C^{18}O$), makes it hard to understand the velocity structure of the underlying gas, which is not under the effect of the outflows. Such an understanding of the underlying gas is essential to reveal the physical properties of the cores from which the stars are being formed. This is one of the aspects of my future work, which I will describe in more detail in Chapter 6.

Part IV

Final remarks

Chapter 6

Future work

6.1 A large study of the Pipe Nebula

6.1.1 B59

The study of the B59 star forming region within the Pipe Nebula (Chapter 5) has shown this region to have a more complex structure than anticipated. Despite the good quality and varied molecular line data that we have, there are some unclear aspects that we are not yet able to answer.

The first goes back to the higher density material. We expected to be able to pick up the emission from the protostellar envelopes with $C^{18}O$, and use that information to derive the physical properties of the cores in B59. Even though this is true for the intermediate density material in B59, in the central region where the protostars are concentrated, the $C^{18}O$ $J=3\rightarrow2$ emission is not straight forward to analyse and interpret, as it seems to be sensitive to the denser material which is being swept up by the outflows. Therefore, this study would benefit from observing lower transitions of $C^{18}O$, to constrain the temperatures and column densities traced by $C^{18}O$, similarly to what I have done with Serpens. Lower transitions of $C^{18}O$ may in fact trace the colder dense gas that was missed by the $J=3\rightarrow2$ transition. In addition, we intent to use an optically thin high density tracer, such as N_2H^+ or NH_3, to map the central region of

B59 and study the dense gas in the envelopes of the protostars. Comparing our current data with the high density gas would allow us to better understand what material is being traced by the $C^{18}O$ J=3→2. Observations of N_2H^+ or NH_3 with high spacial and spectral resolution should also allow a study of the transition to coherence in these B59 cores (e.g. Pineda et al. 2010).

From section 5.5.2, another aspect which is problematic is to distinguish the driving source of each flow, and identification of other possible flows. This is due to the confusion between different outflows close to their driving sources. As such, we aim to observe ^{12}CO emission from the outflows with an interferometer. This would likely reveal the origin of each of the outflows and provide better constrains on inclination angles, orientation, and disrupting power of the flow.

6.1.2 The Pipe Nebula beyond B59

As mentioned in section 5.2.1, the drive to study this region comes from the variety of environments that the Pipe Nebula comprises and its apparent sterility as an ideal place to observe the early conditions for star formation. We have already observed most of the Pipe Nebula in ^{12}CO which will be analysed in the near future, plus some cores in the Stem and the Bowl of the in ^{13}CO and $C^{18}O$, though not as deep as ideal especially given the very weak $C^{18}O$ emission detected there. We expect to be able to finish these observations and bring the noise levels down to the required level and observe a few more cores throughout the Pipe Nebula, as shown in Fig. 5.3 (Chapter 5). The ^{12}CO data and its potential to detect outflows, along with the upcoming SCUBA-2 and Herschel continuum observations in the Pipe Nebula, will then allow us to search for the very youngest sources that could have been missed by Spitzer.

The aim of such a large scale mapping of the Pipe Nebula is to try and understand the physical conditions of these cores along the cloud, and search for evidence of imminent or extremely recent star formation. We know these cores to be young, but we aim to understand if there is something in the Pipe which is responsible for inhibiting

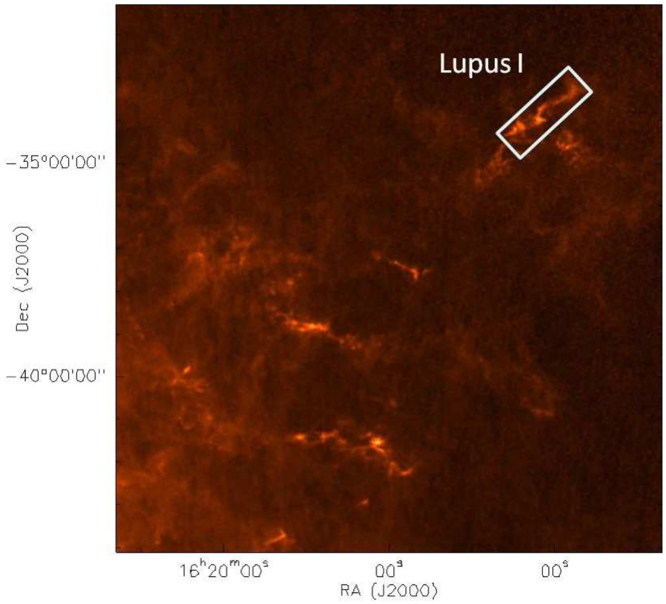

Figure 6.1: Extinction map of the Lupus complex in colour scale, courtesy of Sylvain Bontemps. The Lupus I cloud is shown with the white box and label.

star formation, if the bulk of the Pipe is deemed to remain dormant until an external event changes the conditions in the cores, or if these cores are already on their way to fragment and form new stars. The properties and physical conditions of these cores and their comparison to the B59 star forming region may give us an insight into these questions. Furthermore, our large-scale mapping of the Pipe, being the highest resolution molecular mapping of this region, may help us understand the origin of the filamentary structure of the Pipe. Either by infalling material along magnetic field lines or due to convergent flows, the high spatial and spectral resolution should provide velocity information which will be able to contribute to our knowledge of how the Pipe has/is being assembled.

6.2 Lupus I star forming region

Lupus I is a filamentary molecular cloud - the most massive of the Lupus complex (Fig. 6.1), with a mass of ~250 $M_\odot$. At 150 pc from the Sun (Lombardi et al. 2008), it extends for about 2° (5 pc), parallel to the edge of the Upper-Sco HI shell. Some studies of this region have been made, including a deep Herbig-Haro (HH) object search (Wang and Henning 2009), Spitzer observations (Chapman et al. 2007; Merín et al. 2008) and observations of some molecular lines such as $H^{13}CO^+$ and CO isotopes including ^{12}CO, ^{13}CO, $C^{18}O$ (e.g. Hara et al. 1999; Vilas-Boas et al. 2000; Tothill et al. 2009). Given the low resolution (1.7' or greater) of the molecular line mapping of Lupus I done so far, the velocity distribution is yet poorly understood as the filament presents both smooth and steep velocity gradients (e.g. Tothill et al. 2009). The region has a sharp delineated structure east of the filament, toward the centre of the HI shell, whereas the west of the ridge seems to be more extended (e.g. Tothill et al. 2009). Therefore, a direct influence from the HI shell on the star formation in Lupus I is suspected.

Lupus I currently has a moderate level of star formation activity. The YSOs detected in Lupus I by Spitzer observations (Merín et al. 2008) show a high abundance of Class I and flat sources relative to the Class II and III sources when compared with the other Lupus clouds. This suggests that Lupus I is the youngest star forming region in the complex. The existence of several HH objects in Lupus I, indicates the existence of very young protostars powering further outflows, both yet unseen with the existing observations. The apparent youth of the cloud is an advantage when trying to study the effect or remnants of external triggers on its current episode star formation and it may help answering the question of how a cloud starts the process of collapsing into clumps and cores. The future high resolution observations of Lupus I as part of submillimetre continuum surveys (with SCUBA2 and Herschel) will be able to detect the very young Class 0 sources directly and probe the low-mass end of the Core Mass Function (CMF).

In this context, in May 2010, we used the Mopra 22m telescope to map the Lupus I filament at millimeter wavelengths, providing higher spatial resolution than previous observations of the region. These high resolution observations will be important for future reference and comparison of the gas and the dust emission in this young cluster. They will also allow a study of the physical properties and kinematics of the region,

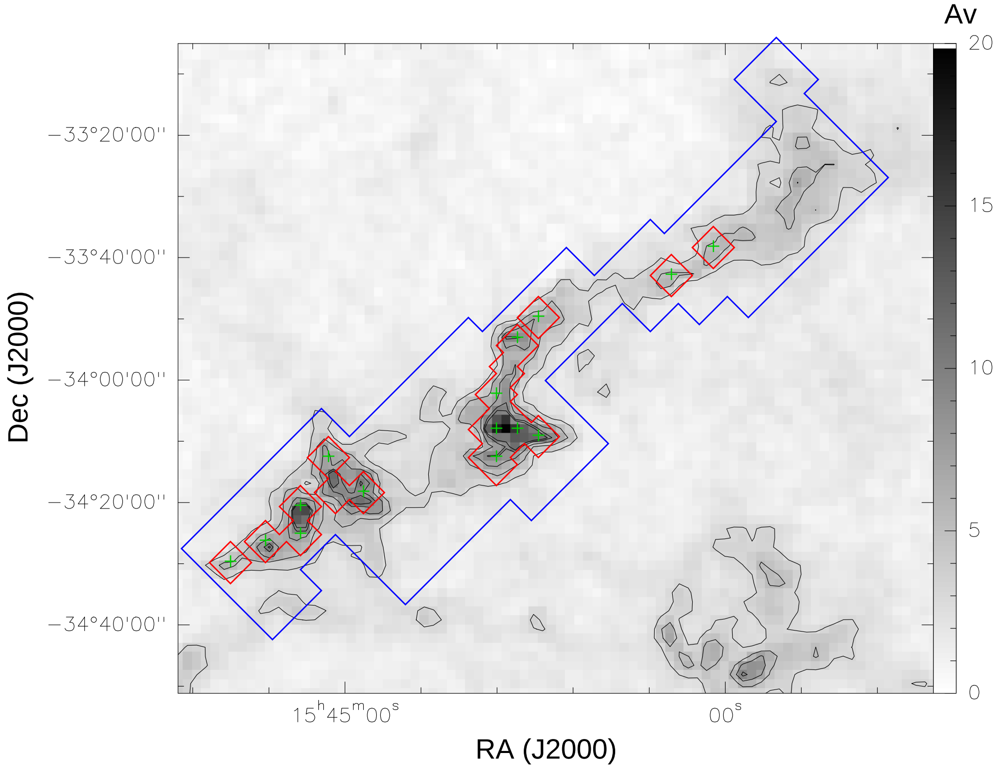

Figure 6.2: Extinction map, same as in Fig. 6.1, zoomed in Lupus I (grey scale and contours), with the areas mapped shown in blue (for the shallow mapping) and in red (for the deep mapping). The green crosses are the regions where we have taken the spectra of high density tracers.

which may help understand if the molecular gas on the sharp edge of ridge is being compressed - resulting on the broadening of the line widths and increased excitation temperatures.

We have mapped the entire Lupus I filament (2308 arcmin^2) with ^{12}CO J=1→0, ^{13}CO J=1→0 and C^{18}O J=1→0 transitions, in a shallow survey with an r.m.s. of 0.5 K in T_A^*, at a spectral resolution of 0.09 kms^{-1} (Fig. 6.2, blue areas). We then increased the sensitivity in the main regions of emission (567 arcmin^2), to a r.m.s. noise level of 0.35 K in T_A^* (Fig. 6.2, red areas). The ^{12}CO data in particular will be used to detect the higher velocity gas from the outflows. The ^{13}CO and C^{18}O data (Fig. 6.3) will be used to access the global dynamics of the cloud and search for signatures of the original trigger of star formation in Lupus I, if still imprinted in the gas. Furthermore, they will

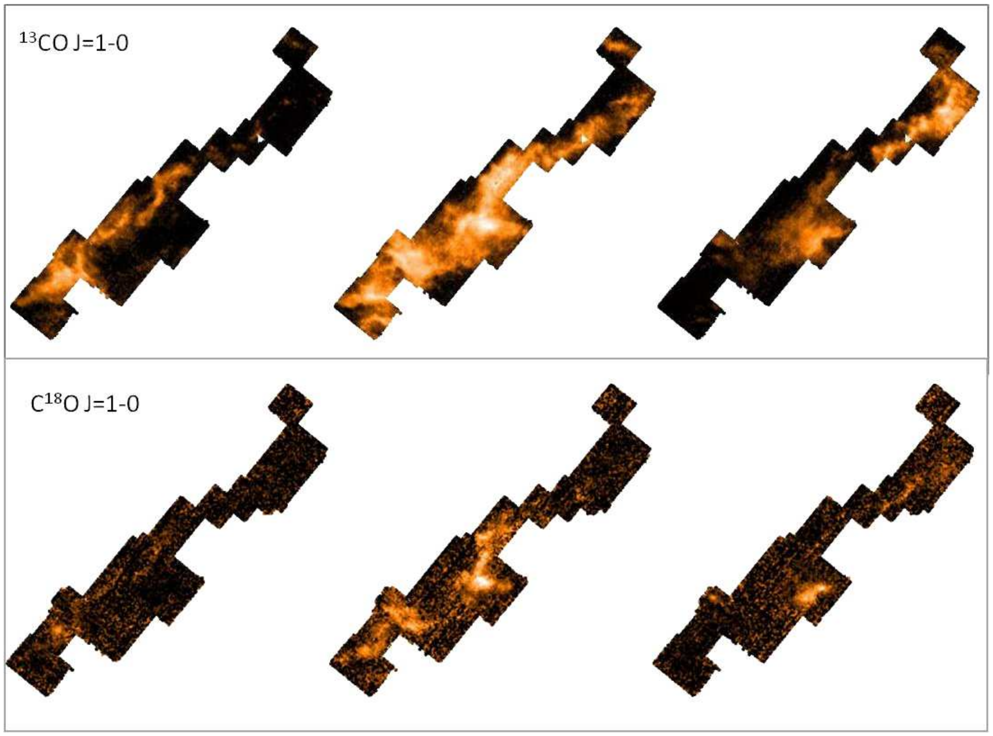

Figure 6.3: Channel maps of the ^{13}CO and C^{18}O J=1→0 emission in Lupus I (top and bottom panels, respectively), from 3 kms^{-1} to 6 kms^{-1}. These are from a preliminary data reduction using Livedata/Gridzilla during the observing run at CSRIO ATNF. Each map includes the shallow and deep mapping mosaicked together using the starlink software.

provide measures of the physical conditions in the different parts of the cloud, which will be important in comparing with other star forming regions (such as Serpens and B59).

To assess the infall rates on the densest cores in the cloud we also took pointed spectra of several both optically thin and optically thick high density tracers (e.g. N_2H^+, HCN, HNC and HCO$^+$, and their rarer ^{13}C isotopes), towards several C^{18}O peaks selected during the observations (Fig. 6.2, green crosses). The presence of infall will be indicated by the detection blue asymmetric line profiles (Zhou 1992) which will be used to determine the infall velocity and hence, mass accretion rate (e.g. Myers et al. 1996). The dense tracers will also be used to search for evidence of chemical evolution between different cores in the region.

Chapter 7

Conclusions

Our knowledge of how star formation occurs has been improving over the years, but there are still aspects of the process which are not yet clear. The very formation of the molecular clouds and origin of their filamentary shapes, the physical processes which prevent or trigger star formation in a given cloud, and also the evolution from the cores in the cloud to the final stars which are formed, are some of the subjects of debate on the past years.

By studying the earliest stages of star formation, my thesis work contributes to our understanding of the initial conditions and triggers of the formation of stars. With the current ability to pursue big surveys with high sensitivity and high angular resolution of star forming regions, both in continuum and molecular lines, it is in the large scale phenomena that I have been most interested in, to understand the structure and physical conditions of the gas embedding young protoclusters.

I have started by studying a well known young and active star forming region in the Gould Belt, the Serpens star forming region. My study of this region using CO isotopologues observed with IRAM 30m has revealed an interesting velocity structure, which had not yet been studied in detail mainly due to the lack of angular resolution to do so. Its complex structure is due to two clouds in the line of sight that seem to merge along the filamentary structure of one of the sub-clusters of Serpens. Combining the IRAM 30m data with JCMT Gould Belt Survey data, I have used the three lower transitions of $C^{18}O$ to study the physical properties of the gas in this region. The temperature of the gas has then shown to be correlated with the velocity structure, in such a way that we suspected those properties to trace back to the trigger of the star formation in Serpens. Putting all the pieces together allowed us to construct a scenario where the two velocity components are from two different clouds that are merging, and that their merger is responsible for a temperature rise and the star formation in the southern part of the region. This scenario has been tested using several SPH models which investigated if the velocity structure that we detect in Serpens could arise from such a collision of two clouds or flows. These tests have shown that for the Serpens observed velocity and filamentary structure to be well reproduced, the geometry of the collision is very important. These models also suggest that the differences between the two sub-clusters of Serpens can be explained if one of them is under the direct influence of a such a triggering event, whereas the other is only marginally affected.

A second part of my thesis is part of an on-going project on the Pipe Nebula. Starting with the only active star forming region in the cloud, B59, I have started to study the structure and dynamics of the gas using CO isotopologues observed with HARP at JCMT. One of the motivations for observing B59 was to provide the link between the starless cores in the remaining Pipe Nebula, and other active star forming regions. However, this study has shown that B59 is very different from Serpens, in several aspects. Firstly, there is emission from $C^{18}O$ in parts of the cloud with no known embedded protostars. Secondly, where there are embedded protostars, the emission from $C^{18}O$ is much broader and seems to be affected by the outflows in the densest material surrounding the protostars. In fact, all the emission in $C^{18}O$ is tracing reliably the dust extinction map, and the shape of this material seems to be correlated with the outflow knots and shells seen in ^{12}CO and ^{13}CO. This is in contrast with Serpens where, even though it is a young region with a greater number of protostars and outflows, the dust continuum emission and the $C^{18}O$ emission were not tracing the outflows at all. For some reason, while the emission from Serpens is showing evidence for its possible triggering event, the emission in B59 is dominated by the effect of outflows in the material. Further observations, however, are required to disentangle the true impact of the outflows in the material, both by observing tracers of the high density material, and by observing the outflows with interferometers to minimise the confusion problem.

The unfinished work on the Pipe, which involves also looking at several other extinction cores in the cloud, will help understanding the conditions in these cores and understand their evolutionary stage, providing an overall picture of what is behind the star formation - or absence of it - in the Pipe Nebula. The other region I will be studying in the future, Lupus I, is again different from both Serpens and the Pipe. Lupus I is undergoing star formation and an external trigger - a shock originating from a nearby OB association - may have been at the origin of its activity, and also responsible for its delineated and sharp-edged structure. Our molecular line observations will provide high angular and spectral resolution to study the kinematics and physical properties or the cloud, and hopefully understand if the cloud is indeed being swept up by a shock.

In our current view on star formation, the studies that I have conducted have mostly shown that each region may have a very different story of how it started forming stars. The study of the gas is essential to understand the lines which tell each story, but it is very hard to find the common points to different star forming regions. The idea of converging flows as mechanisms to form molecular clouds and trigger star formation may be the case for Serpens, but there is no evidence for it in the emission from B59. It may be that the Pipe Nebula is the other extreme case where star formation is regulated by magnetic fields and ambipolar diffusion, and B59 is the only portion of the cloud where gravity has taken over. As such, the only dynamical effect in B59 lies in the protostellar outflows. For a region which is not incredibly dense with the exception of its central core, these outflows assume a great role as they possess enough power to shape the material around it, and perhaps then trigger other episodes of star formation.

References

F. O. Alves, G. A. P. Franco, and J. M. Girart. Optical polarimetry toward the Pipe nebula: revealing the importance of the magnetic field. *A&A*, 486:L13–L16, August 2008. doi: 10.1051/0004-6361:200810091.

J. Alves, M. Lombardi, and C. J. Lada. The mass function of dense molecular cores and the origin of the IMF. *A&A*, 462:L17–L21, January 2007. doi: 10.1051/0004-6361:20066389.

S. Anathpindika. Supersonic cloud collision. I. *A&A*, 504:437–450, September 2009a. doi: 10.1051/0004-6361/200911748.

S. Anathpindika. Supersonic cloud collision - II. *A&A*, 504:451–460, September 2009b. doi: 10.1051/0004-6361/200911762.

P. André. Nearby Protoclusters as Laboratories for Understanding Star Formation on Galactic Scales. *Ap&SS*, 281:51–66, July 2002. doi: 10.1023/A:1019599328220.

P. André, D. Ward-Thompson, and M. Barsony. Submillimeter continuum observations of Rho Ophiuchi A - The candidate protostar VLA 1623 and prestellar clumps. *ApJ*, 406:122–141, March 1993. doi: 10.1086/172425.

P. Andre, D. Ward-Thompson, and M. Barsony. From Prestellar Cores to Protostars: the Initial Conditions of Star Formation. *Protostars and Planets IV*, pages 59–+, May 2000.

H. G. Arce and A. I. Sargent. The Evolution of Outflow-Envelope Interactions in Low-Mass Protostars. *ApJ*, 646:1070–1085, August 2006. doi: 10.1086/505104.

H. G. Arce, D. Shepherd, F. Gueth, C.-F. Lee, R. Bachiller, A. Rosen, and H. Beuther. Molecular Outflows in Low- and High-Mass Star-forming Regions. *Protostars and Planets V*, pages 245–260, 2007.

J. Ballesteros-Paredes. Six myths on the virial theorem for interstellar clouds. *MNRAS*, 372:443–449, October 2006. doi: 10.1111/j.1365-2966.2006.10880.x.

J. Ballesteros-Paredes and L. Hartmann. Remarks on Rapid vs. Slow Star Formation. *Revista Mexicana de Astronomia y Astrofisica*, 43:123–136, April 2007.

J. Ballesteros-Paredes, L. Hartmann, and E. Vázquez-Semadeni. Turbulent Flow-driven Molecular Cloud Formation: A Solution to the Post-T Tauri Problem? *ApJ*, 527:285–297, December 1999a. doi: 10.1086/308076.

J. Ballesteros-Paredes, E. Vázquez-Semadeni, and J. Scalo. Clouds as Turbulent Density Fluctuations: Implications for Pressure Confinement and Spectral Line Data Interpretation. *ApJ*, 515:286–303, April 1999b. doi: 10.1086/307007.

J. A. Barranco and A. A. Goodman. Coherent Dense Cores. I. NH 3 Observations. *ApJ*, 504:207–+, September 1998. doi: 10.1086/306044.

P. Bastien. Gravitational collapse and fragmentation of isothermal, non-rotating, cylindrical clouds. *A&A*, 119:109–116, March 1983.

M. Bate. PhD thesis, PhD thesis, Univ. Cambridge, (1995), 1995.

M. R. Bate. Collapse of a Molecular Cloud Core to Stellar Densities: The First Three-dimensional Calculations. *ApJL*, 508:L95–L98, November 1998. doi: 10.1086/311719.

M. R. Bate. Stellar, brown dwarf and multiple star properties from hydrodynamical simulations of star cluster formation. *MNRAS*, 392:590–616, January 2009a. doi: 10.1111/j.1365-2966.2008.14106.x.

M. R. Bate. The importance of radiative feedback for the stellar initial mass function. *MNRAS*, 392:1363–1380, February 2009b. doi: 10.1111/j.1365-2966.2008.14165.x.

M. R. Bate, I. A. Bonnell, and V. Bromm. The formation mechanism of brown dwarfs. *MNRAS*, 332:L65–L68, May 2002. doi: 10.1046/j.1365-8711.2002.05539.x.

M. R. Bate, I. A. Bonnell, and V. Bromm. The formation of a star cluster: predicting the properties of stars and brown dwarfs. *MNRAS*, 339:577–599, March 2003. doi: 10.1046/j.1365-8711.2003.06210.x.

W. Benz, A. G. W. Cameron, W. H. Press, and R. L. Bowers. Dynamic mass exchange in doubly degenerate binaries. I - 0.9 and 1.2 solar mass stars. *ApJ*, 348:647–667, January 1990. doi: 10.1086/168273.

E. A. Bergin and M. Tafalla. Cold Dark Clouds: The Initial Conditions for Star Formation. *ARA&A*, 45:339–396, September 2007. doi: 10.1146/annurev.astro.45.071206.100404.

L. Blitz. Star Forming Giant Molecular Clouds. In C. J. Lada and N. D. Kylafis, editors, *NATO ASIC Proc. 342: The Physics of Star Formation and Early Stellar Evolution*, pages 3–+, 1991.

L. Blitz. Giant molecular clouds. In E. H. Levy & J. I. Lunine, editor, *Protostars and Planets III*, pages 125–161, 1993.

R. C. Bohlin, B. D. Savage, and J. F. Drake. A survey of interstellar H I from L-alpha absorption measurements. II. *ApJ*, 224:132–142, August 1978. doi: 10.1086/156357.

I. A. Bonnell, M. R. Bate, C. J. Clarke, and J. E. Pringle. Accretion and the stellar mass spectrum in small clusters. *MNRAS*, 285:201–208, February 1997.

I. A. Bonnell, C. J. Clarke, M. R. Bate, and J. E. Pringle. Accretion in stellar clusters and the initial mass function. *MNRAS*, 324:573–579, June 2001. doi: 10.1046/j.1365-8711.2001.04311.x.

S. Bontemps, P. Andre, S. Terebey, and S. Cabrit. Evolution of outflow activity around low-mass embedded young stellar objects. *A&A*, 311:858–872, July 1996.

T. Y. Brooke, T. L. Huard, T. L. Bourke, A. C. A. Boogert, L. E. Allen, G. A. Blake, N. J. Evans, II, P. M. Harvey, D. W. Koerner, L. G. Mundy, P. C. Myers, D. L. Padgett, A. I. Sargent, K. R. Stapelfeldt, E. F. van Dishoeck, N. Chapman, L. Cieza, M. M. Dunham, S.-P. Lai, A. Porras, W. Spiesman, P. J. Teuben, C. H. Young, Z. Wahhaj, and C. W. Lee. The Spitzer c2d Survey of Nearby Dense Cores. IV. Revealing the Embedded Cluster in B59. *ApJ*, 655:364–374, January 2007. doi: 10.1086/510115.

S. Cabrit and C. Bertout. CO line formation in bipolar flows. II - Decelerated outflow case and summary of results. *ApJ*, 348:530–541, January 1990. doi: 10.1086/168261.

L. Cambrésy. Mapping of the extinction in giant molecular clouds using optical star counts. *A&A*, 345:965–976, May 1999.

G. Chabrier. Galactic Stellar and Substellar Initial Mass Function. *PASP*, 115:763–795, July 2003. doi: 10.1086/376392.

G. Chabrier. The Initial Mass Function: from Salpeter 1955 to 2005. In E. Corbelli, F. Palla, & H. Zinnecker, editor, *The Initial Mass Function 50 Years Later*, volume 327 of *Astrophysics and Space Science Library*, pages 41–+, January 2005.

N. L. Chapman, S.-P. Lai, L. G. Mundy, N. J. Evans, II, T. Y. Brooke, L. A. Cieza, W. J. Spiesman, L. M. Rebull, K. R. Stapelfeldt, A. Noriega-Crespo, L. Lanz, L. E.

Allen, G. A. Blake, T. L. Bourke, P. M. Harvey, T. L. Huard, J. K. Jørgensen, D. W. Koerner, P. C. Myers, D. L. Padgett, A. I. Sargent, P. Teuben, E. F. van Dishoeck, Z. Wahhaj, and K. E. Young. The Spitzer c2d Survey of Large, Nearby, Interstellar Clouds. IV. Lupus Observed with MIPS. *ApJ*, 667:288–302, September 2007. doi: 10.1086/520790.

P. C. Clark and I. A. Bonnell. The onset of collapse in turbulently supported molecular clouds. *MNRAS*, 361:2–16, July 2005. doi: 10.1111/j.1365-2966.2005.09105.x.

R. Clausius. *De la fonction potentielle DU Potentiel*. 1870.

C. Combet, T. Lery, and G. C. Murphy. Transit Flow Models for Low- and High-Mass Protostars. *ApJ*, 637:798–810, February 2006. doi: 10.1086/498612.

K. R. Covey, C. J. Lada, C. Román-Zúñiga, A. A. Muench, J. Forbrich, and J. Ascenso. The Age, Stellar Content, and Star Formation Timescale of the B59 Dense Core. *ApJ*, 722:971–988, October 2010. doi: 10.1088/0004-637X/722/2/971.

A. Cunningham, A. Frank, and L. Hartmann. Wide-Angle Wind-driven Bipolar Outflows: High-Resolution Models with Application to Source I of the Becklin-Neugebauer/Kleinmann-Low OMC-I Region. *ApJ*, 631:1010–1021, October 2005. doi: 10.1086/432658.

E. I. Curtis, J. S. Richer, and J. V. Buckle. A submillimetre survey of the kinematics of the Perseus molecular cloud - I. Data. *MNRAS*, 401:455–472, January 2010a. doi: 10.1111/j.1365-2966.2009.15658.x.

E. I. Curtis, J. S. Richer, J. J. Swift, and J. P. Williams. A submillimetre survey of the kinematics of the Perseus molecular cloud - II. Molecular outflows. *MNRAS*, 408: 1516–1539, November 2010b. doi: 10.1111/j.1365-2966.2010.17214.x.

J. E. Dale, I. A. Bonnell, and A. P. Whitworth. Ionization-induced star formation - I. The collect-and-collapse model. *MNRAS*, 375:1291–1298, March 2007. doi: 10.1111/j.1365-2966.2006.11368.x.

C. J. Davis, H. E. Matthews, T. P. Ray, W. R. F. Dent, and J. S. Richer. A burst of outflows from the Serpens cloud core: wide-field submillimetre continuum, CO J=2-1 and optical observations. *MNRAS*, 309:141–152, October 1999.

C. J. Davis, A. Chrysostomou, H. E. Matthews, T. Jenness, and T. P. Ray. Submillimeter Polarimetry of the Protostellar Outflow Sources in Serpens with the Submillimeter Common-User Bolometer Array. *ApJL*, 530:L115–L118, February 2000. doi: 10.1086/312493.

J. Di Francesco, D. Johnstone, H. Kirk, T. MacKenzie, and E. Ledwosinska. The SCUBA Legacy Catalogues: Submillimeter-Continuum Objects Detected by SCUBA. *ApJS*, 175:277–295, March 2008. doi: 10.1086/523645.

C. L. Dobbs. GMC formation by agglomeration and self gravity. *MNRAS*, 391:844–858, December 2008. doi: 10.1111/j.1365-2966.2008.13939.x.

C. L. Dobbs, I. A. Bonnell, and J. E. Pringle. The formation of molecular clouds in spiral galaxies. *MNRAS*, 371:1663–1674, October 2006. doi: 10.1111/j.1365-2966.2006.10794.x.

A. Duarte-Cabral, G. A. Fuller, N. Peretto, J. Hatchell, E. F. Ladd, J. Buckle, J. Richer, and S. F. Graves. The physical and dynamical structure of Serpens. Two very different sub-(proto)clusters. *A&A*, 519:A27+, September 2010. doi: 10.1051/0004-6361/200913919.

A. Duarte-Cabral, C. L. Dobbs, N. Peretto, and G. A. Fuller. Was a cloud-cloud collision the trigger of the recent star formation in Serpens? *ArXiv e-prints*, January 2011.

J. Dubinski, R. Narayan, and T. G. Phillips. Turbulence in Molecular Clouds. *ApJ*, 448:226–+, July 1995. doi: 10.1086/175954.

C. Eiroa, J. M. Torrelles, J. F. Gomez, S. Sakamoto, T. Hasegawa, R. Kawabe, M. Hayashi, and M. M. Casali. Molecular outflows in the Serpens cloud core? - FIRS 1 and SVS 4. *PASJ*, 44:155–158, April 1992.

B. G. Elmegreen. The Stellar Initial Mass Function from Random Sampling in Hierarchical Clouds. II. Statistical Fluctuations and a Mass Dependence for Starbirth Positions and Times. *ApJ*, 515:323–336, April 1999. doi: 10.1086/307011.

B. G. Elmegreen and C. J. Lada. Sequential formation of subgroups in OB associations. *ApJ*, 214:725–741, June 1977. doi: 10.1086/155302.

M. L. Enoch, J. Glenn, N. J. Evans, II, A. I. Sargent, K. E. Young, and T. L. Huard. Comparing Star Formation on Large Scales in the c2d Legacy Clouds: Bolocam 1.1 mm Dust Continuum Surveys of Serpens, Perseus, and Ophiuchus. *ApJ*, 666:982–1001, September 2007. doi: 10.1086/520321.

J. Forbrich, C. J. Lada, A. A. Muench, J. Alves, and M. Lombardi. A Spitzer Census of Star Formation Activity in the Pipe Nebula. *ApJ*, 704:292–305, October 2009. doi: 10.1088/0004-637X/704/1/292.

J. Forbrich, B. Posselt, K. R. Covey, and C. J. Lada. Nothing to Hide: An X-ray Survey for Young Stellar Objects in the Pipe Nebula. *ApJ*, 719:691–699, August 2010. doi: 10.1088/0004-637X/719/1/691.

P. Frau, J. M. Girart, M. T. Beltrán, O. Morata, J. M. Masqué, G. Busquet, F. O. Alves, Á. Sánchez-Monge, R. Estalella, and G. A. P. Franco. Young Starless Cores Embedded in the Magnetically Dominated Pipe Nebula. *ApJ*, 723:1665–1677, November 2010. doi: 10.1088/0004-637X/723/2/1665.

M. A. Frerking, W. D. Langer, and R. W. Wilson. The relationship between carbon monoxide abundance and visual extinction in interstellar clouds. *ApJ*, 262:590–605, November 1982. doi: 10.1086/160451.

G. A. Fuller and E. F. Ladd. The Evolution of the Circumstellar Environment of Embedded Young Stars from Observations of Rare Species of Carbon Monoxide. *ApJ*, 573:699–719, July 2002. doi: 10.1086/340753.

G. A. Fuller and P. C. Myers. Thermal Material in Dense Cores: A New Narrow-Line Probe and Technique of Temperature Determination. *ApJ*, 418:273–+, November 1993. doi: 10.1086/173389.

R. Galván-Madrid, E. Vázquez-Semadeni, J. Kim, and J. Ballesteros-Paredes. Statistics of Core Lifetimes in Numerical Simulations of Turbulent, Magnetically Supercritical Molecular Clouds. *ApJ*, 670:480–488, November 2007. doi: 10.1086/522081.

Y. Gao and Y.-Q. Lou. Global collapses and expansions in star-forming clouds. *MNRAS*, 403:1919–1929, April 2010. doi: 10.1111/j.1365-2966.2009.15651.x.

A. Gazol, E. Vázquez-Semadeni, and J. Kim. The Pressure Distribution in Thermally Bistable Turbulent Flows. *ApJ*, 630:911–924, September 2005. doi: 10.1086/430817.

C. Gerardo Román-Zúñiga, J. F. Alves, C. J. Lada, and M. Lombardi. Deep Near-Infrared Survey of the Pipe Nebula II: Data, Methods, and Dust Extinction Maps. *ArXiv e-prints*, November 2010.

D. M. Gittins, C. J. Clarke, and M. R. Bate. Hydrodynamical simulations of a cloud of interacting gas fragments. *MNRAS*, 340:841–850, April 2003. doi: 10.1046/j.1365-8711.2003.06339.x.

S. C. O. Glover and M.-M. Mac Low. Simulating the Formation of Molecular Clouds. I. Slow Formation by Gravitational Collapse from Static Initial Conditions. *ApJS*, 169:239–268, April 2007. doi: 10.1086/512238.

P. Goldreich and J. Kwan. Molecular Clouds. *ApJ*, 189:441–454, May 1974. doi: 10.1086/152821.

P. F. Goldsmith and W. D. Langer. Population Diagram Analysis of Molecular Line Emission. *ApJ*, 517:209–225, May 1999. doi: 10.1086/307195.

P. F. Goldsmith, M. Heyer, G. Narayanan, R. Snell, D. Li, and C. Brunt. Large-Scale Structure of the Molecular Gas in Taurus Revealed by High Linear Dynamic Range Spectral Line Mapping. *ApJ*, 680:428–445, June 2008. doi: 10.1086/587166.

S. F. Graves, J. S. Richer, J. V. Buckle, A. Duarte-Cabral, G. A. Fuller, M. R. Hogerheijde, J. E. Owen, C. Brunt, H. M. Butner, B. Cavanagh, A. Chrysostomou, E. I. Curtis, C. J. Davis, M. Etxaluze, J. D. Francesco, P. Friberg, R. K. Friesen, J. S. Greaves, J. Hatchell, D. Johnstone, B. Matthews, H. Matthews, C. D. Matzner, D. Nutter, J. M. C. Rawlings, J. F. Roberts, S. Sadavoy, R. J. Simpson, N. F. H. Tothill, Y. G. Tsamis, S. Viti, D. Ward-Thompson, G. J. White, J. G. A. Wouterloot, and J. Yates. The JCMT Legacy Survey of the Gould Belt: a first look at Serpens with HARP. *MNRAS*, 409:1412–1428, December 2010. doi: 10.1111/j.1365-2966.2010.17140.x.

M. Gritschneder, T. Naab, S. Walch, A. Burkert, and F. Heitsch. Driving Turbulence and Triggering Star Formation by Ionizing Radiation. *ApJL*, 694:L26–L30, March 2009. doi: 10.1088/0004-637X/694/1/L26.

F. Gueth and S. Guilloteau. The jet-driven molecular outflow of HH 211. *A&A*, 343: 571–584, March 1999.

A. Hara, K. Tachihara, A. Mizuno, T. Onishi, A. Kawamura, A. Obayashi, and Y. Fukui. A Study of Dense Cloud Cores and Star Formation in Lupus: $C^{18}O$ J = 1-0 Observations with NANTEN. *PASJ*, 51:895–910, December 1999.

L. Hartmann. *Accretion Processes in Star Formation*. January 2001.

L. Hartmann, J. Ballesteros-Paredes, and E. A. Bergin. Rapid Formation of Molecular Clouds and Stars in the Solar Neighborhood. *ApJ*, 562:852–868, December 2001. doi: 10.1086/323863.

P. Harvey, B. Merín, T. L. Huard, L. M. Rebull, N. Chapman, N. J. Evans, II, and P. C. Myers. The Spitzer c2d Survey of Large, Nearby, Interstellar Clouds. IX. The Serpens YSO Population as Observed with IRAC and MIPS. *ApJ*, 663:1149–1173, July 2007a. doi: 10.1086/518646.

P. M. Harvey, N. Chapman, S.-P. Lai, N. J. Evans, II, L. E. Allen, J. K. Jørgensen, L. G. Mundy, T. L. Huard, A. Porras, L. Cieza, P. C. Myers, B. Merín, E. F. van

Dishoeck, K. E. Young, W. Spiesman, G. A. Blake, D. W. Koerner, D. L. Padgett, A. I. Sargent, and K. R. Stapelfeldt. The Spitzer c2d Survey of Large, Nearby, Insterstellar Clouds. II. Serpens Observed with IRAC. *ApJ*, 644:307–325, June 2006. doi: 10.1086/503520.

P. M. Harvey, L. M. Rebull, T. Brooke, W. J. Spiesman, N. Chapman, T. L. Huard, N. J. Evans, II, L. Cieza, S.-P. Lai, L. E. Allen, L. G. Mundy, D. L. Padgett, A. I. Sargent, K. R. Stapelfeldt, P. C. Myers, E. F. van Dishoeck, G. A. Blake, and D. W. Koerner. The Spitzer c2d Survey of Large, Nearby, Interstellar Clouds. VIII. Serpens Observed with MIPS. *ApJ*, 663:1139–1148, July 2007b. doi: 10.1086/518647.

J. Hatchell and G. A. Fuller. Star formation in Perseus. IV. Mass-dependent evolution of dense cores. *A&A*, 482:855–863, May 2008. doi: 10.1051/0004-6361:20079213.

C. Heiles and R. Crutcher. Magnetic Fields in Diffuse HI and Molecular Clouds. In R. Wielebinski and R. Beck, editors, *Cosmic Magnetic Fields*, volume 664 of *Lecture Notes in Physics, Berlin Springer Verlag*, pages 137–+, 2005.

C. Heiles and T. Robishaw. Zeeman splitting in the diffuse interstellar medium-The Milky Way and beyond. In *IAU Symposium*, volume 259 of *IAU Symposium*, pages 579–590, April 2009. doi: 10.1017/S174392130903141X.

F. Heitsch and L. Hartmann. Rapid Molecular Cloud and Star Formation: Mechanisms and Movies. *ApJ*, 689:290–301, December 2008. doi: 10.1086/592491.

F. Heitsch, L. W. Hartmann, A. D. Slyz, J. E. G. Devriendt, and A. Burkert. Cooling, Gravity, and Geometry: Flow-driven Massive Core Formation. *ApJ*, 674:316–328, February 2008. doi: 10.1086/523697.

F. Heitsch, J. Ballesteros-Paredes, and L. Hartmann. Gravitational Collapse and Filament Formation: Comparison with the Pipe Nebula. *ApJ*, 704:1735–1742, October 2009. doi: 10.1088/0004-637X/704/2/1735.

P. Hennebelle and G. Chabrier. Analytical Theory for the Initial Mass Function: CO Clumps and Prestellar Cores. *ApJ*, 684:395–410, September 2008. doi: 10.1086/589916.

P. Hennebelle, R. Banerjee, E. Vázquez-Semadeni, R. S. Klessen, and E. Audit. From the warm magnetized atomic medium to molecular clouds. *A&A*, 486:L43–L46, August 2008. doi: 10.1051/0004-6361:200810165.

K. W. Hodapp. Proper Motions of H_2 Jets and Variability of Young Stars in the Serpens NW Region. *AJ*, 118:1338–1346, September 1999. doi: 10.1086/301003.

M. R. Hogerheijde, E. F. van Dishoeck, G. A. Blake, and H. J. van Langevelde. Tracing the Envelopes around Embedded Low-Mass Young Stellar Objects with HCO + and Millimeter-Continuum Observations. *ApJ*, 489:293–+, November 1997. doi: 10.1086/304755.

M. R. Hogerheijde, E. F. van Dishoeck, G. A. Blake, and H. J. van Langevelde. Envelope Structure on 700 AU Scales and the Molecular Outflows of Low-Mass Young Stellar Objects. *ApJ*, 502:315–+, July 1998. doi: 10.1086/305885.

M. R. Hogerheijde, E. F. van Dishoeck, J. M. Salverda, and G. A. Blake. Envelope Structure of Deeply Embedded Young Stellar Objects in the Serpens Molecular Cloud. *ApJ*, 513:350–369, March 1999. doi: 10.1086/306844.

R. L. Hurt and M. Barsony. A Cluster of Class 0 Protostars in Serpens: an IRAS HIRES Study. *ApJL*, 460:L45+, March 1996. doi: 10.1086/309969.

R. L. Hurt, M. Barsony, and A. Wootten. Potential Protostars in Cloud Cores: H 2CO Observations of Serpens. *ApJ*, 456:686–+, January 1996. doi: 10.1086/176689.

J. H. Jeans. *Astronomy and cosmogony*. 1961.

D. Johnstone and J. Bally. Large-Area Mapping at 850 μm. V. Analysis of the Clump Distribution in the Orion A South Molecular Cloud. *ApJ*, 653:383–397, December 2006. doi: 10.1086/508852.

J. K. Jørgensen, F. L. Schöier, and E. F. van Dishoeck. Physical structure and CO abundance of low-mass protostellar envelopes. *A&A*, 389:908–930, July 2002. doi: 10.1051/0004-6361:20020681.

A. A. Kaas, G. Olofsson, S. Bontemps, P. André, L. Nordh, M. Huldtgren, T. Prusti, P. Persi, A. J. Delgado, F. Motte, A. Abergel, F. Boulanger, M. Burgdorf, M. M. Casali, C. J. Cesarsky, J. Davies, E. Falgarone, T. Montmerle, M. Perault, J. L. Puget, and F. Sibille. The young stellar population in the Serpens Cloud Core: An ISOCAM survey. *Astronomy and Astrophysics*, 421:623–642, July 2004. doi: 10.1051/0004-6361:20035775.

J. Kainulainen, H. Beuther, T. Henning, and R. Plume. Probing the evolution of molecular cloud structure. From quiescence to birth. *A&A*, 508:L35–L38, December 2009. doi: 10.1051/0004-6361/200913605.

S. Kitsionas and A. P. Whitworth. High-resolution simulations of clump-clump collisions using SPH with particle splitting. *MNRAS*, 378:507–524, June 2007. doi: 10.1111/j.1365-2966.2007.11707.x.

R. I. Klein, M. T. Sandford, II, and R. W. Whitaker. Star formation within OB subgroups - Implosion by multiple sources. *ApJL*, 271:L69–L73, August 1983. doi: 10.1086/184097.

R. S. Klessen. One-Point Probability Distribution Functions of Supersonic Turbulent Flows in Self-gravitating Media. *ApJ*, 535:869–886, June 2000. doi: 10.1086/308854.

R. S. Klessen, A. Burkert, and M. R. Bate. Fragmentation of Molecular Clouds: The Initial Phase of a Stellar Cluster. *ApJL*, 501:L205+, July 1998. doi: 10.1086/311471.

R. S. Klessen, J. Ballesteros-Paredes, Y. Li, and M.-M. Mac Low. Gravoturbulent Star Cluster Formation. In H. J. G. L. M. Lamers, L. J. Smith, & A. Nota, editor, *The Formation and Evolution of Massive Young Star Clusters*, volume 322 of *Astronomical Society of the Pacific Conference Series*, pages 299–+, December 2004.

R. S. Klessen, J. Ballesteros-Paredes, E. Vázquez-Semadeni, and C. Durán-Rojas. Quiescent and Coherent Cores from Gravoturbulent Fragmentation. *ApJ*, 620:786–794, February 2005. doi: 10.1086/427255.

J. Koda, T. Sawada, T. Hasegawa, and N. Z. Scoville. The Elongations and Supersonic Motions of Molecular Clouds. *ApJ*, 638:191–195, February 2006. doi: 10.1086/498640.

V. Könyves, P. André, A. Men'shchikov, N. Schneider, D. Arzoumanian, S. Bontemps, M. Attard, F. Motte, P. Didelon, A. Maury, A. Abergel, B. Ali, J.-P. Baluteau, J.-P. Bernard, L. Cambrésy, P. Cox, J. di Francesco, A. M. di Giorgio, M. J. Griffin, P. Hargrave, M. Huang, J. Kirk, J. Z. Li, P. Martin, V. Minier, S. Molinari, G. Olofsson, S. Pezzuto, D. Russeil, H. Roussel, P. Saraceno, M. Sauvage, B. Sibthorpe, L. Spinoglio, L. Testi, D. Ward-Thompson, G. White, C. D. Wilson, A. Woodcraft, and A. Zavagno. The Aquila prestellar core population revealed by Herschel. *A&A*, 518:L106+, July 2010. doi: 10.1051/0004-6361/201014689.

C. Kramer, J. Stutzki, R. Rohrig, and U. Corneliussen. Clump mass spectra of molecular clouds. *A&A*, 329:249–264, January 1998.

P. Kroupa. On the variation of the initial mass function. *MNRAS*, 322:231–246, April 2001. doi: 10.1046/j.1365-8711.2001.04022.x.

C. J. Lada. Star formation - From OB associations to protostars. In M. Peimbert and J. Jugaku, editors, *Star Forming Regions*, volume 115 of *IAU Symposium*, pages 1–17, 1987.

C. J. Lada. The Formation of Low Mass Stars: An Observational Overview. In C. J. Lada and N. D. Kylafis, editors, *NATO ASIC Proc. 540: The Origin of Stars and Planetary Systems*, pages 143–+, 1999.

C. J. Lada and E. A. Lada. Embedded Clusters in Molecular Clouds. *ARA&A*, 41: 57–115, 2003. doi: 10.1146/annurev.astro.41.011802.094844.

C. J. Lada, A. A. Muench, J. Rathborne, J. F. Alves, and M. Lombardi. The Nature of the Dense Core Population in the Pipe Nebula: Thermal Cores Under Pressure. *ApJ*, 672:410–422, January 2008. doi: 10.1086/523837.

E. F. Ladd, G. A. Fuller, and J. R. Deane. C 18O and C 17O Observations of Embedded Young Stars in the Taurus Molecular Cloud. I. Integrated Intensities and Column Densities. *ApJ*, 495:871–+, March 1998. doi: 10.1086/305313.

W. D. Langer and A. A. Penzias. (C-12)/(C-13) isotope ratio in the local interstellar medium from observations of (C-13)(O-18) in molecular clouds. *ApJ*, 408:539–547, May 1993. doi: 10.1086/172611.

R. B. Larson. Turbulence and star formation in molecular clouds. *MNRAS*, 194:809–826, March 1981.

R. B. Larson. Cloud fragmentation and stellar masses. *MNRAS*, 214:379–398, June 1985.

M. R. M. Leão, E. M. de Gouveia Dal Pino, D. Falceta-Gonçalves, C. Melioli, and F. G. Geraissate. Local star formation triggered by supernova shocks in magnetized diffuse neutral clouds. *MNRAS*, 394:157–173, March 2009. doi: 10.1111/j.1365-2966.2008.14337.x.

C.-F. Lee, L. G. Mundy, B. Reipurth, E. C. Ostriker, and J. M. Stone. CO Outflows from Young Stars: Confronting the Jet and Wind Models. *ApJ*, 542:925–945, October 2000. doi: 10.1086/317056.

C.-F. Lee, L. G. Mundy, J. M. Stone, and E. C. Ostriker. CO Outflows from Young Stellar Objects. *ApJ*, 576:294–312, September 2002. doi: 10.1086/341540.

C.-F. Lee, P. T. P. Ho, N. Hirano, H. Beuther, T. L. Bourke, H. Shang, and Q. Zhang. HH 212: Submillimeter Array Observations of a Remarkable Protostellar Jet. *ApJ*, 659:499–511, April 2007. doi: 10.1086/512540.

J. Lequeux. *The interstellar medium*. 2005.

A. Li. On the Absorption and Emission Properties of Interstellar Grains. In C. C. Popescu & R. J. Tuffs, editor, *The Spectral Energy Distributions of Gas-*

Rich Galaxies: Confronting Models with Data, volume 761 of *American Institute of Physics Conference Series*, pages 123–133, April 2005. doi: 10.1063/1.1913922.

Z.-Y. Li and F. Nakamura. Cluster Formation in Protostellar Outflow-driven Turbulence. *ApJL*, 640:L187–L190, April 2006. doi: 10.1086/503419.

M. Lombardi, J. Alves, and C. J. Lada. 2MASS wide field extinction maps. I. The Pipe nebula. *A&A*, 454:781–796, August 2006. doi: 10.1051/0004-6361:20042474.

M. Lombardi, C. J. Lada, and J. Alves. 2MASS wide field extinction maps. II. The Ophiuchus and the Lupus cloud complexes. *A&A*, 489:143–156, October 2008. doi: 10.1051/0004-6361:200810070.

M. Lombardi, C. J. Lada, and J. Alves. 2MASS wide field extinction maps. III. The Taurus, Perseus, and California cloud complexes. *A&A*, 512:A67+, March 2010. doi: 10.1051/0004-6361/200912670.

J. S. Mathis, W. Rumpl, and K. H. Nordsieck. The size distribution of interstellar grains. *ApJ*, 217:425–433, October 1977. doi: 10.1086/155591.

C. F. McKee and E. C. Ostriker. Theory of Star Formation. *ARA&A*, 45:565–687, September 2007. doi: 10.1146/annurev.astro.45.051806.110602.

C. F. McKee, E. G. Zweibel, A. A. Goodman, and C. Heiles. Magnetic Fields in Star-Forming Regions - Theory. In E. H. Levy and J. I. Lunine, editors, *Protostars and Planets III*, pages 327–+, 1993.

B. Merín, J. Jørgensen, L. Spezzi, J. M. Alcalá, N. J. Evans, II, P. M. Harvey, T. Prusti, N. Chapman, T. Huard, E. F. van Dishoeck, and F. Comerón. The Spitzer c2d Survey of Large, Nearby, Interstellar Clouds. XI. Lupus Observed with IRAC and MIPS. *ApJS*, 177:551–583, August 2008. doi: 10.1086/588042.

L. Mestel and L. Spitzer, Jr. Star formation in magnetic dust clouds. *MNRAS*, 116: 503–+, 1956.

M. Micono, G. Bodo, S. Massaglia, P. Rossi, and A. Ferrari. On the matter entrainment by stellar jets and the acceleration of molecular outflows. *A&A*, 364:318–326, December 2000.

F. Motte, P. Andre, and R. Neri. The initial conditions of star formation in the rho Ophiuchi main cloud: wide-field millimeter continuum mapping. *A&A*, 336:150–172, August 1998.

T. C. Mouschovias. Magnetic braking, ambipolar diffusion, cloud cores, and star formation - Natural length scales and protostellar masses. *ApJ*, 373:169–186, May

1991. doi: 10.1086/170035.

A. A. Muench, C. J. Lada, J. M. Rathborne, J. F. Alves, and M. Lombardi. The Nature of the Dense Core Population in the Pipe Nebula: Core and Cloud Kinematics from $C^{18}O$ Observations. *ApJ*, 671:1820–1831, December 2007. doi: 10.1086/523265.

P. C. Myers. Dense cores in dark clouds. III - Subsonic turbulence. *ApJ*, 270:105–118, July 1983. doi: 10.1086/161101.

P. C. Myers. Cluster-forming Molecular Cloud Cores. *ApJL*, 496:L109+, April 1998. doi: 10.1086/311256.

P. C. Myers. Filamentary Structure of Star-forming Complexes. *ApJ*, 700:1609–1625, August 2009. doi: 10.1088/0004-637X/700/2/1609.

P. C. Myers and G. A. Fuller. Density structure and star formation in dense cores with thermal and nonthermal motions. *ApJ*, 396:631–642, September 1992. doi: 10.1086/171744.

P. C. Myers, D. Mardones, M. Tafalla, J. P. Williams, and D. J. Wilner. A Simple Model of Spectral-Line Profiles from Contracting Clouds. *ApJL*, 465:L133+, July 1996. doi: 10.1086/310146.

F. Nakamura and Z.-Y. Li. Magnetically Regulated Star Formation in Three Dimensions: The Case of the Taurus Molecular Cloud Complex. *ApJ*, 687:354–375, November 2008. doi: 10.1086/591641.

D. Nutter and D. Ward-Thompson. A SCUBA survey of Orion - the low-mass end of the core mass function. *MNRAS*, 374:1413–1420, February 2007. doi: 10.1111/j.1365-2966.2006.11246.x.

S. S. R. Offner, C. E. Hansen, and M. R. Krumholz. Stellar Kinematics of Young Clusters in Turbulent Hydrodynamic Simulations. *ApJL*, 704:L124–L128, October 2009. doi: 10.1088/0004-637X/704/2/L124.

L. Olmi and L. Testi. Constraints on star formation theories from the Serpens molecular cloud and protocluster. *A&A*, 392:1053–1068, September 2002. doi: 10.1051/0004-6361:20020959.

T. Onishi, A. Kawamura, R. Abe, N. Yamaguchi, H. Saito, Y. Moriguchi, A. Mizuno, H. Ogawa, and Y. Fukui. NANTEN Observations of the Pipe Nebula; A Filamentary Massive Dark Cloud with Very Low Star-Formation Activity. *PASJ*, 51:871–881, December 1999.

E. C. Ostriker, C.-F. Lee, J. M. Stone, and L. G. Mundy. A Ballistic Bow Shock

Model for Jet-driven Protostellar Outflow Shells. *ApJ*, 557:443–450, August 2001. doi: 10.1086/321649.

P. Padoan, A. Nordlund, and B. J. T. Jones. The universality of the stellar initial mass function. *MNRAS*, 288:145–152, June 1997.

P. Padoan, M. Juvela, A. A. Goodman, and Å. Nordlund. The Turbulent Shock Origin of Proto-Stellar Cores. *ApJ*, 553:227–234, May 2001. doi: 10.1086/320636.

A. A. Penzias. Measurements of isotopic abundances in interstellar clouds. In B. H. Andrew, editor, *Interstellar Molecules*, volume 87 of *IAU Symposium*, pages 397–402, 1980.

N. Peretto and G. A. Fuller. A statistical study of the mass and density structure of Infrared Dark Clouds. *ArXiv e-prints*, September 2010.

N. Peretto, P. André, and A. Belloche. Probing the formation of intermediate- to high-mass stars in protoclusters. A detailed millimeter study of the NGC 2264 clumps. *A&A*, 445:979–998, January 2006. doi: 10.1051/0004-6361:20053324.

N. Peretto, P. Hennebelle, and P. André. Probing the formation of intermediate- to high-mass stars in protoclusters. II. Comparison between millimeter interferometric observations of NGC 2264-C and SPH simulations of a collapsing clump. *A&A*, 464:983–994, March 2007. doi: 10.1051/0004-6361:20065653.

J. E. Pineda, P. Caselli, and A. A. Goodman. CO Isotopologues in the Perseus Molecular Cloud Complex: the X-factor and Regional Variations. *ApJ*, 679:481–496, May 2008. doi: 10.1086/586883.

J. E. Pineda, E. W. Rosolowsky, and A. A. Goodman. The Perils of Clumpfind: The Mass Spectrum of Substructures in Molecular Clouds. *ApJL*, 699:L134–L138, July 2009. doi: 10.1088/0004-637X/699/2/L134.

J. E. Pineda, A. A. Goodman, H. G. Arce, P. Caselli, J. B. Foster, P. C. Myers, and E. W. Rosolowsky. Direct Observation of a Sharp Transition to Coherence in Dense Cores. *ApJL*, 712:L116–L121, March 2010. doi: 10.1088/2041-8205/712/1/L116.

D. J. Price and M. R. Bate. The impact of magnetic fields on single and binary star formation. *MNRAS*, 377:77–90, May 2007. doi: 10.1111/j.1365-2966.2007.11621.x.

D. J. Price and M. R. Bate. Inefficient star formation: the combined effects of magnetic fields and radiative feedback. *MNRAS*, 398:33–46, September 2009. doi: 10.1111/j.1365-2966.2009.14969.x.

D. J. Price and J. J. Monaghan. Smoothed Particle Magnetohydrodynamics - III. Multidimensional tests and the ∇.B= 0 constraint. *MNRAS*, 364:384–406, December 2005. doi: 10.1111/j.1365-2966.2005.09576.x.

J. M. Rathborne, C. J. Lada, A. A. Muench, J. F. Alves, and M. Lombardi. The Nature of the Dense Core Population in the Pipe Nebula: A Survey of NH_3, CCS, and HC_5N Molecular Line Emission. *ApJS*, 174:396–425, February 2008. doi: 10.1086/522889.

J. M. Rathborne, C. J. Lada, A. A. Muench, J. F. Alves, J. Kainulainen, and M. Lombardi. Dense Cores in The Pipe Nebula: An Improved Core Mass Function. *ApJ*, 699:742–753, July 2009. doi: 10.1088/0004-637X/699/1/742.

S. Redfield and J. L. Linsky. The Structure of the Local Interstellar Medium. III. Temperature and Turbulence. *ApJ*, 613:1004–1022, October 2004. doi: 10.1086/423311.

B. Riaz, E. L. Martín, H. Bouy, and R. Tata. 2MASS J17112318-2724315: A Deeply Embedded Low-mass Protostellar System in the B59 Molecular Cloud. *ApJ*, 700: 1541–1551, August 2009. doi: 10.1088/0004-637X/700/2/1541.

K. Rohlfs and T. L. Wilson. *Tools of radio astronomy*. 2000.

C. G. Román-Zúñiga, C. J. Lada, and J. F. Alves. High Resolution Near-Infrared Survey of the Pipe Nebula. I. A Deep Infrared Extinction Map of Barnard 59. *ApJ*, 704:183–195, October 2009. doi: 10.1088/0004-637X/704/1/183.

E. W. Rosolowsky, J. E. Pineda, J. Kauffmann, and A. A. Goodman. Structural Analysis of Molecular Clouds: Dendrograms. *ApJ*, 679:1338–1351, June 2008. doi: 10.1086/587685.

G. B. Rybicki and A. P. Lightman. *Radiative Processes in Astrophysics*. June 1986.

E. E. Salpeter. The Luminosity Function and Stellar Evolution. *ApJ*, 121:161–+, January 1955. doi: 10.1086/145971.

J. Scalo, E. Vazquez-Semadeni, D. Chappell, and T. Passot. On the Probability Density Function of Galactic Gas. I. Numerical Simulations and the Significance of the Polytropic Index. *ApJ*, 504:835–+, September 1998. doi: 10.1086/306099.

F. L. Schoeier, F. F. S. van der Tak, E. F. van Dishoeck, and J. H. Black. Leiden Atomic and Molecular Database (LAMDA) (Schoeier+, 2005). *VizieR Online Data Catalog*, 343:20369–+, February 2005.

N. Z. Scoville, D. B. Sanders, and D. P. Clemens. High-mass star formation due to cloud-cloud collisions. *ApJL*, 310:L77–L81, November 1986. doi: 10.1086/184785.

H. Shang, A. Allen, Z.-Y. Li, C.-F. Liu, M.-Y. Chou, and J. Anderson. A Unified

Model for Bipolar Outflows from Young Stars. *ApJ*, 649:845–855, October 2006. doi: 10.1086/506513.

F. H. Shu and F. C. Adams. Star formation and the circumstellar matter of young stellar objects. In I. Appenzeller and C. Jordan, editors, *Circumstellar Matter*, volume 122 of *IAU Symposium*, pages 7–22, 1987.

F. H. Shu, F. C. Adams, and S. Lizano. Star formation in molecular clouds - Observation and theory. *ARA&A*, 25:23–81, 1987. doi: 10.1146/annurev.aa.25.090187.000323.

R. J. Smith, P. C. Clark, and I. A. Bonnell. Fragmentation in molecular clouds and its connection to the IMF. *MNRAS*, 396:830–841, June 2009. doi: 10.1111/j.1365-2966.2009.14794.x.

L. Spitzer. *Physical processes in the interstellar medium*. 1978.

V. Straižys, K. Černis, and S. Bartašiūte. Interstellar extinction in the area of the Serpens Cauda molecular cloud. *Baltic Astronomy*, 5:125–147, 1996.

K. Sugitani, F. Nakamura, M. Tamura, M. Watanabe, R. Kandori, S. Nishiyama, N. Kusakabe, J. Hashimoto, T. Nagata, and S. Sato. Near-infrared Imaging Polarimetry of the Serpens Cloud Core: Magnetic Field Structure, Outflows, and Inflows in a Cluster Forming Clump. *ApJ*, 716:299–314, June 2010. doi: 10.1088/0004-637X/716/1/299.

Y.-W. Tang, P. T. P. Ho, P. M. Koch, and R. Rao. High-angular Resolution Dust Polarization Measurements: Shaped B-field Lines in the Massive Star-forming Region Orion BN/KL. *ApJ*, 717:1262–1273, July 2010. doi: 10.1088/0004-637X/717/2/1262.

E. J. Tasker and J. C. Tan. Star Formation in Disk Galaxies. I. Formation and Evolution of Giant Molecular Clouds via Gravitational Instability and Cloud Collisions. *ApJ*, 700:358–375, July 2009. doi: 10.1088/0004-637X/700/1/358.

N. F. H. Tothill, A. Löhr, S. C. Parshley, A. A. Stark, A. P. Lane, J. I. Harnett, G. A. Wright, C. K. Walker, T. L. Bourke, and P. C. Myers. Large-Scale CO Maps of the Lupus Molecular Cloud Complex. *ApJS*, 185:98–123, November 2009. doi: 10.1088/0067-0049/185/1/98.

F. F. S. van der Tak, E. F. van Dishoeck, N. J. Evans, II, E. J. Bakker, and G. A. Blake. The Impact of the Massive Young Star GL 2591 on Its Circumstellar Material: Temperature, Density, and Velocity Structure. *ApJ*, 522:991–1010, September 1999. doi:

10.1086/307666.

F. F. S. van der Tak, J. H. Black, F. L. Schöier, D. J. Jansen, and E. F. van Dishoeck. A computer program for fast non-LTE analysis of interstellar line spectra. With diagnostic plots to interpret observed line intensity ratios. *A&A*, 468:627–635, June 2007. doi: 10.1051/0004-6361:20066820.

E. F. van Dishoeck and M. R. Hogerheijde. Models and Observations of the Chemistry Near Young Stellar Objects. In C. J. Lada and N. D. Kylafis, editors, *NATO ASIC Proc. 540: The Origin of Stars and Planetary Systems*, pages 97–+, 1999.

E. Vazquez-Semadeni. Hierarchical Structure in Nearly Pressureless Flows as a Consequence of Self-similar Statistics. *ApJ*, 423:681–+, March 1994. doi: 10.1086/173847.

E. Vazquez-Semadeni. Molecular Cloud Evolution. *ArXiv e-prints*, September 2010.

E. Vázquez-Semadeni and N. García. The Probability Distribution Function of Column Density in Molecular Clouds. *ApJ*, 557:727–735, August 2001. doi: 10.1086/321688.

E. Vázquez-Semadeni, G. C. Gómez, A. K. Jappsen, J. Ballesteros-Paredes, R. F. González, and R. S. Klessen. Molecular Cloud Evolution. II. From Cloud Formation to the Early Stages of Star Formation in Decaying Conditions. *ApJ*, 657:870–883, March 2007. doi: 10.1086/510771.

T. Velusamy and W. D. Langer. Outflow-infall interactions as a mechanism for terminating accretion in protostars. *Nature*, 392:685–687, April 1998. doi: 10.1038/33624.

T. Velusamy, W. D. Langer, and K. A. Marsh. Highly Collimated Jets and Wide-Angle Outflows in HH 46/47: New Evidence from Spitzer Infrared Images. *ApJL*, 668: L159–L162, October 2007. doi: 10.1086/522929.

J. W. S. Vilas-Boas, P. C. Myers, and G. A. Fuller. Dense Cores of Dark Clouds. XII. ^{13}CO and C^{18}O in Lupus, Corona Australis, Vela, and Scorpius. *ApJ*, 532: 1038–1050, April 2000. doi: 10.1086/308586.

R. Visser, E. F. van Dishoeck, S. D. Doty, and C. P. Dullemond. The chemical history of molecules in circumstellar disks. I. Ices. *A&A*, 495:881–897, March 2009. doi: 10.1051/0004-6361/200810846.

A. J. Walsh, P. C. Myers, J. Di Francesco, S. Mohanty, T. L. Bourke, R. Gutermuth, and D. Wilner. A Large-Scale Survey of NGC 1333. *ApJ*, 655:958–972, February

2007. doi: 10.1086/510193.

H. Wang and T. Henning. Herbig-Haro Objects in the Lupus I and III Molecular Clouds. *AJ*, 138:1072–1081, October 2009. doi: 10.1088/0004-6256/138/4/1072.

D. Ward-Thompson, J. Di Francesco, J. Hatchell, M. R. Hogerheijde, D. Nutter, P. Bastien, S. Basu, I. Bonnell, J. Bowey, C. Brunt, J. Buckle, H. Butner, B. Cavanagh, A. Chrysostomou, E. Curtis, C. J. Davis, W. R. F. Dent, E. van Dishoeck, M. G. Edmunds, M. Fich, J. Fiege, L. Fissel, P. Friberg, R. Friesen, W. Frieswijk, G. A. Fuller, A. Gosling, S. Graves, J. S. Greaves, F. Helmich, R. E. Hills, W. S. Holland, M. Houde, R. Jayawardhana, D. Johnstone, G. Joncas, H. Kirk, J. M. Kirk, L. B. G. Knee, B. Matthews, H. Matthews, C. Matzner, G. H. Moriarty-Schieven, D. Naylor, R. Padman, R. Plume, J. M. C. Rawlings, R. O. Redman, M. Reid, J. S. Richer, R. Shipman, R. J. Simpson, M. Spaans, D. Stamatellos, Y. G. Tsamis, S. Viti, B. Weferling, G. J. White, A. P. Whitworth, J. Wouterloot, J. Yates, and M. Zhu. The James Clerk Maxwell Telescope Legacy Survey of Nearby Star-forming Regions in the Gould Belt. *PASP*, 119:855–870, August 2007. doi: 10.1086/521277.

J. P. Williams and P. C. Myers. A Contracting, Turbulent, Starless Core in the Serpens Cluster. *ApJL*, 518:L37–L40, June 1999. doi: 10.1086/312065.

J. P. Williams and P. C. Myers. Evidence for Pressure-driven Flows and Turbulent Dissipation in the Serpens NW Cluster. *ApJ*, 537:891–903, July 2000. doi: 10.1086/309084.

J. P. Williams, E. J. de Geus, and L. Blitz. Determining structure in molecular clouds. *ApJ*, 428:693–712, June 1994. doi: 10.1086/174279.

J. P. Williams, L. Blitz, and C. F. McKee. The Structure and Evolution of Molecular Clouds: from Clumps to Cores to the IMF. *Protostars and Planets IV*, pages 97–+, May 2000.

S. Zhou. In search of evidence for protostellar collapse - A systematic study of line formation in low-mass dense cores. *ApJ*, 394:204–216, July 1992. doi: 10.1086/171572.